



**Ricardo Miguel
Romão Gonçalves**

**Desenho de antenas para sensores passivos em
materiais não convencionais**

**Antenna Design for Passive Sensors in
Non-conventional Materials**



**Ricardo Miguel
Romão Gonçalves**

**Desenho de antenas para sensores passivos em
materiais não convencionais**

**Antenna Design for Passive Sensors in
Non-conventional Materials**

Dissertação apresentada à Universidade de Aveiro para cumprimento dos requisitos necessários à obtenção do grau de Doutor em Engenharia Electrotécnica, realizada sob a orientação científica de Nuno Borges de Carvalho, Professor Catedrático do Departamento de Electrónica Telecomunicações e Informática da Universidade de Aveiro e de Pedro Pinho, Professor Adjunto da Área Departamental de Engenharia Electrónica Telecomunicações e Computadores do Instituto Superior de Engenharia de Lisboa.

Apoio financeiro da Fundação para a Ciência e a Tecnologia (FCT) no âmbito de uma bolsa de investigação com ref. SFRH/BD/91249/2012.

Dedico este trabalho aos meus pais, Mário e Zélia, aos meus tios António e Fernanda, e à minha namorada Joana. Pelo apoio incondicional.

"Education is an admirable thing, but it is well to remember from time to time that nothing that is worth knowing can be taught."

– Oscar Wilde

o júri / the jury

presidente / president

Doutor Armando da Costa Duarte

Professor Catedrático da Universidade de Aveiro (por delegação da Reitoria da Universidade de Aveiro)

vogais / examiners committee

Doutor Glauco Fontgalland

Professor Titular da Universidade Federal de Campina Grande

Doutor Nuno Miguel Gonçalves Borges de Carvalho

Professor Catedrático da Universidade de Aveiro (orientador)

Doutor Henrique Manuel de Castro Faria Salgado

Professor Associado da Faculdade de Engenharia da Universidade do Porto

Doutor João Nuno Pimentel da Silva Matos

Professor Associado da Universidade de Aveiro

Doutora Luísa Rita Brites Sanches Salvado

Professor Auxiliar da Universidade da Beira Interior

agradecimentos / acknowledgements

Em primeiro lugar tenho de agradecer aos meus pais, Mário e Zélia. Pelo incansável apoio, amor e dedicação. Tenho também de agradecer aos meus tios, António e Fernanda, por sempre me incentivarem a perseguir os meus sonhos e por me ajudar a olhar o dia de amanhã com otimismo. Agradeço também aos meus padrinhos, que me ajudaram em todo o meu percurso académico, por sempre acreditarem que era capaz de aqui chegar. E não podia deixar de agradecer especialmente à minha namorada, Joana, por ser o meu porto seguro. Por estar sempre ali para me apoiar nos bons e nos maus momentos desta jornada. E por me mostrar o lado da vida que não vem nos livros.

Além destes, tenho de deixar um agradecimento aos meus orientadores. Ao Prof. Nuno Borges de Carvalho por me ter aceite como seu aluno de doutoramento, e por me ter proporcionado inúmeras oportunidades e experiências que me permitiram crescer, quer em termos científicos quer como indivíduo e por sempre confiar em mim e nas minhas capacidades. E ao prof. Pedro Pinho, pelas diversas trocas de conhecimento, pela boa disposição, pelo constante acompanhamento, preocupação e motivação, por sempre ter uma palavra de incentivo.

É também devido um agradecimento muito especial à Caroline Loss. Pela partilha de conhecimentos, pela entreeajuda no desenvolvimento do trabalho relacionado com as antenas têxteis e pela preciosa ajuda na revisão desta tese e os seus comentários valiosos.

Não posso deixar de agradecer a todos os meus amigos e colegas da Universidade de Aveiro. Ao Roberto Magueta e à Alcídia Duarte, pela ajuda no desenvolvimento das antenas em cortiça e papel e no desenvolvimento do método de caracterização. E aos restantes colegas, por todas as aventuras e desventuras, todos os momentos de farra e acima de tudo boa disposição. Pela partilha de conhecimentos e companheirismo.

Por fim, tenho de agradecer ao Instituto de Telecomunicações de Aveiro, por me ter disponibilizado todas as condições para desenvolver o meu trabalho com sucesso. Em particular ao Paulo Gonçalves e ao Hugo Mostardinha, pela ajuda na construção de protótipos e na execução de medidas dos mesmos.

Palavras-chave:

Antenas impressas, RFID, caracterização de materiais, cortiça, papel, polímeros, têxteis.

Resumo

Motivado pela larga expansão dos sistemas RFID e com o desenvolvimento do conceito de Internet das Coisas, a evolução no desenho e métodos de produção de antenas em suportes de materiais alternativos tem tido uma exploração intensiva nos últimos anos. Isto permitiu, não só o desenvolvimento de produtos no campo da interação homem-máquina, mas também tornar estes produtos mais pequenos e leves. A procura de novas técnicas e métodos para produzir eletrónica impressa e antenas em materiais alternativos é, portanto, uma porta aberta para o aparecimento de novas tecnologias. Isto aplica-se especialmente no mercado dos sensores, onde o peso, o tamanho, o consumo energético, e a adaptabilidade a diversos ambientes, têm grande relevância. Esta tese foca-se no desenvolvimento de antenas com suporte em materiais não convencionais, como os já testados papel e têxteis, mas também na exploração de outros, desconhecidos do ponto de vista eléctrico, como a cortiça e polímeros biodegradáveis usados em impressão 3D. Estes materiais são portanto usados como substrato, ou material de suporte, para diversas antenas e, como tal, as propriedades electromagnéticas destes materiais têm de ser determinadas. Assim, é apresentado neste documento uma revisão de métodos de caracterização de materiais, bem como a proposta de um método baseado em linhas de transmissão impressas, e a respectiva caracterização electromagnética de diversos materiais. Além disso, são propostos desenhos de antenas para diversos cenários e aplicações utilizando os materiais anteriormente mencionados. Com esta tese concluiu-se que a utilização de materiais alternativos é hoje uma realidade e os resultados obtidos são muito encorajadores para o desenvolvimento de um conjunto de sensores para aplicações RFID com uma grande capacidade de integração.

Keywords:

Antenna design, RFID, material characterization, cork, paper, polimers, textiles.

Abstract

The advancement of the design and fabrication of antennas using textiles or paper as substrates has rapidly grown motivated by the boom of RFID systems and the developing concept of the Internet of Things. These advancements have allowed, not only the development of products for man-machine interaction, but also to make these products smaller and lighter. The search for new techniques and methods to produce printed electronics and antennas in alternative materials is therefore an open door for new technologies to emerge. Especially in the sensors market, where weight, size, power consumption and the adaptability to the target application, are of great importance. This thesis focuses on the development of antenna design approaches with alternative materials, such as the already tested paper and textiles, but also others relatively unknown, such as cork and biodegradable polymers used in 3D printing. These materials are applied to act as substrates, or support structures for the antennas. Therefore, their electromagnetic properties need to be determined. Due to that, a review of electromagnetic characterization methods, as well as the proposal of a custom method based on printed transmission lines, is presented in this document. Besides, several antenna designs, for different application scenarios, using the previously mentioned materials, are proposed. With this thesis it was proved that it is possible to develop passive sensors in different alternative materials for RFID applications and others, which shows great promise in the use of these materials to achieve higher integration in sensing and identification applications.

Contents

Contents	i
List of Figures	iii
List of Tables	ix
List of Acronyms	xi
1 Introduction	1
1.1 Motivation	3
1.2 Main objectives	4
1.3 Organization	5
1.4 Original contributions	5
2 State-of-the-art	9
2.1 Textile substrate antennas	9
2.2 Plastic substrate antennas	11
2.3 Ceramic substrate antennas	12
2.4 Paper substrate antennas	13
2.5 Conductive materials	14
3 Dielectrics characterization methods	17
3.1 Electrical properties of materials	19
3.1.1 Electrical conductivity	19
3.1.2 Polarization, susceptibility and permittivity	22
3.1.3 Complex permittivity and dissipation factor	24
3.1.4 Linearity, homogeneity, isotropy, dispersion and relaxation time	26
3.2 Characterization methods	28
3.2.1 Resonant methods	28
3.2.2 Non-resonant methods	39
3.2.3 Single microstrip line characterization	48

3.3	Dielectric properties of non-conventional materials	59
3.3.1	Dielectric properties of paper	60
3.3.2	Dielectric properties of cork	61
3.3.3	Dielectric properties of fabrics	64
3.3.4	Dielectric properties of plastic	64
4	Antennas in non-conventional materials	69
4.1	Antennas on paper	69
4.1.1	Standalone tags on paper	70
4.1.2	Antenna for bottle labeling	73
4.2	Antennas on cork	75
4.2.1	Bottle cork stopper	75
4.2.2	Humidity sensor based on cork	80
4.3	Antennas on fabrics	85
4.3.1	Fully textile microstrip patch antennas	85
4.3.2	Cloth integrated dual band monopole antenna	89
4.4	Additively manufactured antennas	97
4.4.1	Discone antennas	98
4.4.2	Dielectric lens antennas	105
5	Conclusion	115
	Appendice A	119
	Appendice B	123
	Bibliography	229

List of Figures

1.1	Illustration of the RFID back-scattering method for communication.	3
2.1	Louis Vuitton brand logo shaped antenna as proposed in [27].	10
2.2	Flexible bow-tie antenna developed in PEN substrate, proposed in [48]. . . .	12
2.3	Schematic of the ALN-9840 "Squiggle" tag from Alien Technology [®] [62]. . .	13
3.1	Schematic of the electromagnetic characterization method's groups.	18
3.2	Measurement configuration of a square conductivity sample in the Van der Pauw geometry.	20
3.3	Measurement configuration of the colinear four-probe array method.	21
3.4	Illustration of the different types of dielectric polarization. (a) Dipole, (b) atomic and (c) electronic polarizations.	23
3.5	Vector representation of the permittivity in real and imaginary axis.	25
3.6	Permittivity variation with frequency of water at 30° C by the Debye relaxation model. (a) Debye representation and (b) Cole-Cole diagram.	28
3.7	Illustration of the side view of the dielectric rod resonator.	29
3.8	Illustration of the Split-Cylinder Resonator as proposed by Kent.	31
3.9	Illustration of the Ring Resonator structure with the mean radius of the ring denoted as r	33
3.10	Illustration of the Stripline Resonator fixture as proposed in the IPC TM-650 2.5.5.5C.	35
3.11	Illustration of the waveguide structure proposed for the cavity perturbation method.	37
3.12	Illustration of the Split-Dielectric Resonator structure.	38
3.13	Illustration of the coaxial probe measurement feature.	40
3.14	Illustration of the open-air reflection measurement (a) mono-static configuration (b) bi-static configuration.	41
3.15	Illustration of the cross-section cut of a waveguide measurement feature. . .	43
3.16	Illustration of the two different length printed transmission lines with separation of different transmission sections.	45

3.17	Illustration of the open-air transmission/reflection measurement configuration.	48
3.18	Simulation results of the input impedance of a microstrip line terminated with an open circuit for different values of dissipation factor.	50
3.19	Relation between the characteristic impedance of microstrip lines and the input impedance at resonance for perfect conductor lines.	52
3.20	Relation between the K and τ factors with the conductivity of the line conductors for different loss tangent values. (a) Relation of K and (b) relation of τ , with the inverse of the square root of the conductivity.	55
3.21	Convergence of the dissipation factor determination method with the number of iterations, for different conductivity and dielectric losses.	56
3.22	Loss tangent determination for different loss dielectrics with NRW method, approximation (3.80a) and the iterative method.	56
3.23	Photograph of the microstrip transmission lines tested. From left to right: Rogers RT6010 substrate, FR-4 substrate and LDPE (low density polyethylene) substrate.	58
3.24	Probability function of the measured microstrip lines substrate permittivity (ϵ_r) and dissipation factor ($\tan \delta$). (a) Permittivity distribution and (b) Dissipation factor distribution.	59
3.25	Microstrip lines used for permittivity measurement on (a) printer paper substrate and (b) cardboard of recycled paper substrate.	60
3.26	Measured dielectric constant and loss tangent of the samples of 80 g printer paper and cardboard in the range from 0.1 to 4 GHz.	61
3.27	Microstrip lines used for permittivity measurement on (a) natural cork substrate and (b) compressed cork substrate.	62
3.28	Measured dielectric constant and loss tangent of axial and radial samples of natural and agglomerate cork in the range from 750 to 950 MHz.	63
3.29	Photograph of the silver ink microstrip lines on PLA substrate prototypes. . .	66
3.30	Measured dielectric constant and loss tangent of samples of PLA: (a) in the range from 1 to 18 GHz and (b) in the range from 1 to 5 GHz.	67
4.1	RFID tag antenna design for paper substrate. (a) Schematic of the simulation model and (b) prototypes photograph.	70
4.2	Reading range with frequency of the RFID tags on paper and cardboard substrates	71
4.3	Normalized reading range with angle of the second prototype on cardboard (solid line) and the first prototype on paper substrate (dashed line) in the (a) XZ-plane and (b) YZ-plane.	72
4.4	Simulation model of the monopole RFID tag antenna in paper substrate. All dimensions in millimeters.	73

4.5	Simulated radiation pattern of the antenna in different scenarios with a summary of the directivities and efficiencies. (a) Standalone, (b) with the glass and liquid presence and (c) with the reflector in the back side of the bottle. . .	74
4.6	Reading range with frequency of the RFID tags on paper substrate in standalone form and on bottle	74
4.7	Simulation model and photograph of the monopole RFID tag antenna in agglomerate cork, with detail in front and top view. All dimensions in millimeters.	76
4.8	Simulated radiation patterns of the monopole RFID tag antenna considering (a) an empty bottle and (b) a filled bottle.	76
4.9	Simulation model and photograph of the conformal RFID tag antenna with detail in front and side view. All dimensions in millimeters.	77
4.10	Detail of the bottle stopper RFID tag inductive ring design. (a) Constitutive parameters illustration, (b) current distribution in the open loop and (c) current distribution in the closed loop with SMD resistance.	78
4.11	Simulated radiation pattern of the conformal RFID tag considering (a) an empty bottle and (b) a filled bottle.	79
4.12	Reading range with frequency obtained for first prototype (solid line) and second prototype (dashed line), considering (a) an empty bottle and (b) a filled bottle.	80
4.13	Normalized reading range with angle obtained for first prototype (solid line) and second prototype (dashed line) on an empty bottle: (a) XZ-plane and (b) YZ-plane; And on a filled bottle: (c) XZ-plane and (d) YZ-plane.	81
4.14	Passive humidity sensor based on RFID. (a) Schematic of the antenna with the dielectric layered structure and (b) photograph of the prototype. All dimensions in millimeters.	82
4.15	Measurement of the humidity sensor tag for different wetting conditions. (a) Minimum threshold power and (b) equivalent reading range of the tag.	83
4.16	Simulated reflection coefficient of the sensor tag antenna for different permittivity values of the outside cork slabs.	83
4.17	Threshold power variation with humidity, measured within the thermal chamber with humidity control and linearized response for comparison.	84
4.18	Textile microstrip patch antenna design. All dimensions in millimeters.	86
4.19	Photograph of the textile microstrip patch antenna prototypes.	87
4.20	Comparison between simulation and measurements for the reflection coefficient of the different manufacturing techniques of textile antennas.	87
4.21	Textile antenna design and prototype. (a) Schematic of the textile dual-band antenna; (b) Photograph of the front-view of the prototype, and (c) Back-view of the prototype. All dimensions in millimeters.	89

4.22 Simulated radiation patterns of the dual band monopole antenna at (a) 900 MHz and (b) 1800 MHz.	90
4.23 Comparison between simulated and measured reflection coefficient for the three fabric monopoles manufactured with and without steam.	92
4.24 SEM images: cross-section of the antenna assembled without steam on the left and with steam on the right.	92
4.25 Photograph of the embroidered antenna prototypes.	94
4.26 Comparison between simulated and measured reflection coefficient of the embroidered antenna prototypes.	94
4.27 Photograph of the jacket with the embedded textile antenna in the anechoic chamber setup. (a) Jacket in standalone measurement, (b, c) jacket dressed into human subject.	96
4.28 Comparison between simulated and measured reflection coefficient of the integrated antenna with and without the human body presence.	96
4.29 Measured radiation pattern of the integrated antenna into the jacket, with and without the presence of the human body, at (a) 900 MHz and (b) 1800 MHz. .	97
4.30 Illustration of the evolution from dipole, to biconical and to the disccone antenna.	98
4.31 Photograph of the prototypes of the first and second iterations of the disccone antenna.	99
4.32 Schematic of the first and second iterations of the disccone antenna. (a) First disccone antenna schematic with air gap feeding and (b) Second disccone antenna with PLA gap feeding. All dimensions in millimeters.	100
4.33 Simulated versus measured reflection coefficient of the (a) first iteration and (b) second iteration of the disccone antenna.	100
4.34 Simulated radiation patterns of the second iteration of the disccone antenna at (a) 400 MHz, (b) 800 MHz, (c) 1500 MHz and (d) 2000 MHz.	101
4.35 Simulated (dashed line) versus measured (solid line) radiation patterns of the first iteration of the disccone antenna in the XZ-plane at (a) 400 MHz, (b) 800 MHz, (c) 1500 MHz and (d) 2000 MHz.	103
4.36 Simulated (dashed line) versus measured (solid line) radiation patterns of the second iteration of the disccone antenna in the XZ-plane at (a) 400 MHz, (b) 800 MHz, (c) 1500 MHz and (d) 2000 MHz.	104
4.37 Schematic of the slot coupled microstrip patch antenna used to feed the dielectric lens. (a) Front view and (b) bottom view.	106
4.38 Spherical profile dielectric lens antenna. (a) schematic of the lens antenna, (b) photograph of the assembled prototype and (c) photograph of the prototype with all its constitutive pieces. (All dimensions are in mm).	108

4.39	Simulated versus measured reflection coefficient of the (a) hemispherical lens, (b) smaller parabolic lens, (c) larger parabolic lens and (d) comparison between the three lens antenna prototypes.	109
4.40	Parabolic profile dielectric lens antenna. (a) schematic of the small lens antenna, (b) schematic of the large lens antenna and (c) photograph of the prototype with all its constitutive pieces, from left to right, the bottom of the feeding patch antenna, the top microstrip patch and the printed large and small parabolic profile lens. (All dimensions are in mm).	110
4.41	Simulated 3D representation of the normalized radiation pattern of (a) hemispherical lens, (b) smaller parabolic lens and (c) larger parabolic lens.	111
4.42	Simulated (marked black line) versus measured (solid blue line) radiation patterns of the (a) hemispherical lens in the XZ plane, (b) hemispherical lens in the YZ plane, (c) small parabolic lens in the XZ plane, (d) small parabolic lens in the YZ plane, (e) large parabolic lens in the XZ plane and (f) large parabolic lens in the YZ plane.	113
A.1	Schematic of the passive RFID tag antenna monostatic read range measurement setup.	120
A.2	Schematic of the passive RFID tag antenna bi-static read range measurement setup.	120

List of Tables

2.1	Brief summary of conductive materials used for development of antennas and circuits in non-conventional materials.	15
3.1	Typical values for permittivity and dissipation factor of common materials. . .	24
3.2	Simulated results for resonance, corrected resonance and characteristic impedance for a microstrip line on a varying dissipation factor substrate.	51
3.3	Simulated input impedance of several microstrip lines for different substrates	53
3.4	Calculated K and τ coefficients for several lines	54
3.5	Dielectric substrate samples physical dimensions	57
3.6	Estimated values of the three sample dielectric slabs based on the proposed method and reference values from literature	58
3.7	Measured and calculated relevant values for permittivity determination of the paper substrate materials	61
3.8	Measured and calculated relevant values for permittivity determination of the cork substrate materials	62
3.9	Brief summary of the properties of some textile materials and leathers.	65
4.1	Meandered dipole antenna dimensions	71
4.2	List of prototypes developed and techniques used for the manufacturing of textile microstrip patch antennas.	86
4.3	Characteristics of the textile materials used to develop wearable antennas. .	91
4.4	Parameters of the embroidered antenna prototypes.	93
4.5	Simulated directivities and efficiencies of the disccone antennas.	101
4.6	Dimensions of the microstrip patch antennas used to feed the dielectric lens antennas.	107
4.7	Simulated and measured gain and efficiency of the three different lens antenna prototypes and the respective feeding microstrip patch antennas. . . .	111

List of Acronyms

AMC	Artificial Magnetic Conductor
CNC	Computer Numeric Control
DCS	Digital Cellular System
EBG	Electromagnetic Band-gap
EM	Electromagnetic
GPS	Global Positioning System
GSM	Global System for Mobile Communication
HPBW	Half Power Beam Width
IoT	Internet of Things
ISM	Industrial, Scientific and Medical
LCP	Liquid Crystal Polymer
LTCC	Low Temperature Co-fired Ceramics
MMIC	Monolithic Microwave Integrated Circuit
MUT	Material Under Test
NRW	Nicolson-Ross-Wier
PCB	Printed Circuit Board
PDMS	Polydimethylsiloxane
PEN	Polyethylene Naphtalate
PET	Polyethylene Terephtalate
PIFA	Planar Inverted F Antenna
PLA	Polyactic Acid
PTFE	Polyetrafluoroethylene
RF	Radio Frequency
RFID	Radio Frequency IDentification
RR	Ring Resonator
RRM	Ring Resonator Method
SCR	Split Cylinder Resonator
SDR	Split Dielectric Resonator
SEM	Scanning Electron Microscope
SIW	Substrate Integrated Waveguide
UHF	Ultra High Frequency
UWB	Ultra Wide Band
VHF	Very High Frequency
WAP	Wireless Access Point
WLAN	Wireless Local Area Network

Chapter 1

Introduction

Antennas are essential devices for the efficient operation of any wireless system. These are transitional devices that can transform guided radio waves into unguided radio waves that are radiated to the atmosphere and *vice-versa*. Given the large number of wireless communication applications, the requirements of the antennas used in each system are very diverse and more demanding each day. Therefore, the research on antennas is wide and the continuous thrive for new and better antennas attracts many scientists and engineers.

Antennas originated almost one hundred and thirty years ago, by the hand of Heinrich Hertz when he tried to prove the existence of electromagnetic waves. The first antenna he proposed is what is nowadays known as a dipole, many times called the Hertz Dipole in his honor. However, the most influential contributors for the development of antennas and their importance were Nikola Tesla and Guglielmo Marconi. The former more focused on the application of electromagnetic waves for energy transfer, the later more focused on the transmission of information.

Since Hertz experiment, antennas have evolved considerably. On one hand, we have large antenna development for long range transmission systems, such as TV broadcast, radio links and also space communication systems. On the other hand we have small antennas, such as mobile phones, WAPs (Wireless Access Point) and laptops.

In the case of small antennas, engineers have been developing new solutions in order to promote integrability and adaptability of their designs to the desired final purpose of a given device. In the recent years, due to the massification of the wireless telephony services, there has been a large investment in the development of antennas for mobile phones. That subject is still of great interest nowadays due to the growing number of technologies and standards used for mobile communications, which need to be integrated into a single device, and yet, operate seamlessly.

The antennas for current mobile devices are very interesting engineering challenges. The antennas should comply with different frequency bands, present larger bandwidth and higher gain, while maintaining small sizes and conformal structures. Moreover, the development of

the antenna does not take into account solely the antenna by itself, but has to account for the environment of the application scenario. For instance, an antenna for a mobile phone has to take into account the materials that will surround the antenna, such as the remaining electronics, the cellphone shell and the human hands and head, in order to guarantee that the antenna will work properly in the real world.

Antenna design challenges, however, do not arise exclusively in mobile communications. The recent use of microwave frequency radiation in biotechnology and medicine has opened a new gateway for the development of antennas specifically designed to work in the vicinity of the human body. Such as antennas used in reflectometry and tomography, which have large directivity and wide bandwidth in order to get data from the interactions of the radiation with the tissues. And small antennas for body-worn applications, with conformal designs and different radiation characteristics based on the scenario of application. For body-worn applications the development of antennas using textile materials is critical, since it allows the seamless integration of the antenna into clothing, without any extra constraint for the user.

Then there's the increasing number of appliances with wireless communication capabilities. Such as watches, console remotes, TVs, among many others. The increasing need to introduce wireless communication into several devices creates new challenges for antenna design. Which leads us to the advent of the IoT (Internet of Things), also referred as the core of the new industrial revolution, and the explosion of the connected devices. The principle of the IoT is to create very large networks of interconnected devices, from home appliances, to cars and buildings, each full of embedded electronics, sensors and actuators, in which all are able to connect to the internet and create interactions between a user with a computing device, like a smartphone, and the object.

The "things" in this internet connected world can be heart monitoring implants, small analysis devices for food and environment monitoring, to tracking or identification devices for cattle, or even simple tracking devices for lost keys. The purpose of the "things" is to collect data, through a set of sensors, and spread or transmit this data to the internet, therefore creating a data flow between the devices.

On the light of all that has been stated previously on this Introduction chapter, one can say that antenna design is, nowadays, a challenging engineering task that relies heavily on simulations. Requiring knowledge, not only of the established electromagnetic equations, but a wide knowledge of numerical methods of simulation and a clear understanding of the interaction of electromagnetic fields with different materials and their constitutive characteristics.

Considering the above mentioned facts, it is safe to say that the research in antennas is a very active and challenging field with considerable potential to explore. In the following subsections we will be presenting the motivation for this PhD work: What was addressed; It's importance and applications; And how the problem was solved through a set of objectives.

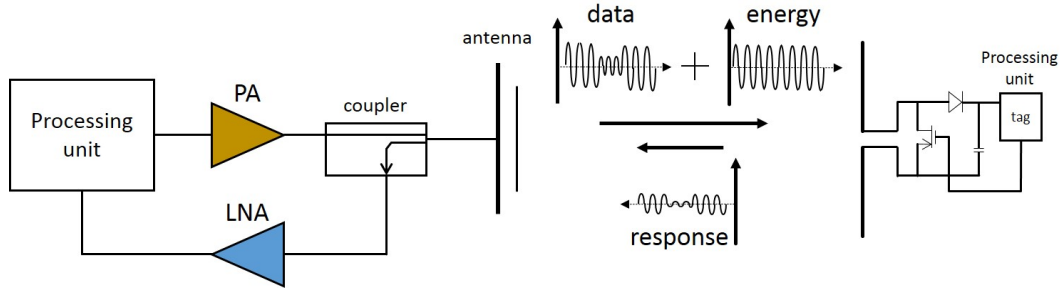


Figure 1.1: Illustration of the RFID back-scattering method for communication.

1.1 Motivation

The concept of the IoT was first envisioned more than thirty years ago, when the first smart device connected to a network was created. It was a Coke vending machine in the Computer Science Department of Carnegie Mellon University [1], back in 1982. A decade further, however, Raji published an article in IEEE *Spectrum* magazine, which better described the whole concept [2]. But it was not until 1999, when the term Internet of Things was coined by Kevin Ashton, the creator of the global standard for RFID (Radio Frequency Identification), which was a technology that was created specially thought for the implementation of this reality [3].

Although the idea has been presented more than thirty years ago, and the technology to create it, nearly twenty, the IoT concept is only recently, effectively, taking shape [4]. In order to make it grow, a large number of sensor nodes with ultra-low power consumption (in operation), ideally battery-less, have to be implemented. Furthermore, all of these devices should be connected to the cloud. In order to accomplish this, antennas are required, and they need to be integrated in the most varied number of scenarios, which create opportunities for the development of innovative approaches. One of the demands is that these antennas are integratable into such varied number of materials, and so be present in a range of alternative to conventional PCB (Printed Circuit Board) materials. Materials such as plastic, paper, fabrics, wood, cork, glass, among others.

As stated previously, one of the key technologies for the development of the concept of the IoT is the RFID technology. The back-scattering communication technique used in RFID, illustrated in Fig. 1.1, allows the development of simple and low-power wireless devices able to sense different sets of data and communicate their data easily and efficiently only when asked to do so, without creating unnecessary clutter in the propagation environment.

RFID technology is applied in an increasing number of applications from identification and localization to various types of monitoring and sensing [5, 6]. Therefore, this technology has been a large driving force into the research of new materials for the fabrication of antennas. The exploration of low-cost easily accessible materials such as textiles, paper or

PET (polyethylene terephthalate) and even plywood [5, 7] has been considered. The development of techniques such as inkjet-printing of conductive inks has allowed the design and manufacture of printed conformal antennas in low-cost flexible substrates, that boosted the RFID acceptance into the market.

The expansion of the RFID technology has boosted the development of new application scenarios for the technology, which, a few years back, was restricted to anti-theft systems and access management. After the employment of RFID to electronic toll collecting systems, luggage tracking and public transportation access management. We've started to see this technology in more complex scenarios and for many different applications. One of such cases is for indoor localization systems [8] or tagging of difficult targets such as liquid filled bottles [9, 10, 11] and metallic objects [12].

In this thesis the aim is to study different materials, such as cork, paper, plastic and textiles, in terms of electromagnetic properties and their suitability for the development of antennas. Ultimately, present different design solutions of antennas integrated into the mentioned materials. Mostly for, but not restricted to, RFID and passive sensing applications.

1.2 Main objectives

As previously stated, this thesis aims at the study of the design and development techniques of antennas in different, alternative, support materials. In order to achieve this larger goal, a set of smaller objectives must be fulfilled. These objectives are described in this section.

The study of characterization techniques and methodologies for the estimation of electromagnetic properties of materials comprises the first part of this thesis. The material's properties are essential to develop antennas that can couple and be embedded into the previously mentioned materials. Conductive and dielectric materials both influence, in their own way, the propagation of the electrical and magnetic fields generated in their vicinity. Therefore, the characteristics of the materials used to build the antenna development and placed in close proximity to it must be well characterized.

The development of the antennas, designed around different materials in order to assure conformability and easy integration with the target applications comprise the second part of this thesis. In this part of the thesis, several antenna prototypes will be developed in different support materials for different kinds of application, for instance: UHF (Ultra High Frequency) antennas for passive sensors and RFID systems; Antennas for common communication technologies, WiFi, Bluetooth and GSM (Global System for Mobile Communications); and antennas that take advantage of dielectric materials in order to enhance their radiation characteristics (e.g. lens antennas for radiation focus).

The global objective of this thesis is therefore to provide proofs of concept that will forge

the future of wireless communications and will pave the way into the IoT.

1.3 Organization

This thesis is organized into five chapters with several sections. In this first chapter an introduction to the thesis work was presented, along with the motivation and objectives. In the following chapter the state-of-the-art relative to antenna development with alternative materials, namely paper, textiles, plastic and ceramics, as well as a revision of conductive materials used, is presented. In Chapter III, an extensive (yet not completely thorough or complete) review of several characterization methods, from resonant methods to broadband methods, to test solid bulk materials or thin sheets, from methods to test semi-solids and liquids, is presented. Along with a method that has been developed during the course of this thesis, to measure the permittivity of a flat dielectric slab material, based on the measurement of the input impedance of a open-circuit terminated microstrip line, presented in section 3.2.3. In Chapter IV several antennas developed with different materials, namely, paper, cork, fabrics and plastic through 3D printing, are presented. Finally in Chapter V some conclusions, regarding the work hereby presented in this document, are drawn and a discussion of the possible future direction of this work is also discussed.

1.4 Original contributions

As stated in the previous sections, the main purpose of this thesis is the development of antennas, for different kinds of applications, using alternative manufacturing materials. A few proposals have been made which have been validated and recognized by the scientific community, through the following original contributions both in international journals and conferences:

Book Chapters:

- N.B. Carvalho, P. Pinho, A. Boaventura, **R. Gonçalves**, R. Correia, “Far-Field Wireless Power Transmission For Low Power Applications”, Chapter 6 in, *Frontiers of Research and Development of Wireless Power Transfer*, CMC Books, Tokyo, 2016

Publications in Journals:

- **R. Gonçalves** *et al.*, “Wireless energy transfer: Dielectric lens antennas for beam shaping in wireless power transfer applications”, *Comptes Rendus Physique* (2016), <http://dx.doi.org/10.1016/j.crhy.2016.11.004>
- **R. Gonçalves**, R. Magueta, P. Pinho, N. B. Carvalho, “Dissipation Factor and Permittivity Estimation of Dielectric Substrates Using a Single Microstrip Line Measurement”,

Applied Computational Electromagnetic Society Journal, Vol. 31, No. 2, pp. 118-125, 2016

- C. Loss, **R. Gonçalves**, C. Lopes, P. Pinho, R. Salvado, “Smart Coat with a Fully-Embedded Textile Antenna for IoT Applications”, *Sensors*, Vol. 16, No. 6, pp. 938, 2016
- **R. Gonçalves**, S. Rima, R. Magueta, P. Pinho, A. Collado, A. Georgiadis, J. Hester, N. B. Carvalho, M. M. Tentzeris, “RFID-based wireless passive sensors utilizing cork materials”, *IEEE Sensors Journal*, Vol. 15, No. 12, pp. 7242-7251, 2015
- L.R. Roselli, N. B. Carvalho, F. Alimenti, P. Mezzanotte, G. Orecchini, M. Virili, C. Mariotti, **R. Gonçalves**, P. Pinho, “Smart Surfaces: Large Area Electronics Systems for Internet of Things Enabled by Energy Harvesting”, *Proceedings of the IEEE*, Vol. 102, No. 11, pp. 1723 - 1746, November, 2014.
- **R. Gonçalves**, A. Duarte, R. Magueta, N. B. Carvalho, P. Pinho, “RFID tags on paper substrate for bottle labelling”, *Procedia Technology*, Vol. 17, No. 1, pp. 65 - 72, November, 2014
- R. Salvado, C. Loss, **R. Gonçalves**, P. Pinho, “Textile materials for the design of wearable antennas: a survey”, *Sensors*, Vol. 12, No. 11, pp. 15841-15857, 2012

Publications in Conferences:

- A. Boaventura, **R. Gonçalves**, D. Belo, P. Pinho, N. B. Carvalho, “A software-defined radio RFID reader design with improved wireless power transfer capabilities”, *Proc. 2016 IEEE Wireless Power Transfer Conference (WPTC 2016)*, Aveiro (Portugal), May 2016
- **R. Gonçalves**, P. Pinho and N. B. Carvalho, “Design and implementation of a 3D printed discone antenna for TV broadcasting system”, *Proc. 2015 IEEE APS/URSI International Symp. (APS 2015)*, Vancouver (Canada), July 2015
- C. Mariotti, **R. Gonçalves**, M. Virilli, N. B. Carvalho, L. Roselli, P. Pinho, “Dual-frequency antennas embedded into the floor for efficient RF “energy evaporation””, *Proc. 2015 IEEE 65th Electronic Comp. and Tech. Conf. (ECTC 2015)*, San Diego (California, USA), May 2015
- C. Mariotti, **R. Gonçalves**, L. Roselli, N. B. Carvalho, P. Pinho, ““Energy evaporation: The new concept of indoor systems for WPT and EH embedded into the floor”, *Proc. 2015 IEEE MTT-S International Microwave Symp. (IMS 2015)*, Phoenix (Arizona, USA), May 2015

- **R. Gonçalves**, P. Pinho, N. B. Carvalho, M. M. Tentzeris, “Humidity passive sensors based on UHF RFID using cork dielectric slabs”, *Proc. 2015 9th European Conference on Antennas and Propagation (EuCAP 2015)*, Lisbon (Portugal), May 2015
- **R. Gonçalves**, P. Pinho and N. B. Carvalho, “Passive Sensors for Food Quality Monitoring and Counterfeiting”, *Proc IEEE Sensors*, Valencia, Spain, November, 2014
- S. Rima, **R. Gonçalves**, A. Collado, A. Georgiadis, N. B. Carvalho, “Passive UHF RFID Enabled Temperature Sensor Tag on Cork Substrate”, *Proc IEEE Int. Conf. on RFID-Technology and Applications*, Tampere, Finland, September, 2014.
- **R. Gonçalves**, R. Magueta, P. Pinho and N. B. Carvalho, “Passive Sensors Embedded Into Logistic Chains”, *Proc. URSI General Assembly*, Beijing, China, August, 2014
- **R. Gonçalves**, R. Magueta, P. Pinho and N. B. Carvalho, “RFID passive tag antenna for cork bottle stopper”, *Proc. 2014 IEEE APS/URSI International Symp. (APS 2014)*, Memphis (Tennessee, USA), July 2014
- **R. Gonçalves**, R. Magueta, A. Duarte, P. Pinho and N. B. Carvalho, “UHF RFID tag antenna for bottle labeling”, *Proc. 2014 IEEE APS/URSI International Symp. (APS 2014)*, Memphis (Tennessee, USA), July 2014
- **R. Gonçalves**, S. Rima, R. Magueta, A. Collado, A. Georgiadis, N. B. Carvalho and P. Pinho, “RFID tags on cork stoppers for bottle identification”, *Proc. 2014 IEEE MTT-S International Microwave Symp. (IMS 2014)*, Tampa Bay (Florida, USA), June 2014
- **R. Gonçalves**, J. Reis, E. Santana, N. B. Carvalho and P. Pinho, “Smart Environment Technology as a Possible Enabler of Smart Cities”, *Proc. 2014 IEEE MTT-S International Microwave Symp. (IMS 2014)*, Florida (US), June 2014
- **R. Gonçalves**, R. Magueta, A. Duarte, N. B. Carvalho and P. Pinho, “Investigation into cork substrate printed antennas for RFID applications”, *Proc. URSI Seminar of the Portuguese Committee*, Lisboa (Portugal), November 2013
- **R. Gonçalves**, N. B. Carvalho and P. Pinho, “Metamaterial inspired compact printed antenna for WLAN applications”, *Proc. 2013 IEEE APS/URSI International Symp. (APS 2013)*, Florida (US), July 2013
- **R. Gonçalves**, N. B. Carvalho, P. Pinho, C. Loss and R. Salvado, “Textile Antenna for Electromagnetic Energy Harvesting for GSM900 and DCS1800 bands”, *Proc. 2013 IEEE APS/URSI International Symp. (APS 2013)*, Florida (US), July 2013
- **R. Gonçalves**, J. Reis, E. Santana, N. B. Carvalho and P. Pinho, “Smart Floor: Indoor navigation based on RFID”, *Proc. 2013 IEEE Wireless Power Transfer Conference (WPTC 2013)*, Perugia (Italy), May 2013

Chapter 2

State-of-the-art

As referred in the previous chapter, the IoT concept is currently a major topic of research and development. Yet, to make this concept reality, there's several aspects of the technology to develop. The concept of the IoT is based on wireless communications, which inherently need antennas. In order to incorporate this communicating systems in every object of our daily lives, there's two approaches to take in antenna development for IoT: On one hand, there's the antenna miniaturization; on the other hand, there's the development of antennas that can be embedded or integrated directly into the objects, that is, antennas developed around different kinds of materials.

There is an extensive work done on antenna miniaturization in the last twenty years [13, 14, 15], especially due to the expansion of the mobile phones [16]. On the other hand, the development of antennas in non-conventional materials, was not much explored until recent years. Especially with the advent of 3D printing in the past couple of years, there's been much more focus on the development of innovative antenna designs with different kinds of materials.

In this chapter, there's an overview of antennas developed with non-conventional materials, and a look into most of these proposals to see which materials have been explored and how. Most of the work developed on this matter has been essentially with textiles, which we present in the first section of this chapter, but there's also antennas developed with plastic, ceramic and paper. There's also a last section on this chapter discussing conductive materials that are used in conjunction with the previously referred dielectric materials, in order to develop antennas.

2.1 Textile substrate antennas

Body worn and body sensing applications are one of the most interesting thematic under the IoT flag. For sports apps or medical use, the development of several sensing platforms

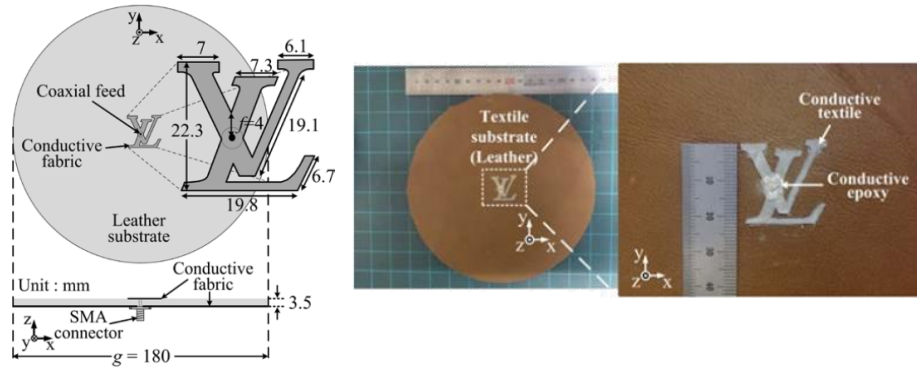


Figure 2.1: Louis Vuitton brand logo shaped antenna as proposed in [27].

that can be seamlessly integrated into clothes are being researched and developed by several institutes and companies around the globe [17, 18]. To make this sensing platforms communicate, they need antennas. These antennas should also be integrated and be conformal to the clothes and be able to operate in the presence of the human body [19].

The first reported proposal of an antenna built on textile materials dates back to 2001, and was proposed by P.J. Massey in [20]. A considerable number of proposals have followed and were reviewed in [21, 22, 23, 24], in which it is clear that the research applied to the development of textile antennas is an active and interesting subject.

Some more recent proposals have been presented, such as [25, 26, 27]. In the first case [25], a PIFA (Planar Inverted F Antenna) built in a felt substrate and three different conductive surfaces is shown. The performance of the several conductors, which are copper tape and two commercial conductive fabrics, is compared to prove the good performance of conductive textiles when compared to a more conductive material. Also, a slotted version of the PIFA is proposed to improve the radiation efficiencies of the antenna in on-body operation regime, with overall efficiencies between 34 and 62%, depending on the body location of the antenna, which are very reasonable radiation results. As for Agneeessens *et al.* [26], they proposed a SIW (Substrate Integrated Waveguide) technique in conjunction with a quarter-mode cutting in order to obtain a whole textile antenna structure, with good mechanical toughness and performance stability. The antenna is also tested on-body and is proven to guarantee relatively the same radiation properties as in off-body operation. In the last case [27], a more applicational venture is taken and the versatility of the textile antennas is put to test by showcasing an antenna with a brand logo shape, which is shown in Fig. 2.1, that can perform nicely at the ISM bands of 2.45 and 5.8 GHz. Other proposals of brand logo shaped antennas can also be found on [28, 29].

The body worn systems are not only endowed with sensing, processing, actuation and communication abilities, but with energy harvesting and storage applications as well, emerging as a solution to the challenges of ubiquitous monitoring of people in several differ-

ent contexts. In this sense, several developments have emerged in the past few years [30, 31, 32, 33].

Besides the design proposals, we've also seen some studies dedicated to the effects of the conductive threads or fabrics in the radiation properties of the antennas, as in [34], the effects of crumpling on the antenna as shown in [35], or even the deterioration effects that the washing cycles have on textile antennas [36, 37].

It is clear, from the results presented by the previously mentioned studies, that textile antennas have some complexity involved in its manufacturing in order for them to perform efficiently. A lot has to be taken into consideration that is usually not an issue for traditional printed antennas on common substrates. From the uncontrolled characteristics of the materials used in the manufacturing, the strain and stresses that these antennas are subject to during their lifetime [38, 39, 40], and the harsh environments they are exposed to, such as washing machines and environmental conditions [41], there is a lot to be considered in order to make a functional antenna on textile materials, that at the same time is seamless, does not constrain the mobility of the user and performs as expected in the vicinity of a human body considering all its range of motion.

2.2 Plastic substrate antennas

Given that the IoT goal is to connect everything to everyone, not only textile sensors and antennas are required. For that reason, other materials like plastic, paper or ceramics have been investigated.

Plastic and paper materials were already being applied in the design and manufacturing of passive RFID tags [5, 6]. But the design of microwave component such as printed filters, couplers and/or antennas, is much more dependent on the characteristics of the substrate than the passive RFID tags based on inductive coupling techniques. However, there is also active RFID tags that work on higher frequencies and, for those, the dielectric properties are important to be known in the design process. Still, the application of passive RFIDs in materials such as paper and plastics, opened the doors for the development of microwave components on the same composites.

In [42] various methods for material characterization are employed to determine the characteristics of a LCP (Liquid Crystal Polymer) composite. Printed transmission lines are designed with the values determined to test and assure the stable characteristics of the material and the good results obtained allowed further development on this material. In [43, 44, 45] antennas and other RF components for different applications designed with a LCP substrate are presented. These have good flexibility allied with robustness that grants them high versatility for different applications. From the results presented in the referred publications, it was proven that LCP can be effectively used as a substrate for printed RF components, in-

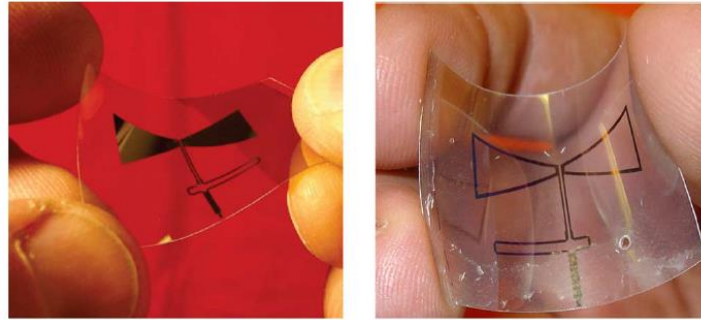


Figure 2.2: Flexible bow-tie antenna developed in PEN substrate, proposed in [48].

cluding antennas, with good performance characteristics over their respective bandwidths thus showcasing the impressively stable performance of LCP as a dielectric substrate.

Another possible substrate are polymeric type materials, such as PEN (Polyethylene Naphthalate) [46, 47, 48] and PET. Once again, also on this type of materials, the results between measurements and simulations agree relatively well and show that it is possible to design efficient antennas with the desired properties in plastic based substrates, if the electromagnetic characteristics are well known. Moreover, this solution is very interesting as it allows the creation of very thin and conformal antennas that can be easily applied to any kind of surface and is more water resistant when compared to the textile antennas, which deteriorate more easily with the washing cycles. An example is shown in Fig. 2.2 from [48].

Furthermore, for higher frequency RFID systems these materials have become interesting. In [49] the design of a printed antenna for an active RFID tag is fabricated and tested for different kinds of materials including paper, well board, plastic and glass. Concluding that plastic allows the design of printed antennas quite similar to a microwave conventional substrate and that the use of silver ink performed quite reasonably in terms of readability range when compared to a typical RFID tag of gold-plated copper on a microwave conventional substrate. In [50] an approach using PDMS (Polydimethylsiloxane) as the substrate and electrical plated thread are used to make an embroidered RFID tag working in the US band, that is able to withstand some deformation and straining, and is also able to operate in the vicinity of other dielectric materials.

2.3 Ceramic substrate antennas

Besides the previously shown textile and plastic antennas, there's also development of antennas on ceramic substrates. The LTCC (Low Temperature Co-fired Ceramic) technology, commonly used for the development of MMIC (Monolithic Microwave Integrated Circuit) chips, was one of the enablers and has also been applied to the design of antennas on ceramics in a wide range of frequencies, from 900 MHz to 60 GHz [51, 52, 53, 54].



Figure 2.3: Schematic of the ALN-9840 "Squiggle" tag from Alien Technology[®] [62].

Besides the LTCC based, there's also some proposals of printed antennas on ceramic substrates like Alumina, (Al_2O_3), by printed screen methods [55, 56]. These were developed for WLAN (Wireless Local Area Network) applications. The higher permittivity, when compared to traditional epoxy FR-4 substrates, allowed the design of smaller antennas. This is probably not the best application, nor reason, to use a ceramic substrate. However, it proves the feasibility of the concept.

The large permittivity of the ceramic materials make them very interesting choices to make very small antennas, that are very useful for different kinds of applications such as mobile communication devices [57, 58] or for biomedical implanted applications [59]. The stability of these materials turn them into interesting targets for constrained applications where very stringent operation performance is required. That is why these substrates have been used for the development of GPS (Global Positioning System) receptor antennas [60, 61].

These, however, are very expensive materials and manufacturing processes. Moreover, they're not easily adaptable to moveable scenarios as the case of on-body applications, where conformal and malleable antennas are required, in order not to interfere with the user. They can be interesting however, for very high temperature application scenarios, or for the exploration of mm-waves for communication, since these are usually isotropic and with stable dielectric properties over wide frequency ranges.

Ceramic ended up being just roughly explored during the development of this thesis work and being discarded from the final results presented, mainly due to lack of publications. However, this brief exploration of the state-of-the-art in ceramic antenna development, being part of the thesis initial proposal, was maintained in the final version.

2.4 Paper substrate antennas

As already mentioned, one of the materials used for RFID applications as a substrate is paper. Not only for HF applications but also for UHF, as the case of the RFID tags sold by Alien Technology[®] [62], as the example shown in Fig. 2.3.

Some techniques for easier fabrication based on inkjet-printing of this kind of antennas have been proposed in [63, 64, 65, 66, 67]. In these cases, conductive silver inks are used in printer cartridges and the antennas are printed directly into paper from a computer design,

like any digital document.

This technique has allowed the development of flexible antennas not only for the RFID systems. There has been recent proposals for UWB (Ultra Wide Band) antennas with paper substrates, which have shown good performance, allowing for high bandwidths, and also average gains and satisfactory radiation patterns, [68, 69].

There's also proposals of more advanced structures designs for antennas on paper substrates. In [70], a monopole antenna backed with an EBG (Electromagnetic Band-Gap) structure, both printed on paper substrate with inkjet conductive ink is presented for a wearable bio-monitoring solution. In [71, 72], AMC (Artificial Magnetic Conductor) structures, both printed on paper, are used to create a printed antenna with good gain, average to wide bandwidth and also low profile.

2.5 Conductive materials

So far we've looked into the possible substrates that can be used to develop conformal antennas for several applications with many different kinds of materials. Nearly all of the before-mentioned antennas are printed into the substrate. However, most of these materials, unlike common substrate materials, don't come previously metalized with copper. In this subsection conductive materials used in the development of these antennas are investigated and discussed.

In the case of the textile antennas, several approaches for the conductive materials have been proposed. Conductive textile materials can be obtained through the integration within their structure of fibres, filaments or yarns that are intrinsically conductive, such as copper, aluminium, stainless steel, silver, carbon, nickel, etc. or by creating coatings with conductive material. These coatings, such as ones with conductive polymers, can be used on fibres, yarns or textile materials, such as woven, knits and nonwovens [73].

The most common approach is the use of a conductive fabrics, such as Zelt (Woven 100% polyamide Cu/Sn plated, manufactured by Less EMF Inc., USA) or Flectron® (Woven 100% polyester Ni/Cu coated, manufactured by Laird Technologies, USA). Also, in the past few years the use of conductive yarns has grown in popularity with the use of embroidery techniques for antenna manufacturing [74, 75, 76]. Another way to integrate conductive yarns into the textiles is through the three-dimensional weaving technique, contributing to improve the mechanical robustness of the textile antennas [77].

Copper tape has also been applied in other surfaces, such as paper or plastic. Copper tape is commonly used to make corrections in electronic circuits connections due to the ease of application and good conductivity values, very close to the annealed copper values. Besides, it is also easy to obtain the antenna and circuit designs with a good degree of accuracy by using methods of production equivalent to those of traditional PCBs, using a

Table 2.1: Brief summary of conductive materials used for development of antennas and circuits in non-conventional materials.

Type	Description	Composition	Conductivity (S/m)
Metallic	Annealed copper	Electrodeposited Cu	5.8×10^6
Metallic	Copper tape	Electrodeposited Cu	$\simeq 4.5 \times 10^6$
Fabric	Zelt [®]	Cu/Sn plated poly-amide	$\simeq 0.1 \times 10^6$
Fabric	Electron [®]	Ni/Cu plated poly-amide	$\simeq 0.1 \times 10^6$
Yarn	Stainless steel	Steel fibers embedded	0.275×10^3
Ink	Silver base ink	Ag nanoparticle solution	up to 2×10^3 ¹
Ink	Graphene base ink	Graphene solution	up to 0.3×10^3 ¹

CNC (Computer Numeric Control) [78] or by chemical treatment using so called sacrificial layers for transfer [79].

Besides these materials, another conductive material used in the before-mentioned developments is conductive ink. This has been successfully used in paper and plastic. The application of conductive ink can be performed with lithography techniques, screen printing, spraying and ink-jet printing. With the later being the most convenient and accurate method to apply the ink to a given material. These have also found use in the development of antennas in textile substrates through screen-printing techniques [80, 81].

A brief summary of some conductive materials referred in this section is presented in Table 2.1. This is not a complete list and does not pretend to be a comprehensive final consultation source for all the available materials, but rather, as a base for comparison between their compositions and conductivity.

¹Depends on sintering process temperature and duration.

Chapter 3

Dielectrics characterization methods

In microwave regime, the dielectric properties of the materials are very important for the design of several components and circuits. For instance, in the development of printed microwave circuits or printed antennas, knowledge of accurate data of the dielectric properties of the substrate are critical. Therefore, dielectric characterization methods at microwave frequencies are of paramount importance and are constantly being improved. Besides, there's an increasing demand for characterization methods of lossy solids and liquids. Typical applications for these range from dielectric measurements of biological tissue for cancer research, building materials and structural integrity verification and electromagnetic shielding.

Printed antennas and transmission lines have dimensions directly related to the wavelength and hence the frequency of the desired system [82, 83]. In turn, the wavelength is dependent on the propagation speed of a given electromagnetic wave, which is dependent on the permittivity and permeability of the propagation medium. A high permittivity medium is referred as a slow material, since it will slow the electromagnetic waves traveling through it. Therefore, in order to efficiently design antennas or RF (Radio Frequency) circuitry, the electrical properties of the materials used as substrates or placed in their vicinity must be known, since the relative permittivity (ϵ_r), the relative permeability (μ_r) and the dissipation factor ($\tan \delta$) (also known as loss tangent) of the material influence the propagation characteristics and, therefore, must be considered during the design of a circuit for microwave applications.

The information regarding these parameters is commonly found on the substrates data-sheets, but this does not happen for day-by-day materials, not intended for electronic applications (e.g. fabrics, ceramics, paper, plastic or cork). In this scenario, when designing RF circuitry using such materials, as substrates or other purposes, characterization in terms of permittivity and losses must be performed.

Permittivity characterization methods can be grouped into several categories. As shown in Fig. 3.1, on a large scale, one can separate them into two major groups, the resonant and non-resonant methods:

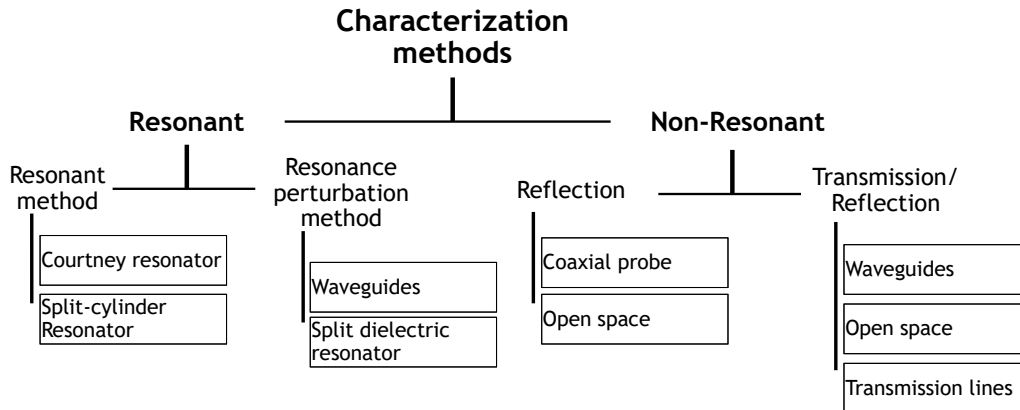


Figure 3.1: Schematic of the electromagnetic characterization method's groups.

- The resonant methods are dependent on resonating properties of dielectrics or cavities. These can also be categorized into two sub-groups, the resonator methods and the resonant-perturbation methods.
- Non-resonant methods are based on the impedance and wave velocities of electromagnetic waves when interacting with different materials. Within non-resonant methods we can then separate two other major groups of characterization methods, the sole reflection and the transmission/reflection methods.

Electromagnetic properties characterization is a very challenging task. Dielectric properties of materials depend on frequency, homogeneity, anisotropy, temperature, and possibly surface roughness (see section 3.1). Due to that, over the years, there has been a large number of methods developed to measure electromagnetic permittivity and permeability. These techniques range from free-space methods, to cavity or dielectric resonators and transmission line techniques. So many methods have been proposed because there's no single method able to test every kind of material, in every state possible, under any condition and at any given frequency. Each method has its own niche of applicability.

A brief discussion of some of these methods is presented in this chapter. The theory underlying each approach is briefly described along with some simulations for verification of the concepts and a small discussion regarding the scenarios of application.

In order to understand the concepts of electromagnetic characterization and to comprehend the presentation of this thesis, in the following section, a review of some relevant electrical properties of materials is presented.

3.1 Electrical properties of materials

Materials can be classified based on their conductivity. Materials with high conductivity ($\sigma \gg 1$) are classified as conductors, also referred as *metals*, and materials with low conductivity ($\sigma \ll 1$) as insulators, also referred as *dielectrics*. What lies in between are referred as semiconductors.

This thesis is mainly focused on the study of dielectric materials. For that reason only a small reference to conductivity and two methods to measure planar conductive sheets are described. The subsequent subsections are devoted to the properties of dielectric materials, that introduce the concepts to understand the set of sections devoted to a more thorough analyses of more methods for dielectrics properties characterization.

3.1.1 Electrical conductivity

The difference between conductors and insulators is essentially the amount of free electrons present, which are responsible for carrying electric current. In *metals*, there's a high amount of free charge (electrons), therefore, when an electric field (\mathbf{E}) is applied, this charges will travel in the opposite direction of the electric field applied, creating a conduction current, as described by the point Ohm's Law.

$$\mathbf{J} = \sigma \mathbf{E} \quad [\text{A/m}^2] \quad (3.1)$$

As the electrons move inside the conductor, due to some applied electric potential, they will find some *resistance*, which according to Ohm's Law is given by [84]

$$R = \frac{V}{I} = \frac{L}{\sigma S} = \frac{L}{\sigma W t} \quad [\Omega] \quad (3.2)$$

where σ is the conductivity of the material, L is the length of the conductor and $S = W \times t$ is the cross section of the conductor, the product of the width (W) by the thickness (t). Therefore, the higher the conductivity of a given conductor, the lower the resistance this one presents to the movement of free charges.

As seen from equation (3.2), the conductivity of a material is related to its resistance. However, this resistance is also dependent of the conductor geometry.

Therefore, in a conductivity measuring apparatus, the resistance may be dependent on the geometry of the electrodes used for measurement. Nevertheless, resistance can be related to sheet resistance, which is independent of the geometry of the conductor. For that reason, conductivity measuring methods usually go about measuring the sheet resistance

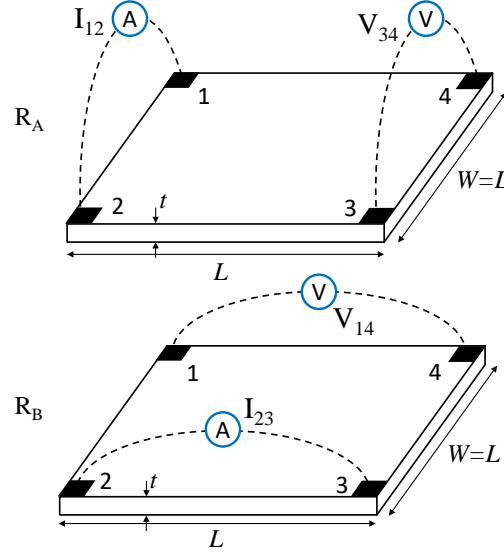


Figure 3.2: Measurement configuration of a square conductivity sample in the Van der Pauw geometry.

of a conductor, then determine the conductivity based on the following constitutive relations

$$\rho = R_s \times t \quad [\Omega\text{m}] \quad (3.3a)$$

$$\sigma = \frac{1}{R_s \times t} \quad [\text{S/m}] \quad (3.3b)$$

being ρ the resistivity and R_s the sheet resistance, which, revisiting equation (3.2), leads to a resistance of

$$R = R_s \frac{L}{W} \quad [\Omega] \quad (3.4)$$

being that the relation L/W gives the number of squares of that particular conductor, reason why the resistance of a given conductor is independent of the size of the conductor, but is actually dependent on the reason of the length over the width.

The two most widely used methods for the measurement of the sheet resistance of thin conductive sheets of material are the Van der Pauw technique [85, 86] and the collinear four-probe array method [87], being both standard methods, the former advised by NIST [88] and the later by ASTM [89], and are both used in industry.

As originally devised by Van der Pauw, one uses an arbitrarily shaped, simply connected (i.e., no holes or nonconducting islands or inclusions), thin-plate sample containing four ohmic contacts placed on the corners of the plate. In this method, a current or voltage potential is applied in a pair of corners and its reciprocal is measured in the opposite corner pair. This is shown in the schematic of a rectangular Van der Pauw configuration in Fig. 3.2.

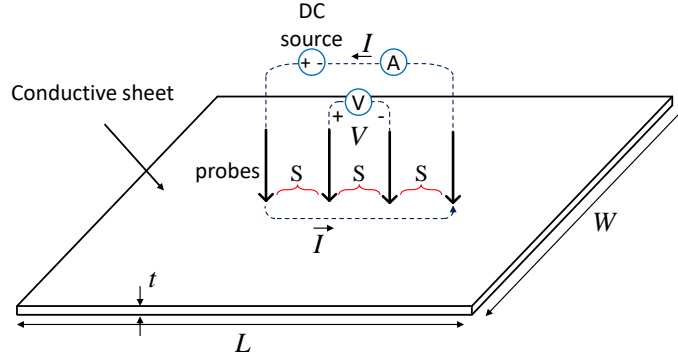


Figure 3.3: Measurement configuration of the colinear four-probe array method.

Van der Pauw demonstrated that there are two resistances R_A and R_B , associated with the corresponding terminals shown in Fig. 3.2, calculated based on

$$R_A = \frac{V_{34}}{I_{12}} \quad [\Omega] \quad (3.5a)$$

$$R_B = \frac{V_{14}}{I_{23}}. \quad [\Omega] \quad (3.5b)$$

These resistances R_A and R_B are related to the sheet resistance R_S through the van der Pauw equation [85]

$$e^{(-\pi R_A/R_S)} + e^{(-\pi R_B/R_S)} = 1, \quad (3.6)$$

which can be solved numerically, or approximated by a polynomial. However, if R_A and R_B are close, which can be achieved if the measured conductor sample is nearly square, then (3.6), can be simplified to

$$R_s = \frac{\pi}{\ln 2} \frac{R_A + R_B}{2}, \quad [\Omega/\square] \quad (3.7)$$

where the conductivity can be obtained if the thickness of the material (t) is known, as shown in 3.3b.

The colinear four-probe array method uses four very small metallic probes in a linear arrangement, with a very small contact area, as shown in Fig. 3.3. In this method, a current is generated and passed through the outer conductors while a voltage is measured in the inside probes. Two constraints are present in this method, one is that careful should be taken in order to guarantee the conductor extends well beyond the edge of the outer probes, the other constraint is that the spacing between probes should be at least ten times the thickness of the conductor. Besides, the method is simplified if equally spaced probes are used, being that the sheet resistance can simply be obtained from the measured voltage and current as follows

$$R_s = \frac{V}{I} \frac{\pi}{\ln 2}, \quad [\Omega/\square] \quad (3.8)$$

and, as mentioned before, the conductivity can be obtained from 3.3b, by knowing the thickness of the material.

The methods presented so far are used to measure the bulk conductivity in DC regime, and although this conductivity is useful, when considering RF systems, the skin effect [84] becomes apparent and the values of sheet resistance tend to increase with the square root of frequency. The sheet resistance can be related to the skin depth in similar fashion as in DC regime (3.3a), however, with regards to the skin depth (δ_s) instead of the thickness (t) of the material, as

$$R_s = \frac{\rho}{\delta_s} = \sqrt{\frac{\pi f \mu}{\sigma}} \quad [\Omega/\square] \quad (3.9)$$

which means the sheet conductivity of the material, tends to drop with the square root of frequency. This is important in some characterization methods using cavities and waveguides, where the losses of the system have to consider the sheet resistance of the conducting walls.

There's more to say about conductors and several other methods and standards to test conductivity of different types of materials, but overall, this concept of conductivity of planar conductors is the most important when designing RF circuits, in order to understand the source of ohmic losses and radiation resistance/efficiency, as presented further in this document. Therefore, this chapter is more devoted to the characteristics of dielectrics and their properties such as susceptibility, permittivity, linearity, isotropy, homogeneity, dielectric strength, and dispersion.

3.1.2 Polarization, susceptibility and permittivity

When an electric field is applied to a dielectric the charges are distended, where the positive charge is displaced towards the direction of the electric field and the negative charge is pulled the other way.

There are three different types of polarization formations within dielectrics, these are illustrated in Figure 3.4. The *dipole or orientational polarization* is evident in materials that have permanent, randomly oriented, dipole moments, even in the absence of an electric field. When an electric field is applied, this dipoles tend to align to the applied field (See Fig. 3.4 (a)). Water is a good example of such a dielectric [90]. The *atomic polarization* is evident in ionic materials, when adjacent positive and negative ions get stretched, when an electric field is applied (see Figure 3.4 (b)). The *electronic polarization* occurs due to the displacement of the electron cloud center of the atoms with regard to the atom nucleus (see Fig. 3.4 (c)). Each dielectric material may present one or more of these dielectric mechanisms and they are responsible for the overall permittivity of the material.

When an electric field is applied to a dielectric slab, there's going to be a positive surface charge density ($+q_{sp}$) in one of the ends of the dielectric slab, and a negative surface charge density ($-q_{sp}$) in the other end. In the middle, the positive and negative end of the formed dipoles will

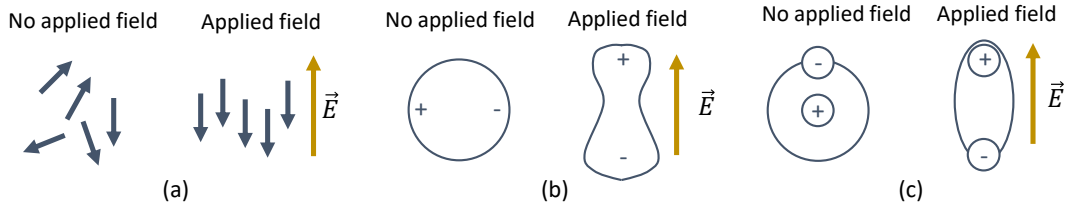


Figure 3.4: Illustration of the different types of dielectric polarization. (a) Dipole, (b) atomic and (c) electronic polarizations.

cancel each other, resulting in a net zero charge density. Thus, there's an electric polarization vector (\mathbf{P}) directed from the negative surface $-q_{sp}$ towards the positive surface $+q_{sp}$, in the same direction as the applied electric field. Since the source creating the electric field is maintained, this bound charges on the ends of the dielectric will force the appearance of more free charges at the conductive surfaces creating the electric field. Otherwise the electric field intensity would diminish.

The electric flux density is related to the applied electric field by the permittivity of the material (eq. 3.10), but within a dielectric it can also be related to the electric flux density of free space by the polarization vector (eq. 3.11) [91].

$$\mathbf{D} = \epsilon \mathbf{E}_a \quad [\text{C/m}^2] \quad (3.10)$$

$$\mathbf{D} = \mathbf{D}_0 + \mathbf{P} \quad [\text{C/m}^2] \quad (3.11)$$

where \mathbf{D}_0 is the electric flux density in free space and is given by $\mathbf{D}_0 = \epsilon_0 \mathbf{E}_a$ and \mathbf{P} whose amplitude is given by $|q_{sp}|$. Therefore, the polarization vector can be related to the electric field as

$$\mathbf{P} = \mathbf{E}_a (\epsilon - \epsilon_0) \quad [\text{C/m}^2] \quad (3.12)$$

since $\epsilon = \epsilon_r \epsilon_0$ we get

$$\mathbf{P} = \mathbf{E}_a \epsilon_0 (\epsilon_r - 1) \quad [\text{C/m}^2] \quad (3.13)$$

which can also be expressed as

$$\mathbf{P} = \epsilon_0 \chi_e \mathbf{E}_a \quad [\text{C/m}^2] \quad (3.14)$$

where χ_e is referred to as the *electric susceptibility*, which is a dimensionless constant that indicates the degree of polarization of a given dielectric to an applied electric field, as

$$\chi_e = \frac{1}{\epsilon_0} \frac{\mathbf{P}}{\mathbf{E}_a} \quad (3.15)$$

Which means that the higher the susceptibility of a material is, the higher the polarization

Table 3.1: Typical values for permittivity and dissipation factor of common materials.

Substance	Relative permittivity (ϵ_r)	Dissipation Factor ($\tan \delta$)
ABS	2.0-3.5	0.005-0.019
Air	1.0006	-
Alumina (99.5%)	9.6	0.0003 @ 10 GHz
Bakelite	3.6	-
Diamond	5.5-10	-
Epoxy Glass	5.2	0.01
FR-4 (low resin)	4.9	0.008 @ 3 GHz
FR-4 (high resin)	4.2	0.008 @ 3 GHz
Fused Silica	3.8	-
Gallium Arsenide (GaAs)	13.1	0.0016 @ 10 GHz
Kapton [®] (type 100)	3.9	-
Neoprene	6.0-9.0	-
Polyethylene	2.26	0.0003 @ 3 GHz
Quartz	4.2	-
Teflon [®]	2.0-2.1	0.00028 @ 3 GHz
Water (distilled)	76.7-78.2	0.157 @ 3 GHz
Wood	1.2-2.1	0.03 @ 3 GHz

of the material when subject to an electric field. Therefore, the greater the capacity of said material to store energy. Which makes the susceptibility intimately related to the relative permittivity (ϵ_r) of a material as

$$\epsilon_r = \frac{\epsilon}{\epsilon_0} = 1 + \chi_e \quad (3.16)$$

and is usually referred to as the *relative permittivity* or static *dielectric constant*.

Considering this, then the dielectric constant is the parameter that indicates the charge storage capabilities, of a given material, relative to free space. The higher the relative permittivity of a material, the higher the charge storage capability of that given material. It is important to note, though, that relative permittivity, as presented in (3.16), represents values at static or quasi-static frequencies. These values vary with changes in frequency. This is discussed in the next subsections. Typical values for permittivity of several materials is shown in Table 3.1 taken from [92].

3.1.3 Complex permittivity and dissipation factor

As stated, the permittivity of a material describes the interaction of that material with an electric field (\mathbf{E}) and is actually a complex value

$$\epsilon_r = \epsilon'_r - j\epsilon''_r \quad (3.17)$$

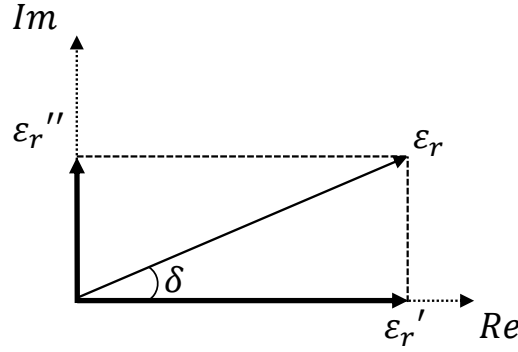


Figure 3.5: Vector representation of the permittivity in real and imaginary axis.

The real part of permittivity (ϵ_r') is a measure of how much energy from an external electric field is stored in a material. The imaginary part of permittivity (ϵ_r'') is called the loss factor and is a measure of how dissipative or lossy a material is. The imaginary part of permittivity (ϵ_r'') is always greater than zero and is usually much smaller than the real part (ϵ_r').

The imaginary part results mainly from the response of the dielectric constituents to the electric field applied. Higher motion of the dielectric mechanisms leads to higher heat generation and, therefore, to higher losses, which can also be seen the other way around. Water has many dipolar moments, which have a response at microwave frequencies, generating an high amount of heat in response to an alternating electric field in the microwave frequencies region. This is the principle behind the food heating process in a microwave oven.

The complex permittivity can be sketched in vector form, as shown in Fig. 3.5, where the real and imaginary component are 90° out of phase. The vector sum of this two components forms an angle δ with the real axis. The $\tan \delta$ is therefore the ratio of the imaginary to the real part of the permittivity. Given this loss representation, the loss of a material is a ratio of the energy lost to the energy stored. The $\tan \delta$ is commonly referred to as loss tangent, or dissipation factor of a given material.

$$\tan \delta = \frac{\epsilon_r''}{\epsilon_r'} \quad (3.18)$$

It's also common to find the complex relative permittivity represented as

$$\epsilon_r = \epsilon_r' (1 - j \tan \delta) \quad (3.19)$$

The imaginary and real part of the permittivity are not completely independent. In fact they are closely related, to such point that, if one knows the complete frequency dependence of either the real or the imaginary part, the complete frequency dependence of the

complement can be calculated based on Kramers-Kronig relations, as [93]

$$\varepsilon_r'(\omega) = \frac{2}{\pi} \int_0^\infty \frac{\omega' \cdot \varepsilon_r''(\omega')}{\omega'^2 - \omega^2} \cdot d\omega' \quad (3.20a)$$

$$\varepsilon_r''(\omega) = \frac{-2\omega}{\pi} \int_0^\infty \frac{\varepsilon_r'(\omega')}{\omega'^2 - \omega^2} \cdot d\omega' \quad (3.20b)$$

3.1.4 Linearity, homogeneity, isotropy, dispersion and relaxation time

The electrical behavior of a given material is characterized by its electrical constitutive parameters, namely the permittivity (ε), permeability (μ) and conductivity (σ).

A material is considered *linear* if its constitutive parameters are not functions of the amplitude applied field. Nearly every material is non-linear, however, the vast majority presents a linear behavior within a certain range of the applied field, and a high non-linear behavior beyond this point [94]. Therefore, most materials are considered linear since they'll be operated well within the linear ranges.

A material is considered *homogeneous* if the constitutive parameters do not depend on the position of the applied field. The vast majority of materials are inhomogeneous. However, the degree of nonhomogeneity of most materials is so small that they're treated as homogeneous nonetheless.

A material is considered *isotropic* if its constitutive parameters do not depend on the direction of the applied fields. Otherwise, the material is considered anisotropic. Regardless of the anisotropy of a material, many times these are characterized in a single direction, and regarded as being isotropic, considering they'll be operated in that single direction, therefore simplifying the characterization process.

A material is considered *dispersive* if its parameters depend on the frequency of the applied fields. All materials are in practice dispersive, and although there are certain materials with very low degrees of dispersiveness, most dielectric materials have a very dispersive permittivity and conductivity. Dispersiveness is closely tied to the mobility of the molecules (dipole moments) that exist in the material.

A material may have several dielectric mechanisms, as described in a previous subsection. Dipole orientation interact strongly at microwave frequencies, where dipole moments will rotate to follow alternating electric fields. This is a very lossy mechanism. Water presents a large number of permanent dipoles, which is why, as stated before, when it is subject to an electric field at microwave frequencies, its temperature rises - once again, this is the principle for food heating with microwave ovens. Electronic and atomic polarization, on the other hand, are called "slow mechanisms", since these are nearly insensitive to alternating fields in the microwave region. Atomic polarization will respond to fields alternating in the infrared region, while electronic polarization mechanisms only respond to fields alternating in the ultraviolet region and beyond. Polymers such as the PTFE (Polytetrafluoroethylene),

most commonly known as Teflon[®], which is hydrophobic, has nearly no permanent dipoles. That is why its permittivity is so stable, and the reason it has such low losses, in the entire microwave region.

Each dielectric mechanism has its own cutoff frequency, which is unique for each material. The cutoff frequency of the dipolar mechanism is characterized by a relaxation effect, while the electronic and atomic mechanisms are characterized by a resonance effect. As the frequency increases dipolar rotation mechanisms tend to drop and the atomic and ionic mechanisms become the main contributors for the permittivity of the material.

The relaxation time (τ) is a measure of the mobility of the dipoles in the material. It is the time required for the dipoles to align to an applied electric field (or the time it takes for a displaced system to return to its random equilibrium state). The relaxation frequency (f_c) is inversely related to the relaxation time

$$\tau = \frac{1}{\omega_c} = \frac{1}{2\pi f_c} \quad (3.21)$$

At frequencies below the relaxation frequency, the dipoles are able to keep pace with the alternating electric field. As the frequency increases, the losses (ϵ_r'') increase and the storage capability (ϵ_r') starts to decrease due to the phase lag between the dipole alignment and the electric field. Above the relaxation frequency the electric field is too fast to influence the dipole rotation. Therefore, this mechanism fades and both ϵ_r' and ϵ_r'' drop to lower values.

The permittivity variation of a material with frequency can be represented by the Debye relation [93]

$$\epsilon_r = \epsilon_\infty + \frac{\epsilon_s - \epsilon_\infty}{1 + j\omega\tau} + \frac{\sigma_s}{j\omega\epsilon_0} \quad (3.22)$$

where ϵ_s is the static permittivity (DC regime), ϵ_∞ is the optical permittivity, σ_s is the static conductivity, while τ is the relaxation time.

The Debye relation for water at 30° C is depicted in Fig. 3.6 (a), where we can see a peak for the losses at the relaxation frequency around 2 GHz.

The Debye relation is usually valid for liquids, but has a slight error in the approximation of the response of polymers. Therefore, it is usual to use the Cole-Cole relation, which is more broad, as [93]

$$\epsilon_r = \epsilon_\infty + \frac{\epsilon_s - \epsilon_\infty}{1 + (j\omega\tau)^{(1-\alpha)}} + \frac{\sigma_s}{j\omega\epsilon_0}, \quad (3.23)$$

where α is a stretch parameter of the relaxation, allowing the representation of the frequency response of several material with the same relaxation time, but different spectra response. If $\alpha \rightarrow 0$ then it reduces to the Debye relation.

Although not so usual, sometimes the relation of the relative permittivity with frequency is represented in a Cole-Cole diagram, as shown in Fig. 3.6 (b).

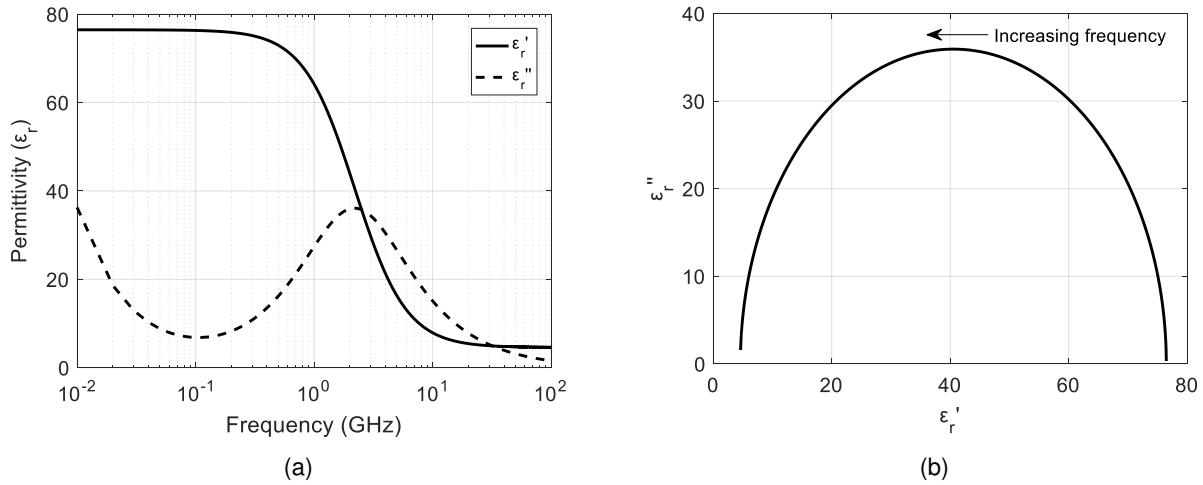


Figure 3.6: Permittivity variation with frequency of water at 30° C by the Debye relaxation model. (a) Debye representation and (b) Cole-Cole diagram.

3.2 Characterization methods

As stated previously, there are several types of characterization methods. Each method is particularly suited for a certain type of material, frequency of operation or testing condition. There are standards institutions, such as IPC (Institute of Printed Circuits), NIST (National Institute of Standards and Technology) and ASTM International (American Society for Testing and Materials), that have defined test methods for permittivity and dissipation factor characterization for industry. Plus, there's several of methods defined by academic institutions. In summary, there's a very large plethora of methods for permittivity characterization.

In this section, a discussion regarding different kinds of methods is presented. It is hard to make a thorough review of the subject and consider all the methods that have been proposed. IPC alone has eleven different standards for permittivity characterization of materials. Therefore, this section tries to briefly describe a few of the most widely used and acknowledged methods, which are, in some cases, used for certification purposes in the industry.

The discussion of characterization methods is split into two major sections, as indicated in Fig. 3.1, the resonant and the non-resonant methods. Within each of these two main sections, a subset of methods is discussed and one or more methodologies to apply those methods are presented.

3.2.1 Resonant methods

Resonant methods tend to have higher accuracy and sensitivities than non-resonant methods. This means that although able to measure the permittivity of materials with a

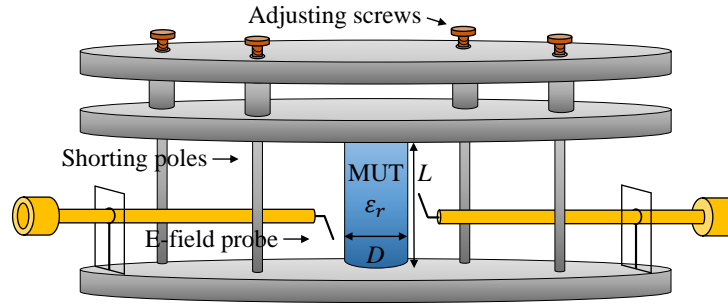


Figure 3.7: Illustration of the side view of the dielectric rod resonator.

higher certainty level, they're also more prominent to errors when testing reasonably lossy materials [95].

There are essentially two different resonant methods for permittivity estimation of dielectric materials: The resonator method, in which the dielectric under test is used as a resonator; and the resonance perturbation method, in which the dielectric under test is used to create a perturbation on a resonant system.

Resonator method

In the resonator method the dielectric under test is used as a resonator, or a key part of a resonating system. The resonator methods that are most used, are the SCR (Split-Cylinder Resonator) [96], which is an evolution of the double-cylinder cavity method proposed by Kent [97, 98, 99] and the Courtney resonator. Which was initially proposed by Hakki and Coleman [100], further analyzed and developed by Courtney [101] and later revised by Kobayashi and Katoh [102, 103].

The Courtney resonator, depicted in Fig. 3.7, uses a specific measurement structure that comprises two metallic disks shorted to each other and a dielectric rod, which is centered in the structure, to form a resonating circuit. To excite the system, two right-angle E field probes are used for coupling with the samples. These probes can be moved inwards or outwards in order to vary the coupling coefficients.

The characteristic equation for the resonant modes TE_{mnl} is given by [101]

$$\left[\frac{\varepsilon_r J'_m(\alpha)}{\alpha J_m(\alpha)} + \frac{K'_m(\beta)}{\beta K_m(\beta)} \right] \left[\frac{J'_m(\alpha)}{\alpha J_m(\alpha)} + \frac{K'_m(\beta)}{K_m(\beta)} \right] = m^2 \left[\frac{\varepsilon_r}{\alpha^2} + \frac{1}{\beta^2} \right] \left[\frac{1}{\alpha^2} + \frac{1}{\beta^2} \right] \quad (3.24)$$

where

$$\alpha = \frac{\pi D}{\lambda} [\varepsilon_r - (l\lambda/2L)^2]^{1/2} \quad (3.25a)$$

$$\beta = \frac{\pi D}{\lambda} [(l\lambda/2L)^2 - 1]^{1/2} \quad (3.25b)$$

where $J_m(\alpha)$ is the m th order Bessel function of the first kind and $K_m(\beta)$ is the m th order modified Bessel function of the second kind, λ is the wavelength, D is the sample diameter, L is the sample length, and $l = 1, 2, 3, \dots$ correspond to the multiple half-wavelengths in the cavity along the axial direction.

If we focus on the TE_{011} resonant mode, then (3.25), can be written as

$$\varepsilon_r = 1 + \left(\frac{\lambda_1}{\pi D} \right)^2 (\alpha_1^2 + \beta_1^2) \quad (3.26)$$

where λ_1 is the wavelength of the TE_{011} resonant frequency, α_1 and β_1 are the first roots of the characteristic equation (3.24) for $m = 0$ and $l = 1$, which leads to the following relation

$$\left(\frac{J'_0(\alpha_1)}{\alpha_1 J_0(\alpha_1)} \right) = - \left(\frac{K'_0(\beta_1)}{K_0(\beta_1)} \right) \quad (3.27)$$

Since β_1 does not depend on ε_r , one can find β_1 based on (3.25b) and then find the solution that satisfies (3.27) to calculate α_1 and reach the value for the relative permittivity, with (3.26) and knowing the physical dimensions of the dielectric sample.

According to Hakki and Coleman [100] the dissipation factor ($\tan \delta$) of the sample can also be calculated according to

$$\tan \delta = \frac{A}{Q_0} - BR_s \quad (3.28)$$

where

$$A = 1 + \frac{W}{\varepsilon_r} \quad (3.29a)$$

$$B = \frac{\lambda_0^3}{\lambda_g} \frac{1 + W}{30\pi^2 \varepsilon_r l} \quad (3.29b)$$

$$W = \frac{J_1^2(\alpha_1)}{K_1^2(\beta_1)} \frac{K_0(\beta_1)K_2(\beta_1) - K_1^2(\beta_1)}{J_1^2(\alpha_1) - J_0(\alpha_1)J_2(\alpha_1)} \quad (3.29c)$$

where W is the ratio between the electric-field energy stored in the outside and inside the dielectric rod [100], R_s is the sheet resistance of the conducting plates (3.9) and σ is the bulk conductivity of the conducting plates of the resonator structure.

Kobayashi [103] also reasoned that in order to obtain an accurate result for the dissipation factor, the value of the surface resistance of the conducting plates had to be known with a very high degree of certainty, and described a procedure to use the same measurement in-

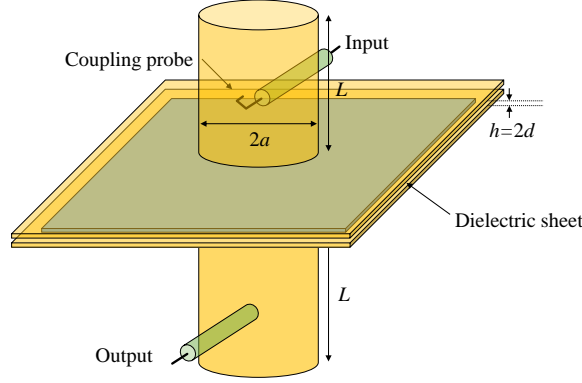


Figure 3.8: Illustration of the Split-Cylinder Resonator as proposed by Kent.

strument, operated in reverse order, using two different samples with known characteristics, to extract the exact surface resistance of the conducting plates.

It is important to note, that to achieve high accuracy with this method, the sample has to have certain dimensions that guarantee that most part of the energy is concentrated inside the dielectric rod, that means satisfying the trapped state condition for the TE_{011} mode [102], that is

$$\frac{D}{L} > x_c, \quad x_c = \frac{2u_0}{l\pi\sqrt{\varepsilon_r - 1}}, \quad J_0(u_0) = 0 \quad (3.30)$$

From (3.30) we can see that the ideal sample dimension is dependent on the permittivity of the material itself. Therefore, a initial educated guess regarding the permittivity of the material under test is necessary.

The disadvantage of this dielectric resonator method is the requirement to prepare a sample with well machined dimensions, which is not always possible, and most times is the major source of error when performing measurements using this method. Therefore, the resonant method proposed by Kent [97, 98], is more appealing, since it is suited to measure thin materials, in the form that is used to be applied in PCB manufacturing, in which the only physical constraint that is introduced is the thickness.

The cylindrical waveguide resonator, commonly referred to as SCR, proposed by Kent, which is illustrated in Fig. 3.8, is essentially composed of a cylindrical cavity that is split in half where a thin slab of dielectric can be introduced for measurement. In this method, a single resonant mode is analyzed and the estimations of the permittivity are obtained from an equivalent model of the split-cylinder resonator. The measured quantities are the resonant frequency of the TE_{01} mode, the insertion loss and the quality factor (Q).

The choice of the TE mode has to do with the fact that in this mode the electric field component is normal do the plane of the dielectric sheet and interacts directly with it, therefore, these modes are usually more sensible to changes in the permittivity. Contrary to the

TM modes where the electric field component is parallel to the plane of the dielectric sheet. The choice of the resonant mode TM_{lm} in particular, the choice of a monopole mode $m = 1$, instead of a dipole mode $m > 1$, has to do with the spacing between adjacent modes, where monopole modes appear more isolated in the spectrum, compared to dipole modes. Besides, if the ratio of the height of half-cavity to the radius of the cavity is $L/a \leq 0.8$, then the TE_{01} is easily identified as the third resonance, since, one expects to observe the modes TE_{11} , TE_{21} and TE_{01} , by order of increasing frequency.

According to [97], the permittivity of the dielectric slab is calculated according to the following expression

$$\varepsilon_r = \frac{1}{\eta^2} [(\theta/\theta_c)^2 + 1] \quad (3.31)$$

where $\theta_c = \pi h/\lambda_c$, $\eta = \lambda_c/\lambda_0$, being λ_c the cutoff wavelength of the waveguide and λ_0 the wavelength of the considered resonant mode, and θ is the eigenvalue of the expression that satisfies the relation of continuity of the fields in the dielectric interface, given by

$$\Phi(\theta, \varphi) = \theta \tan \theta = \left(\frac{h}{2L} \right) \varphi \cot \varphi \quad (3.32)$$

where

$$\theta = \beta h/2 \quad (3.33a)$$

$$\varphi = \beta_0 L \quad (3.33b)$$

$$\beta_0^2 = \left(\frac{2\pi}{\lambda_0} \right)^2 - \left(\frac{2\pi}{\lambda_c} \right)^2 \quad (3.33c)$$

$$\beta = \left[\varepsilon_r \left(\frac{2\pi}{\lambda_0} \right)^2 - \left(\frac{2\pi}{\lambda_c} \right)^2 \right]^{(1/2)} \quad (3.33d)$$

which means that the right side of equation (3.32) can be determined based on experimental measurements and with it, substitute in (3.31), to obtain the permittivity value.

It is worth noting that this expression is only valid if the substrate is well contained within the waveguide and shorted at its edges, otherwise, in the real scenario as shown in the illustration of Fig. 3.8, where the waveguide is open in the middle, the boundary conditions make the expression (3.32) invalid. To correct this problem, approximate functions or experimental calibration as proposed in [98], or numerical analysis tools as proposed in [104], can be used.

Any of the choices leads to a very complicate and intricate problem for solving the system to obtain the correct permittivity. The approximate functions use a subset of error coefficients, which are related to the operating mode of the resonance cavity itself and to the sample dimensions, in such a way that makes this method very sensitive to the correct determination, down to the μm dimensions of the sample.

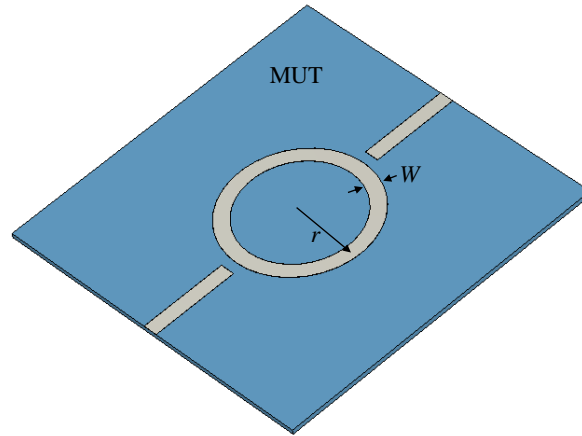


Figure 3.9: Illustration of the Ring Resonator structure with the mean radius of the ring denoted as r .

In order to guarantee the validity of the split-cylinder model, a dielectric shunt with a given thickness should be used that allows no air gaps in the cavity split and has a thickness that satisfies the following condition

$$h \frac{2\pi}{\lambda} \sqrt{\epsilon_r} \ll 1 \quad (3.34)$$

These conditions, however, are not always easy to satisfy. Therefore, extensions to this method have been proposed to relax the constraints imposed by the original model. These approaches use full-wave analysis models for the resonator or estimation based on higher order modes [104, 105].

Besides the cavity methods, there's also the printed circuit characterization methods. In these, the material to be tested is used as substrate to a given printed resonant structure. Although presenting less precision in the characterization, have an advantage of characterizing the material under the operation circumstances. That is, the permittivity component being measured is exactly the same as the one that is used during circuit operation. Therefore, even if the material has some kind of anisotropy, this can be safely discarded. The main disadvantage of this method is the fact that the sample used for testing is lost and cannot be reused for other purposes.

Any printed resonator system can be used for the purpose of this measurement system, however, one of the most widely known is the RRM (Ring Resonator Method) [106, 107, 108]. The main advantage of the printed microstrip ring resonator when compared to other printed structures is that radiation losses of the ring resonator are typically negligible due to the absence of end effects [108]. The structure of the printed RR is presented in Fig. 3.9.

The simplest approach to calculate the permittivity, based on the printed ring resonator method, is to use closed form analytical expressions from transmission line models applied to the ring resonator structure. The resonant frequencies of the two-port microstrip ring

resonator, are approximated by the following expression

$$2\pi r = n\lambda_g \quad (3.35)$$

where r is the mean radius of the ring resonator and $n\lambda_g$ is the wavelength of the n 'th harmonic, where $\lambda_g = \lambda_0 / \sqrt{\varepsilon_{r,eff}}$. Therefore, the effective permittivity of the substrate is related to resonant frequencies of the structure by

$$\varepsilon_{r,eff} = \left(\frac{n\lambda_0}{2\pi r} \right)^2 \quad (3.36)$$

The relative permittivity of the substrate can be calculated from the effective permittivity value and the physical dimensions of the microstrip line based on the approximate expressions described in [65], as

$$\varepsilon_r = \frac{2\varepsilon_{r,eff} + M - 1}{M + 1} \quad (3.37)$$

where

$$M = \left(1 + \frac{12h}{W + \frac{1.25t}{\pi} [1 + \ln(\frac{2h}{t})]} \right)^{-1/2} \quad (3.38)$$

being W the width of the microstrip line, h the thickness of the substrate and t the thickness of the conductor.

From the same approximated expressions for the transmission lines, the loss tangent can be obtained from

$$\tan \delta = \frac{\alpha_d \lambda_g \sqrt{\varepsilon_{r,eff}}}{\pi} \frac{\varepsilon_r - 1}{\varepsilon_r (\varepsilon_{r,eff} - 1)} \quad (3.39)$$

where α_d are the losses due to the dielectric that can be calculated from the total losses of the system (α) subtracted by the losses due to the conductor (α_c) and assuming that the radiation losses are so low that can be neglected. The total losses of the system can be obtained from the insertion loss at the resonant frequency (IL_n) and the insertion loss -3 dB bandwidth (Δ_f) in hertz, as [107]

$$\alpha = \alpha_d + \alpha_c = 0.00909 \times 10^{-9} \times \Delta_f \sqrt{\varepsilon_{r,eff}} (1 - 10^{IL_n/20}) \quad [\text{Np/m}] \quad (3.40)$$

and the conductor losses (α_c), assuming that the ratio of the mean surface roughness of the conductor to the skin depth of the conductor is higher than 1.93, can be obtained from

$$\alpha_c = 10.881 \times 10^{-6} R_s A Z_0 \varepsilon_{r,eff} \left[\frac{W_{eff}}{h^2} + \frac{0.667 \left(\frac{W_{eff}}{h^2} \right)}{1.444 + \frac{W_{eff}}{h}} \right] \quad [\text{Np/m}] \quad (3.41)$$

where R_s is the surface resistance expressed as shown in (3.9), Z_0 is the characteristic impedance of the microstrip line and A is the ratio of the substrate thickness to the microstrip

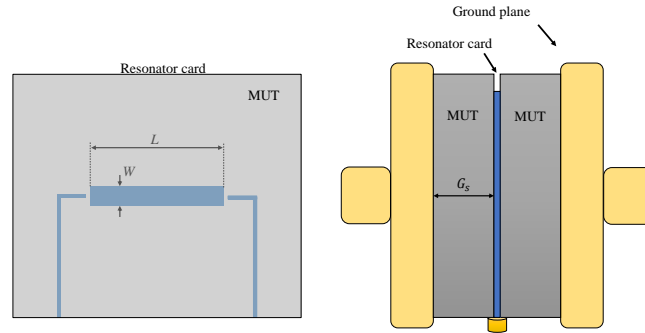


Figure 3.10: Illustration of the Stripline Resonator fixture as proposed in the IPC TM-650 2.5.5.5C.

width, containing a correction for the thickness of the conductor, in the form

$$A = 1 + \left(\frac{h}{W_{eff}} \right) \left(1 + \frac{1.25}{\pi} \ln \left(\frac{2h}{t} \right) \right) \quad (3.42)$$

This method is rather simple to use and does not require any kind of specific fixture for measurement. Also, it does not require any simulation or equivalent model to reach an approximate value for the permittivity of the MUT (Material Under Test). However, one can improve the accuracy of the results if instead of using the closed form equivalent expressions for the microstrip lines as described previously, use simulation models for the RR and then uses optimization algorithms to match the simulation and corresponding measurements of the structure.

Another method based on printed electronics, which is used by microwave substrate manufactures for certification purposes, is the stripline test-fixture. This is defined by the IPC as the IPC TM-650 2.5.5.5C test method and is used by the main microwave substrate manufacturers, such as Rogers Corp.[®], Arlon[®], or Isola[®], as a standard to characterize their materials. This method, as defined by the IPC standard, is valid for frequencies in the X-band.

The stripline resonator fixture used in this method is shown in Fig. 3.10. A printed straight stripline of length L is used as a resonator structure. The dielectric MUT is placed around this resonator structure and then clamped with a large metallic structure that grounds the line on both sides.

The permittivity of the dielectric sample can be calculated based on [109]

$$\varepsilon_r = \left(\frac{n\lambda_0}{2(L + \Delta L)} \right)^2 \quad (3.43)$$

where n is the number of half-wavelengths along the resonant strip of length L and ΔL is a correction factor for the fringing capacitance at the ends of the resonator element. In order

to determine ΔL a set of resonator circuit cards with different lengths, multiples of the same wavelength, should be used. For instance, a set of four resonators of length 9.5, 19.0, 28.6 and 38.1 mm may be used. The resonant frequencies shall be measured for each sample, then a linear regression can be used to determine the slope of the least squares fit, where that slope corresponds to the negative value of ΔL .

As in the previous case, the dissipation factor can be obtained by subtracting the losses of the conductors, from the total losses of the system. Obtained from the quality factors of each, as [109]

$$\tan \delta = \frac{1}{Q} - \frac{1}{Q_c} \quad (3.44)$$

where the total losses can be calculated based on the quality factor as

$$\frac{1}{Q} = \frac{\Delta f}{f_0} \quad (3.45)$$

being Δf the -3 dB insertion loss bandwidth and the conductor losses can be calculated based on

$$\frac{1}{Q_c} = \frac{\alpha_c \lambda_0}{\pi \sqrt{\epsilon_r}} \quad (3.46)$$

where α_c is the attenuation due to the conductors, which can be calculated from

$$\alpha_c = \frac{4R_s \epsilon_r Z_0 \Psi}{(120\pi)^2 G_s} \quad [\text{Np/m}] \quad (3.47)$$

where Z_0 is the characteristic impedance of the stripline, which can be calculated based on

$$Z_0 = \frac{120\pi}{4\sqrt{\epsilon_r} \left(C_f + \left(\frac{W}{G_s - t} \right) \right)} \quad [\Omega] \quad (3.48)$$

and

$$C_f = \frac{1}{\pi} \left(2\Delta\vartheta \ln(\Delta\vartheta + 1) - (\Delta\vartheta - 1) \ln(\Delta\vartheta^2 - 1) \right) \quad (3.49a)$$

$$\Psi = \Delta\vartheta + \frac{2W\Delta\vartheta^2}{G_s} + \frac{\Delta\vartheta^2}{\pi} \left(1 + \frac{t}{G_s} \right) \ln \left[\frac{(\Delta\vartheta + 1)}{(\Delta\vartheta - 1)} \right] \quad (3.49b)$$

$$\Delta\vartheta = \frac{G_s}{G_s - t} \quad (3.49c)$$

where G_s is the ground plane spacing in mm, W is the width of the resonator stripline and t is the thickness of the conductor.

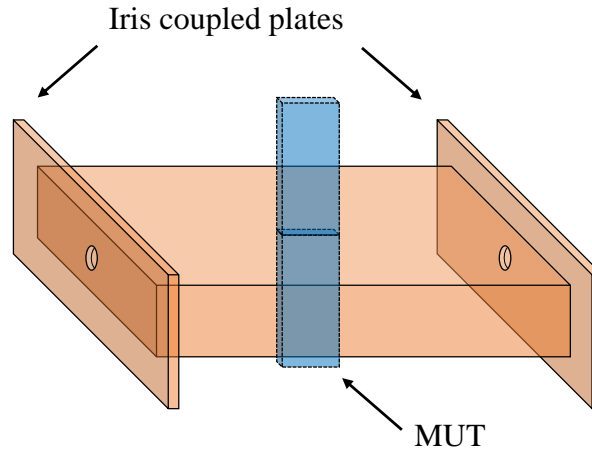


Figure 3.11: Illustration of the waveguide structure proposed for the cavity perturbation method.

Resonant perturbation method

As stated before, in the resonant perturbation method the measured quantities used to determine the permittivity of a given sample material are the resonant shift and the quality factor changes on a given resonant structure, as opposed to the previous case where the sample to test is used as part of the resonant system itself.

There are two main methods based on resonant perturbation techniques, one is the cavity perturbation method and the other is the SDR (Split Dielectric Resonator). The first is defined by the ASTM D2520-13 standard, and used by insulator material manufacturers for permittivity estimation. The second has been defined by the IPC as TM-650 2.5.5.13, and is used by substrate manufacturers.

The cavity perturbation method uses a rectangular waveguide structure, with iris-coupled end plates, with a slot in the middle, where the electric field is maximum, to introduce the dielectric sample to be measured. This fixture is illustrated in Fig. 3.11.

By using a rectangular waveguide resonator for the cavity perturbation technique, the relative permittivity of the sample can be calculated based on

$$\varepsilon'_r = \frac{V_c(f_c - f_s)}{2V_s f_s} + 1 \quad (3.50a)$$

$$\varepsilon''_r = \frac{V_c}{4V_s} \left(\frac{1}{Q_s} - \frac{1}{Q_c} \right) \quad (3.50b)$$

where V_X is the volume, Q_X is the quality factor, f_X is the frequency, and the subscripts c and s stand for the values in an empty cavity and the cavity loaded with the sample, respectively. These expressions are only valid for a sample within certain maximum dimensions limits.

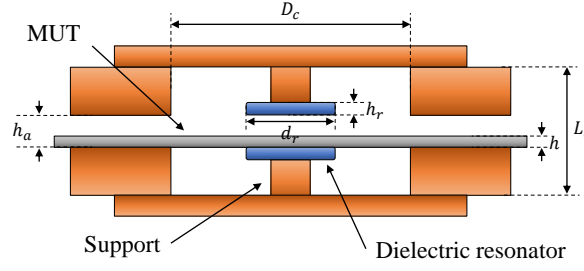


Figure 3.12: Illustration of the Split-Dielectric Resonator structure.

Therefore, the dielectric sample needs to be machined with precision to fit into the cavity and provide that it only interacts with the main component of the electric field in a single mode.

An iris is a thin metal plate across the waveguide with one or more holes in it and is a means of introducing a discontinuity that excites evanescent higher modes, creating filtering effects in waveguides. An iris with a small hole creates a narrowband filter which has an inductive characteristic. The dielectric insert in the waveguide has an equivalent capacitive characteristic, which forms a resonance with the shunt inductance created with the iris. The iris coupled waveguide filter presents a very high Q factor, therefore, the output of the dominant mode presents a very sharp peak, therefore making it easier to identify the dominant mode of resonance and better determine the frequency shift.

The SDR proposed in [96] is an evolution of the structure proposed by Kent and is the most common cavity characterization method available nowadays. These can usually be found for sale from dielectric characterization equipment sellers and are used by microwave substrate manufacturers, such as Rogers Corp.[®], to confirm the results obtained with the stripline resonator test method. The typical SDR structure is shown in Fig. 3.12. In this case, the structure is very similar to the SCR, but the cavity dimensions are reduced, especially the height, due to the introduction of two dielectric disks inside, hold by metallic posts, that create a natural resonance on the structure. The introduction of the dielectric disks with the small height of the metallic enclosure reduces losses due to radiation and create a strong evanescent electromagnetic field inside the cavity outside the dielectric disks region as well as outside the cavity. Simplifying the problem of the air-gap region in the previous method.

As the SCR, the SDR is also operated in the TE_{01} mode, for exactly the same reasons. In the SDR, the permittivity of the dielectric sample is obtained from the measured resonant frequency shift and the quality factor changes by the introduction of the dielectric slab sample. The method to determine the permittivity using this method is iterative and based on the following expression

$$\epsilon_r = 1 + \frac{f_0 - f_s}{hf_0 K_\epsilon(\epsilon_r, h)} \quad (3.51)$$

where h is the thickness of the dielectric sample, f_0 is the resonant frequency of the empty resonator, f_s is the resonant frequency of the cavity with the dielectric sample and $K_\varepsilon(\varepsilon_r, h)$ is a function of the permittivity itself, that can be computed from

$$K_\varepsilon(\varepsilon_r, h) = \frac{f_0 - f_s}{(\varepsilon_r - 1)hf_0} \quad (3.52)$$

To start the iteration process the value of $K_\varepsilon(\varepsilon_r, h)$ is computed to initial value ε_r slightly over 1, and then calculated to its subsequent values obtained from (3.51).

Obtaining the dissipation factor using this method is more complex though. According to Krupka *et al.* [96], one can obtain the loss tangent of the dielectric slab according to

$$\tan \delta = \frac{1}{p_{es}} \left(\frac{1}{Q} - \frac{1}{Q_{DR}} - \frac{1}{Q_c} \right) \quad (3.53)$$

where

$$p_{es} = h\varepsilon_r K_\varepsilon(\varepsilon_r, h) \quad (3.54a)$$

$$Q_c = Q_{c0} K_\varepsilon(\varepsilon_r, h) \quad (3.54b)$$

$$Q_{DR} = Q_{DR0} \cdot \frac{f_0}{f_s} \cdot \frac{p_{eDR0}}{p_{eDR}} \quad (3.54c)$$

being p_{es} , p_{DR} and p_{DR0} the electric energy filling factors for the sample, for the filled dielectric resonator and for the empty dielectric resonator, respectively. Q_{c0} is the quality factor, depending on the conductor losses, of the empty resonator, while Q_{DR0} is the quality factor, depending on the dielectric disk losses, of the empty resonator. In order to obtain these parameters one must use a numerical method to simulate the structure and compute such values. Particularly, Krupka *et al.* [96] used the Reyleigh-Ritz method to compute them.

3.2.2 Non-resonant methods

In the previous section a number of electromagnetic characterization methods based on resonant systems were covered. In this section, another set of methods is presented, but in this case, non-resonant methods. That is, broadband methods. These broadband methods can be based on reflection waves, or on the transmission and reflection wave characteristics when these are propagated through a given MUT. Therefore, this section is split into two subsections, one focused on reflection methods, as is the case of the open-ended coaxial probe, and another focused on transmission/reflection methods, as the case of waveguide or printed transmission lines methods.

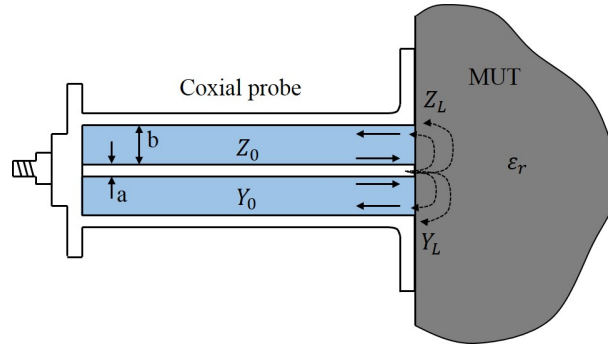


Figure 3.13: Illustration of the coaxial probe measurement feature.

Reflection method

In reflection methods the permittivity is estimated based on the reflection due to impedance differences when a dielectric sample is in the propagation path of a transmission line. One of the most known and used features for dielectric measurements, and which is based on a reflection method, is the open-ended coaxial probe [110]. This has been used for years as a non-destructive testing tool. The versatility of this method is its greatest feature and that's why it has been so widely used in many different areas and applications. It has been applied to the permittivity measurement on solid, semi-solid and liquid materials [111, 112, 113].

In this method the probe is pressed against the test dielectric sample, as shown in Fig. 3.13. The impedance at the side of the MUT is directly related to the dielectric properties of the material, therefore, these properties, namely the permittivity, can be obtained from the reflectivity measurement at the interface.

In order to get the permittivity of the sample, an iterative method is used to search the zero of an error function that is defined as

$$N(\epsilon_r) = |Y_L(\epsilon_r) - Y_m| \quad (3.55)$$

where Y_m is the measured admittance of the sample and $Y_L(\epsilon_r)$ is the theoretical admittance calculated using the aperture model. The aperture model is therefore of crucial importance to obtain the correct estimation of the permittivity of the sample. Several models have been developed, which can be found in [114, 115, 116, 117, 118, 119] and, as explored in [113], full-wave simulation models have also been used. It is out of the scope of this work to explore which model is more appropriate, which might also be dependent on the particular scenario. In most cases, the full-wave simulation models have proven to provide the best approximations.

On another approach, it's also possible to extract the admittance using a calibration method, by measuring a known sample prior to the MUT sample, as shown in [120]. Us-

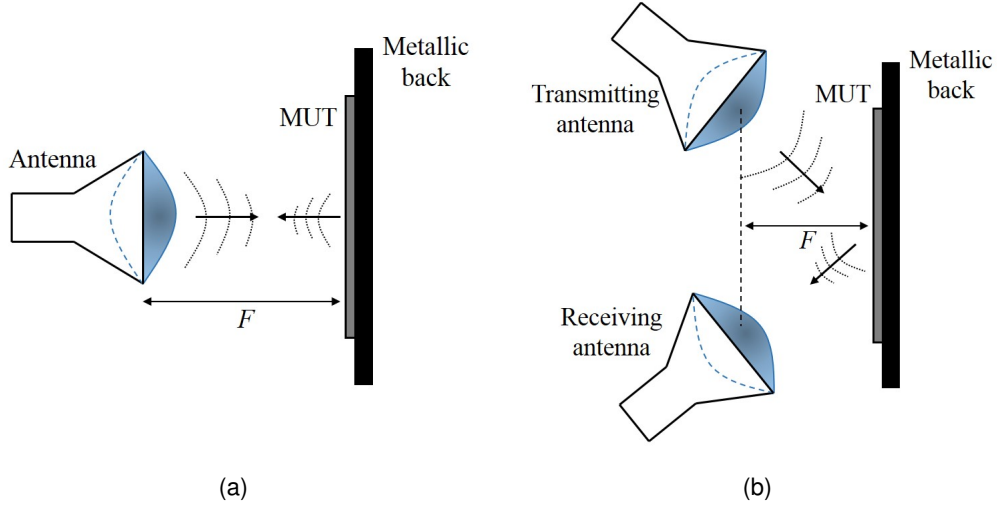


Figure 3.14: Illustration of the open-air reflection measurement (a) mono-static configuration (b) bi-static configuration.

ing an aperture model defined by a capacitance (C_0) and a conductance (G_0) as

$$Y = \sqrt{\varepsilon_m^5} G_0 + j\omega\varepsilon_m C_0 \quad (3.56)$$

we can then use a known dielectric to calculate the G_0 and C_0 parameters of the probe and then use this result to estimate the permittivity of an unknown material. This calibration procedure can also be very useful when applied with any other aperture models.

Another approach using the reflected signal from a dielectric interface to estimate its permittivity is shown in [121, 122] where a free-space environment is used. In this application an antenna is used to radiate towards a planar sample of limited thickness, as illustrated in Fig. 3.14.

The sample's permittivity can be obtained from the reflection coefficient. This reflection can be measured in a mono-static (Fig. 3.14 (a)), or bi-static (Fig. 3.14 (b)) configuration. If we consider the mono-static configuration as described in [121], then the reflection coefficient, which in this case is directly the measured S_{11} can be related to the permittivity as

$$S_{11} = \frac{jz_{\lambda,n} \tan \beta_n d - 1}{jz_{\lambda,n} \tan \beta_n d + 1} \quad (3.57)$$

where $z_{\lambda,n}$ is the wave impedance and β_n is the propagation phase constant which are both dependent on the MUT relative permittivity (ε_r)

$$z_{\lambda,n} = \frac{1}{\sqrt{\varepsilon_r}} \quad (3.58a)$$

$$\beta_n = \frac{2\pi}{\lambda} \sqrt{\epsilon_r} \quad (3.58b)$$

Similar to the previous case for the coaxial-probe, also in this case the permittivity is determined by assuming an initial guess for its value and then determining the correct value by minimizing the error of the function defined as

$$N(\epsilon_r) = |S_{11}^m - S_{11}^c| \quad (3.59)$$

The bi-static configuration is not so advisable because the reflection is dependent on the polarization of the incident wave and different polarizations will lead to different reflections and results. Moreover it caresses from a particular calibration setup that is not easy to perform.

Transmission/Reflection method

Transmission/reflection methods have enjoyed a wide acceptance by engineers and scientists in many fields of applications, from life sciences to electronics, due to their simplicity, ease of measurement, robustness and ability to measure broadband properties of materials. In transmission/reflection measurements a dielectric sample is placed somewhere along the propagation path of a given transmission line and its permittivity can be estimated based on the measurement of the scattering parameters. Since we have access to the transmitted and reflected signals, there's more data available to estimate the permittivity of the samples when compared to the previously mentioned reflection methods.

Nicolson and Ross [123] and Wier [124] have derived explicit formulas for the calculation of the permittivity of a given sample with the measured scattering parameters, which is commonly known as the NRW (Nicolson-Ross-Wier) algorithm. More recently, a few optimizations have been done to overcome the algorithm limitations, such as the estimation at half wavelength multiples of the transmission lines resonance, as shown in [125].

The transmission/reflection methods have been thoroughly analyzed by Baker-Jarvis *et al* in [126, 127, 128]. In this approach the permittivity is obtained through the measurement of the propagation constant of a given transmission line loaded with the MUT. This is a general approach based on transmission lines, therefore, more focus is given towards applicational methods with a given equipment. Nevertheless, the foundations on those references are a solid base to understand how the permittivity of a given material can be obtained through the measurement of the scattering parameters of a transmission line, interacting with a given dielectric sample. A more in-depth explanation about how to get the permittivity values of a sample with the NRW method and the Baker-Jarvis approach can be found in [124, 128].

Direct application of these concepts have been made using different kinds of propagation media. Such as waveguides [129, 130, 131], printed transmission lines [132, 133, 134, 135,

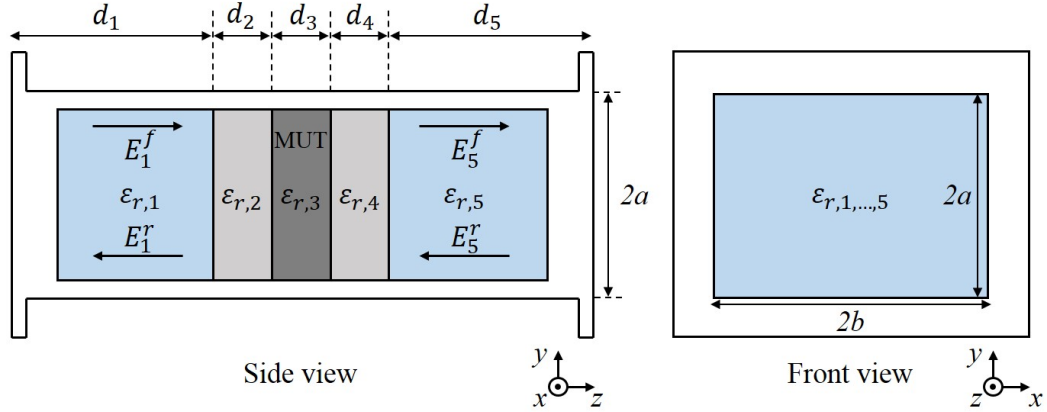


Figure 3.15: Illustration of the cross-section cut of a waveguide measurement feature.

136] or even using focused beam antennas for free-space measurements [137, 138].

Waveguides can be used to estimate the permittivity of solid or semi-solid materials. In the second case, a rigid solid material with known properties must be used to hold the semi-solid in place. This is illustrated in Fig. 3.15. If the MUT is solid, then the holding features (light grey) can be removed which simplifies the problem.

In order to measure the permittivity using this method, a calibration at the ports of the waveguide must be performed, so that the reflection at the interface of the waveguide is fully compensated. Considering the TE_{01} propagating mode inside the waveguide, the electric and magnetic field in each of the layers can be described as

$$E_n(z) = E_n^f e^{-\gamma_n z_n} + E_n^r e^{\gamma_n z_n} \quad (3.60a)$$

$$H_n(z) = H_n^f e^{-\gamma_n z_n} - H_n^r e^{\gamma_n z_n} \quad (3.60b)$$

while the propagation constant can be determined from

$$\gamma = \sqrt{\left(\frac{\pi}{a}\right)^2 - \left(\frac{2\pi}{\lambda}\right)^2 \epsilon_{r,n}} \quad (3.61)$$

Since the tangential components of the fields at the interfaces have to be continuous, (3.60) can be written as

$$E_n^f e^{-\gamma_n d_n} + E_n^r e^{\gamma_n d_n} = E_{n+1}^f + E_{n+1}^r \quad (3.62a)$$

$$H_n^f e^{-\gamma_n d_n} - H_n^r e^{\gamma_n d_n} = H_{n+1}^f - H_{n+1}^r \quad (3.62b)$$

if we relate the magnetic field to the electric field by the wave impedance ($Z_{\lambda,n}$), we get the

following system of eight equations

$$E_1^f e^{-\gamma_1 d_1} + E_1^r e^{\gamma_1 d_1} = E_2^f + E_2^r; \quad \frac{E_1^f e^{-\gamma_1 d_1} + E_1^r e^{\gamma_1 d_1}}{Z_{\lambda,1}} = \frac{E_2^f + E_2^r}{Z_{\lambda,2}} \quad (3.63a)$$

$$E_2^f e^{-\gamma_2 d_2} + E_2^r e^{\gamma_2 d_2} = E_3^f + E_3^r; \quad \frac{E_2^f e^{-\gamma_2 d_2} + E_2^r e^{\gamma_2 d_2}}{Z_{\lambda,2}} = \frac{E_3^f + E_3^r}{Z_{\lambda,3}} \quad (3.63b)$$

$$E_3^f e^{-\gamma_3 d_3} + E_3^r e^{\gamma_3 d_3} = E_4^f + E_4^r; \quad \frac{E_3^f e^{-\gamma_3 d_3} + E_3^r e^{\gamma_3 d_3}}{Z_{\lambda,3}} = \frac{E_4^f + E_4^r}{Z_{\lambda,3}} \quad (3.63c)$$

$$E_4^f e^{-\gamma_4 d_4} + E_4^r e^{\gamma_4 d_4} = E_5^f + E_5^r; \quad \frac{E_4^f e^{-\gamma_4 d_4} + E_4^r e^{\gamma_4 d_4}}{Z_{\lambda,4}} = \frac{E_5^f + E_5^r}{Z_{\lambda,5}} \quad (3.63d)$$

As it is, this system is under determined. However, if the measurement is calibrated at the waveguides planes, so that the coaxial-waveguide transitions are eliminated from the measurement, then there's no reflection at port 2 and as consequence $E_3^r = 0$. Knowing the permittivity of the layer 1 and 5, usually air, of the supporting material 2 and 4, and incident amplitude E_1^f , we have a linear system with eight unknown variables which can, therefore, be solved.

The S-parameters for this system can be defined as

$$S_{11} = \frac{E_1^r}{E_1^f} \quad (3.64a)$$

$$S_{21} = \frac{E_5^f e^{-\gamma_5 d_5}}{E_1^f} \quad (3.64b)$$

To determine the permittivity of the MUT we compare the theoretical estimation of the S-parameters to the measured values. The correct permittivity value $\varepsilon_{r,3}$ is iteratively found by minimizing the error in the form

$$N(\varepsilon_{r,2}) = |S_{11}^c - S_{11}^m|^2 + |S_{21}^c - S_{21}^m|^2 \quad (3.65)$$

To find the minimum of the defined error function, different optimization algorithms can be used. The study of the computational and mathematical complexity of each algorithm is out of the scope of this work.

The disadvantage of this method is that it requires a precise machination of the dielectric sample in order for it to fit inside the waveguide. If the sample does not completely fill the waveguide borders and air-gaps exist between the sample and the waveguide walls, or if the sample is very thin, large errors arise in the estimated values.

Some approaches considering the existence of air-gaps have been developed already, which require even more complex computations. These are shown in [130, 131]. Although these remove some constraints from the sample's physical characteristics, it is not without

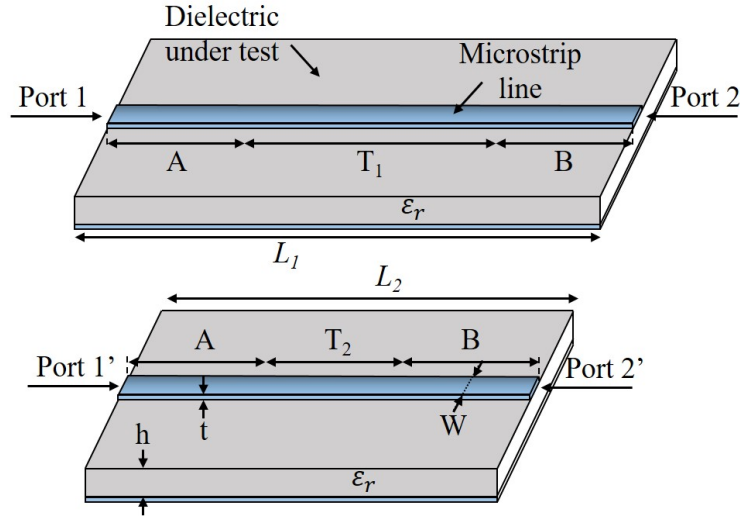


Figure 3.16: Illustration of the two different length printed transmission lines with separation of different transmission sections.

further complications on the computational side or in the obtained measurement errors.

The previous methods are applied to unmetallized substrates. However, most of the times, microelectronics and microwave electronics use conductors deposited directly on a substrate. Printed transmission lines like microstrip, stripline and coplanar strip, or antennas are some examples of these fixtures. In the metalization process part of the metallic particles can penetrate into the dielectric material, changing the permittivity and the losses. Therefore, it is interesting to measure these characteristics on a system as a whole.

A possible approach is the phase differential method, In this approach, the phase constant difference between a particular set of lines and the ideal, free-space, phase constant is used to estimate the permittivity of the substrate that supports the printed lines.

This method was first introduced by Lee *et al* in [132], and was further developed in [133, 134]. In order to estimate the permittivity of a given substrate, two printed transmission lines are needed, as depicted in Fig. 3.16, with the exact same characteristics but with different lengths. With the transmission/reflection measurement data of these two lines, the propagation constant, and therefore the phase constant, can be calculated.

The transmission matrix of each line can be obtained from the measured S-parameters as

$$M_i = \frac{1}{S_{21i}} \begin{bmatrix} (S_{12i}S_{21i} - S_{11i}S_{22i}) & S_{11i} \\ -S_{22i} & 1 \end{bmatrix} \quad (3.66)$$

If we take on two microstrip lines as illustrated in Fig. 3.16, we can separate the different sections of the line and say that the transmission matrix is the product of the transmission

matrices of each depicted section of the form

$$\bar{M}_1 = \bar{A} \cdot \bar{T}_1 \cdot \bar{B} \quad (3.67a)$$

$$\bar{M}_2 = \bar{A} \cdot \bar{T}_2 \cdot \bar{B} \quad (3.67b)$$

which can be solved to reach

$$\bar{M} \cdot \bar{A}^{-1} = \bar{A}^{-1} \bar{T} \quad (3.68)$$

being

$$\begin{aligned} \bar{M} &= \bar{M}_1 \cdot \bar{M}_2^{-1} \\ \bar{T} &= \bar{T}_1 \cdot \bar{T}_2^{-1} \end{aligned} \quad (3.69)$$

The T_i is the transmission matrix of the middle section, so we can say that T is

$$T = \begin{bmatrix} e^{-\gamma \Delta l} & 0 \\ 0 & e^{\gamma \Delta l} \end{bmatrix} \quad (3.70)$$

With this information, we can develop (3.68) to reach an eigenvalue (λ_i) equation in the form

$$\lambda_{1,2} = \frac{1}{2} \left[\text{Tr}(M) \pm \sqrt{\text{Tr}(M)^2 - 4\Delta M} \right] \quad (3.71)$$

where $\text{Tr}(M)$ is the trace and ΔM is the determinant of M .

Since the system is passive, the relation $|e^{-\gamma \Delta l}| < 1$ imposes a particular signal for the solution of (3.71). The propagation constant can then be defined as

$$\gamma = \frac{1}{\Delta l} \ln \lambda_{av} + j \frac{2\pi n}{\Delta l} \quad (3.72)$$

being $\lambda_{av} = \frac{1}{2} \left(\lambda_1 + \frac{1}{\lambda_2} \right)$ the average of the solution of (3.72) and if $\Delta l < \lambda_0/2$ then $n=0$. The effective permittivity of the substrate can be related to the unwrapped phase of the calculated propagation constant as

$$\varepsilon_{eff} = \left(\frac{\beta}{\beta_0} \right)^2 \quad (3.73)$$

The relative permittivity of the substrate can be obtained from the effective value, by the approximate forms for each type of transmission line used in this implementation, as presented in [139]. This method has been further extended in [135, 136], using coplanar lines to estimate the permittivity of superposed dielectrics, instead of the substrate holding the lines.

Another simple method using microstrip lines, is the differential phase length method, which is used by some manufactures, namely Rogers[®], to determine what they present in their datasheets as *Design Dk*, or design dielectric constant. They noticed that the value of permittivity of the material determined based on the IPC TM-650 2.5.5.5C, when used in

RF systems design and EM simulators to simulate planar circuits, especially with microstrip lines, would often lead to errors in the predicted results, coming from an erroneous definition of the permittivity value of the substrates. They realized that using the dielectric constant obtained from microstrip line methods would lead to better matching between simulations and measurements of planar circuits. This happens essentially because the equivalent permittivity estimated with microstrip lines already takes into account effects of melding between the cladding and the substrate during electrodeposition process.

The differential phase length method needs at least two different microstrip lines, built on the same substrate, with exactly the same characteristics except for the length. One of the lines should be considerably larger (electrically speaking) than the other. The electrical length of the lines is related to the propagation phase along the lines times its length, as

$$\beta l = 2\pi\sqrt{\varepsilon_{r,eff}}\frac{f}{c}l \quad (3.74)$$

Therefore, the phase difference of this two lines is closely related to the difference in lengths

$$\Delta\beta = 2\pi\sqrt{\varepsilon_{r,eff}}\frac{f}{c}\Delta l \quad (3.75)$$

By measuring the propagation phase of the two lines, obtained by unwrapping the phase component of the S_{21} parameter, and by knowing the physical size of the lines, one can reach the effective permittivity of the substrate as

$$\varepsilon_{r,eff} = \left(\frac{\Delta\beta}{2\pi f \Delta l} \right)^2 \quad (3.76)$$

the relative permittivity of the substrate can be calculated from the effective permittivity and the physical characteristics of the line, with closed form expressions such as (3.37) [139].

So far we have looked into measurement techniques that require a sample to be in close contact with the testing equipment. However, there are some techniques that allow for the characterization of dielectric without contact. These open-space techniques are very useful for the characterization of materials that are difficult to handle or to characterize their response with temperature or other conditions.

A proposal of the mentioned method is presented in [137, 138]. For the application of this method spot-focusing lens antennas are used, with the MUT being placed in the middle point between the two antennas, at a distance that corresponds to the focal distance, F . The setup is illustrated in Fig. 3.17.

As in the previous transmission/reflection methods, in this case the permittivity is obtained from propagation constant of the waves in the media, in comparison to that of free-space as

$$\varepsilon_r = \frac{\gamma}{\gamma_0} \left(\frac{1 - \Gamma}{1 + \Gamma} \right) \quad (3.77)$$

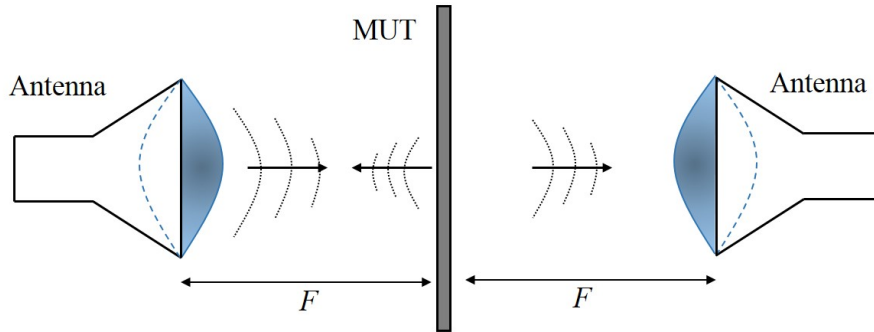


Figure 3.17: Illustration of the open-air transmission/reflection measurement configuration.

where γ and γ_0 are the propagation constant in the MUT and in free-space, respectively. While γ can be obtained from the transmission parameter (T) as described in the NRW method in [83].

This scenario requires that the sample is wide enough so that the diffraction effects of the radiation at the sample edges is negligible. Moreover, it requires a free-space calibration to be performed and that the S-parameters be obtained by time-gating technique instead of direct frequency measurement, in order to reduce ripple that occurs due to source and load mismatches. Also, the sample must be thin enough ($d < \lambda_m$), so that the permittivity holds a single solution. Due to that, samples that cannot hold straight on the supports and that present sagging, increase the complexity of the method since a holder for the sample is required, which is more complex to de-embed from the S-parameters measurements.

3.2.3 Single microstrip line characterization

The printed transmission line methods shown so far have proven to be the most interesting for characterization of the dielectric materials, especially considering most of them are in the form of sheets. This is due to the fact that no additional fixtures of test equipment is needed apart from a VNA (Vector Network Analyzer), and also due to the simplicity of the measurement procedure.

All the materials that were characterized during the course of this thesis, have been so, using the NRW method or the differential phase method presented previously. Although the results obtained with this method have been rather satisfactorily accurate, the faulty sample preparation would introduce a considerable amount of error in the measurement. This happens due to the fact that the conductor part of the microstrip lines used had to be made out of copper tape, which would be cut by hand, or using conductive ink. This would make it very hard to create two lines with the exact same physical characteristics in terms of width. Moreover, the dielectric sheets used, especially in the case of cork, were not always exactly flat and the two lines used would have a slight difference in substrate

thickness. Considering that printed transmission line methods require that both lines used for measurement have exactly the same physical characteristics except for length, errors were being introduced in the measurement due to sample preparation.

To avoid the mentioned problem, we looked into a way of measuring the permittivity of a given substrate using a single microstrip line measurement, which would avoid the problems of trying to prepare two samples with the exact same characteristics. This method has been developed and has been presented in [140]. In this approach a single microstrip line is fabricated and is measured with an *open-circuit load* from the VNA calibration kit.

In a transmission line ended with an open-circuit ($Z_L = \infty$), according to [83], the impedance seen at the entrance of the line along l is

$$Z_{in} = \frac{Z_0}{\tanh \alpha l + j\beta l} \quad (3.78)$$

being Z_0 the characteristic impedance of the line and α and β the propagation constant attenuation and phase, respectively. Considering that $\beta = 2\pi/l$ and $l = \lambda_r/2$, where λ_r is the wavelength at resonance, then we have $\beta l = \pi f/f_r$. If we replace this into 3.78, separate the real and imaginary components and consider the input impedance at one fourth of the resonant frequency ($\beta l = \pi/4$), then 3.78 becomes

$$Z_{in} = Z_0 \left\{ \frac{2 \tanh \alpha l}{1 + \tanh^2 \alpha l} - j \frac{1 - \tanh^2 \alpha l}{1 + \tanh^2 \alpha l} \right\} \quad (3.79)$$

If we assume the losses are positive (which is the case for all natural materials), and considering $Z_{in} = R - jX$, we can say

$$\tanh \alpha l = -\frac{X}{R} + \sqrt{\left(\frac{X}{R}\right)^2 + 1} \quad (3.80a)$$

$$Z_0 = X \frac{1 + \tanh^2 \alpha l}{1 - \tanh^2 \alpha l} = R \frac{1 + \tanh^2 \alpha l}{2 \tanh \alpha l} \quad (3.80b)$$

Recalling the closed form expressions for the characteristic impedance of a microstrip line, according to [139], and transforming them in terms of the effective permittivity of the substrate, we reach

$$\varepsilon_{r,eff} = \left(\frac{60}{Z_0} \ln \left(\frac{8h}{W} + \frac{W}{4h} \right) \right)^2, \quad \text{when } W/h \leq 1 \quad (3.81a)$$

$$\varepsilon_{r,eff} = \left(\frac{120\pi}{Z_0} \frac{1}{\frac{W}{h} + 1.393 + 0.667 \ln \left(\frac{W}{h} + 1.444 \right)} \right)^2, \quad \text{when } W/h > 1 \quad (3.81b)$$

being W the width of the microstrip line and h the thickness of the substrate.

With the knowledge of the effective permittivity of the substrate, one can calculate the

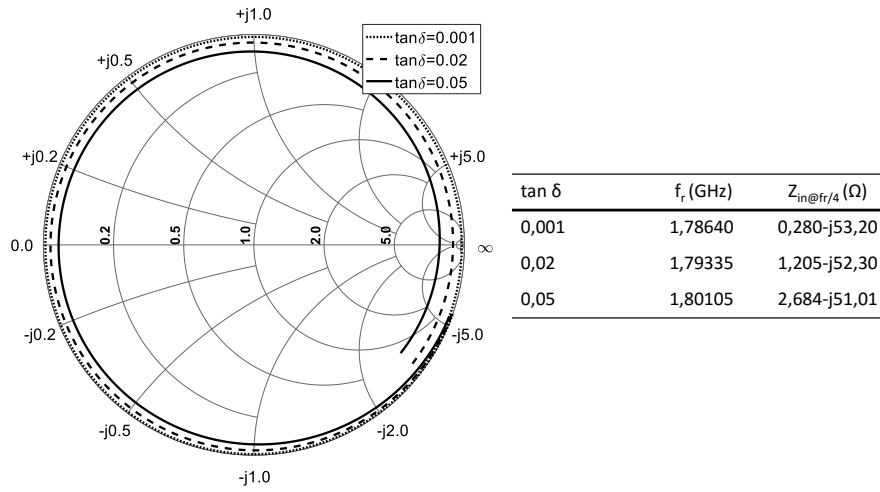


Figure 3.18: Simulation results of the input impedance of a microstrip line terminated with an open circuit for different values of dissipation factor.

relative permittivity [139] of the material with

$$\varepsilon_r = \frac{2\varepsilon_{r,eff} + \frac{1}{\sqrt{1+12h/W}} - 1}{1 + \frac{1}{\sqrt{1+12h/W}}} \quad (3.82)$$

This process to determine the permittivity of the substrate is rather simple, since it requires a single microstrip line prototype and largely simplifies the problem since we only need a single measurement to obtain the permittivity of the material. Therefore, avoiding the problems with repeatability when manufacturing the line prototypes.

One thing to consider when measuring the microstrip line is to effectively use a open-circuit load from the calibration kit of the VNA, otherwise the load impedance at the end of an open line is not infinite nor close to it. Since the line edge will radiate, it will have a finite capacitive impedance which deviate the resonant frequencies of the line and therefore induce an error in the determination of the permittivity.

After a few trials for permittivity measurement with known materials, the values obtained for permittivity were reasonably accurate, but there was a certain degree of error. It has been observed that the increase of the losses of the substrate induce a shift in the resonant frequency when compared to a lossless line. This happens because the losses will create a curling effect in the input impedance of the line as frequency increases, as shown in Fig. 3.18. This shift in the smith chart for the input impedance of the line induces an error in the estimation method, since the characteristic impedance of the line is wrongly estimated for a material with high losses.

This shift in resonance however, is linearly related to the propagation losses. After a considerable number of simulations with microstrip lines with different physical characteris-

Table 3.2: Simulated results for resonance, corrected resonance and characteristic impedance for a microstrip line on a varying dissipation factor substrate.

$\tan \delta$	f_r (GHz)	f'_r (GHz)	$Z_0@_{f_r/4}$	$Z_0@_{f'_r/4}$
0.001	1.78640	1.7817	53.21	53.42
0.02	1.79335	1.7729	52.31	53.25
0.05	1.80098	1.7549	51.01	53.10

tics, each of it, in substrates with varying numbers of dissipation factors, we realized that the frequency at which one should verify the input impedance is not directly one fourth of the resonant frequency, but is actually one fourth of a corrected resonant frequency given by the relation

$$f'_r = \frac{f_r}{1 + \alpha l} \quad (3.83)$$

It is shown in Table 3.2 the calculated characteristic impedance of the three microstrip lines shown in Fig. 3.18, for the normal resonance of the line and the corrected resonance from (3.83). First, it is clear that the characteristic impedance of the line, calculated with the normal resonance, decreases with an increase of the losses. Moreover, it is clear that after the resonance correction, the determined characteristic impedance of the lines is more like each other, which leads to a more accurate estimation of the relative permittivity of the substrate.

So the procedure for correct estimation of the characteristic impedance of the line and therefore, the correct permittivity of the substrate, is to measure the input impedance at one fourth of the first resonance of the line. With that value, calculate αl according to (3.80a), and apply the result in (3.83) in order to obtain the corrected resonance frequency (f'_r). Then, determine the input impedance at one fourth of the corrected resonance and with it calculate the characteristic impedance of the line using (3.80). With knowledge of the characteristic impedance of the line and knowing the physical dimensions of the microstrip line, one can easily obtain the permittivity of the substrate based on (3.81).

The dissipation factor of a substrate used for a microstrip line can be obtained, as shown previously in (3.39), from the permittivity and the propagation losses due to dielectric. The propagation loss is a sum of several losses, which include conductor, dielectric, radiation and leakage losses. If the ground plane is large enough around the transmission line the leakage losses can be neglected. However, unlike the ring resonator structure, the radiation losses of a microstrip line cannot be neglected.

The conductor losses can be calculated using empiric closed form expressions as shown in [141]. However, these expressions are empirical, meaning they're dissociated from what actually is being measured and are frequency independent. Since the losses from the di-

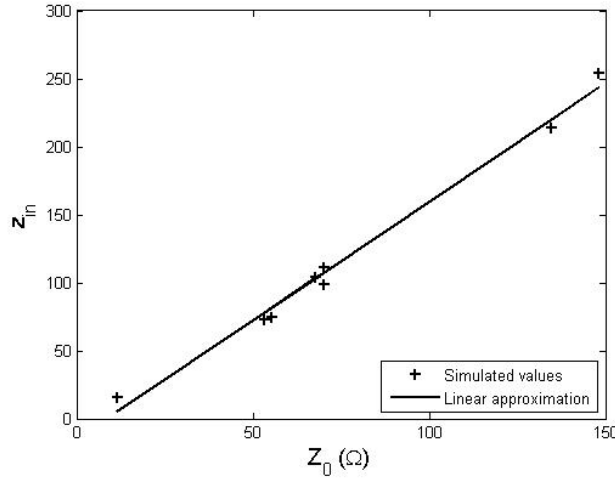


Figure 3.19: Relation between the characteristic impedance of microstrip lines and the input impedance at resonance for perfect conductor lines.

electric change with frequency, a small error in the calculation of the conductor losses can lead to a large error in the overall result.

Using ADS Momentum EM simulator several lines were designed, with different lengths, widths and different values for the substrate permittivity, loss and thickness. Some of the simulated lines and the corresponding obtained impedance results are presented in Table 3.3. Where z_{in} is the input impedance of the line at the resonant frequency, normalized to the reference impedance of 50Ω , when considering the use of perfect conductors (no loss from the conductors). While z_m is the input impedance of the line at the resonant frequency normalized to 50Ω , but considering the conductor losses.

It is noticeable from the presented values, that there is a decrease in the input impedance as the losses increase. Besides, there is a direct proportionality between the characteristic impedance of the lines and the input impedance at resonance. We can see this tendency in Fig. 3.19, where the variation of the characteristic impedance of several lines with their input impedance at resonance, considering $\tan \delta = 0.01$, is depicted.

A possible linearization of the relation between the normalized input impedance and the characteristic impedance of the line is

$$z_{in} = 1.95Z_0 - 27.4 \quad (3.84)$$

and since the loss tangent is inversely proportional to this input impedance, we reach

$$\tan \delta = \frac{0.0195Z_0 - 0.274}{z_{in}} \quad (3.85)$$

This expressions can give a first estimation of the loss tangent. However, it only takes

Table 3.3: Simulated input impedance of several microstrip lines for different substrates

Line characteristics	$\tan \delta$	$z_{in} (\Omega)$	σ (MS/m)	$z_m (\Omega)$
Line 1 $Z_0 = 11.53$ $W = 2$ mm $h = 0.1$ mm $\epsilon_r = 2$	0.01	15.55	1.0	3.03
			10.0	5.87
			58.0	9.01
	0.03	5.15	1.0	2.20
			10.0	3.35
			58.0	4.17
	0.05	3.07	1.0	1.73
			10.0	2.34
			58.0	2.70
	0.01	72.77	1.0	30.43
			10.0	46.99
			58.0	58.28
Line 2 $Z_0 = 53.23$ $W = 1$ mm $h = 1$ mm $\epsilon_r = 8$	0.03	24.20	1.0	16.62
			10.0	20.51
			58.0	22.42
	0.05	14.49	1.0	11.42
			10.0	13.10
			58.0	13.84
Line 3 $Z_0 = 70.18$ $W = 2$ mm $h = 1$ mm $\epsilon_r = 1.8$	0.01	110.94	1.0	60.39
			10.0	47.28
			58.0	48.91
	0.03	36.77	1.0	28.50
			10.0	33.09
			58.0	35.08
	0.05	21.93	1.0	18.94
			10.0	20.67
			58.0	21.38
Line 5 $Z_0 = 148.13$ $W = 1$ mm $h = 3$ mm $\epsilon_r = 2$	0.01	254.03	1.0	137.74
			10.0	190.75
			58.0	221.63
	0.03	84.09	1.0	65.18
			10.0	75.63
			58.0	80.19
	0.05	50.29	1.0	43.29
			10.0	47.28
			58.0	48.91

Table 3.4: Calculated K and τ coefficients for several lines

$\tan \delta$	σ (MS/m)	τ	K
0.01	1.0	210.63	0.858
	10.0	141.62	0.673
	60.0	118.54	0.426
0.03	1.0	139.59	0.600
	10.0	114.82	0.349
	60.0	105.18	0.185
0.05	1.0	125.45	0.436
	10.0	109.28	0.228
	60.0	103.62	0.114

into account the dielectric loss. In order to consider the remaining sources of losses in the microstrip line, for the correct calculation of the dissipation factor, we consider a normalized impedance z_m that tends towards z_{in} as the conductivity increases, which can be also devised by the results on Table 3.3. This relationship can be approximated by the following expression

$$z_{in} = z_m \left(1 - K e^{\frac{Z_0 W}{\tau}} \right)^{-1} \quad (3.86)$$

where W is the width of the line in millimeters, Z_0 is the characteristic impedance of line, and K and τ are two constant values that depend on the losses. To reach the correct factors K and τ , equation (3.86) can be rearranged in order to get a relation between K , τ and $Z_0 W$, as follows

$$Z_0 W = \tau \ln \left(1 - \frac{z_m}{z_{in}} \right) - \tau \ln K \quad (3.87)$$

since z_m is the input impedance considering all the losses, which will tend towards z_{in} as the conductivity increases, one can calculate the K and τ factors for different loss tangents and different conductivity values. By doing so, we reached the values presented in Table 3.4.

According to these values, we can see that there is an inverse linear relation of K and τ with the square root of the conductivity as depicted in Fig. 3.20.

Based on these results K and τ are a linear relation of the inverse of the square root of the conductivity as follows

$$K = \frac{a_K}{\sqrt{\sigma_a}} + b_K \quad (3.88a)$$

$$\tau = \frac{a_\tau}{\sqrt{\sigma_a}} + b_\tau \quad (3.88b)$$

where σ_a is an educated guess of the conductivity value and the values a_τ , b_τ , a_K and b_K

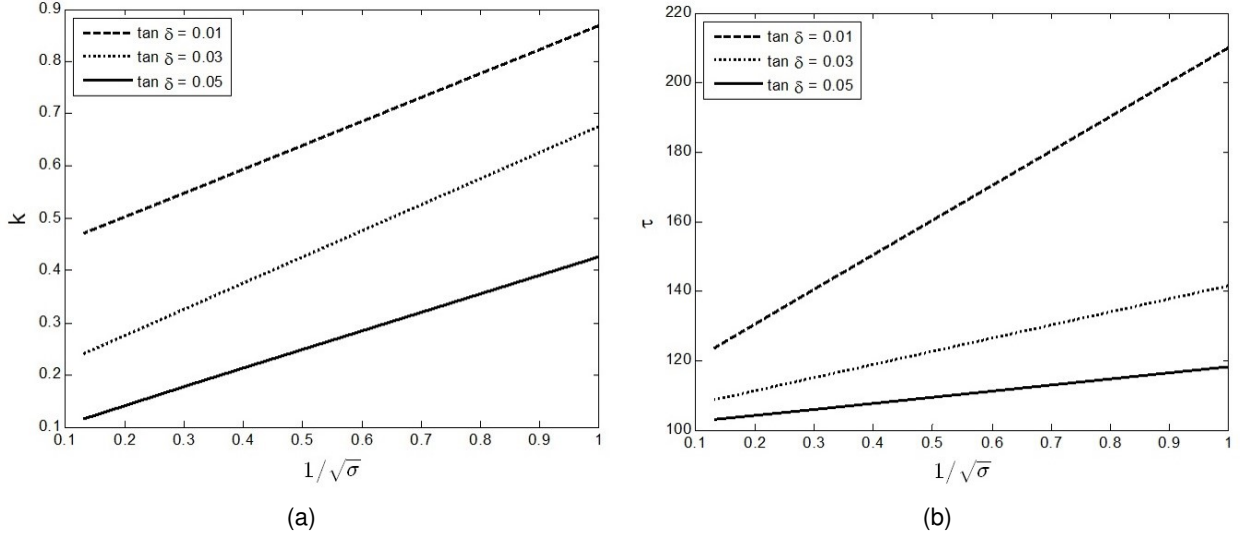


Figure 3.20: Relation between the K and τ factors with the conductivity of the line conductors for different loss tangent values. (a) Relation of K and (b) relation of τ , with the inverse of the square root of the conductivity.

are obtained from a linearization that relates to the loss tangent as follows

$$a_K = 0.475 - 2.105 \tan \delta \quad (3.89a)$$

$$b_K = \frac{0.0644}{\sqrt{\tan \delta}} - 0.203 \quad (3.89b)$$

$$a_\tau = 115.6 - 1991.0 \tan \delta \quad (3.89c)$$

$$b_\tau = \frac{1.097}{\sqrt{\tan \delta}} + 95.53 \quad (3.89d)$$

Since these factors depend on the loss tangent themselves, this becomes an iterative problem.

The algorithm is described as follows: Start by calculating a first approximation to the loss tangent with (3.85), after that we can calculate the K and τ factors that allow the calculation of (3.86). Using that new estimated input impedance (z_m) recalculate the loss tangent with (3.85), by replacing z_{in} with z_m .

A good approximation for the loss factor is achieved usually after four iterations, as is shown in the convergence graphic depicted in Fig. 3.21. From the results in Fig. 3.21 we can see that, independently of the loss tangent or the conductivity, the method converges for a very reasonable value after the fourth iteration. Moreover, even for very different conductor loss values, the method converges for a very approximate dielectric loss; therefore, showcasing low dependence on this parameter. This means that, even if the conductivity value is not precise, one can reach accurate dielectric loss values.

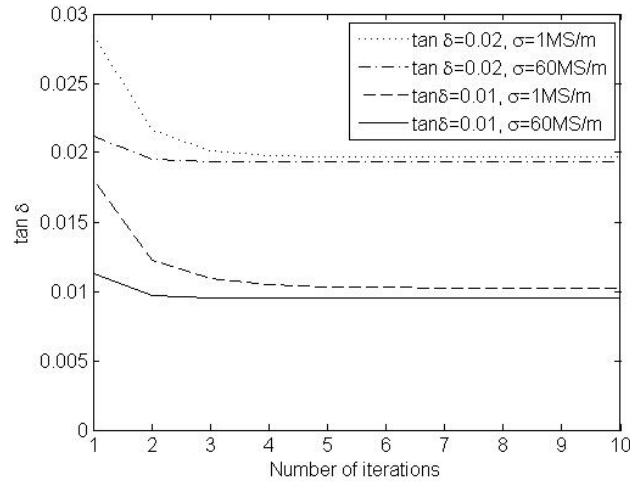


Figure 3.21: Convergence of the dissipation factor determination method with the number of iterations, for different conductivity and dielectric losses.

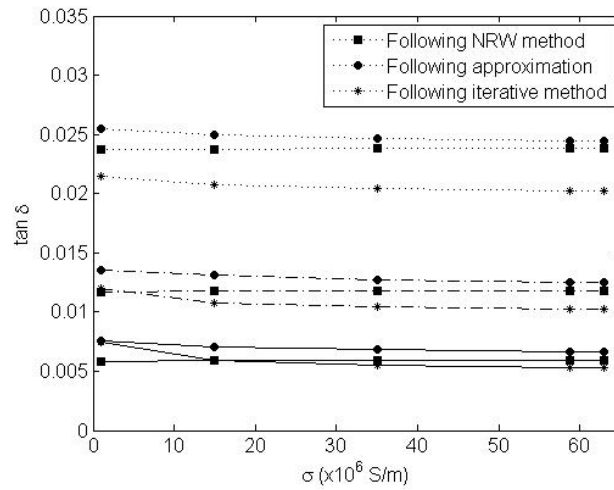


Figure 3.22: Loss tangent determination for different loss dielectrics with NRW method, approximation (3.80a) and the iterative method.

A comparison about the estimation of the loss tangent with three different methods is shown in Fig. 3.22. These results are obtained from simulation for dielectrics with different losses ($\tan \delta = 0.01, 0.02$ and 0.005).

In the calculation of the loss tangent with the NRW method, the total losses are obtained from

$$\alpha = -\frac{\ln |T|}{l} \quad (3.90)$$

where T is the transmission matrix obtained from the NRW method, which can be calculated

Table 3.5: Dielectric substrate samples physical dimensions

Material	L (mm)	h (mm)	W (mm)	W_s (mm)
FR-4	39.6	1.59	0.8	18
RT6010	44.2	0.64	1.0	26
LDPE	46.0	1.00	1.16	31

from the S parameters, as [142]

$$T = \frac{S_{11} + S_{21} - \Gamma}{1 - (S_{11} + S_{21})\Gamma} \quad (3.91)$$

Either when using the NRW or the approximation (3.80a), the losses due to leakage and radiation are discarded. In these methods the total propagation loss constant is calculated and the portion corresponding to the conductor losses is subtracted. The conductor losses are obtained according to the expressions in [141].

From the results depicted in Fig. 3.22, it is clear that the iterative method proposed, leads to better estimations of the loss tangent, independently of the dielectric or conductor losses, when compared to other estimation methods.

In order to verify the proposed method, three different substrates with known dielectric properties and different permittivity values, namely, a Rogers[®] RT6010 laminate, a FR-4 with low resin laminate and a LDPE (Low Density Polyethylene) laminate, were used to fabricate microstrip lines for measurement purposes. As we can see from Table 3.5, we used different ratios for the line, so that the calculations would fall into the different intervals for each.

The microstrip lines on the Rogers and the FR-4 substrates were etched traditionally, using a milling process. For the plastic, since these had no conductor electrodeposited in it, we used copper tape for the conductive parts of the lines. The prototypes are depicted in Fig. 3.23.

The effective permittivity is calculated using the previously described expressions to extract $\varepsilon_{r,eff}$, from which one can calculate the relative permittivity (ε_r) of the substrate. In order to obtain better results one can consider the effective width of the lines (W_e), as described in [139].

As for the loss tangent determination the iterative method as described previously in this section should be used. The method stops when the variation of the value between iterations is very small or when you reach a negative value, in which case, the current and previous values should be discarded and second to last value obtained is the one considered the closest to the loss tangent of the dielectric under test.

The results obtained for the considered lines based on the measurements and calculations described, yield the results presented in Table 3.6.

Comparing the obtained values for the permittivity and the dissipation factor with the re-

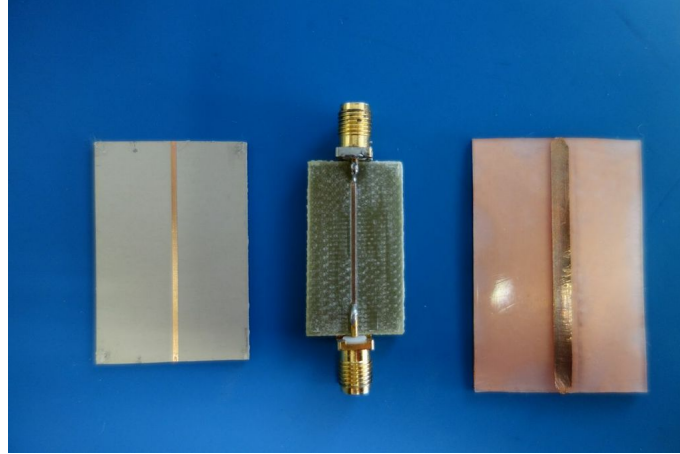


Figure 3.23: Photograph of the microstrip transmission lines tested. From left to right: Rogers RT6010 substrate, FR-4 substrate and LDPE (low density polyethylene) substrate.

Table 3.6: Estimated values of the three sample dielectric slabs based on the proposed method and reference values from literature

Material	Z_0 (Ω)	ϵ_r	Ref. ϵ_r	$\tan \delta$	Ref. $\tan \delta$
FR-4	93.3	4.29	4.3-4.7	0.018	0.01-0.04
RT6010	36.9	10.15	10.20	0.003	0.0023
LDPE	84.8	2.30	2.20-2.35	0.07	0.001

ported values in the materials datasheets we can see a good agreement. However, these values are only relative references since the frequencies and methods used to characterize such materials differ. Besides, it is known, as stated earlier, that these parameters are dependent on frequency and temperature. Therefore, it is expected to observe some differences regarding the estimated values. Nevertheless, a statistical analysis has been conducted in order to assess the stability of the measurement method. It is shown in Fig. 3.24, the probability function of the estimated permittivity and dissipation factor, for the three different substrates.

From the results obtained one can see that the estimation of the permittivity of the LDPE and FR4 are rather accurate, with obtained values in close relation to the reported in the literature. The estimation of the RT6010 substrate has shown the highest deviation from the documented values, since the obtained estimations for permittivity range from 9.8 to 10.8, with the highest incidence around 10, while the manufacturer reports a permittivity of 10.2 to 10.8. It is therefore clear that, although the method shows reliable results for low and medium permittivity materials, it may provide worst estimations for higher permittivity and low loss materials.

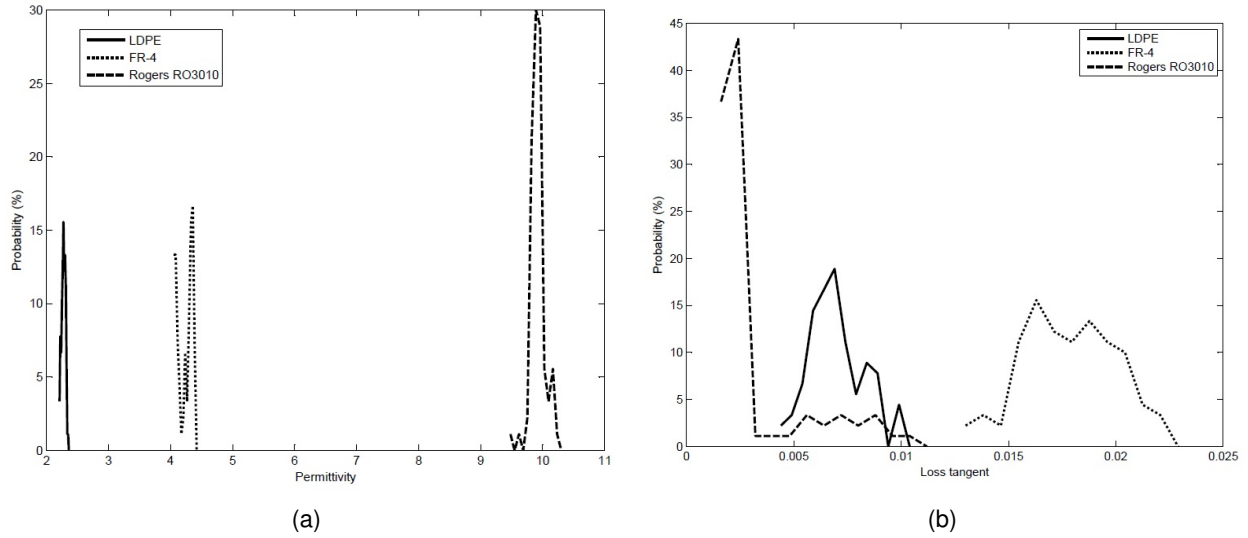


Figure 3.24: Probability function of the measured microstrip lines substrate permittivity (ϵ_r) and dissipation factor ($\tan \delta$). (a) Permittivity distribution and (b) Dissipation factor distribution.

3.3 Dielectric properties of non-conventional materials

After a review of the methods for electromagnetic material characterization, in this section, the characteristics, permittivity and dissipation factor, for different types of alternative materials is presented.

Although there are many methods for electromagnetic characterization, many of them require specific equipment for measurement, or in other cases it requires the material sample to be machined to a specific shape or form, such as the resonant methods based on cavities. In many cases the platform for measurement is not available or the equipment for sample machining is not available or even the sample is not prone to machining. Therefore, the methods chosen to characterize the materials analyzed during the course of this thesis, are the printed transmission lines methods, due to the easy fabrication process and availability of testing and measurement equipment. Besides, as stated before, since the materials will be used as substrate for printed electronic circuits, methods that use printed transmission lines provide values more close to those that should be considered for design purposes than the actual real value of permittivity of the material (See section 3.2.2 on Microstrip line measurements). The results shown in this section were, therefore, obtained with either the dual microstrip line NRW method, or single microstrip line method, and in some cases both.

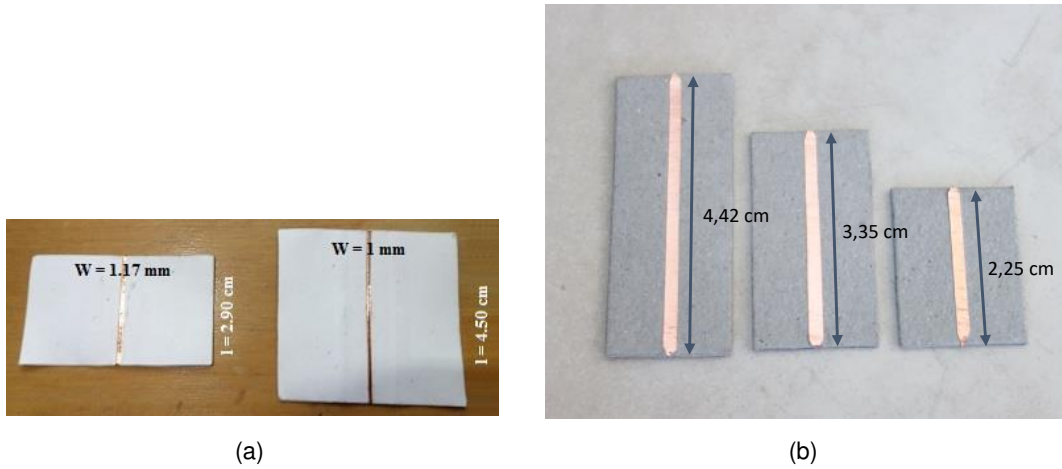


Figure 3.25: Microstrip lines used for permittivity measurement on (a) printer paper substrate and (b) cardboard of recycled paper substrate.

3.3.1 Dielectric properties of paper

Two types of paper substrate was tested, the current 80 g office printer paper and a recycled cardboard like compressed paper, as shown in Fig. 3.25. The 80 g paper substrate has a thickness of 0.1 mm while the cardboard substrate has 1.1 mm. The microstrip lines on the 80 g paper where cut with approximately 1 mm of width, subject to slight differences since these were cut by hand, while the lines on the cardboard substrate where cut with a width of 2 mm. Different length microstrip lines were built, in order to apply the two length line method presented in section 3.2.2 and the single microstrip line measurement presented in section 3.2.3, which takes benefit of multiple line measurements in order to decrease the error of the estimation.

Using the single microstrip line measurement, the medium value of permittivity obtained for the 80 g paper was of 1.715, while for the cardboard was of 1.82. The results of the measurements used for the calculation are summarized in Table 3.7. The medium value of the dissipation factor of the 80 g paper was of 0.0182, which is rather high, but acceptable since it's comparable to a regular FR-4 substrate losses, and expected, when compared to other references [92]. On the other hand, the medium value of the dissipation factor of the cardboard was of 0.0703, which is unexpectedly high.

In order to confirm the results obtained from the single microstrip line measurement, the two length line method as described in [134] was used. For the cardboard substrate the large and medium lines were considered for measurement and the smaller line was discarded, since the results from the application of the single line method shown that the smaller line presented the larger deviation from medium values. The lines were measured from 100 MHz up to 4 GHz, since this was the maximum frequency of measurement, imposed by the length

Table 3.7: Measured and calculated relevant values for permittivity determination of the paper substrate materials

Material	Line	$\tanh(\alpha l)$	f'_0 (GHz)	Z_0 (Ω)	ϵ_r	$\tan \delta$
80 g paper	small	0.0486	2.829	22.24	1.70	0.0176
	large	0.0443	1.923	19.38	1.73	0.0188
cardboard	small	0.0243	3.297	79.29	1.80	0.0738
	large	0.0276	2.399	73.68	1.83	0.0666
	large	0.0286	1.910	74.52	1.82	0.0704

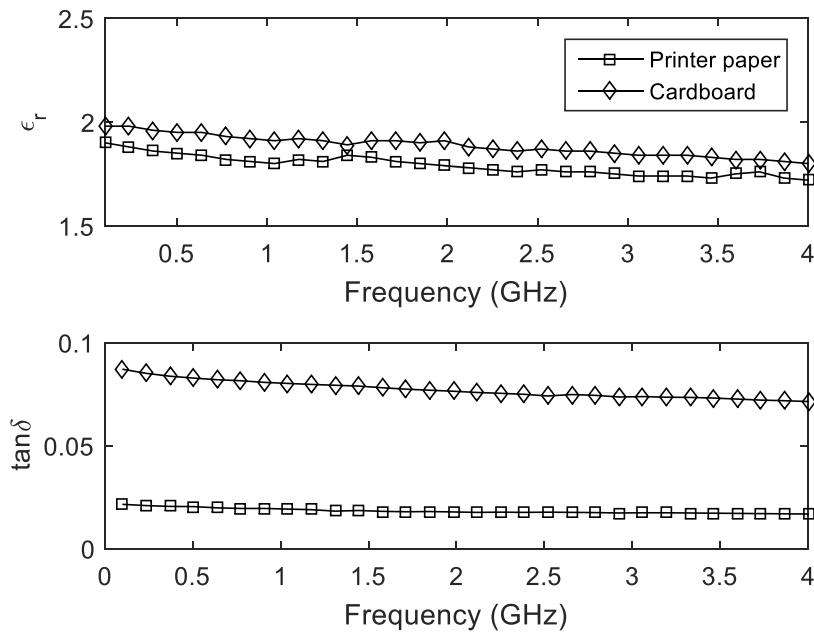


Figure 3.26: Measured dielectric constant and loss tangent of the samples of 80 g printer paper and cardboard in the range from 0.1 to 4 GHz.

difference between the smaller and the larger line in printer paper substrate. The results obtained from the application of this method are depicted in Fig. 3.26.

From the results depicted in Fig. 3.26 one can see that they confirm the estimations with the single line method, although the permittivity obtained with this method was slightly higher for both samples. It's also possible to observe that there is a decrease in the permittivity and the losses with the increase in frequency. This is common for most dielectric materials, as explained in section 3.1.4 about dispersion.

3.3.2 Dielectric properties of cork

Two types of cork material were tested for permittivity, a natural piece of cork and a compressed piece made of an agglomerate of cork pieces and wood, as shown in Fig.

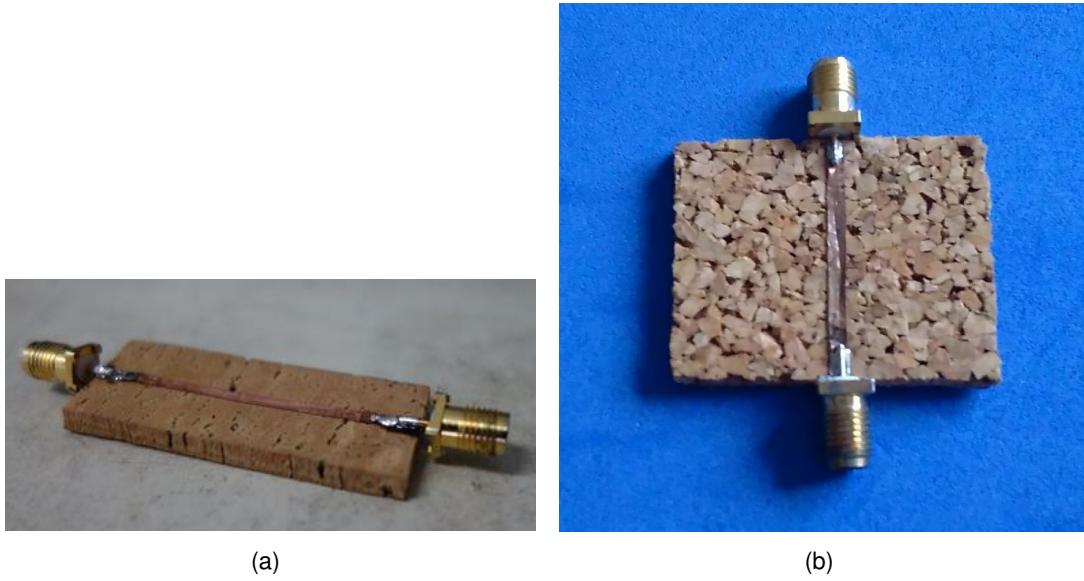


Figure 3.27: Microstrip lines used for permittivity measurement on (a) natural cork substrate and (b) compressed cork substrate.

Table 3.8: Measured and calculated relevant values for permittivity determination of the cork substrate materials

Material	Line	$\tanh(\alpha l)$	f'_0 (GHz)	Z_0 (Ω)	ϵ_r	$\tan \delta$
natural cork	small	0.0106	1.363	149.33	1.32	0.084
	large	0.0132	1.045	152.05	1.31	0.058
compressed cork	small	0.0041	1.399	165.01	1.39	0.0273
	large	0.0064	1.072	164.99	1.40	0.0256

3.27. The two natural cork substrate microstrip lines were cut with approximately 2.3 mm of width, with lengths of 48.5 and 72.5 mm, in a substrate with 3.85 mm of thickness. The two compressed cork microstrip lines were also cut with approximately 2 mm of width, with lengths of 41.0 and 61.0 mm, in a substrate with 4.85 mm of thickness.

Using the single microstrip line measurement, the medium value of permittivity obtained for natural cork was of 1.32, while for the compressed cork was of 1.40. The results of the measurements used for the calculation are summarized in Table 3.8. The medium value of the dissipation factor of the natural cork was 0.084 and for the compressed cork of 0.0273. This means that cork is a very lossy material, and can be essentially useful as a radiation absorber.

The cork has many air gaps inside, and as expected the permittivity values of the cork are rather low. The loss values, however, are considerably high. Although cork has remnants of water content inside, which make it a rather lossy material, the high loss values obtained from the single microstrip line method can, and probably have, another source of error, that

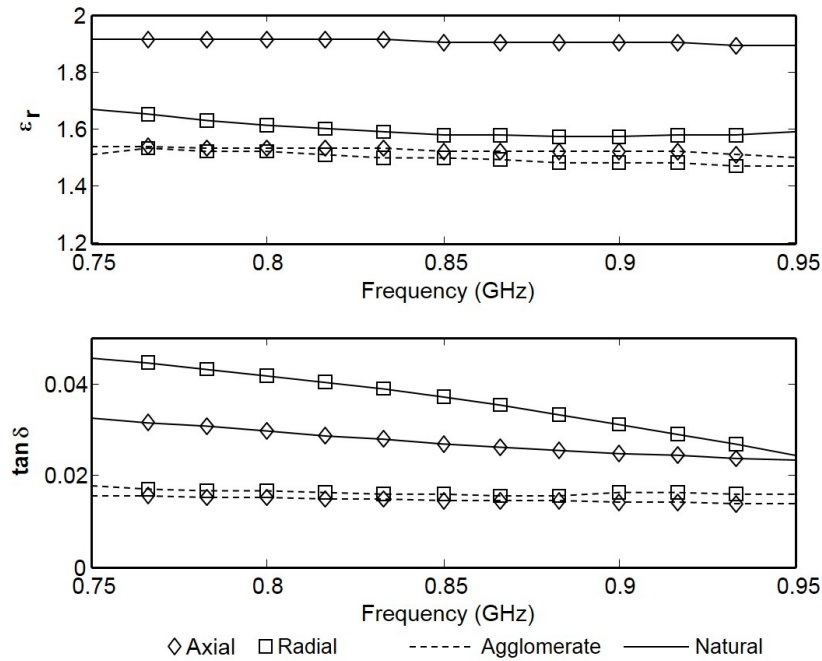


Figure 3.28: Measured dielectric constant and loss tangent of axial and radial samples of natural and agglomerate cork in the range from 750 to 950 MHz.

is due to the imperfect open-circuit load. The single microstrip method requires the line to be terminated by a perfect open-circuit ($Z_L = \infty$), in order to emulate that load, the open-circuit load from the calibration kit of the VNA was used, which approximates an open-circuit rather well. However, the microstrip line to coaxial interface creates a discontinuity which will alter the impedance of the load, making it quite finite. And the lower the impedance of the load, the higher the estimated losses for the substrate are and the lower the permittivity, due to changes in the determined characteristic impedance of the line.

As in the case for the paper substrate, the two-length line method was used to confirm the previously calculated results and also to depict the permittivity of cork with frequency. However, in this case, another pair of lines was fabricated in which the line conductor is placed orthogonal to the first case. This was done in order to evaluate the anisotropic behavior of the cork. The obtained permittivity and loss tangent for the cork slabs is depicted in Fig. 3.28.

The values obtained with the two-line length method are approximate to the values determined with the single microstrip line measurement for the agglomerate cork, with a slight difference in permittivity, with values of approximately 1.5 which are close to the 1.4 of permittivity determined with the single line method, and a slight difference for losses in the range of 0.018 to 0.019 when compared to the 0.026 obtained with the single line method. The natural cork however, presents a considerable difference.

The natural cork slab sample does not present a completely flat surface, having several slight bumps that lead to an erroneous thickness measurement. Besides, it has a considerable surface roughness, that although unmeasured, is observable to the naked eye. This bumps and roughness in the surface are responsible for creating air gaps in the interface between the conductor line and the substrate, therefore lowering the overall permittivity value that is measured. Moreover, due to the uneven, nearly random, distribution of air holes in the material, natural cork is a rather inhomogeneous and anisotropic material. The results in Fig. 3.28 show that natural cork is rather inhomogeneous and anisotropic, since in one direction the substrate presents a value for permittivity that is considerably different from the value obtained in another direction.

The anisotropic characteristic is also possibly present in the agglomerate cork, since one of the surfaces of the cork is more rigid and compact than the other. Nevertheless, the agglomerate cork slabs are more flat and present a smoother surface than the natural cork samples. In the agglomerate cork, however, the anisotropy is in the same component of the electric field, therefore, it's equal for both microstrip lines. For that reason, the permittivity results for the agglomerate cork are essentially the same for both directions (see Fig. 3.28). Which proves that the agglomerate cork is isotropic in the horizontal plane and nearly homogeneous.

3.3.3 Dielectric properties of fabrics

Fabrics have been widely studied by several research groups and there's references for the characteristics of different types of fabrics already published. The characterization of some fabrics with the microstrip line methods was tried, however, without much success. Nevertheless, many fabrics have already been studied, and the data for their properties is readily available. A summary of some fabrics properties is made in Table 3.9.

There are more references of fabrics characterization available, but in some cases they present simply other methods to characterize the same materials or use methods for very low frequencies, below 1 MHz, or very high frequencies, above 100 GHz, that are not interesting for the applications envisioned in this thesis. For that reason the list in Table 3.9 is not a complete thorough list of all the textiles that have been characterized before, but a summary of a few fabrics and leathers characterized around frequencies of interest and that could be potentially interesting for the development of wearable devices.

3.3.4 Dielectric properties of plastic

Many substrate materials are made of plastic compounds, as is the case of FR-4 and laminates from known RF substrate providers such as the 3000 series from Rogers Corp.[®], which is based on PTFE. The electrical properties of polymers are actually important for

Table 3.9: Brief summary of the properties of some textile materials and leathers.

Reference	Frequency	Material	Thickness (mm)	ϵ_r	$\tan \delta$
[143]	9.8 GHz	100% Nylon 6.6 fabric	-	2.823	0.0268
			-	2.7522	0.0242
			-	2.7801	0.0283
[144]	1.5 GHz	Cordura [®] fabric	0.5	1.1-1.7	-
[145]	2.4 GHz	Fleece fabric	3.0	1.04	-
[27]	2.45 and 4.5 GHz	Cowhide leather	0.7	1.76	0.0009
		Sheepskin leather	0.7	2.50	0.0035
		Oiled sheepskin leather	0.7	2.66	0.085
		Scratched cowhide leather	0.7	3.13	0.15
		Oiled cowhide leather	0.7	2.30	0.04
[146]	2.45 GHz	100% washed CO (Cotton)	3.0	1.51	-
		100% CO Denim [®]	2.84	1.67	-
		65% PES (Polyester), 35% CO fabric	3.0	1.56	-
		100% CO fabric	3.0	1.47	-
		100% PES	2.85	1.44	-
[147]	UWB (3.1 -10.6 GHz)	100% PAN (Polyacrylonitrile) fabric	0.5	2.6	-
[148]	8-11 GHz	E-Glass G7628	0.210	4.80 - 5.00	0.003-0.11
		E-Glass G880	0.152	3.84-4.00	
		Kevlar K141	0.254	3.97-4.05	
		Kevlar K151	0.254	3.88-4.04	
[149]	1 - 6 GHz	Felt fabric	4.0	1.215	0.016
		Denim woven	-	1.6	0.05

materials used in electrical insulation, therefore, many providers provide this characteristics for the products they're selling, as the case for Goodfellow[®], which provides an extensive catalog of polymer materials [150] for many different applications, including flat slabs that can be used for substrates, as used in the previous section to prove the validity of the single microstrip line characterization method.

There's one plastic, however, which has been explored during the development of this thesis, that is PLA (Polylactic Acid), which we characterized due to lack of information regarding its electrical properties. PLA is a biodegradable thermoplastic derived from renewable resources. Although its electrical properties were already studied by some groups of material science for different applications [151], these were only evaluated up to 1 MHz, and the

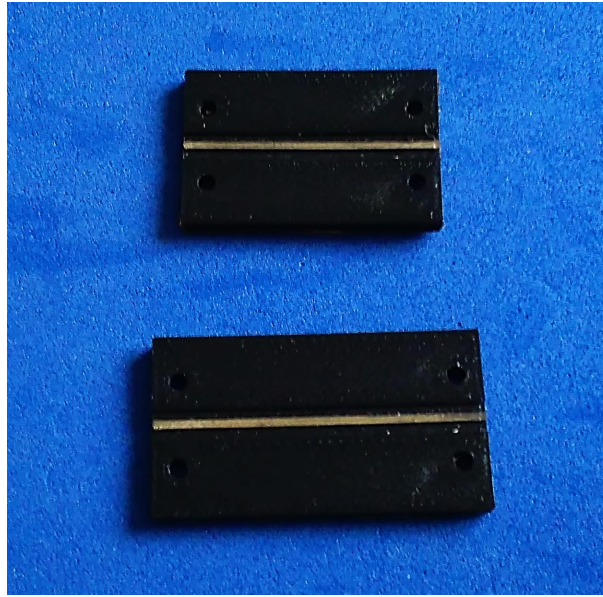


Figure 3.29: Photograph of the silver ink microstrip lines on PLA substrate prototypes.

dielectric properties in the microwave region were fairly unknown until a pair of years ago, when 3D printing started to be used for the development of antennas and microwave circuits [152].

Given the interest in designing antennas for microwave frequencies in the X and K -band region the two-line method was used for characterization of the PLA up to the 18 GHz. In order to do this, two microstrip lines were fabricated using conductive silver ink as shown in Fig. 3.29. The substrate was 3D printed with the BeeTheFirst 3D printer from BeeVeryCreative, with a thickness of approximately 2 mm, and the width of the line of approximately 1 mm. The use of conductive silver ink allowed for a better precision in the width and uniformity of the conductive strip. Besides, it avoids the problem of air gaps in the interface between conductor and substrate that arise when copper tape was used.

The results for the permittivity and loss tangent obtained for the PLA are depicted in Fig. 3.30. As can be seen in the obtained results, the permittivity demonstrate a strange behavior with frequency. There's a considerable variation of the permittivity along the frequency and it is not constant, by decreasing at the lower frequencies and then increasing again. The variation in the losses is also very high, however, it is clear that there are two peaks for the losses, one when the permittivity starts to increase around 6 GHz, and another when it starts to decrease again, around 15 GHz.

Recalling the polarization properties of dielectrics, and since in this method we're observing a wide frequency interval, this variation of the permittivity and losses can be associated to the frequency interval where the atomic polarization start to cease and the electronic polarization moments become the main contributors for the permittivity value of the dielectric.

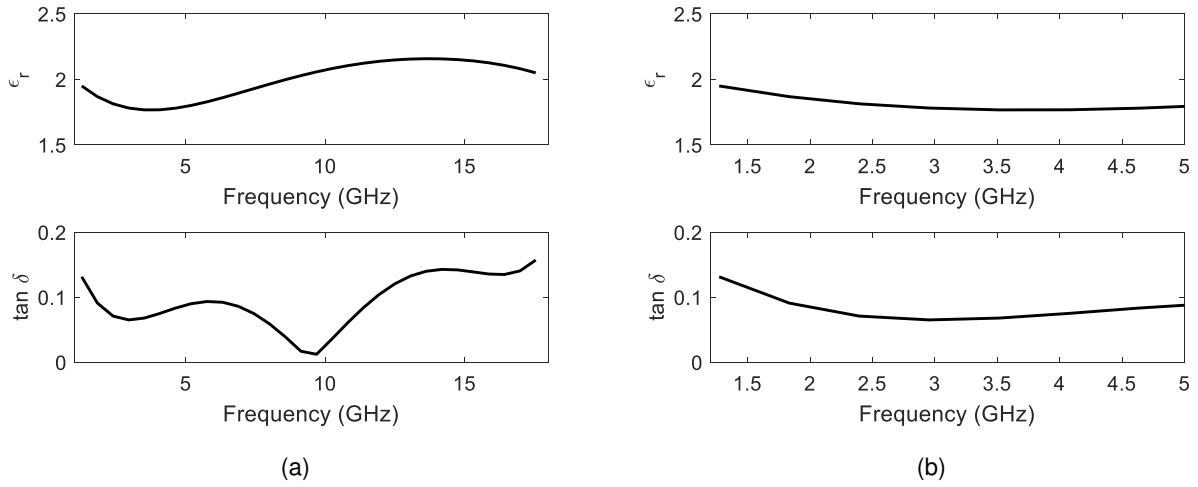


Figure 3.30: Measured dielectric constant and loss tangent of samples of PLA: (a) in the range from 1 to 18 GHz and (b) in the range from 1 to 5 GHz.

However, this is just a conjecture and a more broadband analysis of the material is needed in order to confirm this claim. Besides, considering the limitations that this method imposes on the lines dimensions, the range of frequencies tested are beyond the possible limits regarding the difference in lengths. Therefore, some of the information regarding permittivity and loss tangent beyond 5 GHz may be prone to errors of estimation. For that reason, it is shown in Fig. 3.30 (b) the permittivity and loss tangent estimated in the valid range of frequencies, where we can see a more reasonable variation of these parameters.

As in the paper and cork cases, we recurred to the single microstrip line method in order to determine the permittivity of the material, with which, a value of $\epsilon_r = 2.04$ was obtained. However, due to the size of the microstrip line, the frequency at which the permittivity of the substrate is being determined with the single microstrip line method is its resonant frequency, at 1.655 GHz, which is far from the X and K -band frequencies. Compared to the two-line method, the single line method estimated an higher value for permittivity but in close agreement between each other. Designing a single microstrip line for these bands would make it very small and other problems would arise for measurement of the sample, such as lack of space for conectorizing and large coupling between both ports.

Chapter 4

Antennas in non-conventional materials

By the end of chapter 3, the constitutive parameters of several non-conventional materials, which were studied during the course of this thesis, have been presented. With this knowledge, a few antennas have been designed and developed for different applications, with a larger focus on RFID.

The major interest in developing antennas in non-conventional materials, such as paper or textiles, is to be able to introduce some kind of tracking and data logging capability, which is a plus for logistics purposes, in common products and appliances, taking advantage of the light weight and conformability properties of these. Due to that, RFID has been the major target application in the development of antennas in non-conventional materials.

In this chapter we will describe a set of different antennas designed for several applications, where each section covers the designs on antennas with a specific type of material.

4.1 Antennas on paper

One of the first materials that was explored, for the development of antennas in non-conventional materials was paper. This bio-degradable material is very interesting due to its low-cost, its physical characteristics, such as the light weight and small thickness, and is also an eco-friendly material.

Different prototypes of tag antennas were developed, both in common 80 g printer paper and in cardboard material. Whilst the first one was targeted for bottle labeling, the second one was targeted for identification of cardboard boxes. In the later case, the design was rather simplified since no objects were considered to be in the vicinity of the tag. The former case was more complex, since besides the support substrate, the presence of the glass from the bottle and the liquids inside were also considered during design and simulation.

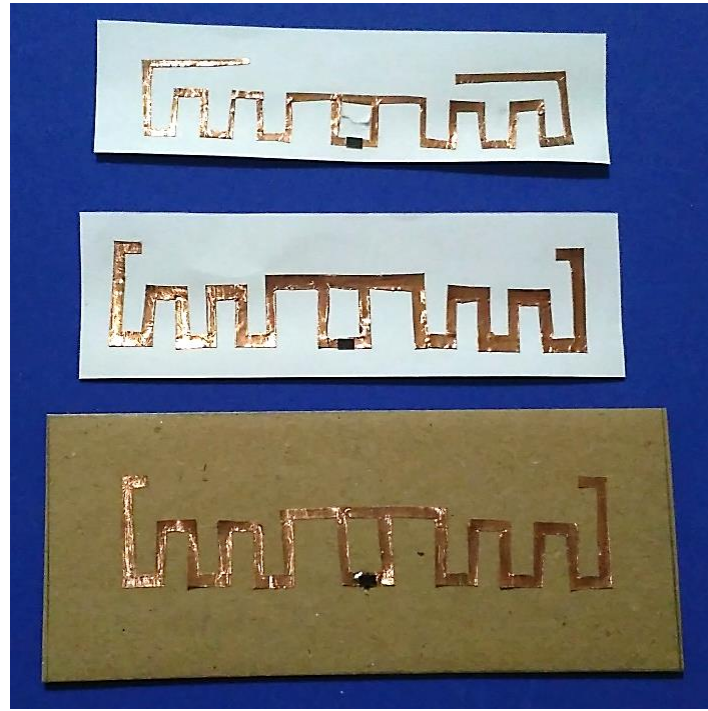
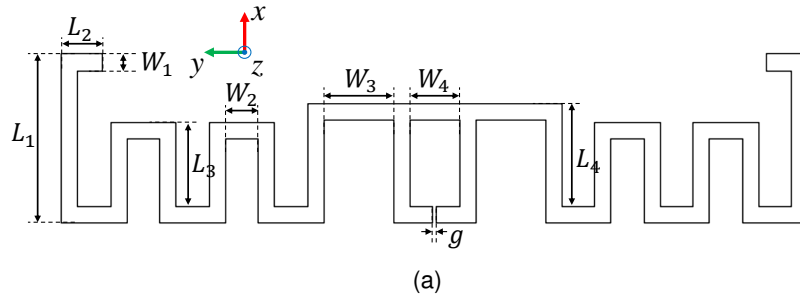


Figure 4.1: RFID tag antenna design for paper substrate. (a) Schematic of the simulation model and (b) prototypes photograph.

4.1.1 Standalone tags on paper

The first approach was to design a simple tag antenna, developed with paper substrate, as shown in Fig. 4.1, with the dimensions explicated in Table 4.1. It comprises a meandered dipole with an inductive ring designed to match the Murata LXMS31ACNA-010 tag chip, that has an input impedance of $12-j112\Omega$ at 866 MHz. The dipole was manufactured manually by cutting a piece of copper tape into its form. This was the introductory step for RFID tag antenna design and optimization.

Due to the difficult manufacturing process of the prototype, which led to a performance below our expectations (see Fig. 4.2 for reference), the tag was adapted in order to make it

Table 4.1: Meandered dipole antenna dimensions

Prototype	Parameters	dimensions (mm)
Prototype 1 (Paper substrate)	L_1, L_2, L_3	15.0, 20.0, 9.0
	L_4, W_1, W_2	9.0, 1.0 , 4.5
	W_3, W_4, g	8.5, 6.5, 0.5
Prototype 2 (Cardboard substrate)	L_1, L_2, L_3	20.5, 5.0, 10.25
	L_4, W_1, W_2	12.5, 2.0 , 4.0
	W_3, W_4, g	8.5, 6.0, 0.5

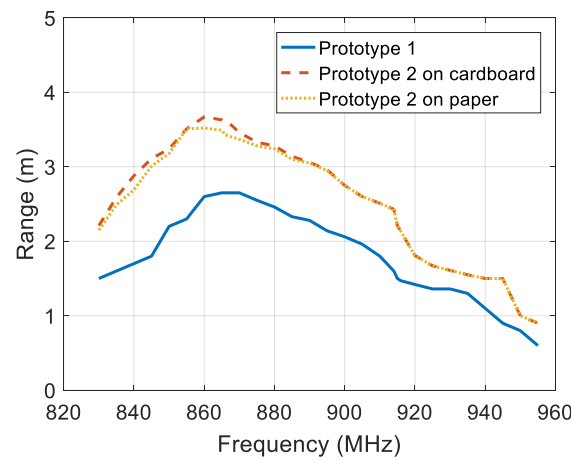


Figure 4.2: Reading range with frequency of the RFID tags on paper and cardboard substrates

easier to fabricate. The new version comprises the dimensions explicit in the second row of Table 4.1.

This second version was slightly adapted to maximize its efficiency for a cardboard substrate instead of the paper substrate. The cardboard has a lower permittivity than the paper substrate, however, it has a larger thickness, therefore, the differences from using one substrate or the other are very slight. In result, the tag can be applied in a sheet of paper or on a cardboard piece and obtain essentially the same results, as shown in Fig. 4.2. The performance of the tag antennas namely reading ranges with swept frequency and angle were performed according to the methodology described in Appendix A.

From the results depicted in Fig. 4.2, we can see that the first prototype of the RFID tag on paper substrate presents the worst performance. The cause for this can be mainly attributed to manufacturing problems, since hand-cutting the copper tape with such small margins is a very difficult task. This led to a non-optimal performance of the tag, since the impedance match is not perfect, and also, a small correction (approximately 1 mm) to the length of the end arms was needed, to correct the resonating frequency of the dipole.

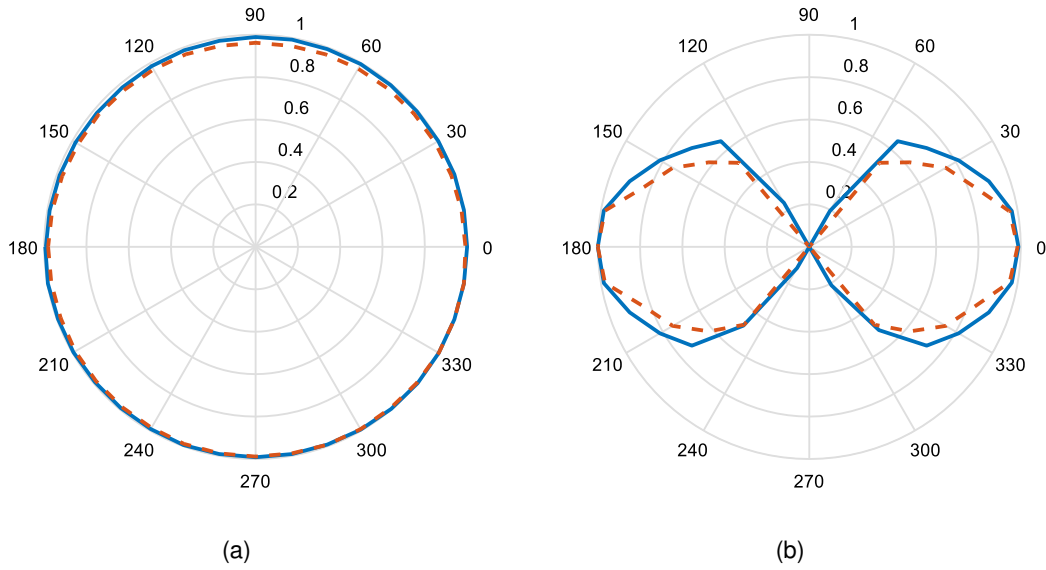


Figure 4.3: Normalized reading range with angle of the second prototype on cardboard (solid line) and the first prototype on paper substrate (dashed line) in the (a) XZ-plane and (b) YZ-plane.

Nevertheless, maximum reading ranges of 2.65 m and 1.50 m were obtained at 866 and 915 MHz respectively, which is a reasonable reading range for UHF RFID tags.

The second prototype, designed to reduce the manufacturing errors using larger margins, has evidently shown a better performance. With maximum reading ranges of 3.43 and 2.21 m at 866 and 915 MHz, respectively. Being that on a cardboard substrate we can see a very slight difference at 866 MHz, with a maximum reading range of 3.6 m. This is due to the fact that this antenna was designed having the cardboard substrate in mind, however, since, as stated, the differences in impedance matching are not significant between substrates, the reading range difference is only noticeable at the frequencies where the antenna presents the better matching.

The measured reading ranges with sweeping angle represent an approximation to the radiation patterns of the antennas. The normalized reading ranges for both orthogonal cut-planes of the antenna, are shown in Fig. 4.3.

The expected omnidirectional characteristics of the RFID tag antennas is clearly present in plots depicted in Fig. 4.3. There's very small differences between prototypes, except for the fact that the cardboard prototype provides a narrower pattern, which is indicative of a higher directivity, that is also another factor for the higher reading ranges reported.

It is also worth noting that in both cases the tag is only detectable within 120° angle range, which is roughly over its HPBW (Half Power Beam Width). This happens since the tags are being tested at +3dB from the minimum activation power at a fixed distance, therefore, it is

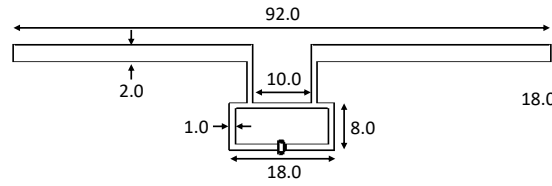


Figure 4.4: Simulation model of the monopole RFID tag antenna in paper substrate. All dimensions in millimeters.

expected to observe a pattern which responds within the HPBW range.

4.1.2 Antenna for bottle labeling

The antenna is based on a dipole with a matching inductive ring in order to match the RFIC input capacitance. The straight dipole approach was chosen given the good bandwidth characteristics of these kind of antenna, which promotes robustness to the environment changes. That is compared to the meandered topology, in which the turns in the arms reduce the inductance per unit length of the arm, due to capacitive coupling between them. Therefore, making the straight arm dipole less sensitive to differences in the dielectric environment around it.

This antenna was designed to have in consideration the presence of the bottle close to it. For that purpose it was designed with water inside ($\epsilon_r=78.3$ at 25°C [153]), and the glass of the bottle ($\epsilon_r=4.8$).

The antenna design is shown in Fig. 4.4. Where the dimensions presented are final, for the whole system considered.

The bottle considered for this design was of a spirits beverage, with a rectangular shape. The presence of the water right behind the antenna is very impactful in the radiation of the antenna. To overcome this problem, a reflector plane, made of a conductive tape, was placed in the back of the bottle with a dimension of 115x80 mm. The size of the reflector was obtained by optimization with EM simulation.

The radiation pattern with a summary of the efficiencies and directivities obtained from the antenna are shown in Fig. 4.5.

From the results shown, it is clear that the presence of the water has a very considerable effect in the radiation. However, the use of the reflector on the back of the bottle allows the system to perform reasonably. By providing a slight increase in the directivity and a very slight increase in the radiation efficiency.

The reading range obtained for the RFID tag antenna in paper substrate for bottle labelling is shown in Fig. 4.6.

Since the antenna was tuned to operate in the vicinity of the liquids, there was no expectations regarding the operation of the tag antenna when standalone, however, as seen

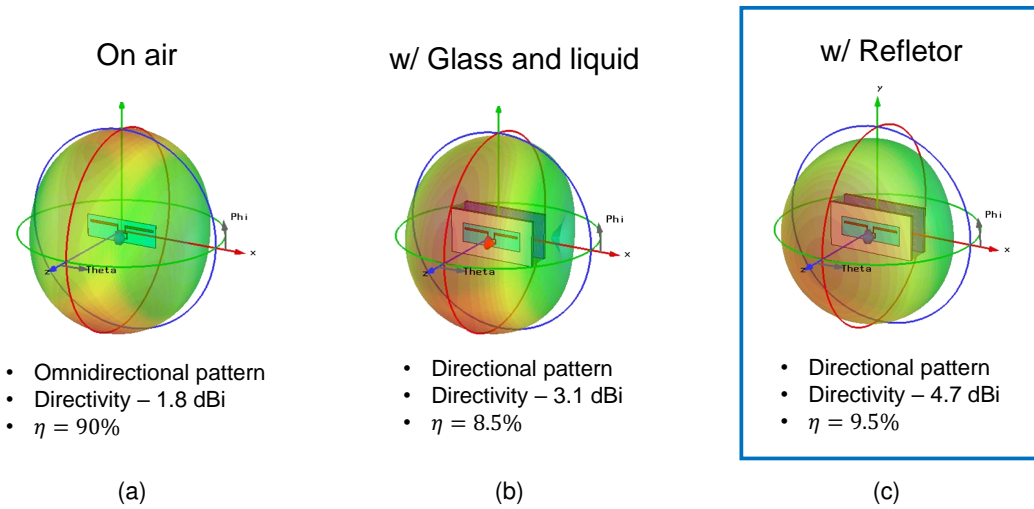


Figure 4.5: Simulated radiation pattern of the antenna in different scenarios with a summary of the directivities and efficiencies. (a) Standalone, (b) with the glass and liquid presence and (c) with the reflector in the back side of the bottle.

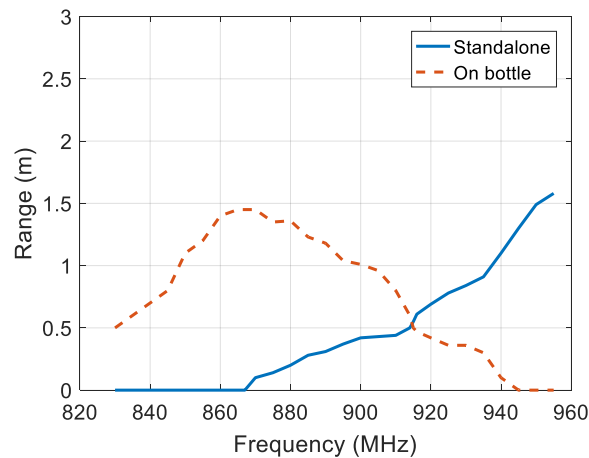


Figure 4.6: Reading range with frequency of the RFID tags on paper substrate in standalone form and on bottle

from the results in Fig. 4.6, it actually presents a very reasonable reading range although being shifted in frequency. Nevertheless, the antenna in the bottle presents a maximum reading range of 1.48 m, which is very good and above expectations considering the low radiation efficiency estimated during simulations.

4.2 Antennas on cork

Cork is a very interesting material, economically speaking it's one of the major export assets in Portugal, therefore, it is highly interesting to develop technology on a support that can possibly create a product with high impact on the economy. Not only that, cork has a particular set of characteristics that make it rather interesting for sensing applications and IoT applications. Cork is used for sound and thermal isolation in many different scenarios, from buildings to spacecrafts. Therefore, the addition of remote battery free sensors on such a support material can offer a wide range of applicability.

This section introduces the cork as a possible substrate for the implementation of antennas at UHF band and explores its use for the development of a passive humidity sensor. Two different types of UHF RFID tag antennas are presented. The first design is a compact design based on a meandered monopole antenna to be placed inside a bottle cork stopper, shown in Fig. 4.7. The second prototype is a miniaturized configuration of a dipole antenna, achieved by reducing the antenna to the matching ring and a lumped component, shown in Fig. 4.9. This is wrapped around the surface of a regular bottle cork stopper. The bottle cork stoppers were simulated having in consideration a glass bottle in empty and filled conditions. Water is very close to wine from an electromagnetic perspective, therefore, it was used in simulation, to provide a better approximation to the real operation environment.

4.2.1 Bottle cork stopper

In this subsection we used agglomerate pressed cork and designed an antenna for an RFID tag that could be inserted into a cork stopper for a wine bottle.

The proposed RFID tag antenna design for the wine bottle cork stopper is depicted in Fig. 4.7. This topology was chosen in order to reduce the size of the antenna when compared to a dipole, therefore, allowing it to fit inside a typical glass bottle neck.

As shown in Fig. 4.7, the antenna is connected to a conductive circular disk on the top of the cork stopper that operates as a large impedance matching stub. Similar to the previous cases, there is an inductive loop at the feed point, in order to match the antenna to the complex input impedance of the chip. In this case, a UCODE SL3ICS1002 from NXP, which has an input impedance of $16-j158 \Omega$ at 866 MHz.

The radiation pattern is essentially omnidirectional which was expected considering the antenna geometry. This can be observed in the simulation results depicted in Fig. 4.8 (a). However, this is true when the bottle is empty. The simulation model was adapted to consider a glass ($\epsilon_r=4.8$) bottle with a thickness of 6 mm, which is the typical thickness of the glass from common wine bottles. The presence of liquid inside the bottle has a considerable effect on the radiation pattern, which is shown in Fig. 4.8 (b). As stated before, for simulation purposes, water was considered inside the bottle, since from an electromagnetic simulation

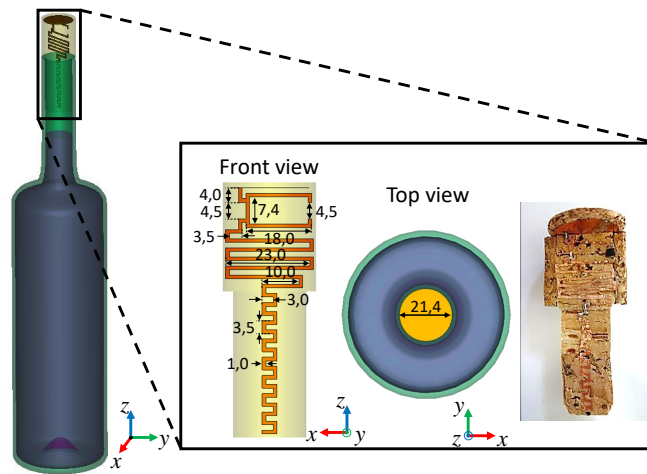


Figure 4.7: Simulation model and photograph of the monopole RFID tag antenna in agglomerate cork, with detail in front and top view. All dimensions in millimeters.

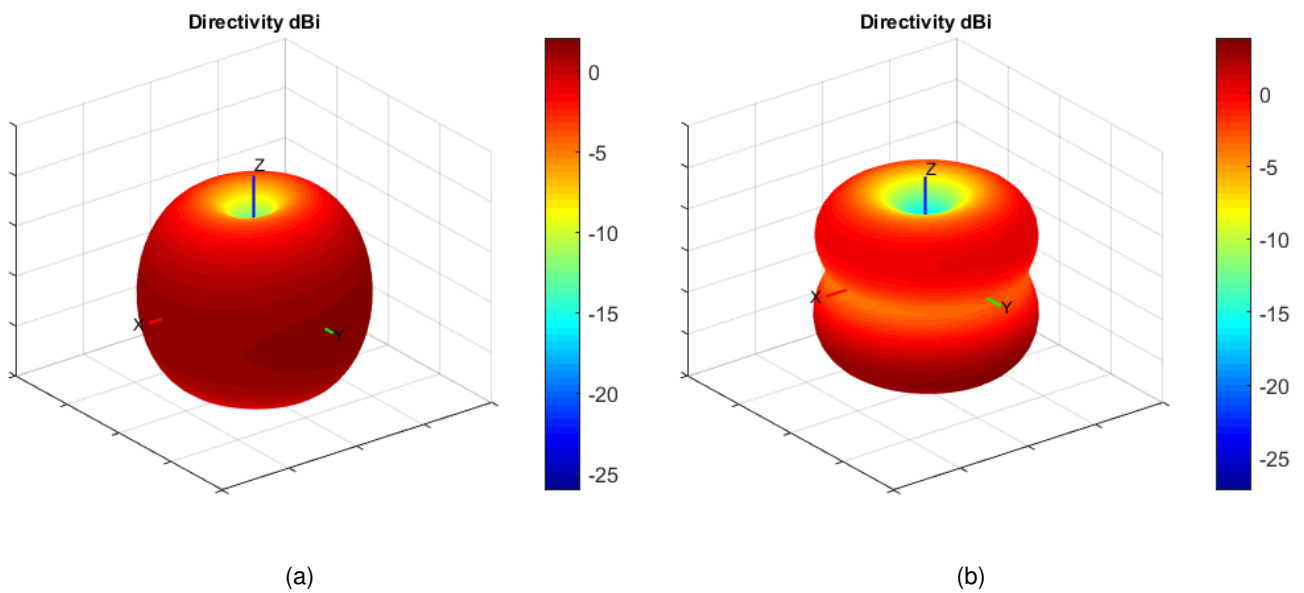


Figure 4.8: Simulated radiation patterns of the monopole RFID tag antenna considering (a) an empty bottle and (b) a filled bottle.

perspective it will render similar results to wine. Water has an estimated permittivity of 78.3 at 25 °C [153]. The edge of the water level is set at a distance of 15 mm from the stopper edge, which corresponds to the wine level inside a bottle in an upright position.

The liquids inside the bottle will contribute to an absorption and dispersion of the electromagnetic radiation, therefore, the radiation efficiency obtained is considerably affected, with a significant drop from 91% to less than 20%. Nevertheless, it is still possible to get an acceptable reading range from this tag even inserted into a filled bottle.

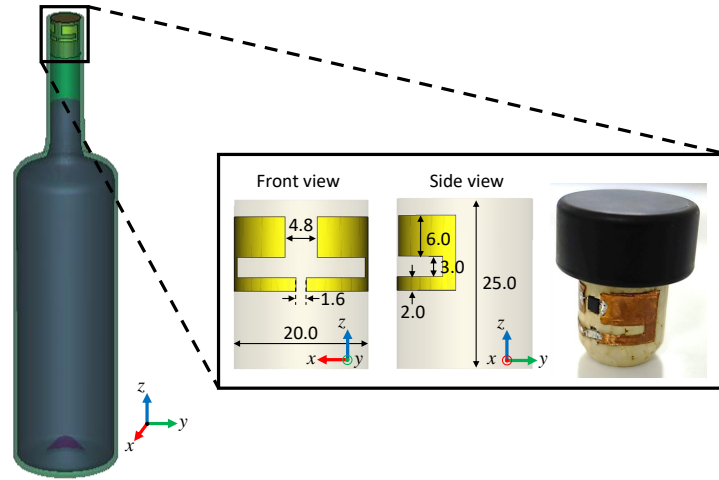


Figure 4.9: Simulation model and photograph of the conformal RFID tag antenna with detail in front and side view. All dimensions in millimeters.

This prototype has rather large dimensions that extrude the top of the bottle. Due to the visual impact it was decided to further reduce the size of the antenna in order to make it fit into regular bottle stoppers. The proposed prototype was designed in order to fit on the surface of a regular T-cork stopper, which is a stopper commonly found on liquors, that provides a secure grip while applying little deformation to the antenna. The proposed prototype is presented in Fig. 4.9.

In order to miniaturize the antenna, a SMD resistor of $6.2 \, \Omega$ is used in the impedance matching ring in order to reduce the size while maintaining a good matching of the antenna impedance. The thought process to create this design was starting with a regular RFID tag, and by knowing some general rules of how the variation of the parameters such as the width and length of the inductive ring affect the input impedance matching, such as described in [154]. Therefore, by cutting the dipole arms and modeling only the inductive ring, as shown in Fig. 4.10 (a), one can achieve an input impedance with an inductive characteristic that matches the imaginary part of the chip impedance. However, the lack of the dipole arms makes the impedance of the ring, nearly purely inductive. To introduce a certain degree of resistance, a SMD resistance was used, placed in between the top loop of the ring, the highest resistive point. Therefore, lowering the parallel resistance value and increasing the input resistance seen at the port, as shown in Fig. 4.10 (b) and (c).

This implementation dissipates power through the resistor, therefore reducing the overall efficiency of the antenna in nearly 90%. However, the impedance mismatch before the insertion of the resistor corresponds to a reflection of $\Gamma = 0.98$, which results in a total efficiency below 1%, that is effectively lower when compared to the efficiency with the resistive element, which is around 5%. Moreover, this is a relevant drop if we consider the antenna in the vacuum, however, with the presence of the liquids the overall efficiency of the antenna would

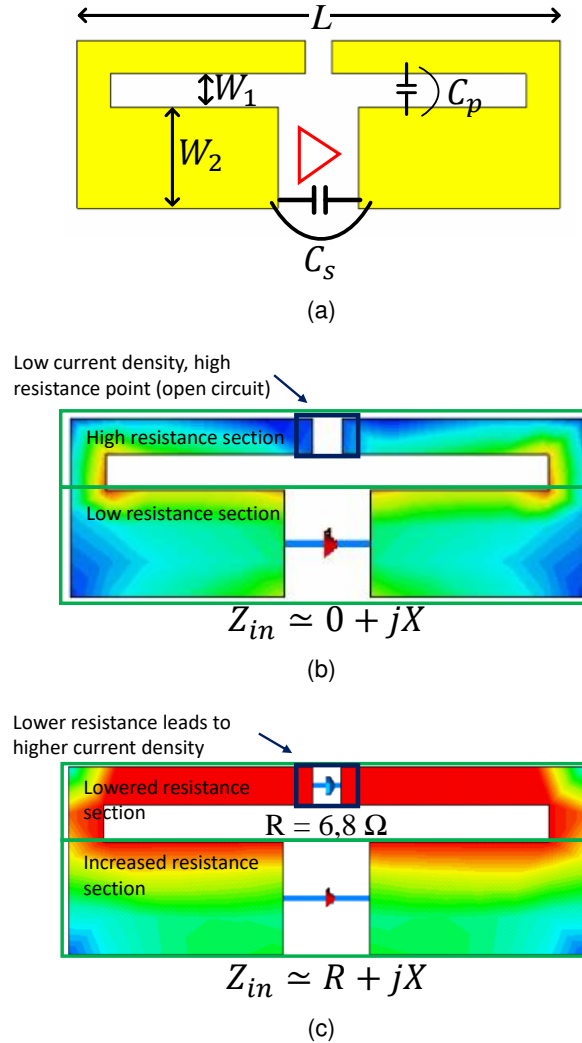


Figure 4.10: Detail of the bottle stopper RFID tag inductive ring design. (a) Constitutive parameters illustration, (b) current distribution in the open loop and (c) current distribution in the closed loop with SMD resistance.

be severely affected anyway, so the overall efficiency of the tag in the working environment renders the losses from the resistive element rather meaningless.

The antenna is simulated in two different scenarios, one in an empty and another with a water filled bottle, for comparison. As before, the presence of the liquid has a large influence in the radiation pattern and also in the total efficiency, which is rather expected since, as referenced before, water being a highly energetic material absorbs electromagnetic energy [155]. The changes of the radiation pattern of the antenna when considering the empty bottle versus the liquid filled bottle are depicted in Fig. 4.11.

Due to the radiation efficiency reduction in this prototype the reading range of the tag

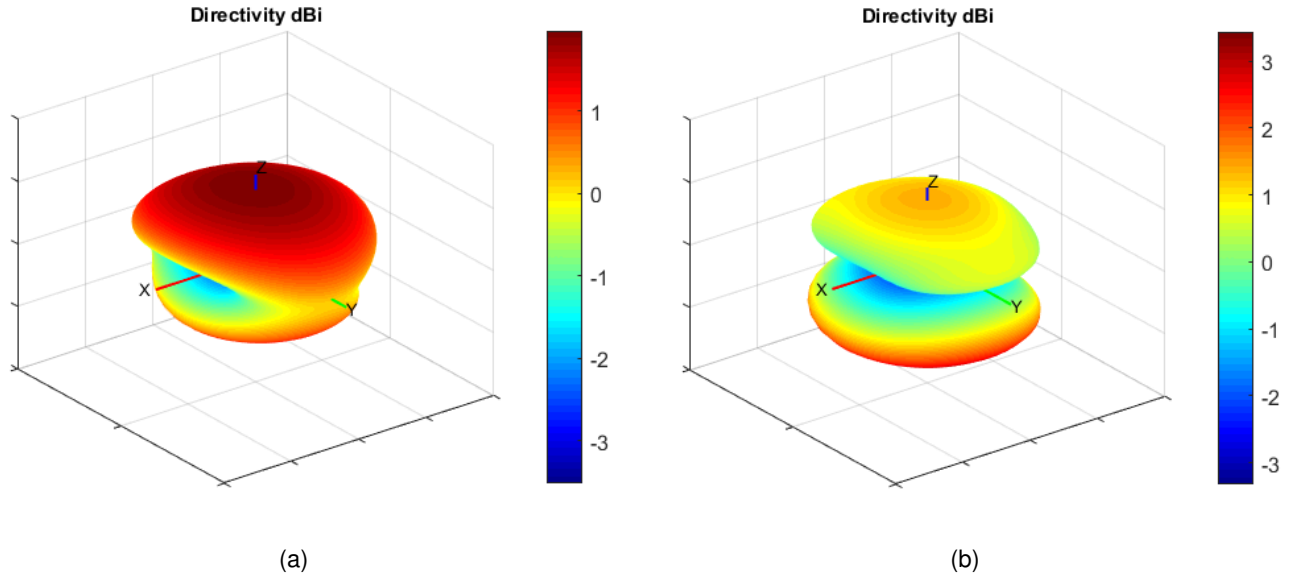


Figure 4.11: Simulated radiation pattern of the conformal RFID tag considering (a) an empty bottle and (b) a filled bottle.

is considerably reduced, but that is a reasonable price to pay for the ability to implement a RFID antenna inside a regular cork stopper.

As the antennas on paper substrate, these also have complex input impedance. Therefore, they could not be measured directly into a VNA or in an anechoic chamber. So, as in the previous cases for the paper tags, the way to provide an estimate as to the best matched frequency of the antenna as well as a rough estimation of the radiation pattern, the reading range was measured using the procedures as described in appendix A. The obtained reading range for swept frequency is shown in Fig. 4.12, while the reading ranges obtained for swept angles in the XZ and YZ planes is shown in Fig 4.13.

It is important to note that the work presented in this section is meant as a proof of concept. That is, this investigation goes into the development of possible RFID tag antennas that can work within the vicinity of liquids while inserted into glass bottles. When we consider the possibility of industrialization of these designs, some issues arise which can only be tackled with a careful design, having into consideration the cork manufacturing and the bottling processes. For instance, the bottle tag of Fig. 4.7 is not a common shape cork stopper, therefore, a new cork stopper model would need to be used and the bottling processes would need to adapt to this new shape, besides, the manufacturing process of the cork stopper would also need to be revised. In the case of the tag in Fig. 4.9, due to its application on the surface of the cork and its compact size, it can be used with common shaped stoppers. However, since it is located on the surface, it requires some cover material around the cork, which is not advisable. Besides, it requires the bottling to be done slowly and with little

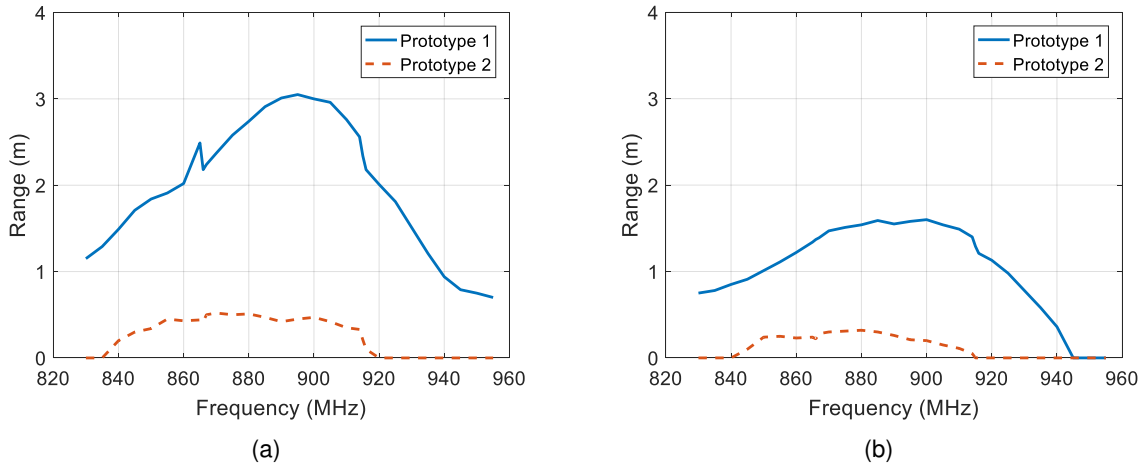


Figure 4.12: Reading range with frequency obtained for first prototype (solid line) and second prototype (dashed line), considering (a) an empty bottle and (b) a filled bottle.

pressure, contrary to what is the current bottling process.

In summary, these prototypes serve as a proof of concept into the design of RFID tags for bottle labeling, but some constraints need to be addressed to make them viable for industrialization process.

4.2.2 Humidity sensor based on cork

In order to develop a passive humidity sensor, cork was used as the sensing substance. Cork is a porous dielectric material, and as such absorbs water. This means that it is sensitive to humidity changes. In order to determine to which extent the cork permittivity changes with the difference in water content, permittivity measurements were performed on the dry and soaked cork slabs, using the two-line method, according to [134], with microstrip lines.

Looking back at the data in section 3.3.2, it is noticeable that the permittivity changes considerably, between 1.5 when dry to 3 when in wet condition. Which proves the water absorptive properties of the cork. Besides, one can also observe an increase in the losses, from around 0.015 when dry to 0.04 when wet.

In order to develop the passive sensor, a UHF RFID antenna was designed to be inserted in between two cork slabs. Given the low precision method of hand-cutting copper tape, in this development a different technique was experimented. This new prototype antenna was developed using an inkjet printing technique.

The conductive part is done with a silver based ink, that is prepared in house with a high density silver particle solution from ANP [156].

Being cork so porous, when inkjet printing directly on top of it the ink is absorbed and spread around. Therefore, in order to be able to create a precise printing of an antenna on it,

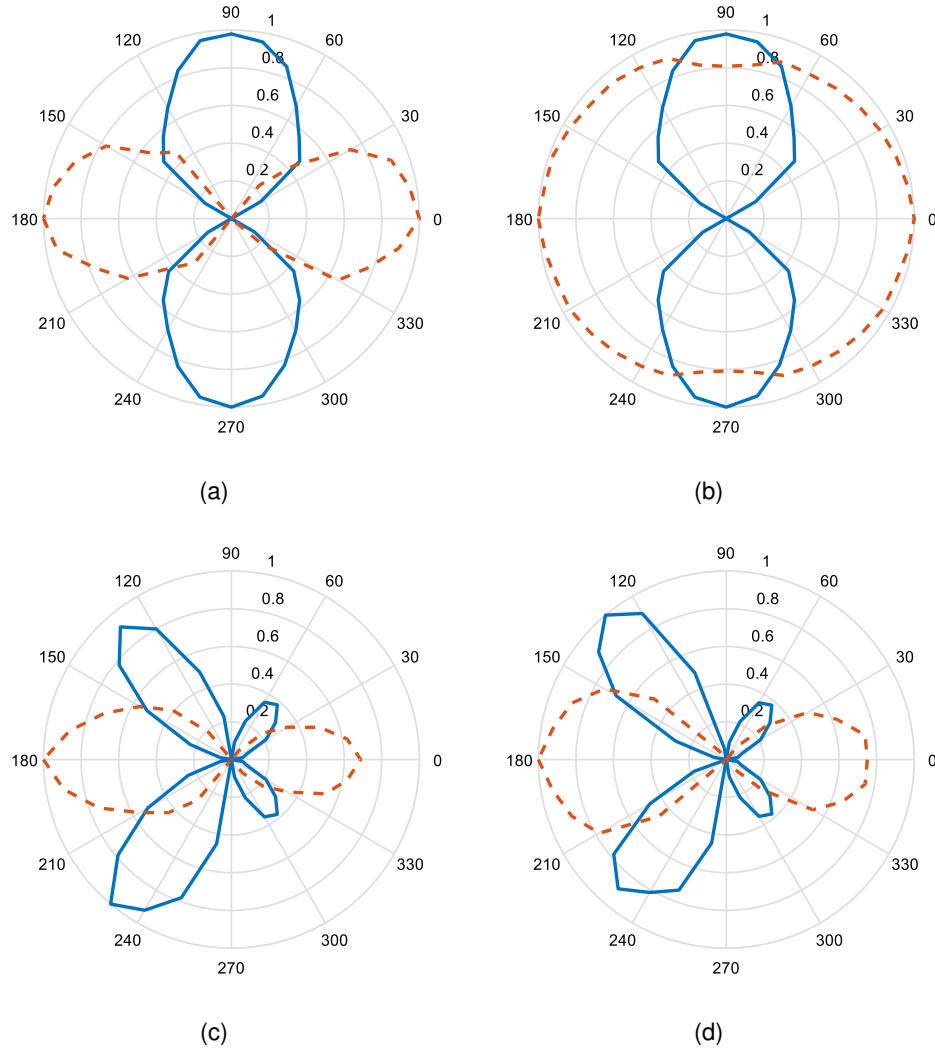


Figure 4.13: Normalized reading range with angle obtained for first prototype (solid line) and second prototype (dashed line) on an empty bottle: (a) XZ-plane and (b) YZ-plane; And on a filled bottle: (c) XZ-plane and (d) YZ-plane.

a dielectric coating surface has to be created to support the silver ink printing without spilling. Epoxy and SU-8 were used for this purpose. By placing a slim layer of epoxy on the surface of the cork we were able to create a smooth surface for printing. Then SU-8 was printed on top of the epoxy in order to create a surface with high surface tension to sustain the ink in place.

The simulation model comprised four different dielectric layers. An epoxy layer followed with a SU-8 layer, on top of which the metallic part of the antenna was placed, and two different layers of cork in each side. The fact that the water will spread from the outside to the inside of the cork slabs was taken into account, therefore, the two cork layers considered.

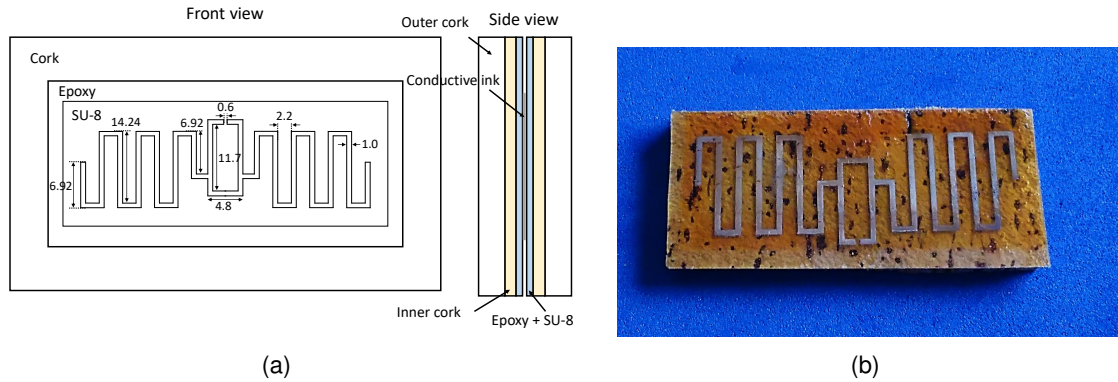


Figure 4.14: Passive humidity sensor based on RFID. (a) Schematic of the antenna with the dielectric layered structure and (b) photograph of the prototype. All dimensions in millimeters.

A slim one in the inside with a fixed permittivity equivalent to the dry cork, and an outside shell with a varying permittivity to simulate varying humidity levels. The proposed prototype is shown in Fig. 4.14.

The antenna was designed to match the input impedance of a Higgs 4 RFID chip from Alien at 915 Mhz, which corresponds to $18.4 + j181.2 \Omega$. The size and placement of the inductive ring is determined according to the guidelines from [157].

In order to access the behavior of the tag, the minimum threshold power to turn on the tag is measured at each frequency. For this specific tag antenna, instead of the range measurement method as described in the Appendix A, a specific measurement equipment from Voyantic was used. The access to this equipment was limited in duration, it was only available during the short period of time that this part of the project was being developed. For that reason all the other measurements were performed with the technique described in Appendix A except for this specific tag, in that Tagformance 7 by Voyantic has been used.

The advantage of using the Tagformance 7 is that it performs a calibration of the propagation environment prior to the measurements of the reading range. This is useful since the measurements are usually being performed indoor, therefore, the path loss is different from the one predicted with the Friis formula, as described in Appendix A. Although the approximation of the propagation environment with the Friis formula gives a reasonable approximation, a calibration process to the propagation environment will always provide a more realistic estimate of the real reading ranges of the RFID tags.

Using this equipment, the transmitted power that is needed to obtain a valid response from the tag was measured, which is related to the reading range of the tag. The transmitting powers needed to activate the tag for each frequency and for different wet conditions of the cork slabs is shown in Fig. 4.15. The frequency at which the tag presents the lowest turn on power corresponds to the frequency at which the antenna has the better match to the chip

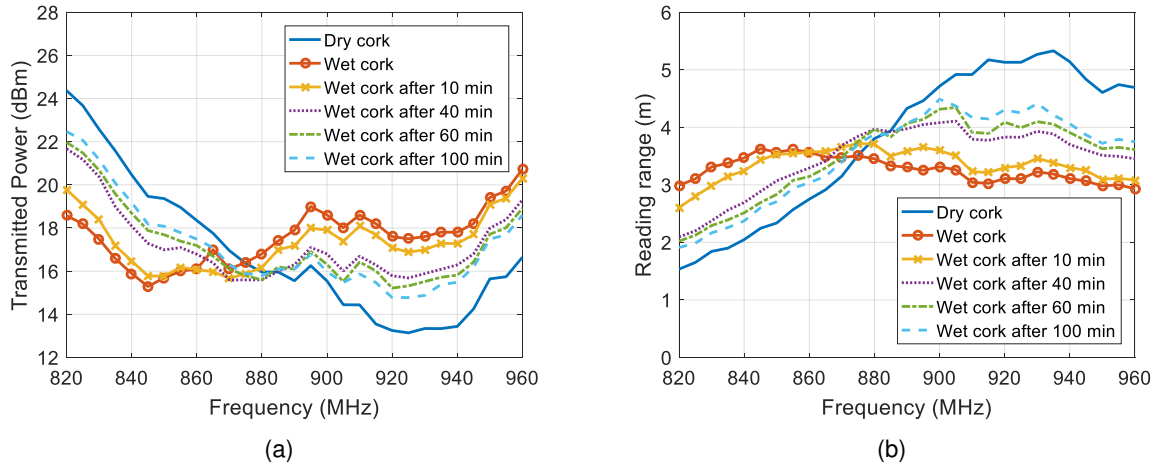


Figure 4.15: Measurement of the humidity sensor tag for different wetting conditions. (a) Minimum threshold power and (b) equivalent reading range of the tag.

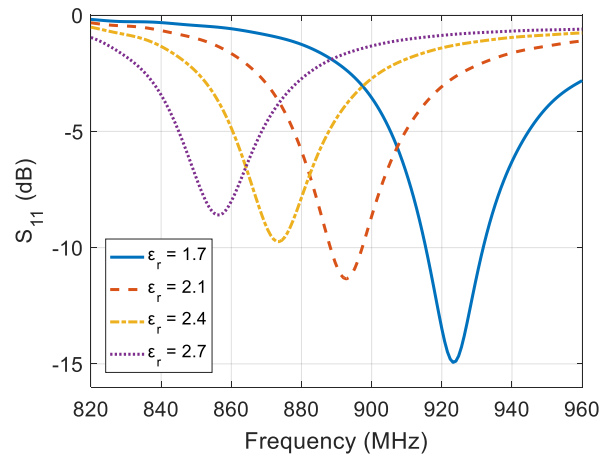


Figure 4.16: Simulated reflection coefficient of the sensor tag antenna for different permittivity values of the outside cork slabs.

input impedance.

By looking to the transmitted power measurements it is easy to identify a shift in the matched resonance of the antenna to the chip for different humidity values. Being that when dry the better match is at 920 MHz, as expected, since this was the design frequency, but right after spraying the cork slabs with water, that resonance is shifts downward to 845 MHz and requires more power to active, which is indicative of a mismatch in input impedance. This behavior agrees with simulations as shown in Fig. 4.16. Where the different permittivities try to emulate the different humidity levels.

Comparing the simulation and the measurements we can see a relationship between the

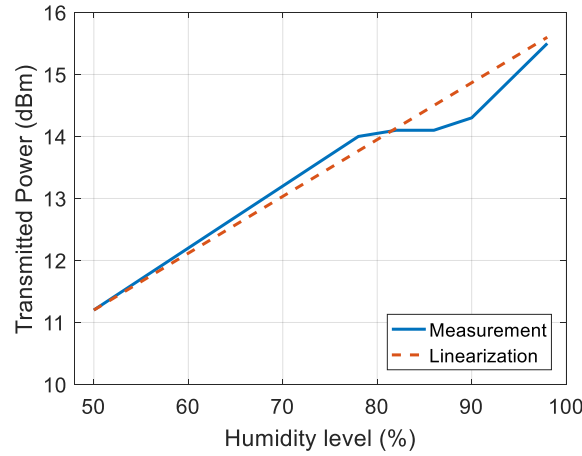


Figure 4.17: Threshold power variation with humidity, measured within the thermal chamber with humidity control and linearized response for comparison.

threshold power to turn on the tag and the reflection coefficient of the sensor tag antenna. For a permittivity of 1.7, which corresponds to the near dry cork, the resonant frequency is around 920 MHz where a good match (reflection coefficient at -15 dB) is obtained, which correlates to the lowest threshold power measured, happening for the dry cork at 920 MHz. While for a permittivity of 2.8, which is almost the value obtained for 100%, the resonance is around 850 MHz with a poor match (reflection coefficient at -8 dB), which correlates to the wet condition with the lowest threshold happening at 845 MHz with 3 dB difference to the dry condition.

Another measurement was performed inside a thermal chamber with humidity control. In this case, the threshold power was measured at a single frequency of 915 MHz and evaluated for different humidity levels. There's a threshold power difference of roughly 4.4 dB, between 50 to 96% relative humidity. The threshold power variation with humidity is shown in Fig. 4.17.

This behavior confirms the response obtained for the previous measurements by spraying and drying the cork. The absolute threshold power difference, between this measurement and the one shown in Fig. 4.16, is due to the propagation environment in which the measurements were made. The thermal chamber has metallic walls, therefore the propagation inside is unknown and random with multiple reflections happening. For that reason, the frequency sweep was not performed, and an accurate threshold power couldn't be obtained, since the propagation environment is very different from open space. Nevertheless, the change in threshold power in relation to humidity condition is considerable and can be considered viable independent of the environment.

4.3 Antennas on fabrics

Being one of the most investigated materials by the time this work was started, fabrics were a relatively known material, with a considerable number of research articles dedicated to the development of high frequency electronics with its support. Nevertheless, as stated before, due to the advent of the Internet of Things and the increasing interest in the 'wearables' development, the design and development of communication electronics embedded in fabrics and clothing is an highly interesting subject. Therefore, during the course of this thesis, the development of some antennas using fabrics as support has been investigated as well.

This section is mostly devoted to a dual-band textile antenna for GSM900 and DCS1800 frequency bands that has been presented in [30, 19], and to some microstrip patch antennas that have been use to study characteristics and performance of several textiles and their usefulness for the development of integrated antennas.

4.3.1 Fully textile microstrip patch antennas

One of the first steps investigated regarding textile antennas was the manufacturing technique. Most of the proposals analyzed in the state of the art used glue to attach the layers of materials of the textile antennas, while some examples used embroidery and conductive yarns over dielectric fabrics. Point being, there are other methods to develop a textile antenna, besides, when developing wearable antennas one has to consider the possibility that these will be subject to washing processes. Therefore, a set of prototypes of a microstrip patch antenna were developed employing different manufacturing techniques, and were measured in order to investigate which method presents the best compliance. After that, the prototypes that proved the best were washed in a regular washing machine in cold water program, to avoid shrinkage, and measured again to verify the impairments that the washing cycle could create and evaluate which method is the best for the development of wearable antennas. All the prototypes were developed with the same substrate, Cordura® ($\epsilon_r = 1.7$) and the same conductive fabric, used for both the patch and in the ground plane, Zelt® ($\sigma = 1.75 \times 10^6 \text{ S/m}$). The patch was dimensioned to resonate at 2.45 GHz and its schematic is shown in Fig. 4.18.

The different techniques and the corresponding prototype number are summarized in Table 4.2. The photograph of the corresponding prototypes can be found in Fig. 4.19.

A comparison between the simulation and the measured reflection coefficient for all the prototypes is shown in Fig. 4.20. Were antennas 2 and 4 are not shown, due to the fact that the considered manufacturing technique did not produce a viable antenna at all and, therefore, the results were immediately discarded.

When manufacturing this antennas, although a laser cutting machine was used, it is im-

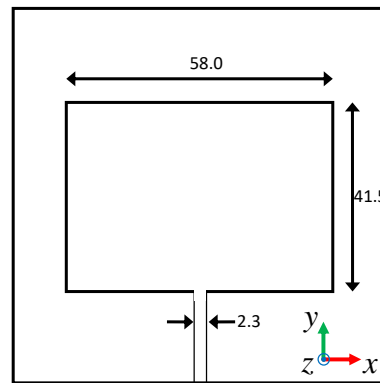


Figure 4.18: Textile microstrip patch antenna design. All dimensions in millimeters.

Table 4.2: List of prototypes developed and techniques used for the manufacturing of textile microstrip patch antennas.

Prototype	Manufacture technique	Description
Ant. 1	Interlining Fast2Fuse	0.1 mm thick thermal adhesive interlining applied with ironing
Ant. 2	Resin in between layers	Strong resin is applied between fabric layers
Ant. 3	Machine sewing	Machine sewed with non-conductive yarn in a 5 pts/cm spacing pattern
Ant. 4	Resin on the surface	Strong resin is applied covering the complete surfaces of both sides of the antenna
Ant. 5	Interlining Fixorete Losango	0.1 mm thick thermal adhesive interlining applied with ironing
Ant. 6	Interlining Fixorete Losango	Interlining applied only around the borders of the conductive surface
Ant. 7	Interlining Fixorete Continuo	0.1 mm thick thermal adhesive interlining applied with ironing
Ant. 8	Interlining Fixorete Continuo	Interlining applied only around the borders of the conductive surface
Ant. 9	Isolating glue in the edges	Isolating glue is applied around the edges of the conductive layers
Ant. 10	Isolating glue in all the surface	Isolating glue is applied in all the surface of the conductive layers
Ant. 11	Isolating glue in small isles	Isolating glue is applied in all the surface of the conductive layers in small isles with 1 cm separation
Ant. 12	Super glue around the edges	Super glue is applied around the edges of the conductive layers
Ant. 13	Super glue in all the surface	Super glue is applied in all the surface of the conductive layers
Ant. 14	Super glue in small isles	Super glue is applied in all the surface of the conductive layers in small isles with 1 cm separation
Ant. 15	Fabric glue around the edges	Fabric glue is applied around the edges of the conductive layers
Ant. 16	Fabric glue in all the surface	Fabric glue is applied in all the surface of the conductive layers

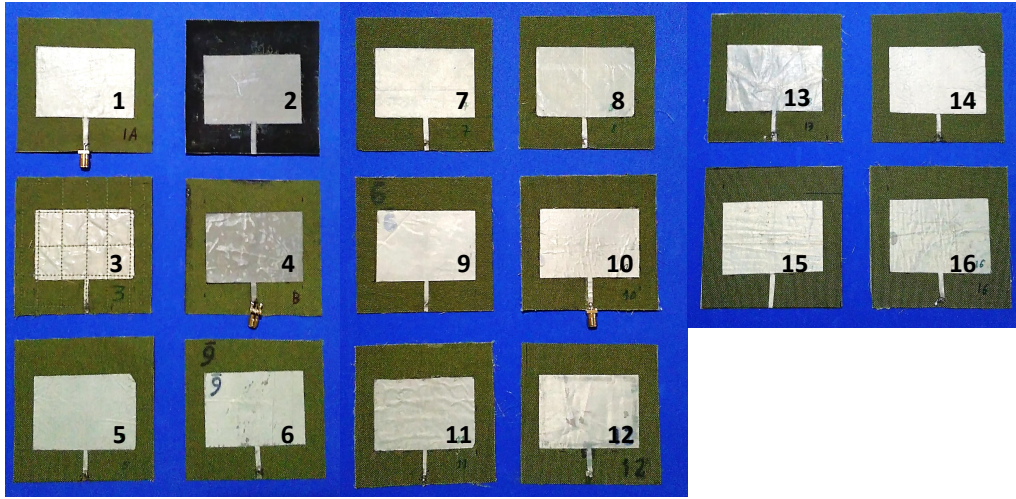


Figure 4.19: Photograph of the textile microstrip patch antenna prototypes.

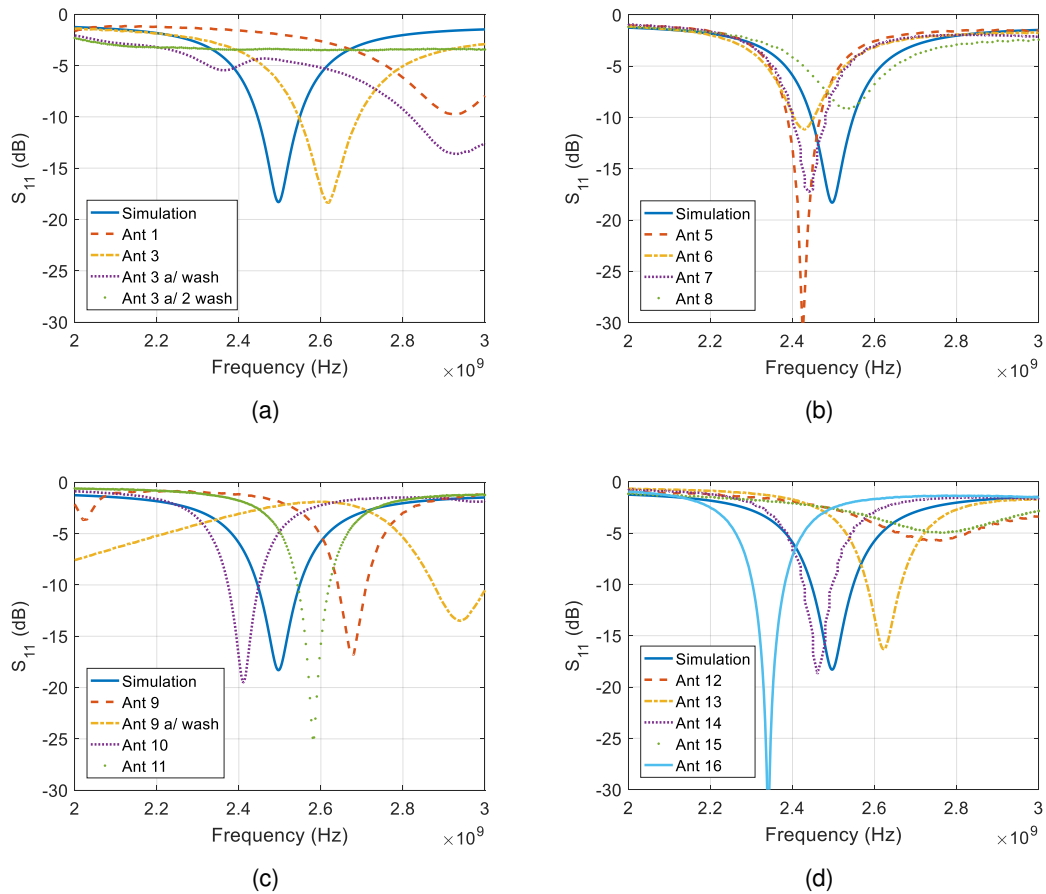


Figure 4.20: Comparison between simulation and measurements for the reflection coefficient of the different manufacturing techniques of textile antennas.

portant to keep in mind that there are tolerances in the dimensions of the patch. Since the substrate is very thin, a small error in the patch length can result in a considerable shift in the resonant frequency of the antenna, or a slight difference in the width can impose a considerable change in the antenna impedance. Nevertheless, from the results of the reflection coefficient, the prototypes that provided the best results were Antenna 3, 5, 7, 10, 11, 13 and 14. Where prototype 14 has nearly matched the simulation results, whilst prototypes 3, 11 and 13 presented a slight shift upwards and prototypes 5, 7 and 10 presented a slight shift downwards in frequency.

From this results we can say that, thick interlining as the case of antenna 1 should be avoided or accounted for in simulation in order to reach satisfactory results. Resins cannot be used at all, since when dried they become rigid and can easily break or shatter. Interlining, super glue and isolating glue are good solutions, but have to be applied in all the surface of the patch and ground plane, to completely unify the layers. Applying small isles of glue all around the surfaces creates the same bonding effect and therefore is also advisable. Applying glue or interlining only around the edges creates air gaps between layers that change the permittivity of the medium, and lead to shifts and bad impedance matching, as seen in the results for prototypes 6, 8, 9 and 12. Fabric glue proved to be the worst glue from all the tested samples.

Given this results, this prototypes were put to wash inside a regular washing machine, along with other clothes and detergent, in what can be considered normal washing conditions. The only prototypes that came out of the washing process, in good apparent good condition, were prototype 3 and 9. However, due to the already bad performance of prototype 9 before washing, it was rendered a bad solution for implementation of textile antennas.

Contrary to initial expectations, the sewed prototype antenna has presented a relatively satisfactory result. This was unexpected since the sewing process creates an uneven surface on the patch forming possible air holes between the patch and the substrate that would considerably change its impedance. Besides, the sewing could possibly create shorting points by carrying conductive fibers from the patch to the conductive textile on the ground plane, and *vice-versa*. Nevertheless, this technique presents the most sturdiness from all the techniques tested, which proved able to survive the washing process more than one time, unlike all the other prototypes. However, after washing, although the antenna came out in seemingly good conditions, after measuring it was realized that there was a considerable degradation in performance. Still, the prototype was washed a second time, and although some visible tearing on the edges of the patch was already visible, the antenna remained apparently intact. After measuring, an even further degradation of the obtained reflection coefficient is observed.

It should be noted however, that glued prototypes came out of the washing process completely torn apart. All the layers of textiles were split from each other. However, the interlin-

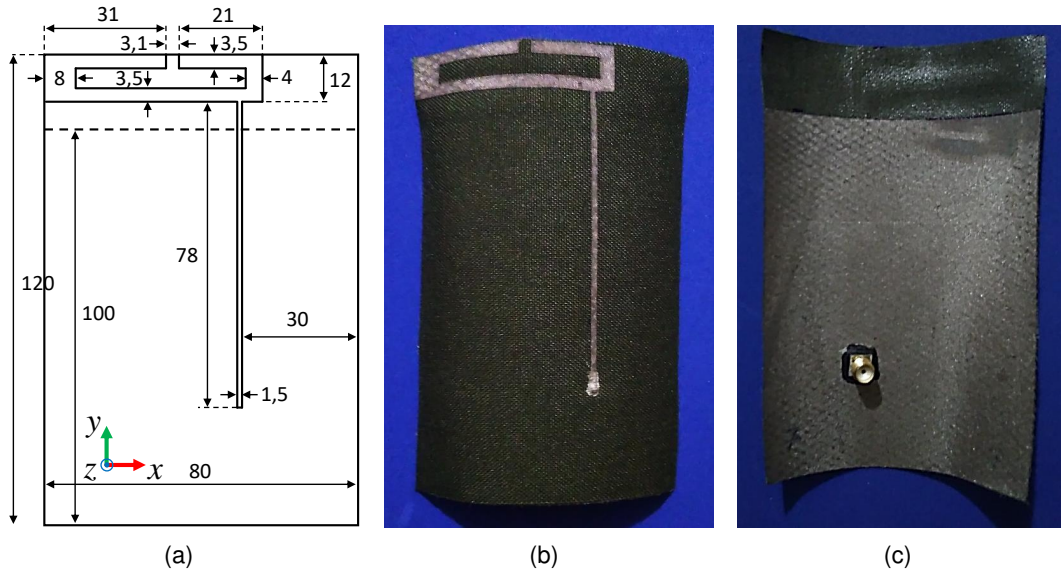


Figure 4.21: Textile antenna design and prototype. (a) Schematic of the textile dual-band antenna; (b) Photograph of the front-view of the prototype, and (c) Back-view of the prototype. All dimensions in millimeters.

ing prototypes were almost able to withstand the washing process, coming out still together, apart from the edges of the patch and the ground plane, that became detached.

In summary, none of the previously mentioned methods is a solution for the implementation of all textile antennas. Therefore, impermeabilization of the antennas, or a different structure using superstrates in order to keep the conductive parts hidden from the surfaces, has to be considered. Considering the results obtained so far, the impermeabilization of textile antennas with interlining of thermal adhesive layers, or the use of superstrates, bonded with thermal adhesive layers seems to be the solution for the manufacturing of all textile antennas.

4.3.2 Cloth integrated dual band monopole antenna

The antenna that has been presented in [30, 19] is based on a dual folded monopole structure, in which the shorter arm will resonate at the highest frequency band, and the longer arm will be resonant at the lowest frequency band. The feed point is chosen so that the impedance at that point is real, therefore, a single feed line is sufficient to get to a 50Ω input impedance. The design of the dual monopole antenna is shown in Fig. 4.21.

This antenna presents an omnidirectional radiation characteristic, which is shown in the simulated radiation patterns in Fig. 4.22, where one can see that, although, at 900 MHz the radiation pattern is seamless and mainly resultant from the monopole arm, with barely any influence from the presence of the nearby ground plane, the same is not true at the highest

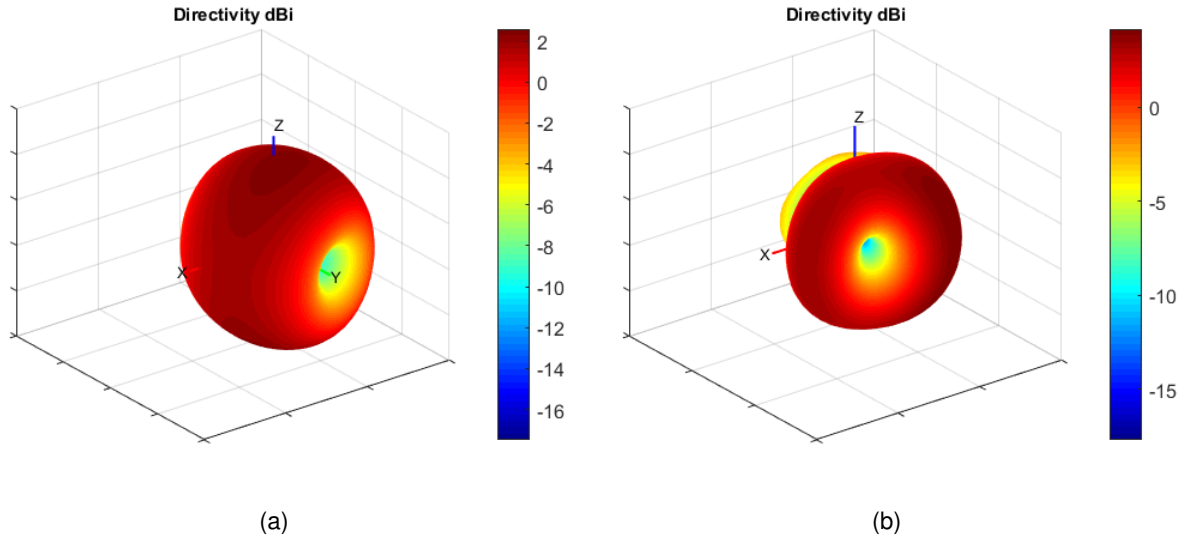


Figure 4.22: Simulated radiation patterns of the dual band monopole antenna at (a) 900 MHz and (b) 1800 MHz.

frequency. Being that at 1800 MHz a clear deformation to the radiation pattern is observable, nonetheless, it still presents an omnidirectional characteristic.

With this design, seven prototypes were built using different manufacturing techniques, namely, two prototypes with thermal adhesive lamination and five prototypes with embroidering. After a final reasoning, this antenna was integrated into a jacket, fully embedding it into its constituting materials.

It is not suffice to say that the correct knowledge of the properties of the materials used for the design and simulation of antennas is of paramount importance. When textile antennas are considered, other matters surface and become relevant, such as the surface roughness of the material, the surface tension they can comply and the moisture regain factors, which have been discussed in [22]. In this work, all materials used to manufacture the wearable antennas are commercially available and described in Table 4.3. For the dielectric substrate a synthetic fabric with low regain was chosen, in order to minimize the effect of the moisture absorption on lowering the resonance frequency of the antenna.

Beyond choosing the textile materials, the construction technique of the antenna is also crucial because the textile materials are highly deformable. The geometrical dimensions of the conductive patch and of the dielectric substrate should remain stable when connecting them, as the mechanical stabilization of both materials is essential to preserve the desired characteristics of the antenna. The geometrical precision of the conductive patch is also critical as the proposed antenna has thin details, as shown in Fig. 4.21. Moreover, the technique to connect the various layers should not affect the electrical properties of the conductive layers.

Table 4.3: Characteristics of the textile materials used to develop wearable antennas.

Dielectric Materials	Fabric	Mass per Unit Surface (g/m²)	Thickness (mm)	ϵ_r	$\tan \delta$
	Cordura Light	280	0.5	1.9	0.0098
Conductive Materials	Fabric	Mass per Unit Surface (g/m²)	Thickness (mm)	Conductivity (MS/m)	
	Zelt	55.87	0.06	1.75	
	Yarn	Linear Mass (dtex)¹	-	Conductivity (MS/m)	
	Silverpam	250	-	0.005	
Other Materials	Fabric	Mass per Unit Surface (g/m²)	Thickness (mm)		
	Atlantic	120	0.3		
	Adhesive Sheet Type	Mass per Unit Surface (g/m²)	Thickness (mm)		
	Fixorete Losango	0.28	0.01		

One of the techniques that allows an easy assembly of the antenna layers and good stability and resistance to tear of the structure is by using thermal adhesive sheets in between layers. Thermal adhesive sheets are very thin layers of bonding material that is activated with heat. They're applied in between the layers to be bonded and ironed with the fabric materials together. However, careful should be taken during the ironing process in order to avoid the use of steam, which will cause an oxidation of the conductive layer, therefore increasing its electrical resistivity.

Three prototypes of the antenna were produced using this technique. In the first case the antenna was cut in a direction that was parallel to the fabric warp and bonded with steamless ironing. In the second case, the same cut was performed by the layers were bonded with steamy ironing. In the third case the antenna was cut with a 45° angle to the fabric warp and bonded with steamless ironing. In all cases the monopole was cut using a laser cutting machine for precision purposes. This allowed us to observe the effects of steam in the ironing process and the influence of the cut direction in the conductive fabric.

The measured reflection coefficient obtained for each antenna is shown in Fig. 4.23.

According to the measured results on Fig. 4.23, we can see a higher frequency shift in the antenna made using steam in the ironing process. In order to investigate the source of the problem the thickness of the antenna was measured using a compressional tester. For the antenna without steam the thickness is 0.62 mm, and for the antenna with steam is 0.60 mm. This difference can be due the higher compaction of the materials when steam is applied. As one can see from the SEM (Scanning Electron Microscope) images in Fig. 4.24, in the

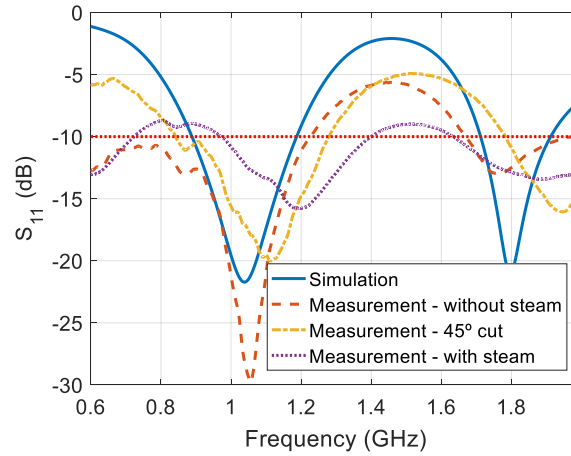


Figure 4.23: Comparison between simulated and measured reflection coefficient for the three fabric monopoles manufactured with and without steam.

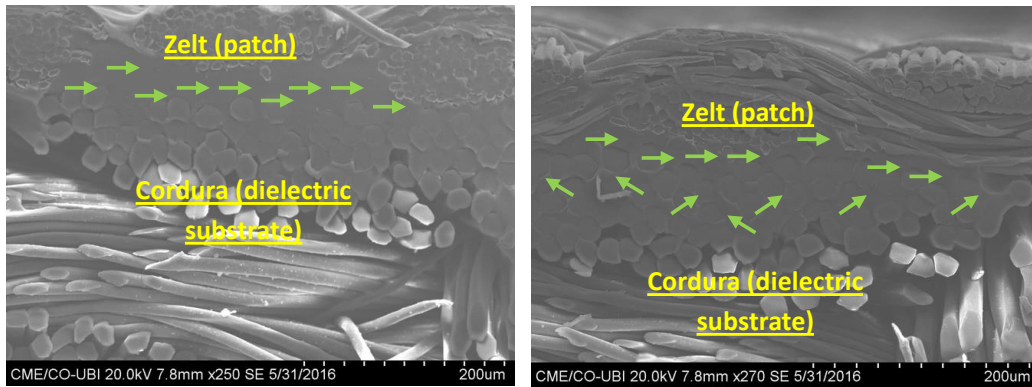


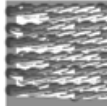
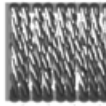
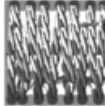
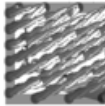
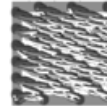
Figure 4.24: SEM images: cross-section of the antenna assembled without steam on the left and with steam on the right.

antenna without steam the adhesive sheet (see yellow arrows) remains as interface between the conductive and dielectric layers. However, when the steam is applied, the adhesive sheet has merged with the textile structure (see green arrows). This effect may be responsible for a decrease in conductivity due to the presence of the glue among the conductive yarns. Also, the presence of the adhesive sheet into the Cordura fabric, will have an impact in the substrate's permittivity. Moreover, the shift in the frequency can be affected due to other factors, such as the manufacturing process.

Nevertheless, it is worth noting that this effect can be further studied, and these effects can be accounted for, during the antenna design, in order to be compensated, which is rather important if one pretends to develop antennas on clothes that will eventually be subject to ironing with steam.

Comparing the two cut directions, from the results in Fig. 4.23, the measurements match

Table 4.4: Parameters of the embroidered antenna prototypes.

Prototype	1	2	3	4	5
Description	Horizontal step stitch	Vertical "Satin" stitch	Vertical step stitch	Diagonal step stitch (152°)	Diagonal step stitch (30°)
Draft of stitch					
Number of stitches	1255	2084	1378	1360	1361
Yarn consump. (g)	0.27	0.39	0.22	0.23	0.27
Yarn consump. per area(g/m ²)	489	706	398	416	489

reasonably with simulation. Both cuts have shown an upwards shift in the resonance frequencies. However, apart from the frequency shift, the diagonal cut matches relatively well to simulation, as the parallel cut shows a worst behavior. The frequency shift can be attributed to manufacturing tolerances when cutting the fabric, which led the actual length of the monopole arms to fall shorter than supposed to. However, for the parallel cut case, the difference is beyond the simple frequency shift and there's a considerable difference in matching even at the lower bands. This effect is difficult to understand, but, an obvious conclusion one can take from this results is that a 45° cut of the fabric warp direction leads to a better precision of fabrication. Nevertheless, the reflection coefficient is low at the operating frequencies, meaning that the antenna presents a low impedance mismatch at both, GSM and DCS bands.

The embroidering is a promising method in terms of repeatability and mass-manufacturing [158], as the embroidered antennas do not need cutting or lamination process, thus reducing the production costs. In this section, the embroidering technique to produce antennas that can be easily applied in clothing as an emblem is explored. This way the embroidering technique may possibly increase the interest in the development of textile antennas into clothing.

Five prototype antennas were developed with this technique, using an automatic embroidering machine, which are shown in Fig. 4.25. The antennas were embroidered in the Atlantic fabric using the Silverpam yarn (see Table 4.3). The parameters of the embroidery are described in Table 4.4. The orientation of the stitch was considered by performing stitches along four different directions, for prototype antennas 1, 3, 4 and 5. The number of stitches was considered by varying the float of the stitch, between antennas 2 and 3. To avoid possible differences in the fringe effects occurring in the feed line, due to the different directions of the stitches, all antennas have feed line embroidered with horizontal step stitch.

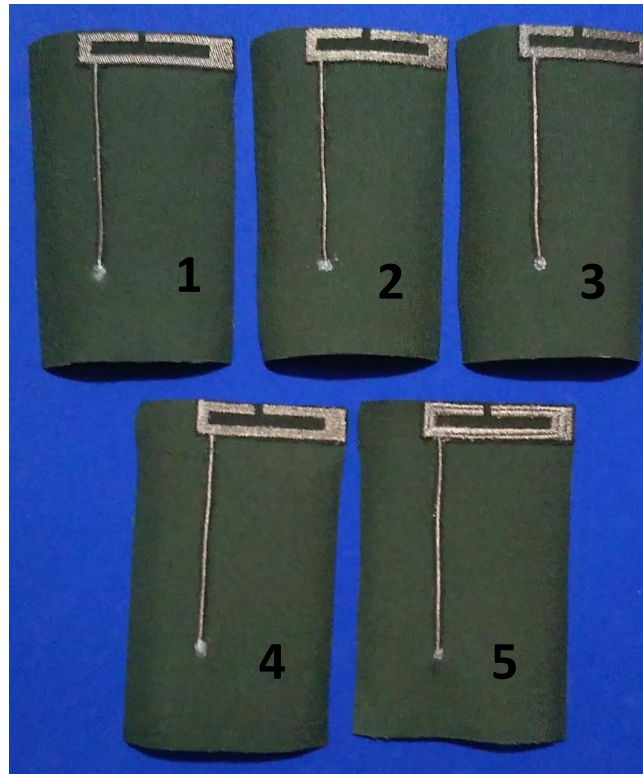


Figure 4.25: Photograph of the embroidered antenna prototypes.

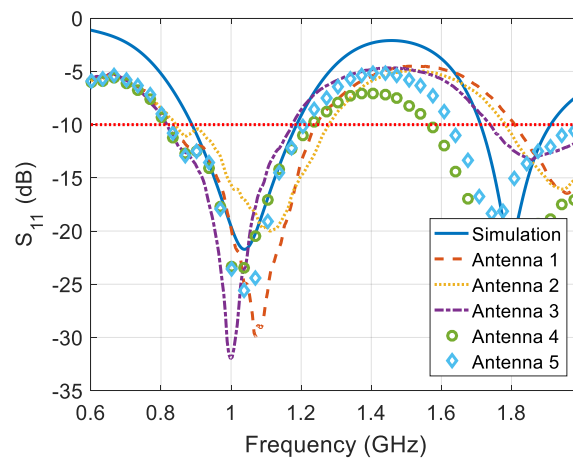


Figure 4.26: Comparison between simulated and measured reflection coefficient of the embroidered antenna prototypes.

Simulated *versus* measurements of the reflection coefficient, for the five embroidered antenna prototypes, are shown in Fig. 4.26. The measurements match fairly to the simulations, with all the prototypes showing a slight upwards shift in the lowest resonant frequency. Being that, prototype 3 is the one with the best match to the simulation.

The fact that the prototype 3 presents the best match can be attributed to the fact that the embroidery stitch direction is parallel of the feed line, therefore, homogenizing the current flow. Antennas 4 and 5 present a very similar behavior that indicates that the angle of the diagonal direction has little influence on the current flow, rather, it supports the statement that only the difference in interface between the feed line and the monopole arms plays a major role in the input impedance match of the antenna. Coherently, antenna 1 shows the highest shift of the resonant frequency, being that direction of the embroidery stitch in the monopole arms is perpendicular to the feed line, corroborates with the previous assumptions.

Comparing different types of stitches with the same alignment, in antenna 2 a "Satin" stitch was used to compare to a simple vertical stitch, such as antenna 3. Even though the direction of the embroidery in antenna 2 is coincident with the direction of current flowing from the feeding line, as in the antenna 3, the reflection coefficient difference between both antennas is rather considerable. However, in antenna 2, the direction of the stitch is rotated along the arms, besides, the particular characteristic of the "Satin" stitch creates a lump in the middle of the monopole arms. Both this characteristics can have a large influence in the current distribution along the antenna, which in turn, affect its impedance, which explain the difference in the results, as well as the difference between simulation and measurement.

After this study, the antenna design proposed has been integrated into a fully fabricated jacket. But, unlike previews proposals as described in [29, 27], where the antennas are built ex-situ and posteriorly integrated in the lining of the cloth or pockets, or even glued to the cloth, this prototype was manufactured directly in the clothing with the same textile materials composing the jacket.

The antenna was integrated using the thermal adhesive sheets technique. The coat is fabricated with Cordura® and a 3D fabric (reference 3003-3D fabric, from LMA). This way, we could verify the influence of the human body and the integration effects in the antenna behavior. The jacket with the integrated antenna is shown in Fig. 4.27, where it is also shown the setup to measure the behavior with a human body.

It is possible to see the agreement between the simulated and measured values of reflection coefficient, even in the on-body measurements, in Fig. 4.28. The textile antenna presents an operating frequency range capable of completely covering the GSM900 (880-960 MHz) and the DCS 1800 (1710-1880 MHz) bands.

Even after integrated on clothing, the radiation pattern of the antenna is clearly omnidirectional. The Fig. 4.29 shows the differences in the radiation pattern between the measurement of the standalone antenna fully integrated into the smart coat structure and the measured on-body performance. The results depicted in Fig. 4.29 correspond to the XZ-plane. Due to the configuration of the antenna placement on the jacket, this is the only measurable plane (see Figure 4.27). Nevertheless, it is the most relevant plane in order to evaluate the omnidirectional characteristic of the antenna. Moreover, given the position

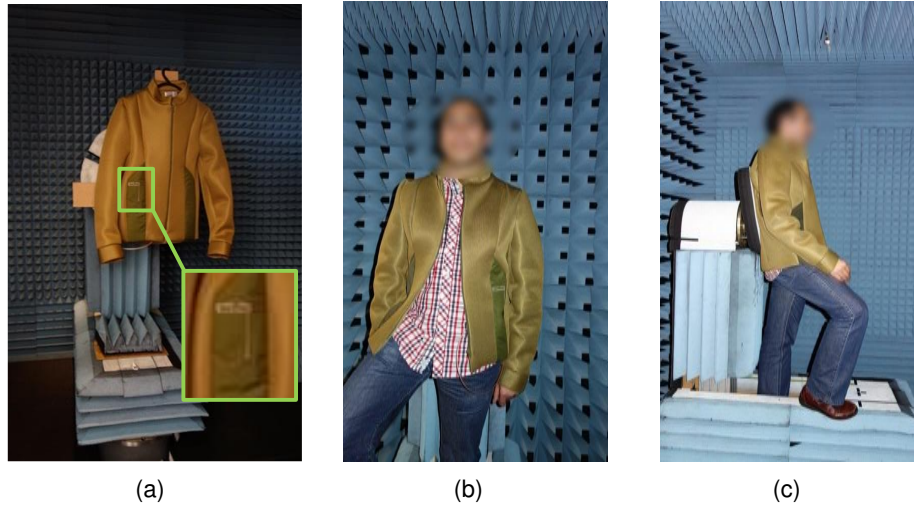


Figure 4.27: Photograph of the jacket with the embedded textile antenna in the anechoic chamber setup. (a) Jacket in standalone measurement, (b, c) jacket dressed into human subject.

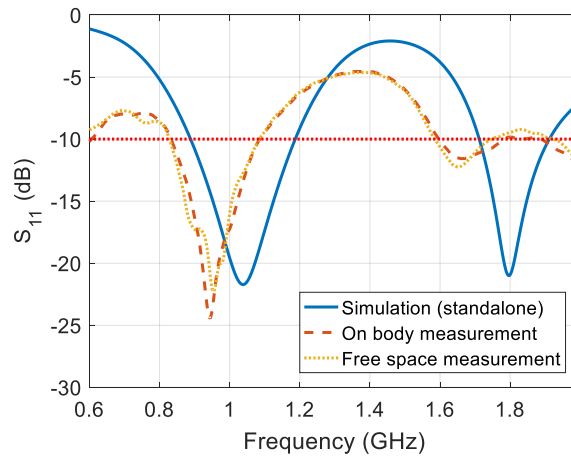


Figure 4.28: Comparison between simulated and measured reflection coefficient of the integrated antenna with and without the human body presence.

of the antenna on the jacket, shown in Fig. 4.27, it is clear that the direction at which the antenna will be less subject to influence from the jacket or person occurs at nearly 30° in broadside direction. This is confirmed by the measurement results depicted in Fig. 4.29.

According to the measured results on Fig. 4.29, we can see that the presence of the jacket and mainly the person, influence the radiation characteristic as expected. In the empty jacket measurement, we can see that when the jacket is between the probe antenna and the test antenna, around 160° , there's a reduction in the antenna gain, this is due to the presence of a large dielectric body, that is the jacket. Nevertheless, the antenna showcases a nearly

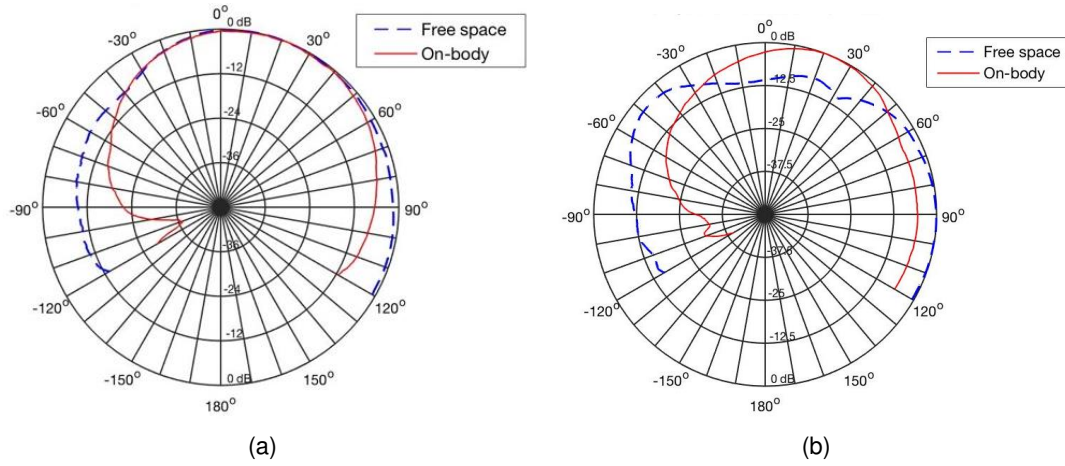


Figure 4.29: Measured radiation pattern of the integrated antenna into the jacket, with and without the presence of the human body, at (a) 900 MHz and (b) 1800 MHz.

omnidirectional pattern. The on-body performance is different. Since the human body is a large dielectric mass, comparable to water as in the previous bottle applications, it absorbs, reflects and refracts electromagnetic waves. We can see from the measurements that when the body is between the probe and the test antenna, at 180° , it will absorb a great deal of radiation and reflect the rest in the opposite direction, shielding the test antenna, creating a null of radiation at this point. While, when the body is right behind the test antenna, at 30° broadside, leaving the best clearance, its when the antenna showcases the best transmission. This happens for both frequencies, being even more clear at 1800 MHz.

4.4 Additively manufactured antennas

Additive manufacturing technology, namely 3D printing, has seen a major massification in the past few years. The expansion of the small scale and desktop grade 3D printers and large access to the printing material at low costs has allowed the exploration of this technology for prototyping purposes in research and academia.

In this thesis the use of 3D printing technology has been used for antenna development in two very different applications, and also different from the RFID applications shown so far. On one hand, an antenna for an RF digital system with agile frequency operation, which required an omnidirectional radiation and wideband frequency of operation for broadcast purposes. On the other hand, very high gain antennas at *K*-band for space communications and wireless power transfer applications.

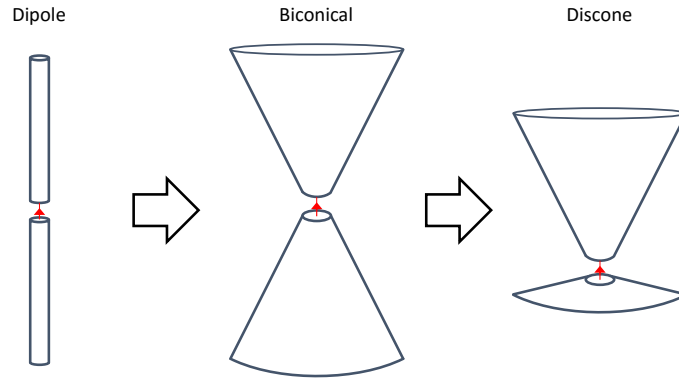


Figure 4.30: Illustration of the evolution from dipole, to biconical and to the discone antenna.

4.4.1 Discone antennas

On a first approach to antenna development with 3D printing, a printed plastic structure was used mainly for support of a discone antenna. Although the properties of the material had to be considered during simulation, due to being in such close contact with the conducting parts of the antenna, the plastic in this scenario was used solely for support purposes and presented a very slight influence (practically negligible) in the radiation properties of the antenna.

A discone antenna is based on the biconical antenna, which is an evolution of the dipole (see Fig. 4.30). The discone can be thought of as a monopole, but the principle of operation is actually different, since in the monopole there must be a ground, and the disc in the discone is not a ground plane, but a rather large impedance matching stub.

The operational characteristics of the discone antenna are mainly dependent on the radius of the bottom and top and the height of the cone. Rules of thumb for discone antenna design, as provided by [159], state that the disc radius and the height of the cone are related to the minimum frequency of operation of the antenna, where the cone height should be close to a quarter wavelength at the lowest operating frequency, and the disc around 0.7 times the height of the antenna. The cones bottom (smallest surface) and the gap between the cone and the disc controls the input impedance and is used to guarantee the impedance match. This will inherently influence the maximum operational frequency. These dimensions were initially estimated and further optimized through EM simulation in order to achieve an operating bandwidth between 0.4 and 2.5 GHz.

A first iteration was done and presented in [160], which is shown in Fig. 4.31. In this, the gap between the cone and the disc was air, and therefore, the cone had to be glued to a support ring structure. Besides, the conductors were applied in the exterior which made them more prone to ripping and pilling. This caused the antenna to be rather fragile, specially in the feeding point since the weight of the cone broke the contact point of the feeding pin



Figure 4.31: Photograph of the prototypes of the first and second iterations of the discone antenna.

several times during the measurements of the antenna. Due to that, a second iteration was designed, where the antenna was composed of a single piece and, therefore, the gap between the cone and the disc was filled with PLA, being that the conductive part was applied in the inside of the PLA structure, as shown in Fig. 4.31.

The schematic with the dimensions of the first and second iterations of the discone antennas is shown in Fig. 4.32. To make the discone antenna into a single printing piece for robustness, forced the top radius of the cone to decrease and the bottom radius to increase. The reduction of the cone top radius and the increase in the cone bottom radius led to a smaller bandwidth of operation, but allowed the operation nearly at the same starting frequency, even though the height of the cone was reduced by 10 mm.

The first discone has a fractional bandwidth of more than 200%, starting at 420 MHz up until 3.5 GHz in simulation and 3.2 GHz for the measured prototype. Since the upper band is much larger than the needed frequencies for the system that would go up until 2.5 GHz at most, the second iteration could be slightly condensed and the operation bands are comprised between 420 MHz and 2.40 GHz in simulation and between 380 MHz and 2.54 GHz for the measured prototype. The simulated versus measured reflection coefficient is shown in Fig. 4.33.

The radiation pattern of the discone antenna is essentially omnidirectional. It is perfectly omnidirectional for frequencies where the dimension of the cone are below one wavelength, where the radiation pattern is the product of the fundamental mode of operation of the antenna, this is shown in the radiation pattern in Fig. 4.34 (a) and (b). For higher frequencies, higher order modes are excited and the resulting radiation pattern changes. Moreover, the electrical size of the disc increases for higher frequencies and it starts to act as a ground

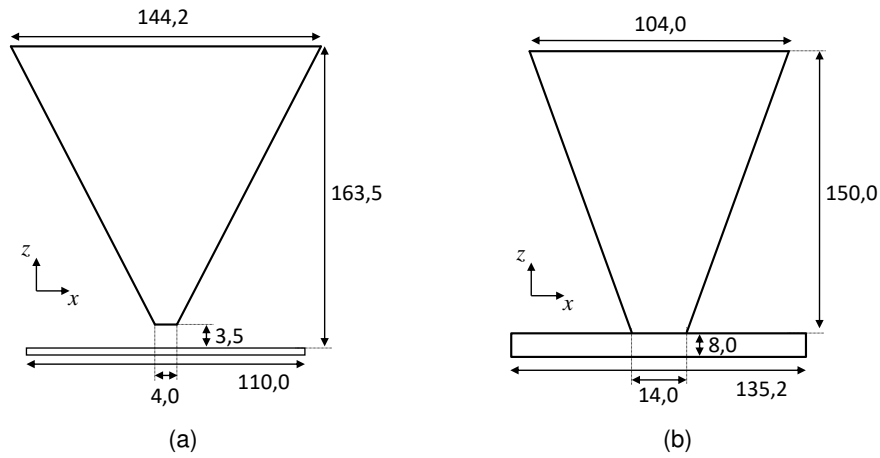


Figure 4.32: Schematic of the first and second iterations of the discone antenna. (a) First discone antenna schematic with air gap feeding and (b) Second discone antenna with PLA gap feeding. All dimensions in millimeters.

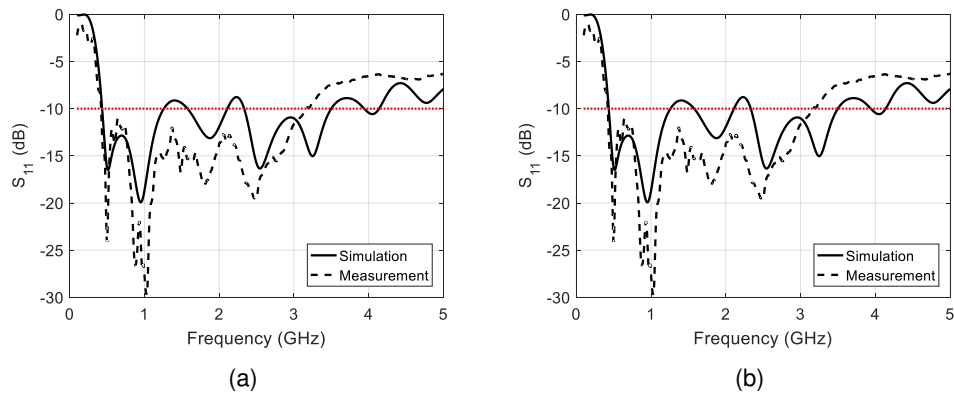


Figure 4.33: Simulated versus measured reflection coefficient of the (a) first iteration and (b) second iteration of the discone antenna.

plane, which leads to a tilt of the radiation pattern, the same behavior that is observed in monopole antennas, this is observable in Fig. 4.34 (c). Which eventually leads to an almost isoflux-kind radiation pattern at the upper end of the operating band as observed in Fig. 4.34 (d).

The directivities follow the increase in the electrical size of the antenna, and the tightening effect on the radiation pattern, as the frequency increases, is accompanied by an increase in the maximum directivity of the antenna. The simulated directivities and efficiencies are summarized in Table 4.5.

As expected, the antenna presents very high radiation efficiencies as is usual for dipole and monopole type antennas only subject to the losses in the conductors.

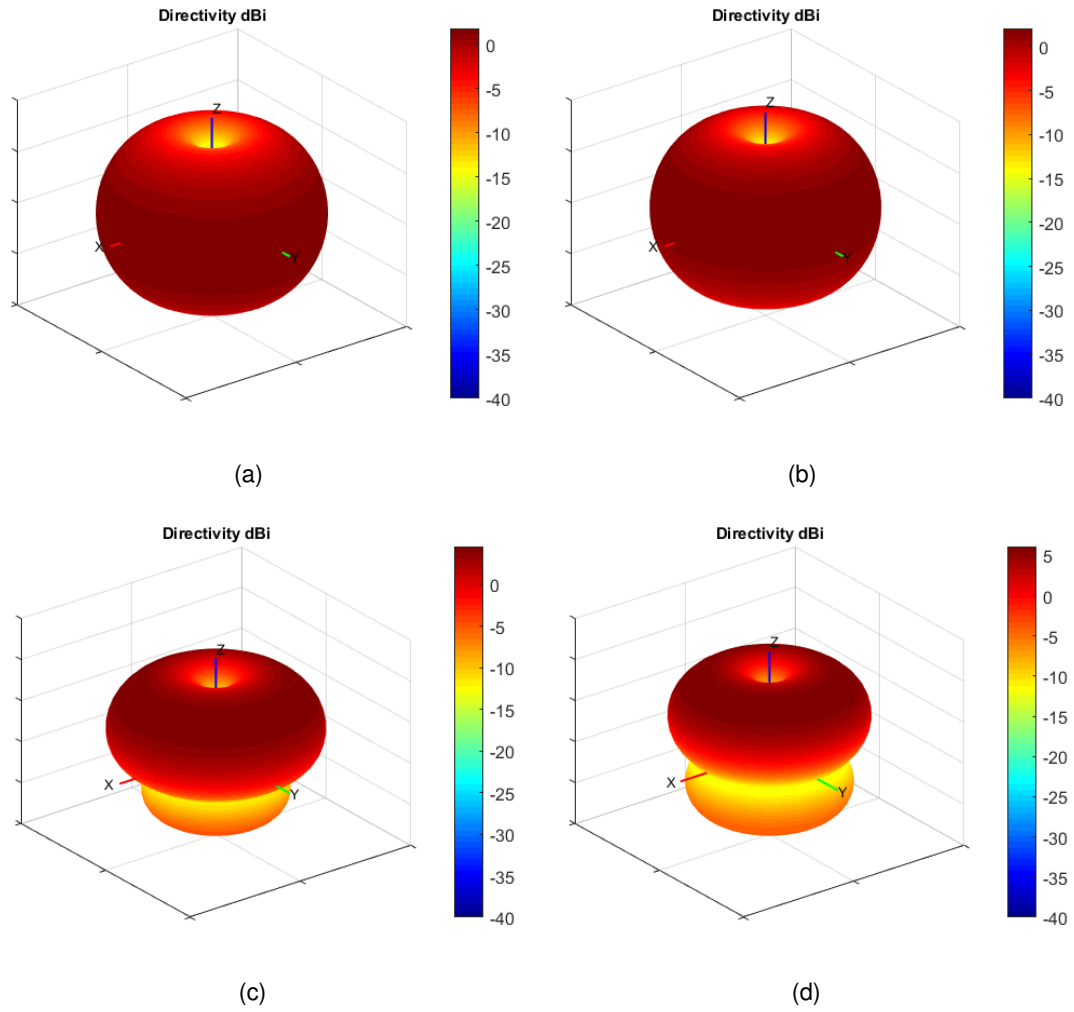


Figure 4.34: Simulated radiation patterns of the second iteration of the discone antenna at (a) 400 MHz, (b) 800 MHz, (c) 1500 MHz and (d) 2000 MHz.

Table 4.5: Simulated directivities and efficiencies of the discone antennas.

Prototype	Frequency (MHz)	Directivity (dBi)	Radiation efficiency(%)
Discone 1	400	1.48	97.7
	800	2.26	99.8
	1500	4.41	99.8
	2000	6.03	99.9
Discone 2	400	1.64	98.2
	800	2.16	99.9
	1500	4.58	99.9
	2000	6.14	99.8

Only the XZ plane was considered for measurement, since being the antenna essentially omnidirectional, the XZ plane is symmetric to the YZ plane, and the XY plane is equivalent at all frequencies and having no nulls would provide little ground for comparison.

The simulated versus measured results of the radiation patterns for the first prototype at four different frequencies is shown in Fig. 4.35, whilst the simulated versus measured results of the radiation patterns for the second iteration prototype are shown in Fig. 4.36. It is clear, from the results depicted for both antennas, that there is a good agreement between simulations and measurements for the radiation patterns. Although the measurement for the first prototype at 1500 MHz is missing, given the good agreement between simulation and measurement obtained for the remaining frequencies, one can expect the antenna to behave similarly to the simulation prediction, also at this frequency.

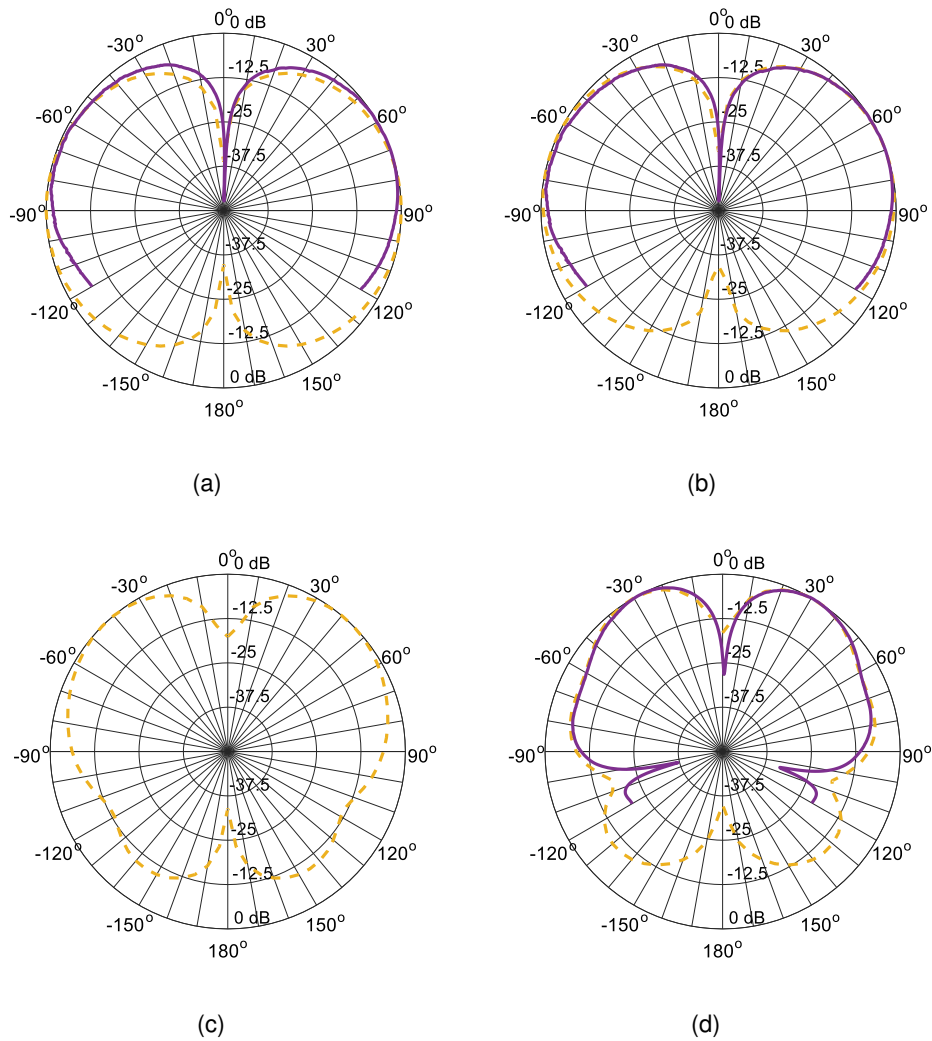


Figure 4.35: Simulated (dashed line) versus measured (solid line) radiation patterns of the first iteration of the discone antenna in the XZ-plane at (a) 400 MHz, (b) 800 MHz, (c) 1500 MHz and (d) 2000 MHz.

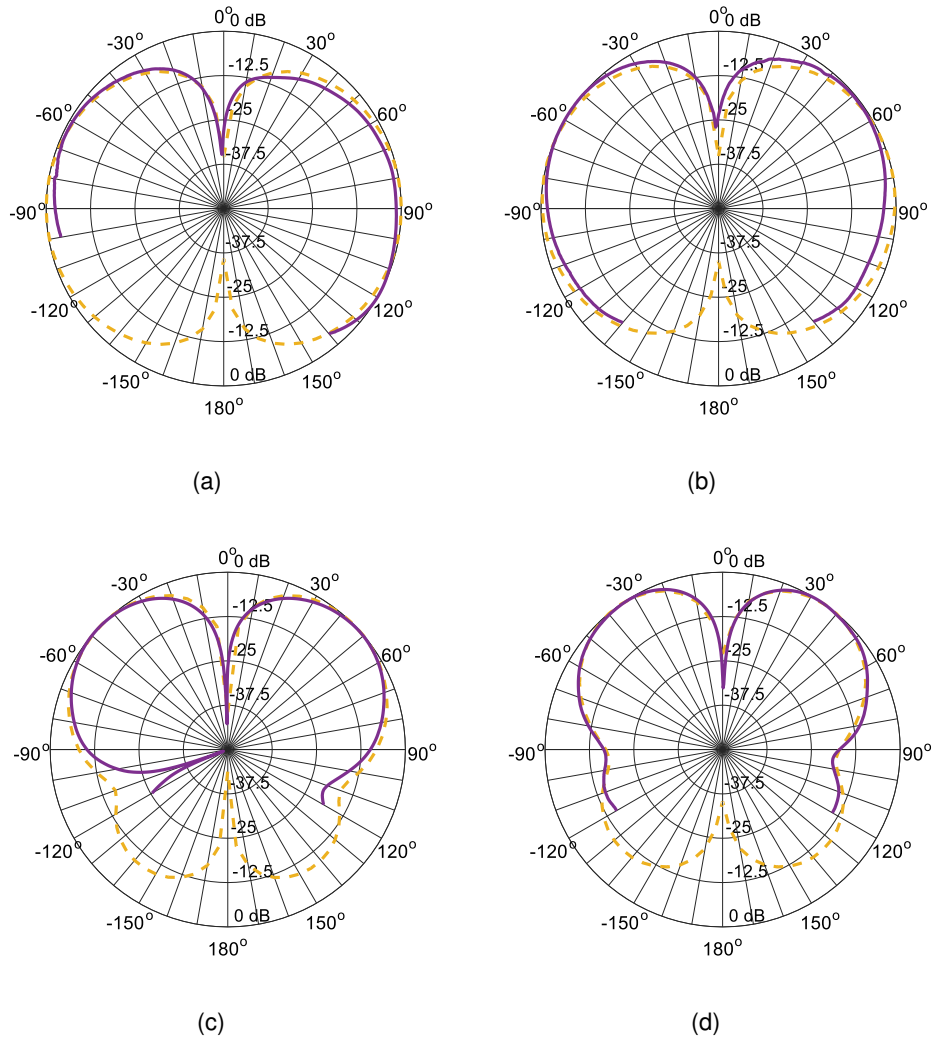


Figure 4.36: Simulated (dashed line) versus measured (solid line) radiation patterns of the second iteration of the discone antenna in the XZ-plane at (a) 400 MHz, (b) 800 MHz, (c) 1500 MHz and (d) 2000 MHz.

4.4.2 Dielectric lens antennas

Besides the discone antennas, 3D printing has been used for the development of dielectric lens antennas. These dielectric lens antennas can be used to create very high gain antennas, particularly interesting for wireless power transfer applications at microwave frequencies in the K -band.

Lenses are used to shape wavefronts and are usually classified as dielectric lenses or constrained lenses [161]. Dielectric lenses were traditionally harder to fabricate and more expensive since they were fabricated using injection molding, which required the construction or acquisition of specific molds for each lens. This cost is significantly reduced when we consider the fabrication with 3D printers. Besides, it also allows to speed up the prototyping phase.

The lens size are bound to the radiation properties one pretends to achieve. That is, the profile of the lens can be shaped in order to provide the highest gain possible (narrower beam), provide broader beams, or even be shaped to provide a isoflux type pattern [162, 163].

The size of the lens should be of several wavelengths in order to effectively shape the radiation pattern. Therefore, at low frequencies the size and weight can prohibit its use. At higher frequencies, where the lens can have reasonable physical sizes while being several decades of wavelengths in length have other limitations that come from the losses inherent to the dielectric material used in the lens. Dielectrics, as described in the previous chapter, have losses that affect the propagation inside the lens. If the lens is very large and the dielectric is very lossy the radiation efficiency of the antenna can drop significantly. Nevertheless, dielectric lens are an attractive solution to achieve high gain and to easily manipulate radiation characteristics of antennas, specially when working on high frequencies above X -band.

The lens can have flat surfaces, in either the focal plane or the wave-front, spherical surfaces on both planes, but can also take arbitrary shapes, in order to achieve a very particular radiation shape [164]. The design of the lens is tightly connected to the refractive index of the material used, therefore, it is highly dependent on the permittivity of the dielectric. For 3D printing the dielectric lens the material that was used was PLA, that has been previously described and whose characteristics have been presented in the previous section 3.3.

The dielectric lens developed started from a spherical profile shape and evolved into a parabolic profile shaped lens, in order to optimize the obtained radiation gain. Another aspect that was evaluated, was the use of dielectric filled or air filled gap between the feeding antenna and the dielectric lens.

There are different types of antennas that can be used to feed a dielectric lens, being the most common feed antenna used the horn antenna. The second most common feed antenna for dielectric lenses are microstrip patch antennas, which was the chosen structure to feed the developed 3D printed dielectric lens antennas. The microstrip antenna is easy

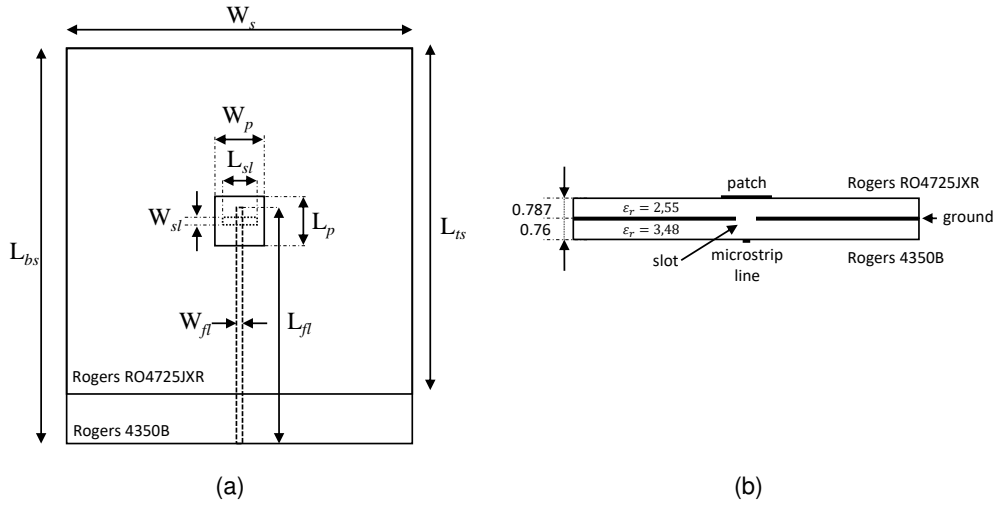


Figure 4.37: Schematic of the slot coupled microstrip patch antenna used to feed the dielectric lens. (a) Front view and (b) bottom view.

to design and has the advantage of being easier to fabricate and much lower cost, which is very important to consider for prototyping purposes. Moreover, it enables a more compact and lightweight design when compared to a horn antenna.

Three different dielectric lens antennas were designed and tested. A spherical lens antenna and a parabolic lens antenna with the same focal plane radius, and another parabolic lens antenna, with the same profile curve but a larger focal plane radius and increased height, for improved directivity.

For feeding purposes, a slot coupled, square microstrip patch antenna was developed. The slot coupled design is used to avoid interference that could disrupt the radiation pattern by isolating the feed line and the patch electric fields. The schematic of the slot coupled microstrip patch antenna is shown in Fig. 4.37. The dimensions used for the patch antenna for each different lens are described in Table 4.6.

Usually for the design of a lens antenna, one picks a geometry according to the application and the radiation shape one pretends and then optimizes the dimensions, from geometric optics rules [165], in order to guarantee that most of the radiated field components of the feeding antenna hit the lens and are bent to a given direction, therefore, shaping the radiation to a given form. However, in this particular case, there's an interest in keeping the lens constrained to a maximum physical size of 20 mm of base radius due to integration purposes. This does not allow a complete maximization of the directivity, nevertheless, the only free variable, the focal point distance, was determined in order to provide the maximum available directivity for this configuration, which led to an increase of 8 dBi of the directivity when compared to the microstrip patch antenna on its own.

The spherical profile lens antenna was the first step since it is the easiest lens geometry

Table 4.6: Dimensions of the microstrip patch antennas used to feed the dielectric lens antennas.

Prototype	Parameters	Dimension (mm)
Hemispherical	W_s, L_{bs}, L_{ts}	40.00, 50.00, 40.00
	W_p, L_p, L_{fl}	6.42, 6.42, 33.05
	W_{fl}, L_{sl}, W_{sl}	1.15, 3.71, 0.60
Parabolic	W_s, L_{bs}, L_{ts}	70.00, 80.00, 70.00
	W_p, L_p, L_{fl}	5.30, 5.30, 42.80
	W_{fl}, L_{sl}, W_{sl}	1.8, 3.90, 0.60

to implement, where one just has to adjust the radius of the lens base and optimize the focal distance. To avoid complications with errors in the estimated permittivity of the dielectric, we considered air filling in the gap between the patch and the lens focal plane, as it is shown in Fig. 4.38.

The measured reflection coefficient of the spherical lens antenna matches with the simulations and we can see it is centered around 13.2 GHz, as shown in Fig. 4.39 (a).

In order to increase the directivity of the antenna the approach that is proposed in [166] was followed, by converting the spherical profile of the first lens into a parabolic profile, that follows the expression

$$y = h \sqrt{1 - \frac{x^2}{r^2}} \quad (4.1)$$

being h the height of the lens and r the radius of the lens base. The base height follows the relation mentioned in [166], which is obtained from geometrical optics optimization, and that places the focal plane at a distance of $L = h/\epsilon_r$, if the base is filled with dielectric, which was the case for this new lens prototypes. This led to an antenna as shown in Fig. 4.40. Since the base of the lens is filled with dielectric material, that is superposed to the microstrip patch antenna feeding the lens, it will affect the resonance of the microstrip patch, therefore, a correction to its dimensions had to be performed. That is the reason why the dimensions of the feeding microstrip patch antenna are different for the spherical and for the parabolic profile lens, as presented in the previous Table 4.6.

Contrary to the spherical profile lens, the measured reflection coefficient of the parabolic profiles lenses, exhibit an upwards shift in terms of resonance. This is due to, probably, two different aspects of the lens: An inaccurate value of permittivity considered for simulation; The warping effect at the base of the pieces that can occur in 3D printing.

The characterization of the permittivity of the material is prone to errors, therefore, the true value of the permittivity of the lens can be slightly different that the one considered for simulation. However, the permittivity of the lens would have to be less than 1.6, in order for

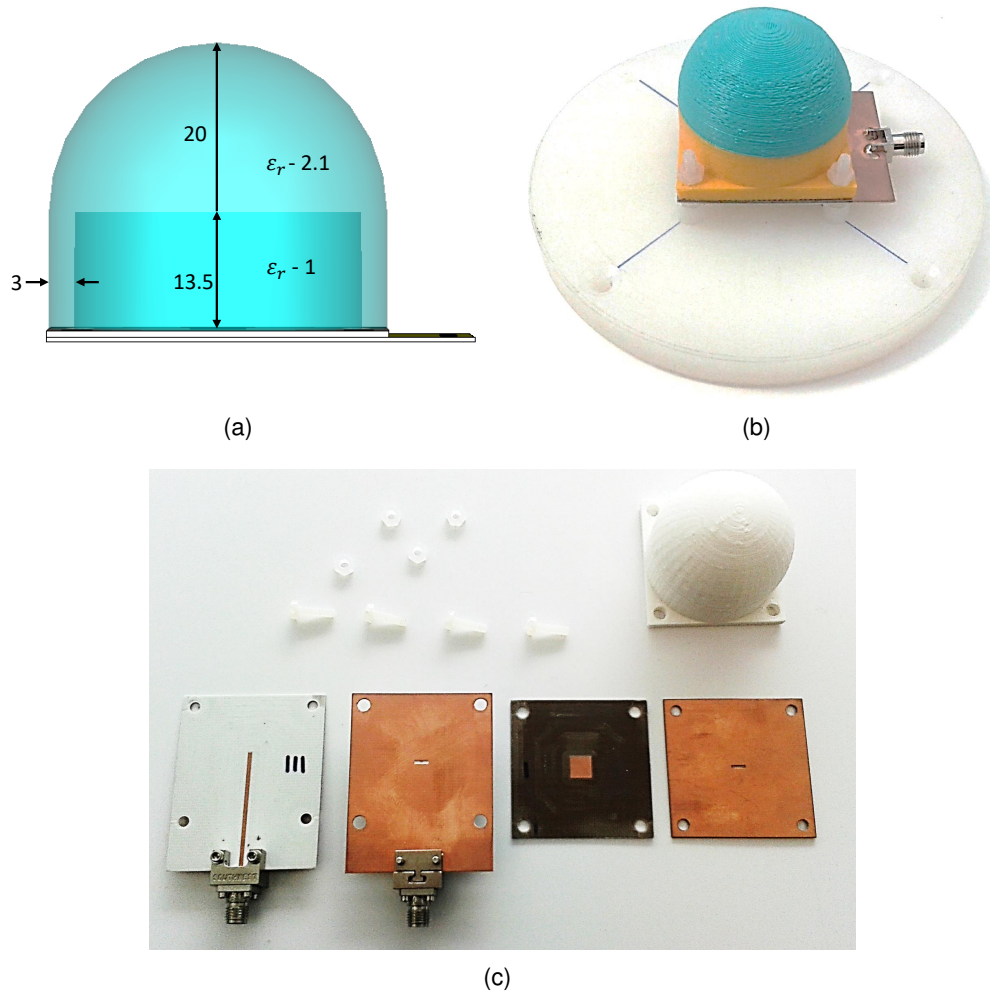


Figure 4.38: Spherical profile dielectric lens antenna. (a) schematic of the lens antenna, (b) photograph of the assembled prototype and (c) photograph of the prototype with all its constitutive pieces. (All dimensions are in mm).

the resonant frequency in simulation to match the measured values. This is a very large difference from the measured permittivity for PLA and such an error magnitude is not reasonable. Therefore, the inaccuracies in permittivity value estimation are most certainly not the only cause for the deviation between simulations and measurements.

By looking at the reflection coefficients depicted in Fig. 4.39 (b) and (c) it is clear that the larger lens, has a larger deviation compared to simulations, than the smaller lens. What is also observed is that in the larger lens, the warping effect observed in the edges of the lens base is more prominent. Warping is an effect that occurs when the plastic material being printed does not adhere completely to the printing bed and tends to bend upwards as the printing goes on, particularly in narrow edges of the object. For larger objects the

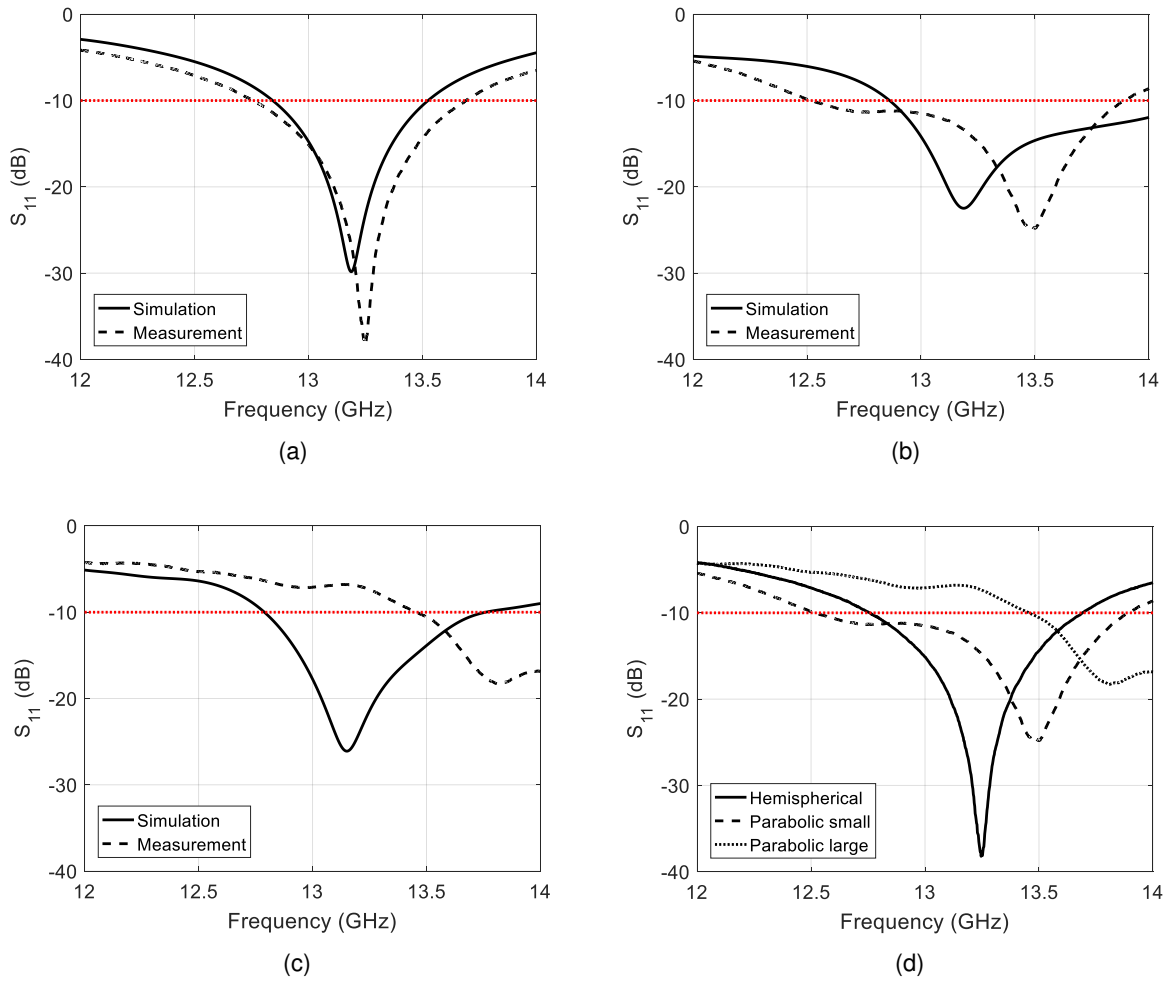


Figure 4.39: Simulated versus measured reflection coefficient of the (a) hemispherical lens, (b) smaller parabolic lens, (c) larger parabolic lens and (d) comparison between the three lens antenna prototypes.

probability of occurrence increases and is sometimes very difficult to avoid it. Although the lens base were sanded in order to minimize surface roughness and the warping effects, truth is the bases are not perfectly flat as considered in simulation. Therefore, the bending that they exercise over the microstrip patch board is most certainly a source for the differences observed between simulation and measurement. Which is also consistent with the fact that the larger lens creates a larger shift in resonant frequency.

The simulated normalized radiation pattern of each lens is shown in Fig. 4.41. Whilst the simulated versus measured normalized radiation pattern obtained for the three lens prototypes are depicted in Fig. 4.42. The HPBW (Half-Power Beam Width) difference between simulation and measurement was of 6° for the spherical lens antenna in the XZ plane, nearly 0° in the YZ plane, 2° in the XZ plane and the YZ plane for the smaller parabolic profile an-

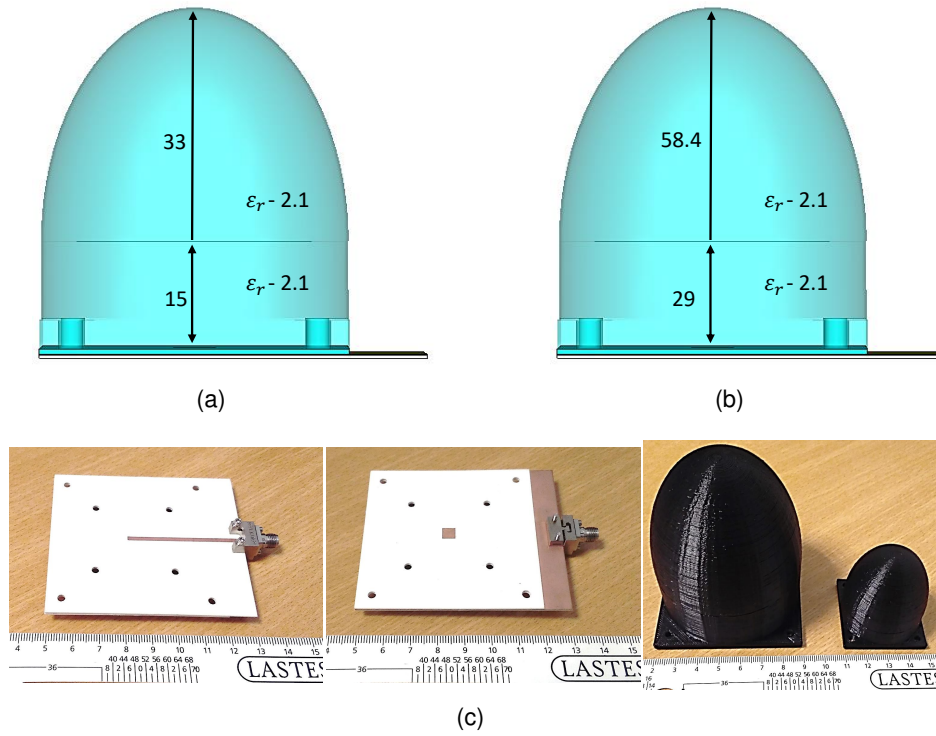


Figure 4.40: Parabolic profile dielectric lens antenna. (a) schematic of the small lens antenna, (b) schematic of the large lens antenna and (c) photograph of the prototype with all its constitutive pieces, from left to right, the bottom of the feeding patch antenna, the top microstrip patch and the printed large and small parabolic profile lens. (All dimensions are in mm).

antenna and 1.6° in the XZ and less than 1° in the YZ plane of the larger parabolic profile lens antenna. Therefore confirming the good agreement between simulation and measurements in both planes measured.

In terms of gain and efficiency obtained for each approach, it is shown in Table 4.7, the values obtained with simulation. In terms of measurements, the spherical lens antenna has proved the worst performance, with a measured gain of 11.2 dBi, nearly 1 dB below the simulated value. The parabolic lens antennas have provided a good agreement between simulations and measurements, with a measured gain of 14.2 dBi, actually slightly higher than the simulated gain, for the small parabolic lens, and a measured gain of 18.2 dBi, for the large parabolic lens.

From the results in Table 4.7 one can also see the increased directivity from the use of a single microstrip patch element compared to the application of a dielectric lens, with an increased of 6.1 dB for the spherical lens, 7 dB for the small parabolic lens and 11.4 dB for the large parabolic lens (in terms of simulation). As well as the increase between each of the lens, with an increase of 1.7 dB between the spherical and the parabolic lens with the

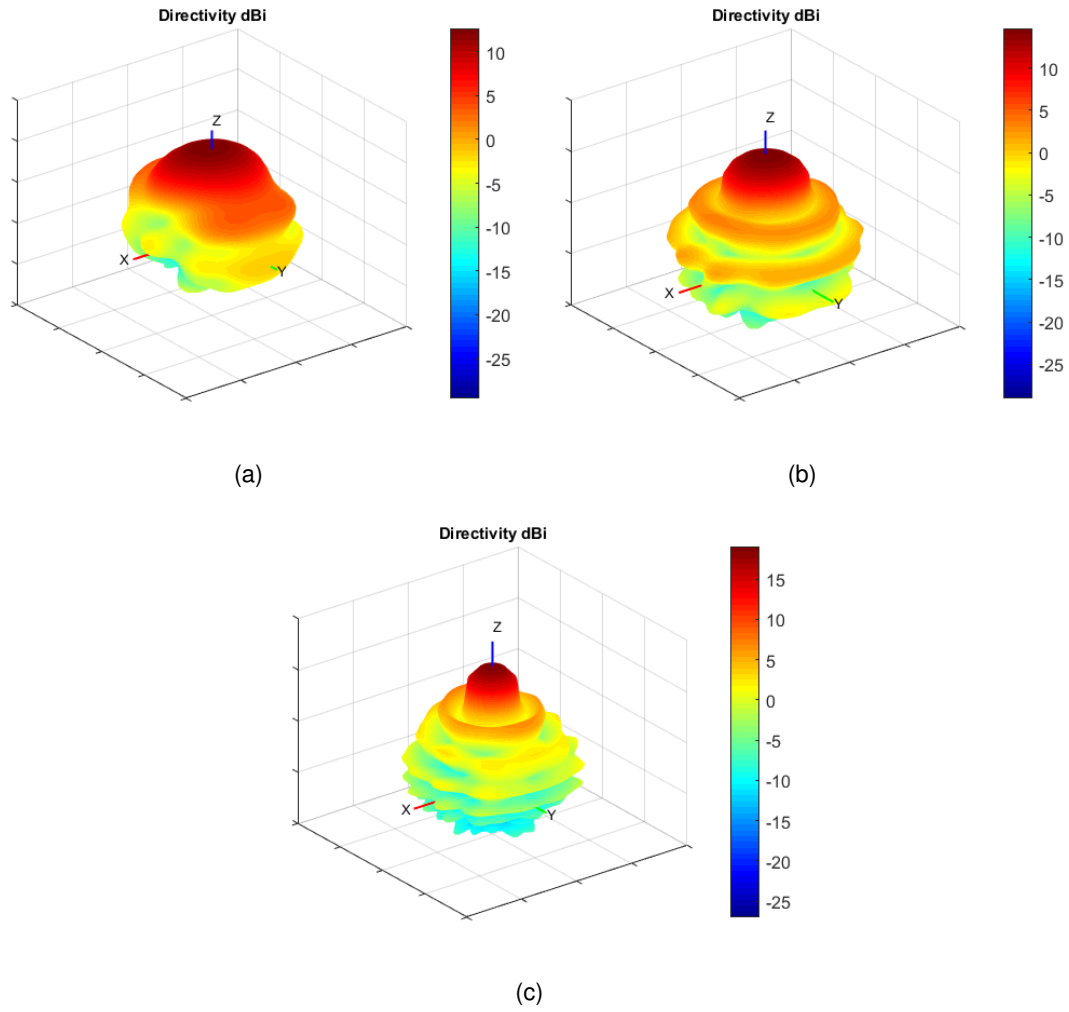


Figure 4.41: Simulated 3D representation of the normalized radiation pattern of (a) hemispherical lens, (b) smaller parabolic lens and (c) larger parabolic lens.

Table 4.7: Simulated and measured gain and efficiency of the three different lens antenna prototypes and the respective feeding microstrip patch antennas.

Prototype	Sim. Gain (dBi)	Meas. Gain (dBi)	Efficiency (dB/%)
Spherical lens	12.3	11.2	-0.35 / 92.3%
Small parabolic lens	14.0	14.2	-0.62 / 86.7%
Large parabolic lens	18.4	18.2	-0.67 / 85.7%
Small patch standalone	6.2	-	-0.37 / 91.8%
Large patch standalone	7.0	-	-0.7 / 85.1%

same base radius dimensions and an increase of 4.4 dB between the smaller and the large parabolic lens.

It is clear, from the demonstrated values, that one can achieve very high gains by using dielectric lenses. Due to limitations concerning the maximum volume of fabrication of the available 3D printer, it was impossible to test larger models in order to verify the limits. However, besides the physical constraints concerning the size and weight that the lens will showcase, it is comprehensible that there is going to be a limit to the possible radiation gain one can obtain, that will be bound by the decrease in radiation efficiency as the lens increases in size and the losses in the dielectric become more noticeable.

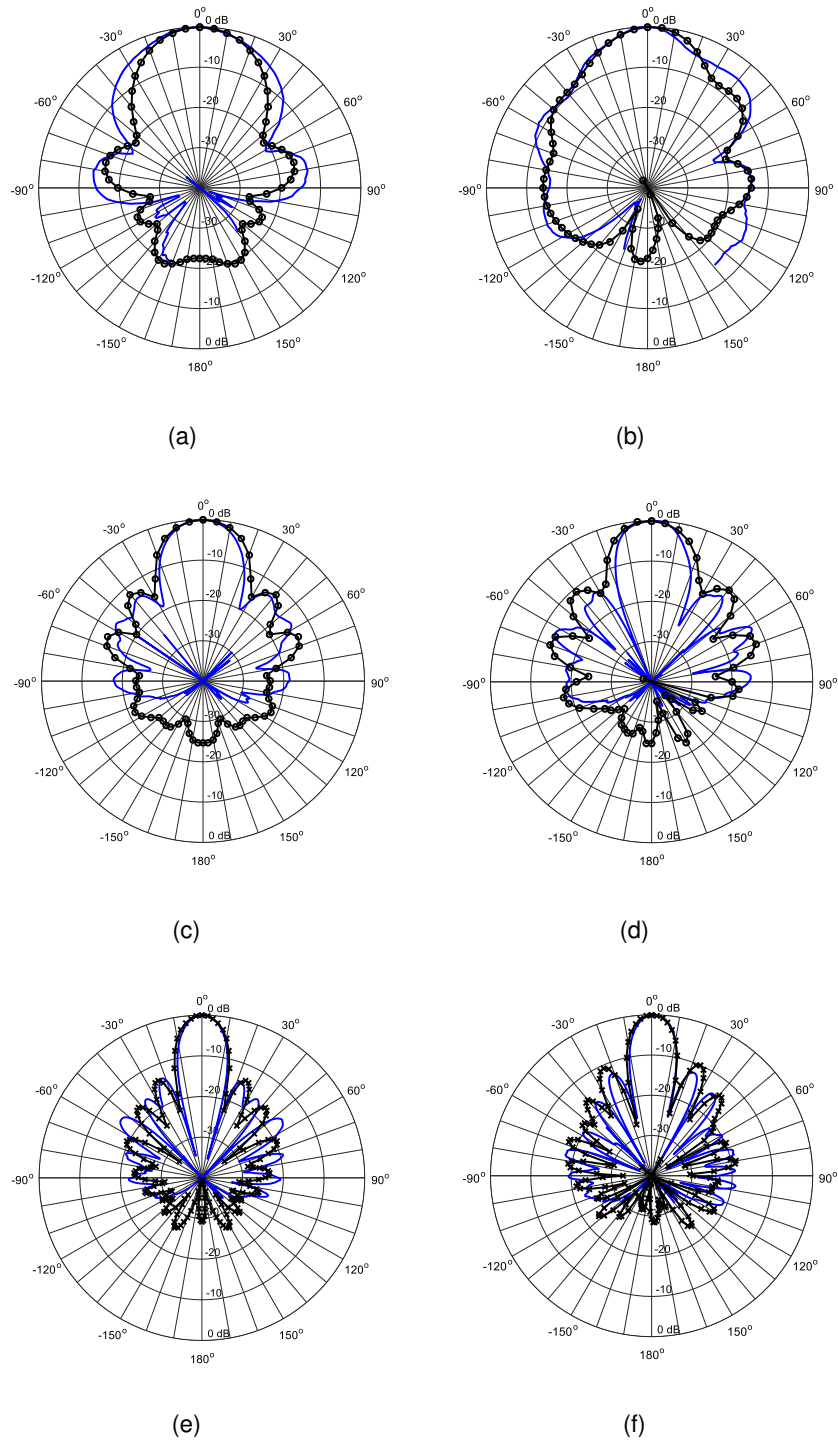


Figure 4.42: Simulated (marked black line) versus measured (solid blue line) radiation patterns of the (a) hemispherical lens in the XZ plane, (b) hemispherical lens in the YZ plane, (c) small parabolic lens in the XZ plane, (d) small parabolic lens in the YZ plane, (e) large parabolic lens in the XZ plane and (f) large parabolic lens in the YZ plane.

Chapter 5

Conclusion

Given the recent developments in battery-less sensors, body worn technology for logistic and medical applications, and the overall exploration of systems for different application scenarios under the flag of the IoT, for which wireless communication is critical, the development of conformal, seamless and embedded antennas has become an important research issue.

A large part of this PhD work has focused on the study of dielectric characterization methods. Many different methods, from resonant methods to broadband methods were covered. During this study, realizing which methods were possible to implement with the in-house equipment and features available was important. Many of the methods studied, specially the resonant cavity based methods, as well as the coaxial probe or the waveguide methods, required special equipment or features to implement. Other methods were so sensible to feature model characteristics that would require large corrections and several iterations in order to achieve high certainty results for a particular material under test. Also, most of the resonant methods, as well as the waveguide methods, require a specific machination of the dielectric sample under test, which is not always possible. So considering the equipment availability and the limitations concerning the dielectric material samples for testing, printed transmission line methods were concluded to be the best possible way to characterize the different set of dielectric materials under study, since the dielectric samples in most cases were flat, or could easily be machined to a flat slab, and the printed transmission line methods could provide a reasonable accuracy in the estimation of the permittivity, not so much about the dissipation factor, of all the different dielectrics considered. Besides, the measurement setup is simple and quick.

The two-length microstrip line method was, therefore, the most widely used method for substrate characterization. Nevertheless, one of the problems that was faced during the implementation of this method in materials such as cork and paper, was the ability to create a pair of microstrip lines that had the exact same physical characteristics, apart from length. Since these lines were manufactured with copper tape on top of the dielectric material, it was not easy to have two stripes of copper with the exact same width and perfectly straight

along all the length, which in some occasions led to erroneous results, demanding another set of lines to be manufactured with better precision. Due to that, a method for the permittivity estimation using a single microstrip line measurement was developed. This method was successfully used to determine the permittivity of three different and known substrates with different values of permittivity. Concluding that the method presents larger errors when determining low loss and high permittivity substrates.

Using the two-length line method and the developed single microstrip line method, three different materials were characterized and presented in this thesis: Two types of paper, two types of cork and a single batch of black PLA. Although these two characterization methods have a certain degree of uncertainty associated, the estimated values have proven to provide very good approximations to the real values of each material, when applied to the design of different antennas.

Regarding the design of antennas with alternative materials, most of the antennas designed were for passive tags based on RFID systems. The first approaches were the design of tags on paper substrate for bottle labeling. The implementation of antennas that can work in the vicinity of a liquid filled bottle is a challenging task, since the liquid is very lossy and will hinder the radiation efficiency of the antenna close by. This efficiency loss occurs due to the high dielectric value of the water and its lossy nature, which interacts strongly with the fields and fades the overall radiated energy. Nevertheless, by placing a reflecting plane in one of the faces of the bottle opposed to the antenna, one is able to reduce the effect of the liquid. The interrelations of this scenario are yet to be understood and, therefore, in order to the correct design of the tag antenna and the size and placement of the reflection plane can only be obtained through optimization of simulation.

Still of the development of RFID tags for bottle identification, cork was explored as support material. Two prototypes were developed, one based on a monopole approach, and another a miniaturized approach, comprising only the inductive ring and a lumped resistor. Unlike the paper tags that were envisioned to be placed on the label of the bottles, the cork RFID tags are used as cork stoppers for the bottles. That simplified the problem regarding the vicinity of liquids. Nevertheless, in both cases, the presence of the liquids inside the bottle have proved to largely influence the resulting radiation pattern. Still, two working prototypes that do not require any special reflector plane have been designed and which proved functional. Although one of the prototypes was very large for a practical cork stopper, the miniaturized version is seamlessly integrated into the bottles and we were able to achieve at least 0.5 m of communication range at 866 MHz. Even though the communication range is rather short for a typical RFID system, it's a constraint that is easily acceptable considering the application scenario and given the miniaturization factor achieved.

Cork has also proved useful as a sensing mechanism for humidity. A passive sensor tag based on RFID was developed using cork as sensing device and it was shown that it is

possible to determine the ambient humidity around it with a reasonable precision. When the humidity in the air increases, more water molecules get trapped inside the air holes present in the cork, due to this, the permittivity of the cork increases, which if placed around an RFID tag antenna will de-tune the input impedance of the antenna and create a resonant frequency shift. Based on a simple calibration method, one is able to infer the ambient humidity based on the activation power of the tag at a given target frequency.

Concerning the developments with fabrics, since this was the most studied subject and there was already a great deal of research into the development of antennas with textile materials, a greater focus was given to manufacturing techniques of textile antennas. Several prototypes of a fully textile microstrip patch antenna were developed, with different construction techniques, in order to evaluate which provided the best compliance with the simulation and which could resist washing in a regular washing machine program. It was proven that the interlining process with thermal adhesive layers and the sewing processes were the ones that provided the closest to simulation results, rendering these the best construction processes. However, only the sewed prototype has proved to resist washing process intact, although after washing, a degradation on the measured results was evident. It was concluded that a successful all textile antenna had to be manufactured with a different structure. Probably recurring to the interlining with thermal adhesive layers, but with impermeabilization layers around it in order to safeguard the antenna structure during the washing process.

Taking into consideration the manufacturing techniques experimented for the microstrip patch antenna, another prototype was designed, in this case a dual band monopole antenna, that would allow the testing of another manufacturing technique and the impairments arising in the integration of such antennas into a real piece of clothing. The monopole antenna was developed with two different manufacturing techniques, the interlining with thermal adhesive layers, which proved the best approach for microstrip patch type antennas, and also embroidery, which is only possible to use for groundless antennas as the case of the printed monopole. For the embroidered antennas, five different types of embroidering was tested and it was concluded that when doing embroidery, the direction of the stitch should be coincident to the surface current flow direction in the antenna. Nevertheless, interlining with thermal adhesive layers has proven to be the most reliable manufacturing technique. The integration of the antenna was simple and the antenna has proven good reliability even when operating close to the human body with some movements associated. As expected, the radiation pattern is affected by the presence of the human body, that works as a shielding structure. Nevertheless, careful placing of the antenna in the clothing can turn the human body presence into a benefit. Bending, stretching and compressing was not tested, however, the reasoning behind this, is that these effects are very hard to overcome. Therefore, one should choose the best possible location in the clothing so that the antenna is subject to the least possible bending, stretching or shrinking during operation.

Finally, 3D printing was used to create plastic support structures for antennas and to create lenses able to shape the radiation for a given antenna. On the first approach, 3D printing was used to create a compact UWB table top discone antenna, with a fractional bandwidth of nearly 1.6:1. This antenna has been widely used by the amateur radio community for communications in the VHF band. The developed prototype was aimed at a frequency agile system with operating services in the UHF, L and S bands (433.9 MHz, 915 MHz and 2.45 GHz, respectively). The first approach to the discone antenna, although successful in terms of operating conditions, had a clear integrity and stability problem, which made it impossible to obtain all the radiation pattern measurements since the structure kept breaking the contact at the feed point. This structural problem was resolved in the second prototype, which was also more compact than the first, while maintaining essentially the same operating band as the primer. In summary, when developing 3D printed structures careful with the structure integrity is of high importance.

The second approach to 3D printing was the development of dielectric lenses. Dielectric lens are used to shape wavefronts, much like reflectors, and can provide highly directive radiation patterns. Three different lenses were designed and developed using 3D printing, where a single slot coupled microstrip patch antenna was used as feeding source. The first lens was a spherical wave front lens with compact size, which is the most simple wavefront shape lens design. Nevertheless, the overall gain of the spherical lens antenna was 11.3 dBi, which is more than 5 dB improvement in gain compared to the single microstrip patch antenna radiation. In the second lens design, the radius of the lens base was kept the same, but the wavefront shape was changed from spherical to parabolic, which resulted in an improved gain of 3 dB in comparison to the spherical lens, with an overall gain of 14.2 dBi. In the last lens prototype, the same parabolic profile from the second lens was kept, but the radius of the base was increased in order to further improve the antenna gain, reaching a final measured gain of 18.2 dBi.

Appendice A

The antennas for passive tags are usually differential in nature. Moreover, they're matched for a complex impedance at the target frequency. Therefore, for measurement purposes, one needs to use an adapted tag antenna with a matching network for 50Ω and connect an SMA. This will inherently modify the results of the antenna. Even deembedding the matching network piece the results will never be accurate, since its difficult to create a replica of the single matching network piece for calibration purposes.

The best way to judge the tag antenna in terms of matching with frequency, its to look at its reading range in relation to frequency. To implement it, one can use a monostatic scenario, using a VSG (Vector Signal Generator), an antenna to transmit and receive the signals and a digital oscilloscope or a VSA (Vector Signal Analyzer), as shown in Fig. A.1, or use a bi-static scenario, using a VSG, an antenna connected directly to the VSG and another one connected to the VSA, as shown in Fig. A.2.

In order to evaluate the distance of communication with the tag, a query is sent to the tag and the back-scattered response is analyzed to see if a modulation is discernible. The back-scattered signal from the RFID tag is received by the digital oscilloscope which can be configured to perform the FFT over the received time window and show the frequency spectrum. A VSA can also be used to check the frequency spectrum. Since the tag uses ASK (Amplitude Shift Keying) to modulate the back-scatter signal, the presence of the tag response is discerned by the presence of sub-carriers around the interrogation carrier.

In order to determine the read range, a fixed distance (d) between the antenna and the RFID tag is set and then the transmitted power from the generator is varied to find the minimum threshold power (P_{th}) necessary to turn on the tag. The read range for a given transmitted power (EIRP) can be determined using the following expression

$$R = d \sqrt{\frac{\text{EIRP}}{P_{th} L_c G_t}}, \quad (\text{A.1})$$

where L_c are the losses due to cables and directional coupler between the signal generator and the antenna and G_t is the gain of the transmitting antenna.

This way, by sweeping the frequency of the interrogation carrier, one can determine the

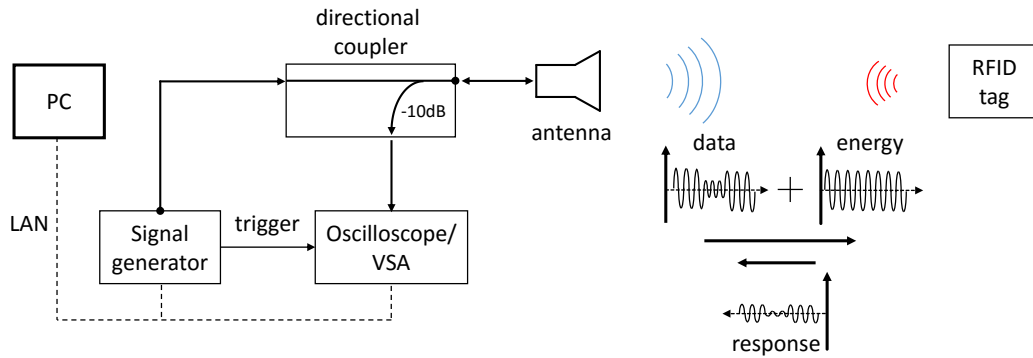


Figure A.1: Schematic of the passive RFID tag antenna monostatic read range measurement setup.

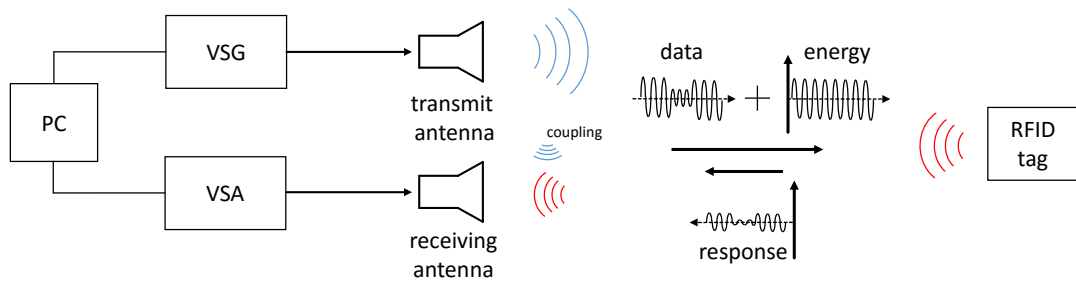


Figure A.2: Schematic of the passive RFID tag antenna bi-static read range measurement setup.

reading range of the tag with frequency, which gives a rough estimation to how well the antenna is matched at each frequency. However, this is just a rough estimation, due to two essential reasons: Since most measurements are done in an indoor environment, the propagation channel is subject to multi-path, while expression (A.1), being based on the Friis propagation formula, is valid for a free-space environment; The other reason being the non-linear response of the tag chip. While the second reason is not so important, since in terms of tag characterization, the reading range is actually more important than the reflection coefficient of the antenna itself, the first reason can be relevant.

The fact that the tag measurements are performed in indoor environments, means that the channel is subject to multipath, which makes the Friis formula estimation for the propagation path invalid. It does not necessarily mean that the reading ranges estimated using expression (A.1) are completely wrong, but might present a certain degree of inaccuracy, that may be relevant. In order to overcome this problem, a solution is to use a standard, perfectly characterized, RFID tag at the measuring distance, with which one can characterize

the forward and backward propagation path at each frequency of interest. This is a procedure that is used when doing range measurements with a dedicated equipment such as the Tagformance from Voyantic, mentioned in Chapter 3.

The reading range measurements can also be used to characterize the radiation pattern of a given RFID tag. For this particular measurement the frequency, the power and the distance of the tag are fixed. The distance is chosen so that the threshold power to activate the tag is, at least, less than 6 dB below the EIRP. The tag is kept on top of a protractor and the threshold power to activate it is measured for each angle, the reading range is then calculated using (A.1). This way, obtaining the maximum read ranges of the tag for swept angle.

Appendice B

For reference purposes, in this appendix a collection of the publications in International Journals, as listed in the first chapter of the thesis, is added.

[J1] - R. Salvado, C. Loss, **R. Gonçalves**, P. Pinho, "Textile materials for the design of wearable antennas: a survey", *Sensors*, Vol. 12, No. 11, pp. 15841-15857, 2012

Review

Textile Materials for the Design of Wearable Antennas: A Survey

Rita Salvado ^{1,*}, Caroline Loss ¹, Ricardo Gonçalves ² and Pedro Pinho ²

¹ Unidade de Investigação Materiais Têxteis e Papeleiros, Universidade da Beira Interior, 6201-001 Covilhã, Portugal; E-Mail: caroline.loss@hotmail.com

² Instituto de Telecomunicações, Campus Universitário de Santiago, 3810-135 Aveiro, Portugal; E-Mails: rgoncalves@av.it.pt (R.G.); ptpinho@av.it.pt (P.P.)

* Author to whom correspondence should be addressed; E-Mail: rita.salvado@ubi.pt; Tel.: +351-275-319-852; Fax: +351-275-319-723.

Received: 18 October 2012; in revised form: 5 November 2012 / Accepted: 6 November 2012 / Published: 15 November 2012

Abstract: In the broad context of Wireless Body Sensor Networks for healthcare and pervasive applications, the design of wearable antennas offers the possibility of ubiquitous monitoring, communication and energy harvesting and storage. Specific requirements for wearable antennas are a planar structure and flexible construction materials. Several properties of the materials influence the behaviour of the antenna. For instance, the bandwidth and the efficiency of a planar microstrip antenna are mainly determined by the permittivity and the thickness of the substrate. The use of textiles in wearable antennas requires the characterization of their properties. Specific electrical conductive textiles are available on the market and have been successfully used. Ordinary textile fabrics have been used as substrates. However, little information can be found on the electromagnetic properties of regular textiles. Therefore this paper is mainly focused on the analysis of the dielectric properties of normal fabrics. In general, textiles present a very low dielectric constant that reduces the surface wave losses and increases the impedance bandwidth of the antenna. However, textile materials are constantly exchanging water molecules with the surroundings, which affects their electromagnetic properties. In addition, textile fabrics are porous, anisotropic and compressible materials whose thickness and density might change with low pressures. Therefore it is important to know how these characteristics influence the behaviour of the antenna in order to minimize unwanted effects. This paper presents a survey of the key points for the design and development of textile antennas, from the

choice of the textile materials to the framing of the antenna. An analysis of the textile materials that have been used is also presented.

Keywords: wearable antenna; flexible antenna; textile materials; dielectric properties

1. Introduction

Body worn systems endowed with sensing, processing, actuation, communication and energy harvesting and storage abilities are emerging as a solution to the challenges of ubiquitous monitoring of people in applications such as healthcare, lifestyle, protection and safety [1]. Accordingly, the new generation of clothing will be able to sense, communicate data and harvest energy in a nonintrusive way [1,2]. The wearable antenna is thus the bond that integrates cloth into the communication system, making electronic devices less obtrusive. To achieve good results, wearable antennas have to be thin, lightweight, low maintenance, robust, inexpensive and easily integrated in radio frequency (RF) circuits [3–6]. Thus, planar antennas are the preferred type of antenna as, despite the fact their maximum attainable bandwidth-efficiency is significantly lower than the theoretical limit for electrically small antennas, they allow an excellent integration of the antenna with the RF circuits, feeding lines and matching circuits on a standard multilayer board material [4]. Therefore, they might be integrated in cloth in a minimally intrusive way [2,5]. In particular, the microstrip patch antennas are good candidates for body-worn applications, as they mainly radiate perpendicularly to the planar structure and also their ground plane efficiently shields the body tissues [5,7]. Specific requirements for the design of wearable antennas are thus: planar structure; flexible conductive materials in the patch and ground plane; and flexible dielectric materials [3,5,8]. The characteristics of the materials are crucial for the behaviour of the antenna. For instance, the permittivity and the thickness of the dielectric substrate mainly determine the bandwidth and the efficiency performance of the planar antenna [4]. Also, the conductivity of the ground plane and of the patch is an important factor in the efficiency of the antenna and must be the highest possible.

Textile materials, being universally used and easily available, are possible materials to design wearable antennas for in- and on-Body Area Networks (BAN). The characterization of their electric and electromagnetic properties is essential for the design of the antenna [8]. Electrical properties of conductive textiles have been accurately characterized using the Transmission Line Method [9], Cavity Method [10] and MoM-segment Method [11], and their surface resistivity are often given by specialized producers. Therefore, specific conductive textiles, sometimes designated electrotiles, that are commercially available have been successfully used in antennas [5,12–16]. Ordinary textile fabrics have been used as dielectric substrates. However, little information is found on the electromagnetic properties of regular commercialized textiles. Therefore, this paper is focused on the analysis of textile materials, mainly dielectric fabrics, that have been used in antennas [2,17–22].

The following section presents an overview of the influence of some features of the textile materials, dielectrics and conductive ones, in the behaviour of the antennas. It also gives some guidelines for the choice of materials for the design of textile antennas. Later, Section 3 reviews the textile materials that have been used to develop different wearable antennas, focusing on the regular

fabrics used as dielectrics and listing their relative permittivity and loss tangent values. Furthermore, Section 4 presents an overview of guidelines for the construction of planar and wearable antennas and the techniques used to assemble the various materials. Finally, Section 5 presents the main conclusions of this work.

2. Important Features of Textile Materials in the Design of Wearable Antennas

Fabrics are planar fibrous materials which properties are mainly determined by the properties of the component fibres and the structure of the yarns and/or of the fabric. They are porous materials, in which the density of the fibres, air volume and size of the pores determine general behaviour, for instance, air permeability and thermal insulation. Accordingly, fabrics are flexible and compressible materials which thickness and density might change with low pressures. Moreover, the main orientation of the fibres and/or yarns introduces an intrinsic planar anisotropy of general properties. Plus, fibres are constantly exchanging water molecules with the surroundings, which affects their morphology and properties. All these features are somehow difficult to control in real applications of textiles, therefore it is important to know how they may influence the behaviour of the antenna in order to minimize any unwanted effects. Moreover, some characteristics of the textile materials known to influence the performance of the antenna and referred in the literature are reviewed in this section.

2.1. The Dielectric Constant (Relative Permittivity) of the Fabrics

The constitutive parameter of dielectrics is the permittivity, ϵ , that is a complex value parameter. It is usually expressed as a relative value ϵ_r : $\epsilon = \epsilon_0 \epsilon_r = \epsilon_0(\epsilon'_r - j\epsilon''_r)$, where ϵ_0 is the permittivity of vacuum, which is 8.854×10^{-12} F/m [17]. In general, the dielectric properties depend on the frequency, temperature, and surface roughness [17], and also on the moisture content, purity and homogeneity of the material [18]. The real part of the relative permittivity, ϵ'_r , is called the dielectric constant, but one must note that it is not constant in frequency. The ratio of the imaginary part to real part is called the loss tangent, $\tan\delta = \epsilon''_r / \epsilon'_r$.

Some researchers have studied and reviewed the dielectric properties of textiles [19–21]. As textile materials are anisotropic materials, their characterization also depends on the electric field orientation. This anisotropy is fully described with a permittivity tensor, although in most practical applications like the ones surveyed in this paper, a specific component of this tensor is enough to characterize the behaviour of the textile material for a specific application. Thus, the relative permittivity describes the behaviour of the material tested under a specific electric field orientation and frequency.

The dielectric behaviour of textile materials depends on the properties of the constituent fibres and polymers [19], and on the fibre packing density in the fibrous material [18,20]. However, textile fabrics are rough, porous and heterogeneous, having air in between the fibres, making their characterization difficult [23]. In addition, the ability of the fibres to absorb moisture must also be considered in the characterization of the dielectric behaviour of textiles, as will be explained further in Section 2.4. Thus, the accurate measurement of dielectric characteristics of textiles is challenging and different experimental techniques have been used, such as the Cavity Perturbation Method [4,10], MoM-segment method [9], Resonance Method [21], Free Space Method [24] and Transmission Line

Method [25–27]. Among these techniques, the simplest ones and thus very promising ones are the techniques based on the measurement of the behaviour of transmission lines [25–27].

In general, textiles present a very low dielectric constant as they are very porous materials and the presence of air approaches the relative permittivity to one. As an example, Table 1 shows the dielectric properties of normal textile fabrics, possible dielectric substrates, that were obtained with a waveguide cavity method, under 2.6 GHz [10].

Table 1. Dielectric Properties of normal fabrics tested in [10].

Nonconductive Fabric	ϵ'_r	$\tan\delta$
Cordura [®]	1.90	0.0098
Cotton	1.60	0.0400
100% Polyester	1.90	0.0045
Quartzel [®] Fabric	1.95	0.0004
Cordura/Lycra [®]	1.50	0.0093

The low dielectric constant reduces the surface wave losses which are tied to guided wave propagation within the substrates. Therefore, lowering the dielectric constant increases spatial waves and hence increases the impedance bandwidth of the antenna, allowing the development of antennas with acceptable efficiency and high gain [3,28–30]. Again, one should note that the relative permittivity value changes with the moisture content of the substrate affecting the bandwidth of the antenna [2,29].

2.2. Thickness of the Dielectric Fabrics

The bandwidth and efficiency performance of a planar microstrip antenna is mainly determined by the substrate dielectric constant and its thickness [4,31]. As referred before, the changes in permittivity may change the antenna bandwidth, but lowering the substrate permittivity can also increase the resonance frequency of the antenna.

As textile materials present a quite narrow range of permittivity values, it is therefore their thickness, which values may present much larger variations, that will mainly determine the bandwidth as well as the input impedance of the antenna and so its resonance frequency [28]. The thickness of the dielectric material is thus crucial in the design of antennas [2,31]. For a fixed relative permittivity, the substrate thickness may be chosen to maximize the bandwidth of the planar antenna. However, this value may not optimize the antenna efficiency. Therefore, the choice of the thickness of the dielectric material is a compromise between efficiency and bandwidth of the antenna [4,31].

The influence of the thickness on the bandwidth (BW) of the antenna may be explained by Equation (1), where Q is the antenna quality factor:

$$BW \sim 1/Q \quad (1)$$

The Q factor is influenced by the space wave (Q_{rad}) losses, the conduction ohmic (Q_c) losses, the surface waves (Q_{sw}) and dielectric (Q_d) losses as shown in Equation (2) [32]:

$$\frac{1}{Q_t} = \frac{1}{Q_{rad}} + \frac{1}{Q_c} + \frac{1}{Q_d} + \frac{1}{Q_{sw}} \quad (2)$$

For thin substrates ($h \ll \lambda_0$) the quality factor associated with radiation (Q_{rad}) is usually the dominant factor and is inversely proportional to the height of the substrate [32]. Therefore, increasing the height of the substrate lowers the Q factor (Q_t). As the Q-factor decreases with an increased aperture between the patch and the ground planes of the antenna, a thicker substrate allows a larger antenna bandwidth [5].

Moreover, the thickness of the substrate also influences the geometric sizing of the antenna. This means that a thick substrate with low relative permittivity (value between 1 and 2) results in a large patch and a thin substrate with the same dielectric constant results in a smaller patch [5].

There are commercially available fabrics with a very diverse range of thickness values. Plus, nominal thickness values are given in any technical data sheet, allowing a careful choice of the material based on the required thickness. Moreover, accurate values of the thickness of fabrics under specified pressure are easily obtained by simple standard methods, such as ISO 5084:1996 and ASTM D374-99(2004) or with a Digimatic Indicator [31]. Therefore, the thickness of the fabrics is a feature that may guide the search for suitable textile dielectrics.

2.3. The Electrical Surface Resistivity of the Conductive Fabrics

Fabrics are planar materials and therefore their electrical behaviour may be quantified by the surface resistance and characterized by the surface resistivity. The surface resistance, which unit is (Ω), is the ratio of a DC voltage to the current flowing between electrodes of specific configuration that are in contact with the same face of the material under test [33]. The surface resistivity is the ratio of the DC voltage drop per unit length to the surface current per unit width. Surface resistivity is thus a property of the material, not depending on the configuration of the electrodes used for the measurement. It is usually expressed in Ohm/square (Ω/sq ; Ω/\square) [34].

Despite the existence of several standard methods, *i.e.*,

- AATCC Test Method 76-2011: Electrical Surface Resistivity of Fabrics
- ASTM D4496: 2004 Standard Test Method for D C Resistance or Conductance of Moderately Conductive Materials
- ISO 10965:2011: Textile floor coverings—Determination of electrical resistance
- ISO 21178:2005: Light conveyor belts—Determination of electrical resistance

to measure the surface resistance and resistivity of textile fabrics, they are dedicated to moderately conductive materials and are still aim of analysis [35]. An accurate characterization of highly conductive fabrics demands other techniques, such as for instance the ones based on transmission lines and waveguide cavities [9–11,36].

For the antenna design, the relevant parameter is the conductivity of the fabric, σ , which unit is Siemens per meter (S/m). It is related to the surface resistivity, ρ_s , by Equation (3), where t is the thickness of the fabric:

$$\sigma = 1/(\rho_s \cdot t) \quad (3)$$

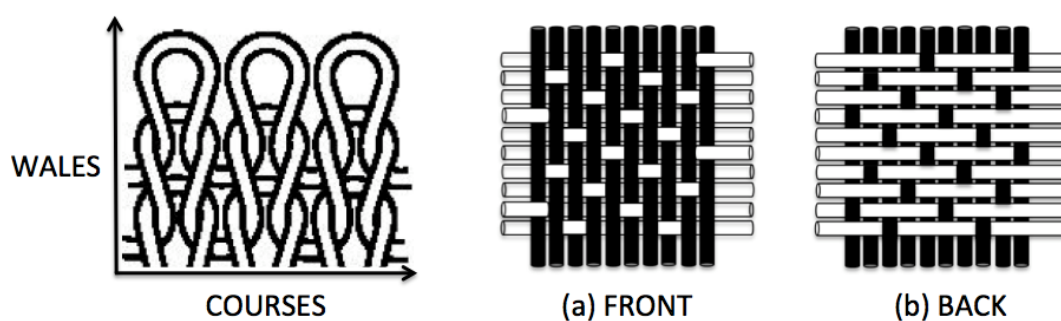
Besides the dielectric constant of the substrate, the choice of the conductive fabric for the patch and the ground planes is also very important to assure a good performance of the antenna. In general these fabrics must have a very low electrical surface resistance in order to minimize the electric losses and

thus increase the antenna efficiency. Despite the fact that the surface resistance value should be constant over the area of the antenna [2], the fabric may present some heterogeneities, such as for instance some discontinuities in the electric current. If these discontinuities are parallel to the surface current they will not interfere with the electromagnetic fields [37], but if discontinuities impede the flow of the electrical current, the fabric resistance will increase [2]. The structure of the fabric should thus be considered, seeking to determine the density, the continuity and the alignment of the conductive components, which may be fibres, filaments or surface covers. In [2] the studied fabrics having conductive fibres performed better than the coated fabrics, because of discontinuities that increased the surface resistance of the coated fabrics. In [10] higher conductive thread density in the woven fabric results in higher effective conductivity.

Wovens and knits with electric surface resistivity below $1 \Omega/\square$ are commercially available (e.g., Less EMF Inc. at <http://www.lessemf.com> or Shieldex Trading at <http://www.shielextrading.net>) and have been successfully used [2,24,26]. However, knits may present higher anisotropy than wovens, showing different electric surface resistance along the longitudinal and the transversal directions and this anisotropy may increase with the knit deformation. Indeed, in fabrics composed of conductive threads, conductive paths exist in all directions through the conductive threads and/or inter-contact points across threads [10]. According to Locher *et al.* [2], for the studied knit material that is composed of silver plated polyamide fibres, deformations under 8% of elongation along the direction of the wales slightly change the surface resistivity. However, when elongating the knitted fabric along the direction of the courses the electric surface resistivity results stable up to 3% of elongation but then increases and at 8% of elongation it reaches triple the initial value.

The influence of the structure of the fabrics on the surface resistivity may be better understood looking at Figure 1 that shows schemes of regular patterns of fabrics: the jersey knit and the satin 5 weave patterns. If the conductive threads in the weave pattern are along the intended direction for current flow, woven patterns are much more efficient in terms of electrical conduction than knit patterns, because the conductive paths in woven are better aligned with the current direction, which minimizes the conductive losses, as concluded in [10].

Figure 1. Schemes of: (left) Jersey knit; (middle and right) satin 5 woven; (a) front and (b) back.



Moreover, fabrics present differences between their faces that should be considered when positioning the conductive fabric in a planar assemblage. For instance, in Figure 1 the right and back sides of the satin 5 woven are clearly different. In [10], a satin 5 woven composed of conductive yarns (represented

by white rods in Figure 1) and non-conductive yarns (represented by black rods) was tested in a microstrip resonator measurement to study the effect of the differences among faces on the electrical properties of planar structures, as wearable antennas. It was proved that keeping the conductive face against the dielectric substrate is preferred for lowering the electrical losses.

2.4. The Moisture Content of the Fabrics

Textiles always establish a dynamic equilibrium with the temperature and humidity of the air surroundings they are in contact with, as the fibres are constantly exchanging water molecules with the air. However, the amount of water that a material takes until reaching this equilibrium depends on the type of material. The extent to which a material is sensitive to moisture is described by its regain, which is defined, by the ratio of the mass of absorbed water in specimen to the mass of dry specimen, expressed as a percentage, [20]. In [20], page 169 shows the relation between regain and relative humidity of the air (RH), for various textile fibres, compiling studies made by several authors. Indeed, for the same RH conditions, there are textile fibres with largely different moisture contents. For instance, at 65% RH, wool fibre might present a regain of 14.5%, cotton might present a regain of 7.5% and polyester fibre might present a regain of 0.2% [20].

In general, the moisture absorption changes the properties of the fabrics. Because of this, textile metrology is performed always in a conditioned environment (20 °C and 65% RH). Also, for commercial transactions there are national legislations setting nominal values of moisture content that are values close to the regain obtained at 65% relative humidity.

Water has a dielectric constant of $\epsilon'_r = 78$ at 2.45 GHz and 25 °C [31]. Although this value depends on the salinity, temperature and frequency [38], water has a much higher and more stable dielectric constant than textile fabrics, whose dielectric constant is generally in the range $\epsilon'_r = 1 - 2$ because of their high porosity, as previously presented. Therefore, when water is absorbed by the textile fibres or is trapped into the fabric structure, it changes the electromagnetic properties of the fabric, increasing its dielectric constant and loss [2,5,19,20,31]. Charts presenting the relationship between the RH of the air or the moisture content of various fibres and their dielectric properties can be found in [20]. Additionally, several authors have been correlating the electromagnetic properties of fabrics to their absorption properties [31,38].

Likewise, the absorbed water by or trapped into the textile components of the antenna dramatically changes the behaviour of the antenna. The higher permittivity of the water drives the performance of the antenna, reducing its resonance frequency [2,6] and bandwidth [9,29,31].

Beyond these effects, when textile fibres absorb water they swell transversely and axially, causing tightening of the fabrics [20,39]. This tightness affects the dimensional stability of the fabrics and therefore affects the dimensional stability of the antenna, influencing its behaviour [2]. The swelling of the fibres also contributes to the change of the dielectric properties, as swollen fibres decrease the porosity of the fabric [39]. Indeed, as seen above, the low relative permittivity values of the fabrics are mainly determined by the presence of air in them. In [20] (page 227), experimental results from several authors are compiled, showing that values of swelling in water vary the same way as the values of the regain of the fibres. For instance, when cotton is in water, its cross section area might swell 40%, whilst polyamide only swells 3.2% [20].

Moreover, water absorption by the fibres is an exothermic reaction and the released heat of wetting is the greatest for the highly absorbing fibres. This affects the temperature and thus the electromagnetic properties of the material. More details and data quantifying these effects can be found in [20].

Therefore, climatic changes altering the relative humidity of the air or environmental water, ice and snow conditions will influence the textile antenna performance [31,40]. In the same way, when the antenna is used close to the skin, the hydrophobicity and the regain of the fabric are very important features [28,41] as the fabric will absorb moisture from the skin.

In general, the characteristics of antennas based on textile materials with small moisture absorption values (regain less than 3%) are more stable [31]. Therefore, materials with low regain are preferable for use as substrates and the same conclusion applies to the textile conductive components of the antenna.

2.5. Mechanical Deformations of the Dielectric and Conductive Fabrics

A curvature on a human body consists of a superposition of bends in arbitrary directions. Because of their excellent flexibility and elasticity textile materials adapt well to these surfaces. However, when the textile fabric adapts to the surface topology it bends and deforms, causing changes to its electromagnetic properties and thus influencing the antenna performance [2,29,42]. Indeed, the bending and the elongation of the dielectric fabric influences its permittivity and its thickness, which affects the resonance frequency of the antenna and especially the bandwidth, as previously explained [28].

Moreover, the variation of the geometric dimensions of the textile components of the antenna due to their elongation and/or compression diminishes the geometric precision of the shape of the antenna affecting its behaviour, which may change its resonance frequency [28].

In addition, from the point of view of manufacturing antennas, the elasticity of the fabrics is an inconvenience as it makes difficult the precise definition and cut of the shape of the components and also makes difficult the superposition of the several materials without folds. Wovens and nonwovens, being more stable fabrics than knits, allow higher geometrical accuracies of the frame of the antenna. In general, the accuracy depends on the thickness of the component yarns or fibres. For instance, conductive woven may allow an accuracy of about ± 0.15 mm [2]. For these reasons knits are not stable enough for the dielectric of an antenna. However, as further presented in Section 4, they might be suitably stabilized if assembled with a more rigid textile material, such as a fabric with high tensile strength.

3. Textile Materials Used in Wearable Antennas

Wearable antennas are a recent research subject, although one of the first proposals on the subject appeared in 2001 [3], when Salonen *et al.* [22], presented a Planar Inverted F Antenna (PIFA) for dual-band operation, built on a flexible unspecified substrate. It was intended to be placed in the sleeve of clothing and operate at GSM (900 MHz) and Bluetooth (2.4 GHz) frequency, although the lower band was not achieved, the antenna still showed good performance, even for human-body presence, around the 2.4 GHz band. Later in 2003, they presented an antenna built on a textile substrate intended for WLAN applications [43], where results are claimed to be acceptable.

Furthermore, in 2004 Salonen *et al.* [28] proposed a GPS antenna with circular polarization, in which they have experimented with five different synthetic fabric materials as dielectric substrates.

The conductive parts were made of copper tape. The dielectric synthetic materials used were: (1) Vellux[®], which is a 5 mm thick fabric covered on both surfaces with thin layers of plastic foam; (2) synthetic felt, which is a 4 mm thick nonwoven in which fibres are looser on the surface than in the centre; (3) Delinova 200[®], which is a strong fabric made of polyamide Cordura[®] fibres laminated with Gore-Tex membrane, weighing about 370 g/m² and having a thickness of 0.5 mm; (4) fleece, which is a very soft polyester fabric with 4 mm thickness, commonly used in sportswear; (5) upholstery fabric, which is composed of three fabric layers bound together resulting in a thin (1.1 mm) fabric of polyester and acrylic that has firmness. The relative permittivity, ϵ'_r , of the five fabrics was measured by a cavity perturbation method, at 1.575 GHz, and the values ranged between 1.1 and 1.7. Among the studied fabrics, the one made of high tenacity polyamide fibres (Cordura[®]) was pointed out as the more interesting fabric for the development of a flexible antenna, because of its constant thickness and its high resistance. These properties allow more stable geometric dimensions of the antenna.

More recent demonstrations on wearable antennas for Personal Area Networks (PANs) to operate in the 2.45 GHz Industrial, Scientific and Medical (ISM) band and for GPS applications are presented in [5,12]. In these examples, antennas for wearable protective clothing intended for professional use under rough conditions are presented and their behaviour in various practical scenarios is discussed. High performance aramid fabric that can withstand high temperatures is used as substrate while conductive textiles, like *Shieldit*[®] and *FlecTron*[®], are used for the antenna patch and ground plane. These antennas have shown acceptable performance, even in a real environment with human-body presence and when subjected to bending and deformations.

Locher *et al.* [2] have built four purely textile wearable patch antennas for Bluetooth applications. They have used three electrical conductive fabrics: (1) a nickel-plated woven fabric (with plating thickness about 250 nm applied on the fabric surface); (2) a silver-plated knitted fabric; (3) a silver-copper-nickel-plated woven fabric. Fabric (3) is the one preferred for building textile antennas with geometric precision, as it is woven and not knitted and its electric surface resistance was more homogeneous than the one of fabric (1). For the dielectric substrate, they used two types of fabrics: (1) woollen felt of 1,050 g/m² with a thickness of 3.5 mm and (2) polyamide spacer fabric, of 530 g/m², with a thickness of 6 mm. The felt was dimensionally more stable and harder to bend, whereas the spacer fabric was lighter and more elastic due to its knitting-based structure. The dielectric properties were measured by a transmission line method, at a frequency of 2.4 GHz, obtaining as results for the felt: permittivity $\epsilon'_r = 1.45$ and loss tangent $\tan\delta = 0.02$, and for the spacer fabric: permittivity $\epsilon'_r = 1.14$ and the loss tangent was negligible. The four different antennas produced have shown good performance and could satisfy the Bluetooth specifications, even when subjected to bending effects. However the antennas lose their circular polarization when subject to bending.

The same year, Tronquo *et al.* [13] presented rectangular-ring textile antennas for body area networks (BAN) that are circularly polarized, covering a bandwidth of more than 190 MHz. For the conductive antenna patch and ground plane they used the conductive fabric named *Flectron*[®], that is a thin copper plated fabric with low surface resistivity, lesser than 0.1 Ω/\square . For the dielectric substrate they used a fleece fabric of 2.56 mm thickness. Its dielectric properties were measured testing antennas and they obtained a relative permittivity of $\epsilon'_r = 1.25$.

In 2007, Zhu and Langley [18] developed a dual-band coplanar patch antenna integrating electromagnetic bandgap material (EGB), to operate at the 2.45 and 5.8 GHz wireless bands. The

conductive parts were made of *Zelt*[®] fabric while the dielectric substrate was a thin felt, with 1,1 mm thickness, and with relative permittivity $\epsilon'_r = 1.30$ and $\tan\delta = 0.02$.

Matthews and Pettitt presented in [44] three types of antennas which are integrated into clothing, a broadband wire dipole, a bowtie and a spiral antenna, operating in frequencies from 100 MHz to 1 GHz. They have tested different materials (textiles and others), different frames and manufacturing techniques. Among the tested conductive materials there are conductive ribbon, conductive paint and ink, conductive nylon fabric (that is also adhesive on the back face), phosphor bronze mesh fabric (also adhesive on the back face), conductive thread, liquid crystal polymer (LCP) and copper coated fabric. The phosphor bronze mesh, LCP and copper coated fabric have the advantage that the antennas can be directly soldered to. In some antennas, a conducting epoxy was used to bond materials, but this shows some lack of robustness. In terms of radio frequency (RF) performance of the designed antennas, the spiral antenna, in which the spiral is broidered with conductive thread, performed worse than any other antenna and was clearly loss. Overall, based on RF performance, the most attractive materials to design wearable antennas were the textile fabrics: the conductive nylon and the copper coated fabrics.

In [16] the stability and efficiency of wearable and washable antennas are discussed for textile antennas in which the conductive parts were screen-printed with conductive ink. These antennas have shown acceptable performance. The combination of screen-printing with a breathable thermoplastic polyurethane (TPU) coating assured the performance was maintained even after several wash cycles. An embroidered technique was used in [45,46] to sew conductive fibres into polymer and fabric substrates, and it was proved that by increasing the density of the embroidering stitching, the conductivity of the conductive section is increased and also the accuracy of fabricated prototypes, which allowed better conformance with the simulations. Dipole, spiral and microstrip patch antennas were fabricated with this technique and presented very good RF performance when compared to the corresponding rigid copper structures. Moreover, these antennas when made on flexible polymer substrates conform well to curved surfaces and thus maintain their performance. Table 2 summarizes the main characteristics of the textile materials that have been used to develop wearable antennas, focusing mainly in the dielectric materials.

The performance of the textile antennas presented earlier can be improved with integrated solutions, for instance, if diversity techniques such as Multiple-Input Multiple Output (MIMO) are considered [47], or, as shown in [48], with the introduction of a low-noise amplifier (LNA) in a wearable garment which was used to achieve an active integrated antenna, increasing the sensitivity and the gain of the overall system.

Declercq *et al.* [13] showed another integrated solution consisting of an aperture-coupled antenna on a textile and foam substrate, with a flexible solar cell, for tracking and monitoring solutions. Instead of integrating a LNA to increase the wearable antenna performance, Zhu and Langley [11,12] developed a dual-band coplanar patch antenna, to operate in the 2.45 and 5.8 GHz wireless bands, in which they integrated an electromagnetic band gap (EBG) to reduce body-presence effects and increase antenna gain. As shown in Table 2, the conductive parts were made of *Zelt*[®] fabric while the dielectric substrate was a thin felt with relative permittivity $\epsilon'_r = 1.30$ and $\tan\delta = 0.02$. They proved that the introduction of the 3×3 array EBG with the coplanar patch could reduce the radiation towards the body by 10 dB, while increasing the antenna gain in 3 dB.

Table 2. Comparison of the textile materials used to design wearable antennas.

Reference	Application	Dielectric material				Conductive material	Performance
		Material	h (mm)	ϵ_r	$\tan \delta$		
[22]	GSM (900 MHz) and Bluetooth (2.4 GHz)	Unspecified material	0.236	3.29	0.0004	-	Acceptable
[43]	WLAN (2.4 GHz)	Fleece fabric	3	1.04	-	Knitted copper fabric	Acceptable
[28]	GPS (1.5 GHz)	<i>Cordura</i> [®]	0.5	Between 1.1 and 1.7	-	Copper tape	Good
[5,12]	ISM (2.4 GHz) and GPS (1.5 GHz)	Fleece fabric	2.56	1.25	-	<i>Flectron</i>	Acceptable to Good
[13]	ISM (900 MHz)	Polyurethane protective Foam	11	1.16	0.01	<i>Flectron</i>	Acceptable
[14,15]	WLAN (2.4 GHz and 5.8 GHz)	Felt	1.1	1.30	0.02	<i>Zelt</i>	Acceptable
[16]	ISM (2.4 GHz)	Cotton/Polyester	2.808	1.6	0.02	<i>Flectron</i> /Conductive ink	Acceptable
[6,46]	Not specific (2–2.4 GHz)	Polydimethylsiloxane (PDMS)	-	3.0–13	0.02	Embroidered conductive fibres	Good
[2]	Bluetooth (2.4 GHz)	Polyamide spacer fabric	6	1.14	Negligible	Silver-copper-nickel plated woven fabric	Good
[2]	Bluetooth (2.4 GHz)	Woollen felt	3.5	1.45	0.02	Silver-copper-nickel plated woven fabric	Good

4. Construction of Wearable Antennas

After choosing the textile materials to design an antenna, their assemblage in the antenna is also crucial and specific, as they are very deformable materials. Thus, the conformation of the conductive patch with the dielectric substrate is critical [2]. Many authors have been improving the manufacturing processes [2,5,24,27] to construct textile antennas and some guidelines can be summarized as follows:

(1) The geometrical dimensions of the patch should remain stable while connecting to the dielectric substrate as the mechanical stabilization of both materials is essential to preserve the desired antenna characteristics [2,31]. In the microstrip patch antennas developed by Hertleer *et al.* [31] an alteration of no more than 0.5 mm on the length or the width of the patch influenced the performance of the antenna by causing a slight shift of the antenna characteristics. For this reason, woven fabrics, being more stable, are preferred to make the patches. However, the antenna geometrical stability can be achieved if at least one component is less deformable. For example, bonding using an adhesive sheet with a deformable patch, such as a conductive knit, with a less deformable substrate, such a woven dielectric, results in a stable frame [2,28].

(2) The techniques used to connect the various layers must not affect the electrical properties of the patch, such as its surface resistivity, nor the properties of the substrate. Connections using adhesive sheets or conductive fabrics with a thermal adhesive face have shown good results [2,5,29,31]. Indeed, the adhesive remains at the interface of the materials and therefore the surface resistance of the patch and the relative permittivity of the substrate are not significantly changed. However, in [29] the authors

show that the adhesive layer introduces extra losses in the substrate. This process of attachment of the superposed layers is very simple to perform by a simple ironing operation. However, attention should be made to the ironing process, in special if the patch is made of a fabric with metallic components. Indeed, the oxidation of the metallic component, due to the hot moistening of the fabric, may increase the surface resistance of the fabric and so decrease the efficiency of the textile antenna [27].

Connection with seams is an alternative technique [7,31] but it presents some difficulties. Firstly, the seam must be plane, without wrinkling, what might be difficult to achieve with deformable materials. Secondly, the stitch passes through all materials: the patch, then the substrate and further the ground plane of the antenna, which may cause electrical shorts between them. In Locher *et al.* [2] report that the sewing needle has pulled conductive fibres from the patch through the substrate, shorting the patch with the ground plane.

Another technique is connecting with liquid adhesives [31]. However, it is difficult to apply a thin layer of glue. This difficulty introduces heterogeneity and in the zones where there are accumulations the glue may play the role of insulator between the conductive yarns of the patch. Furthermore, these adhesives are usually stiff and brittle, and so they cannot be applied in an area-wide manner on textiles as they will interfere in their flexibility [2]. In order to obtain a uniform thickness of the attachment of the several layers, Tronquo *et al.* [29,31] perform an additional stitch, in addition to the glue.

In [5] a smooth fabric was added to both faces of the substrate to optimise the attachment of the conductive components.

(3) The positioning of the textile components must consider the differences between right and back faces, in terms of roughness and of density of conductive elements [7,10]. In [10], a satin 5 woven was tested in a microstrip resonator, placing it in two positions: (1) with the right face against the dielectric substrate and (2) with the back face, the conductive one, against the dielectric substrate. It was observed that when the conductive face is placed on the top of the substrate and so underneath the nonconductive yarns of the nonconductive face, most of the electrical field is contained in the substrate. Thus, the dielectric loss in the nonconductive yarns is minimized.

(4) The core of the antenna may be obtained by stacking low-loss fabrics [7], adjusting this way the desired thickness of the substrate. However this introduces heterogeneities in the substrate due to the extra layers of air between the fabrics, influencing its dielectric properties.

(5) Finally, the connections at the antenna terminals may also be critical as in wearable and flexible antennas these connections have to be mechanically robust. In general, textile fabrics cannot be directly soldered to (an exception is *Flectron*[®] that already showed good resistance to soldering [5]). Therefore conductive epoxy has been used, but some concerns remain as this connection is not very resistant [44].

5. Conclusions

The developed wearable antennas are mainly planar ones, specifically microstrip patch antennas, because they mainly radiate perpendicularly to the planar structure and also their ground plane efficiently shields the human body. The bandwidth and efficiency performance of a planar microstrip antenna is mainly determined by the substrate dielectric constant and its thickness.

In general, textiles present a very low dielectric constant, between 1 and 2, as they are very porous materials and the presence of air approaches the relative permittivity to one. The low dielectric constant reduces the surface wave losses that are tied to guided wave propagation within the substrates. Therefore, lowering the dielectric constant increases spatial waves and hence increases the impedance bandwidth of the antenna. However, lowering the substrate permittivity can also increase the resonance frequency of the antenna, allowing the development of antennas with acceptable efficiency and high gain.

In addition, the ability of the fibres to absorb moisture must also be considered in the characterization of the dielectric behaviour of textiles. Water has a much higher and more stable dielectric constant than textile fabrics. Therefore, when water is absorbed by the textile fibres or is trapped in the fabric structure, it changes the electromagnetic properties of the fabric, increasing its dielectric constant and loss tangent. Likewise, the absorbed water by or trapped into the textile substrate reduces the resonance frequency and bandwidth of the antenna. In general, the characteristics of antennas based on textile materials with small moisture absorption (regain less than 3%) are more stable. Therefore, materials with such low regain values are preferable for use as substrates and as conductive components of the antenna.

The thickness of the dielectric material is also crucial in the design of antennas. For a fixed relative permittivity, the substrate thickness may be chosen to maximize the bandwidth of the planar antenna. However, this value may not optimize the antenna efficiency. Therefore, the choice of the thickness of the dielectric material is a compromise between efficiency and bandwidth of the antenna. Moreover, the thickness of the substrate also influences the geometric sizing of the antenna.

The conductive fabrics for the patch and the ground planes must have a very low electrical surface resistivity in order to minimize the electric losses and so increase the antenna efficiency. There are several conductive textile fabrics, and also yarns, available on the market that has been successfully used in planar antennas. Coated fabrics might perform worse than the fabrics having conductive fibres, because of discontinuities that may increase the surface resistivity. Wovens and nonwovens, being more stable fabrics than knits, allow higher geometrical accuracies of the frame of the antenna and thus may be preferred to make the patch. In general, the sizing accuracy of the patch made of woven fabric depends on the thickness of the component yarns.

After choosing the textile materials, their assemblage may also be critical, as the elongation and bending causes mechanical deformations that interfere with the antenna behaviour. The presence of at least one textile material presenting high tensile strength, high bending rigidity and stable geometry stabilizes the frame of the antenna. When connecting the various layers making up the antenna, the positioning of the textile fabrics must consider differences between right and back faces in terms of roughness and of density of conductive elements, in order to minimize losses.

Finally, despite the fact the performance of the textile antennas can be improved with integrated solutions and despite the major progresses already achieved in the development of wearable antennas, further study and better characterization of ordinary and conductive textile materials may still offer relevant improvements to their design and to the optimization of their behaviour.

Acknowledgments

The authors acknowledge the Portuguese FCT/MCTES for financing the project PTDC/EEA-TEL/122681/2010-PROENERGY-WSN-Prototypes for Efficient Energy Self-Sustainable Wireless Sensor Networks and the European Union (FP7-PEOPLE-2009-IAPP) for financing the project No. 251373 INSYSM (Intelligent Systems for Structures Strengthening and Monitoring).

References

1. Bonfiglio, A.; De Rossi, D. *Wearable Monitoring Systems*, 1st ed.; Springer: New York, NY, USA, 2011; p. 100.
2. Locher, I.; Klemm, M.; Kirstein, T.; Tröster, G. Design and Characterization of Purely Textile Patch Antennas. *IEEE Trans. Adv. Pack.* **2006**, *29*, 777–788.
3. Gupta, B.; Sankaralingam, S.; Dhar, S. Development of Wearable and Implantable Antennas in the Last Decade: A Review. In *Proceedings of Mediterranean Microwave Symposium (MMS)*, Guzelyurt, Turkey, 25–27 August 2010, pp. 251–267.
4. Brebels, S.; Ryckaert, J.; Boris, C.; Donnay, S.; De Raedt, W.; Beyne, E.; Mertens, R.P. SOP Integration and Codesign of Antennas. *IEEE Trans. Adv. Pack.* **2004**, *27*, 341–351.
5. Hertleer, C.; Rogier, H.; Member, S.; Vallozzi, L.; Langenhove, L.V. A Textile Antenna for Off-Body Communication Integrated into Protective Clothing for Firefighters. *IEEE Trans. Adv. Pack.* **2009**, *57*, 919–925.
6. Zhang, L.; Wang, Z.; Psychoudakis, D.; Volakis, J.L. Flexible Textile Antennas for Body-Worn Communication. In *Proceedings of IEEE International Workshop on Antenna Technology*, Tucson, AZ, USA, 5–7 March 2012; pp. 205–208.
7. Kaija, T.; Lilja, J.; Salonen, P. Exposing Textile Antennas for Host Environment. In *Proceedings of 2010 Military Communications Conference*, San Jose, CA, USA, 31 October–3 November 2010; pp. 737–742.
8. Liu, N.; Lu, Y.; Qiu, S.; Li, P. Electromagnetic Properties of Electro-Textile for Wearable Antennas Applications. *Front. Electr. Electron. Eng. China* **2011**, *6*, 553–566.
9. Shaw, R.; Long, B.; Werner, D.; Gavrin, A. The Characterization of Conductive Textile Materials Intended for Radio Frequency Application. *IEEE Trans. Anten. Propag.* **2007**, *49*, 28–40.
10. Ouyang, Y.; Chappell, W.J. High Frequency Properties of Electrotiles for Wearable Antenna Applications. *IEEE trans. Anten. Propag.* **2008**, *56*, 381–389.
11. Cottet, D.; Gryzb, J.; Kistein, T.; Tröster, G. Electrical Characterization of Textile Transmission Lines. *IEEE Trans. Adv. Pack.* **2003**, *26*, 182–190.
12. Hertleer, C.; Rogier, H.; Vallozzi, L.; Declercq, F. A Textile Antennas Based on High-Performance Fabrics. In *Proceedings of 2nd European Conference on Antennas and Propagation*, Edinburgh, UK, 11–16 November 2007; pp. 1–5.
13. Declercq, F.; Georgiadis, A.; Rogier, H. Wearable Aperture-Coupled Shorted Solar Patch Antenna for Remote Tracking and Monitoring Applications. In *Proceedings of 5th European Conference on Antennas and Propagation*, Rome, Italy, 11–15 April 2011; pp. 2992–2996.

14. Zhu, S.; Langley, R. Dual-Band Wearable Antennas over EBG Substrate. *Electr. Lett.* **2007**, *43*, 141–142.
15. Zhu S.; Langley, R. Dual-Band Wearable Textile Antennas over EGB Substrate. *IEEE Trans. Anten. Propag.* **2009**, *57*, 926–935.
16. Scarpello, M.L.; Kazani, I.; Hertleer, C.; Rogier, H.; Ginste, D.V. Stability and Efficiency of Screen-Printed Wearable and Washable Antennas. *IEEE Anten. Wireless Propag. Lett.* **2012**, *11*, 838–841.
17. Baker-Jarvis, J.; Janezic, M.D.; DeGroot, D.C. High-Frequency Dielectric Measurements. *IEEE Trans. Instrum. Meas.* **2010**, *13*, 24–31.
18. Brandão, D.P.L. *Tecnologia da Electrecidade: Materiais Usados em Electrotecnia*; Fundação Calouste Gulbenkian: Lisbon, Portugal, 1983.
19. Bal, K.; Kothari, V.K. Measurement of Dielectric Properties of Textile Materials and Their Applications. *Indian J. Fibre Text.* **2009**, *34*, 191–199.
20. Morton, W.E.; Hearle, W.S. *Physical Properties of Textile Fibres*, 4th ed.; Woodhead Publishing: Cambridge, UK, 2008.
21. Sankaralingam, S.; Bhaskar, G. Determination of Dielectric Constant of Fabric Materials and Their Use as Substrates for Design and Development of Antennas for Wearable Applications. *IEEE Trans. Instrum. Meas.* **2010**, *59*, 3122–3130.
22. Salonen, P.; Keskilammi, M.; Rantanen, J.; Sydanheimo, L. A Novel Bluetooth Antenna on Flexible Substrate for Smart Clothing. In *Proceedings of Conference of IEEE International Conference on Systems, Man, and Cybernetics*, Tucson, AZ, USA, 7–10 October 2001; pp. 789–794.
23. Hasar, U.C. A New Microwave Method for Electrical Characterization of Low-Loss Materials. *IEEE Microw. Wirel. Compon. Lett.* **2009**, *19*, 801–803.
24. Harmer, S.W.; Rezgui, N.; Bowring, N.; Luklinska, Z.; Ren, G. Determination of the Complex Permittivity of Textiles and Leather in the 14–40 GHz, Millimetre-Wave Band Using a Free-Wave Transmittance Only Method. *IET Microw. Anten. Propag.* **2008**, *2*, 606–614.
25. Yue, H.; Virga, K.L.; Prince, J.L. Dielectric Constant and Loss Tangent Measurement Using a Stripline Fixture. *IEEE Trans. Compon. Pack. A* **1998**, *21*, 441–446.
26. Moretti, A. Estudo do Brim Santista Visando Aplicações em Antenas têxteis. M.S. Thesis, Universidade Estadual de Campinas, Campinas, Brazil, 2011.
27. Declercq, F.; Rogier, H.; Hertleer, C. Permittivity and Loss Tangent Characterization for Garment Antennas Based on a New Matrix-Pencil Two-Line Method. *IEEE Trans. Anten. Propag.* **2008**, *56*, 2548–2554.
28. Salonen, P.; Rahmat-samii, Y.; Schafth, M.; Kivikoski, M. Effect of Textile Materials on Wearable Antenna Performance: A Case Study of GPS Antenna. In *Proceedings of IEEE Antennas and Propagation Society International Symposium*, Monterey, CA, USA, 20–25 June 2004; pp. 459–462.
29. Tronquo, A.; Rogier, H.; Hertleer, C.; Langenhove, L.V. Applying Textile Materials for the Design of Antennas for Wireless Body Area Networks. In *Proceedings of EuCap2006: First European Conference on Antennas and Propagation*, Nice, France, 6–10 November 2006.
30. Hertleer, C.; Tronquo, A.; Rogier, H.; Langenhove, L.V. The Use of Textile Materials to Design Wearable Microstrip Patch Antennas. *Text. Res. J.* **2008**, *78*, 651–658.

31. Hertleer, C.; Laere, A.V.; Rogier, H.; Langenhove, L.V. Influence of Relative Humidity on Textile Antenna Performance. *Text. Res. J.* **2009**, *80*, 177–183.
32. Balanis, C.A. *Antenna Theory: Analysis and Design*, 3rd ed.; Wiley Interscience: Hoboken, NJ, USA, 2005.
33. Webster, H.G. *The Measurement, Instrumentation, and Sensors Handbook*; Springer: Berlin, Germany, 1999.
34. Maryniak, W.A.; Uehara, T.; Noras, M.A. *Surface Resistivity and Surface Resistance Measurements—Using a Concentric Ring Probe Technique. Application Note*; Trek, Inc.: Medina, NY, USA, 2003; pp. 1–4.
35. Kacprzyk, R. Measurements of the Volume and Surface Resistance of Textile Materials. *Fibres Text. East. Eur.* **2011**, *19*, 47–49.
36. Lilja, J.; Salonen, P.; Maagt, P.D.; Zell, N.K. Characterization of Conductive Textile Materials for Softwear Antenna Characterization of Conductive Textiles. *Antennas and Propagation Society International Symposium*, Charleston, SC, USA, 1–5 June 2009; doi:10.1109/APS.2009.5171853.
37. Salonen, P.; Rahmat-Samii, Y.; Hurme, H.; Kivikoski, M. Effect of Conductive Material on Wearable Antenna Performance: A Case Study of WLAN Antennas. In *Proceedings of IEEE Antennas and Propagation Society International Symposium*, Monterey, CA, USA, 20–25 June 2004; pp. 455–458.
38. Wang, X.; Xu, W.; Wenbin, L. Study on the Electrical Resistance of Textiles under Wet Conditions. *Text. Res. J.* **2009**, *79*, 753–760.
39. Canteri, A.; Avancini, F.; Neves, J.D.; Crespim, L. *Resistência a Penetração/Absorção de Água*; Universidade Estadual de Maringá: Goioerê, Brazil, 2000; pp. 1–40.
40. Kaija, T.; Lilja, J.; Salonen, P. Exposing Textile Antennas for Harsh Environment. In *Proceedings of 2010 Military Communications Conference*, San Jose, CA, USA, 31 October–3 November 2010; pp. 737–742.
41. Volakis, J.L.; Gullu, K. Novel Materials for RF Devices. In *Proceedings of IEEE Antennas and Propagation Society International Symposium*, Honolulu, HI, USA, 9–15 June 2007; pp. 1701–1704.
42. Bayram, Y.; Zhou, Y.; Shim, B.S.; Xu, S.; Zhu, J.; Kotov, N.A.; Volakis, J.L. E-Textile Conductors and Polymer Composites for Conformal Lightweight Antennas. *IEEE Trans. Anten. Propag.* **2010**, *58*, 2732–2736.
43. Salonen, P.; Hurme, H. A Novel Fabric WLAN Antenna for Wearable Applications. In *Proceedings of IEEE International Symposium of Antennas and Propagation Society*, 22–27 June 2003; pp. 100–103.
44. Matthews, J.C.G.; Pettitt, G. Development of Flexible, Wearable Antennas. In *Proceedings of EuCAP 2009: 3rd European Conference on Antennas and Propagation*, Berlin, Germany, 23–27 March 2009; pp. 273–277.
45. Wang, Z.; Zhang, L.; Bayram, Y.; Volakis, J.L. Embroidered Conductive Fibers on Polymer Composite for Conformal Antennas. *IEEE Trans. Anten. Propag.* **2012**, *60*, 4141–4147.
46. Volakis, J.L.; Zhang, L.; Wang, Z.; Bayram, Y. Embroidered Flexible RF Electronics. In *Proceedings of IEEE International Workshop on Antenna Technology*, Tucson, AZ, USA, 5–7 March 2012.

47. Vallozzi, L.; Torre, V.P.; Hertleer, C.; Rogier, H.; Moeneclaey, M.; Verhaevert, J. Wireless Communications for Firefighters Using Dual-Polarized Textile Antennas Integrated in Their Garment. *IEEE Trans. Anten. Propag.* **2010**, *58*, 1357–1368.
48. Dierck, A.; Declercq, F.; Rogier, H. Review of Active Textile Antenna Co-Design and Optimization Strategies. In *Proceedings of IEEE International Conference on RFID-Technologies and Applications*, Sitges, Spain, 15–16 September 2011; pp. 194–201.

© 2012 by the authors; licensee MDPI, Basel, Switzerland. This article is an open access article distributed under the terms and conditions of the Creative Commons Attribution license (<http://creativecommons.org/licenses/by/3.0/>).

[J2] - **R. Gonçalves**, A. Duarte, R. Magueta, N. B. Carvalho, P. Pinho, "RFID tags on paper substrate for bottle labelling", *Procedia Technology*, Vol. 17, No. 1, pp. 65 - 72, November, 2014

Conference on Electronics, Telecommunications and Computers – CETC 2013

RFID tags on paper substrate for bottle labelling

Ricardo Gonçalves^{a,b,*}, Alcídia Duarte^b, Roberto Magueta^b, Nuno B. Carvalho^{a,b}, Pedro Pinho^{a,c}^a*Instituto de Telecomunicações, Aveiro, Portugal*^b*Universidade de Aveiro, Aveiro, Portugal*^c*Instituto Superior de Engenharia de Lisboa, Lisboa, Portugal*

Abstract

In this paper we present a possible solution for an RFID tag antenna to be used in bottle labels. To develop this solution we used a transmission line method in order to estimate the permittivity and the dissipation factor of the paper to be used as substrate and also the glass that is present in the bottles. Two prototypes were developed and test were performed with an Alien ALR-8800 RFID reader, with which we demonstrated the proper functioning conditions of the proposed tag and how it surpasses commercially available RFID tags.

© 2014 The Authors. Published by Elsevier Ltd. This is an open access article under the CC BY-NC-ND license

(<http://creativecommons.org/licenses/by-nc-nd/3.0/>).

Peer-review under responsibility of ISEL – Instituto Superior de Engenharia de Lisboa, Lisbon, PORTUGAL.

Keywords: UHF antennas; paper substrate; bottle label RFID;

1. Introduction

Radio frequency identification (RFID) is currently a major enabling technology. It's being extensively used in many different kinds of applications and is one of the most promising bets for the development of the Internet of Things concept. Among its current applications, there's the identification of products in stores and warehouses, anti-theft systems, animal tracking, luggage handling and access management in buildings and public transports. [1]

There are different types of RFID systems that are classified based on the behaviour of the ID tag. Therefore, there are passive, semi-passive and active RFID systems, where the passive type is one particular case in which the reception tag does not possess any kind of power source (i.e. battery).

The purpose of this paper is to show the design of a RFID antenna for a passive tag operating at 866 MHz. The purpose of this antenna is to be placed on expensive spirit beverage bottles for tracking and labelling. Hence we've characterized the dielectrics on the scenario considered (paper and glass) and developed a few approaches for antennas that could be used for the considered purpose.

* Corresponding author. Tel.: +351 234 377 900.

E-mail address: rgoncalves@av.it.pt

2. Dielectric characterization

In order to develop the RFID antenna we had to characterize the dielectrics that would be used. To do so, we used a transmission line method by extracting the characteristic impedance of a microstrip line. We built microstrip lines in paper and glass substrates, as shown in Figure 1.

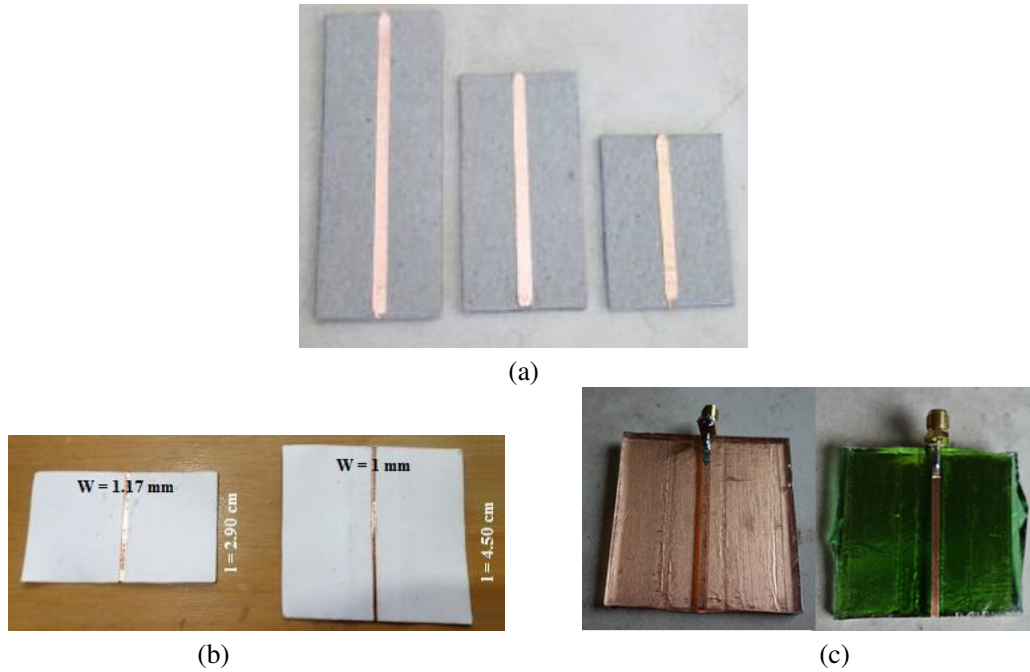


Fig. 1. Microstrip lines with (a) pressed paper, (b) 80g paper and (c) glass substrates.

According to [2] the input impedance of a transmission line at point l , being l the length of the line, is given by

$$Z_{in}(l) = Z_0 \frac{Z_L + Z_0 \tanh(\gamma l)}{Z_0 + Z_L \tanh(\gamma l)} \quad (1)$$

Since the propagation constant $\gamma = \alpha + j\beta$ and considering that the line is terminated by an open-circuit, we can reach

$$Z_{in} = \frac{Z_0}{\tanh(\alpha l + j\beta l)} \quad (2)$$

Since the phase constant, also known as *wave number*, can be defined as $\beta = \frac{2\pi}{\lambda}$, means that $\beta l = \pi \frac{f}{f_0}$, being f_0 the resonant frequency. So if we look at the input impedance at 1/4 of the resonant frequency of the line terminated by an open-circuit and using trigonometric rules we can separate the real and imaginary components to reach

$$Z_{in} = Z_0 \left\{ \frac{2 \tanh(\alpha l)}{1 + \tanh^2(\alpha l)} - j \frac{\tanh^2(\alpha l)}{1 + \tanh^2(\alpha l)} \right\} \quad (3)$$

Since in these cases the losses will be always positive, this would not be true for metamaterials only, and writing $Z_{in} = R \pm jX$, we can say

$$\tanh(\alpha l) = -\frac{X}{R} + \sqrt{\left(\frac{X}{R}\right)^2 + 1} \quad (4)$$

and, therefore, we can determine the characteristic impedance of the line as

$$Z_0 = R \frac{1 + \tanh^2(\alpha l)}{2 \tanh(\alpha l)} \quad (5)$$

Using a vector network analyzer (VNA) we found the first resonance of the microstrip lines and then determined the characteristic impedance of the line by measuring the input impedance at one fourth of that frequency and applying it in (5). Using the microstrip line impedance expression and according to [3] we could determine the substrate effective permittivity by

$$\epsilon_{ref} = 3600 \cdot \left[\frac{\ln \left(\frac{8h}{W} + \frac{W}{4h} \right)}{Z_0} \right]^2 \quad (6)$$

in cases for which the the width, W , of the line is smaller than the height, h , of the substrate, or otherwise, can be determined by

$$\epsilon_{ref} = \left[\frac{120\pi}{Z_0} \cdot \frac{1}{\frac{W}{h} + 1.393 + 0.667 \ln \left[\frac{W}{h} + 1.444 \right]} \right]^2 \quad (7)$$

which then led us to the substrate relative permittivity as

$$\epsilon_r = \frac{2\epsilon_{eff} + \frac{1}{\sqrt{1+12h/W}} - 1}{1 + \frac{1}{\sqrt{1+12h/W}}} \quad (8)$$

The loss tangent was determined based on the Nicolson-Ross-Wier (NRW) method [4,5]. The NRW method is used to determine to total losses in the printed transmission line as

$$\alpha = -\frac{\ln(|T|)}{l} \quad (9)$$

being l the line length and T the transmission coefficient define as

$$T = \frac{S_{11} + S_{21} - \Gamma}{1 - (S_{11} + S_{21})\Gamma} \quad (10)$$

being Γ the reflection coefficient of lossy lines, define as

$$\Gamma = \Lambda \pm \sqrt{\Lambda^2 - 1} \quad (11)$$

in which Λ is

$$\Lambda = \frac{1 - S_{21}^2 - S_{11}^2}{2S_{11}} \quad (12)$$

By knowing the conductivity one can reach the conductor losses and, according to [3], then use it to determine the loss tangent as

$$\tan \delta = \frac{\sqrt{\epsilon_{eff}}(\epsilon_r - 1)}{\pi\epsilon_r(\epsilon_{eff} - 1)} \frac{c}{f} \cdot (\alpha - \alpha_c) \quad (13)$$

The measured input impedance of the lines is depicted in Figure 2. The resonant frequencies, the input impedances measured and the characteristic impedance of the lines are shown in Table 1.

Table 1. Measured resonant frequency and impedances of the microstrip lines.

Dielectric	f_0 (GHz)	$Z_{in}@f_0$ (Ω)	Z_0 (Ω)
80g Paper	2.966	512.08	17.24
Pressed paper	3.380	823.24	72.90
Bottle glass	1.337	2306.0	71.83
Window glass	1.093	2452.0	88.29

The permittivity and loss tangent obtained for the different dielectrics is shown in Table 2. Although the pictures in Figure 1 show different lines in the same substrates, the values presented in the tables stand for the smallest lines since these are the ones with less losses. The other lines were used as control subjects.

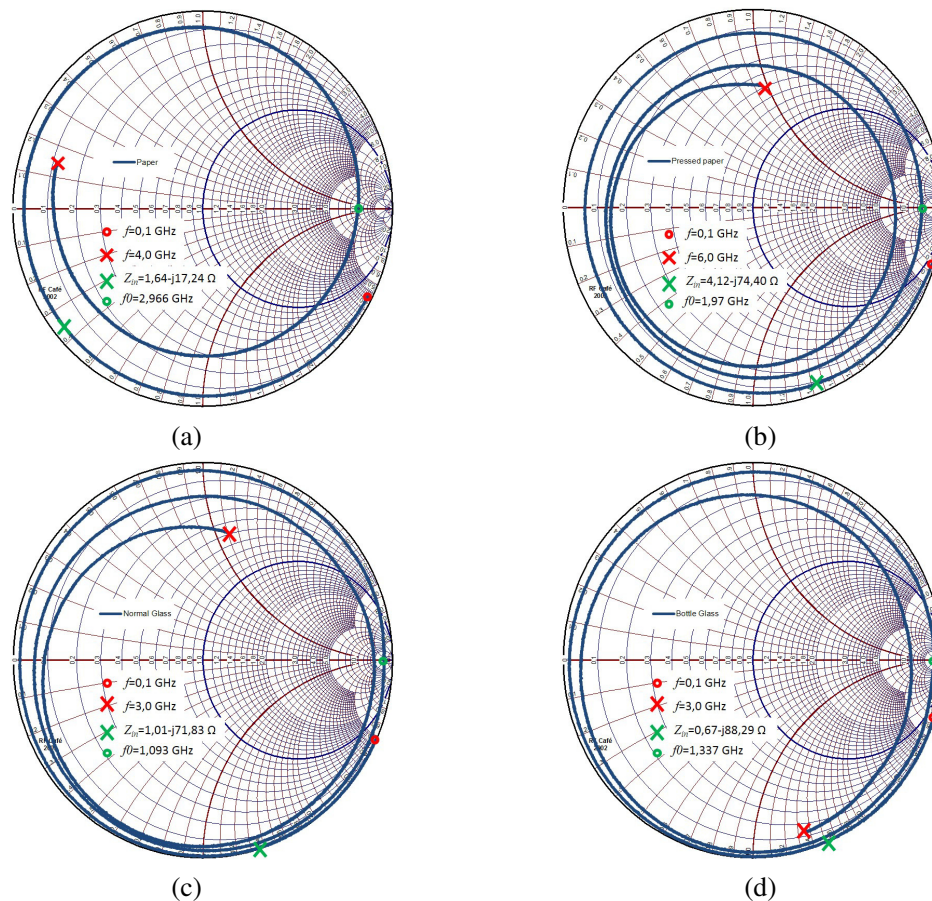


Fig. 2. Measured input impedance of the microstrip line in (a) 80g paper, (b) pressed paper, (c) normal glass and (d) bottle glass substrates.

Table 2. Determined permittivity and loss tangent for the different dielectric materials.

Dielectric	ϵ_r	$\tan \delta$
80g Paper	1.72	0.0182
Pressed paper	1.82	0.0703
Bottle glass	4.84	0.0302
Window glass	5.29	0.0223

3. RFID tag design

The conductive parts of the RFID tags were made using a copper strip that was cut and pasted into paper. The RFID chip used for the tag design is a NXP SL3ICS1002 with an input impedance of $16-j148\Omega$.

For simulation CST Microwave Studio was used [6]. It does not allow the definition of complex ports, therefore, a capacitor with a capacitance equivalent to the chip (1.242 pF) was placed in series with a 16Ω port in order to emulate the chip input impedance.

A first approach to the tag design in order to prove the correct characterization of the materials was based on a traditional design, by using a ring plus a meandered dipole as shown in Figure 3.

The ring creates an inductive effect that with the antenna arms matches with the chip's input capacitance. The arm length sets the resonant frequency. As the antenna is essentially a dipole so its radiation pattern will be omnidirectional, as is shown in Figure 4 (a).

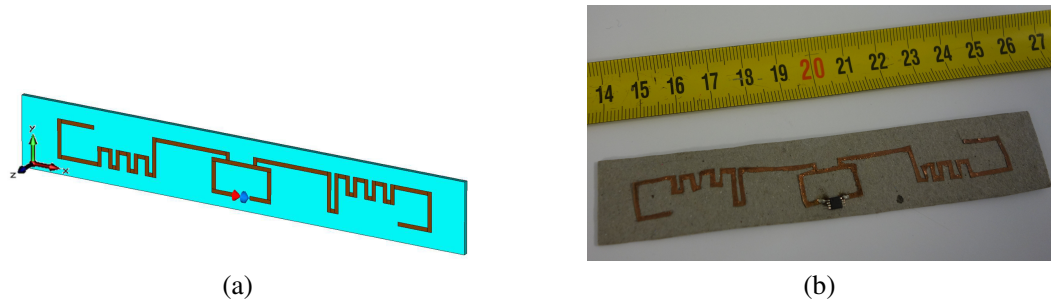


Fig. 3. First prototype of a RFID tag antenna on paper substrate: (a) simulation model (b) prototype.

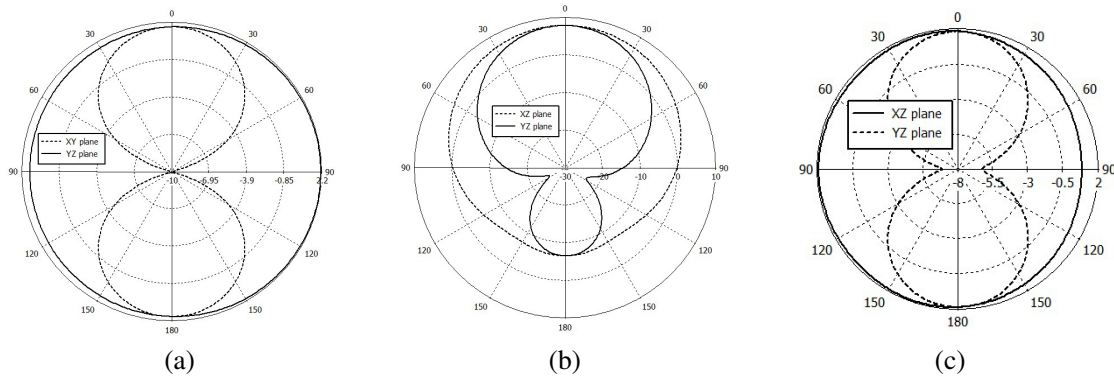


Fig. 4. Simulated radiation pattern of the (a) first (b) second and (c) third prototype of the RFID tag.

Due to the small radiation gain, as reported in Table 3, the reading distances of the tag were small, although satisfactory as it is shown in Figure 8. Therefore, a second tag was designed. In order to increase the gain of the antenna a reflective plane was introduced. The simulation model and prototype of the second tag is shown in Figure 5.

The introduction of the reflective plane imposed a complete change in the antenna geometry. Due to the small thickness of the substrate and the relatively low work frequencies the size of the antenna becomes quite large. Increasing the initial geometry indefinitely didn't lead to any possible solution. Therefore, we decided to remove the matching ring in the input and connect to a dipole with a impedance match step in each arm.

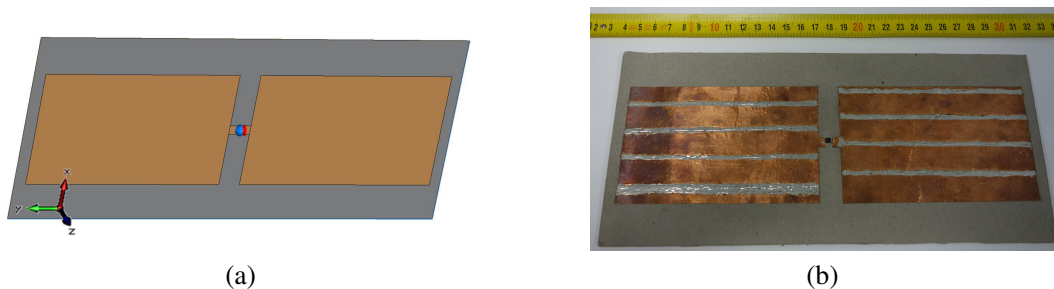


Fig. 5. Second prototype of a RFID tag antenna on paper substrate: (a) simulation model (b) prototype.

By using a reflective plane, the omnidirectional characteristic is lost and a directive pattern is achieved with a much higher directivity, as shown in Figure 4 (b). The drawback of the reflective plane is the increase of the antenna size and decrease in the antenna bandwidth as is proven in Figure 6.

Although the simulation results look promising the experimental results were not so good. Figure 8 shows the reading range measurements obtained for the different RFID tags, in which we can see that the prototype 2 presented the poorest results. This might be due to several reasons, but the main problem is related to the very small bandwidth associated to this antenna. Any slight deviation of the resonant frequency would completely mismatch the antenna

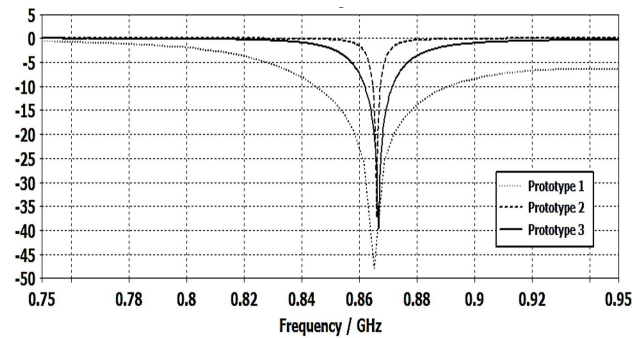


Fig. 6. Simulated return loss for the different RFID antenna prototypes.

and therefore severely reduce the radiation gain of the antenna, given the manufacturing process of the antenna, this is a very plausible cause for the poor results obtained.

After the first two trials a third prototype was built, this time in 80g paper substrate to be easily integrated into a bottle label. Given the mismatch problems observed in the second prototype, we rescued the meandered dipole design, but made some changes in order to reduce the overall size of the antenna and make it easier to build. The last prototype is shown in Figure 7, from which we can see that it is the smallest of the three presented prototypes.

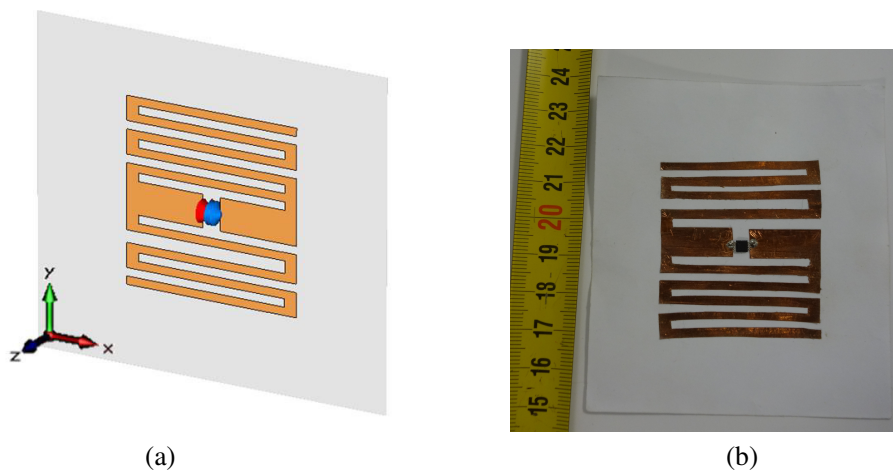


Fig. 7. Third prototype of a RFID tag antenna on paper substrate: (a) simulation model (b) prototype.

The return loss obtained for the different prototypes is shown in Figure 6. From the results, we can observe the bandwidth of the different prototypes. As expected, the second prototype as obtained the smallest bandwidth, while the first prototype obtained the highest. The third prototype stands in the middle. Although no reflective plane was used for this antenna, the size reduction is the main reason for this bandwidth reduction. However, due to the decrease in bandwidth, there was an improvement in the antenna efficiency, as shown in Table 3.

According to [7] there is a relation between the antenna bandwidth, which is bound to its quality factor and the efficiency of an antenna. Although the relation is not direct, the point is that an antenna cannot present a high efficiency while showcasing large bandwidths.

Table 3. Simulated efficiency and gain for the different antenna prototypes.

Antenna	Efficiency (%)	Gain (dB)
Prototype 1	52.2	-0.70
Prototype 2	99.3	7.74
Prototype 3	84.4	1.18

Since no reflective plane was used the radiation pattern of this last prototype is omnidirectional, as is the case of the first prototype. This is shown in Figure 4 (c).

4. RFID tag measurements

In order to assess the performance of the antennas these were tested with a commercial RFID reader, the Alien ALR8800 that is EPC Gen2 compatible. The measurement setup was in accordance to the proposed in [8]. The tags were placed upon a cardboard structure and aligned to the reader. The distance of communication was varied and the output power of the reader was varied to allow valid readings. The reading distances are depicted in Figure 8.

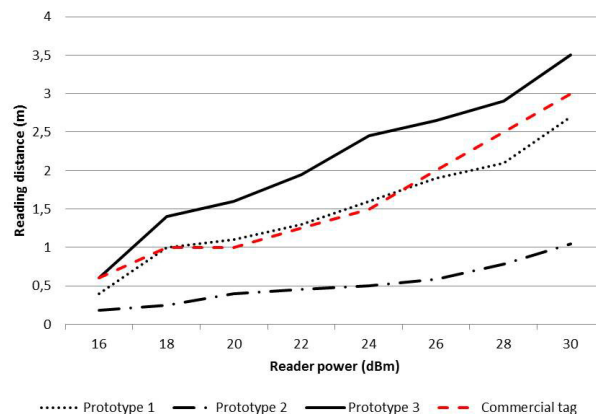


Fig. 8. Measured reading distances of the RFID tags.

The results obtained from the reading distance tests confirm the expectations based on the antenna characteristics presented in the previous section. The last prototype has shown the best performance, even beating a commercial tag solution for half a meter at maximum power. The second prototype has shown very poor results considering the antenna simulated characteristics as shown previously. However, as stated before, this poor performance is most probably due to the large bandwidth constraint associated to this antenna.

5. Integration into a bottle

The purpose of the development of these antennas is to integrate them into bottle labels, therefore we tested their performance when placed in close proximity to liquids, that is, attached to the glass of water and wine filled bottles.

Unfortunately none of the prototypes was able to shown any good performance in this scenario. The presence of the dielectrics such as glass and water completely change the propagation characteristics around the antennas, therefore destroying the matching that was previously obtained. We rebuilt the simulation models of the third prototype, by considering the presence of an empty bottle, as shown in Figure 9, and the glass by itself was able to change the antenna matching completely as shown by the return loss obtained from simulation in Figure 10.

It is therefore needed, to readjust the antenna's dimensions in order to match it for the proper resonant frequency when in the vicinity of dielectrics such as glass and water or wine. Besides, it is expected that the tag designed for such environment will not work without the presence of these elements. The challenge is therefore the design of a tag antenna that will be able to work when the bottle is filled with liquid either in the vertical and horizontal position.

6. Conclusion

The results shown in this paper present two major contributions. First, the permittivity estimation of common 80gr paper and window and bottle glasses. Secondly, the proposal of an RFID tag antenna that is small enough and built in a thin paper substrate that is suitable to be applied into bottle labels. When the behaviour of the developed tag

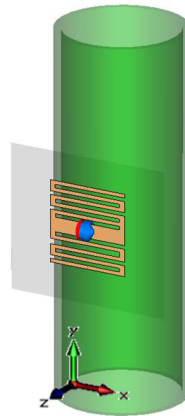


Fig. 9. Third prototype of a RFID tag on paper substrate simulation model with bottle glass.

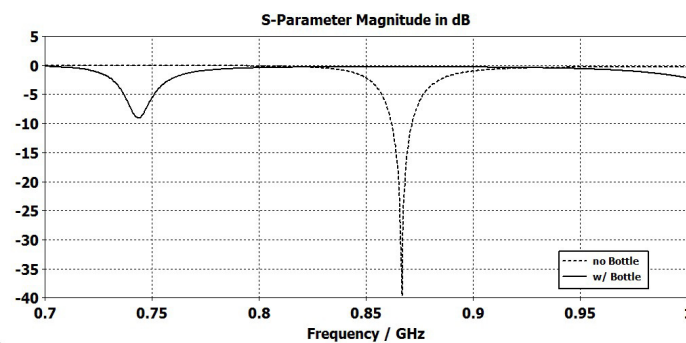


Fig. 10. Simulated return loss of the third RFID antenna prototype with the glass bottle.

is compared with a commercially available RFID tag in a plastic card, we were able to slightly enhance the reading range and robustness to misalignment. However, when placed in the vicinity of liquids, eg. in a bottle surface, the antenna is mismatched and therefore the reading range is severely affected. As a future work reference we expect to develop an RFID antenna that is matched in the presence of the bottle and can work in the presence and absence of the liquids such as water or wine.

Acknowledgements

The authors acknowledge the Portuguese FCT/MCTES for financing the PhD grant SFRH/BD/91249/2012 under which this work was developed.

References

- [1] K. Finkenzeller. RFID Handbook: Fundamentals and Applications in Contactless Smart Cards and Identification. 1st ed. John Wiley & Sons, Ltd; 2003.
- [2] Kevin Boyle and Yi Huang. Antennas From Theory to Practice. 1st ed. Wiley; 2008.
- [3] D. M Pozar. Microwave Engineering. 3rd ed. Wiley; 2005.
- [4] A. M. Nicolson and G. Ross. Measurement of the intrinsic properties of materials by time-domain techniques. IEEE Transactions on Instrumentation and Measurement 1970; 19:377–382.
- [5] W. B. Weir. Automatic measurement of complex dielectric constant and permeability at microwave frequencies. Proceedings of the IEEE 1974; 62:33–36.
- [6] Computer Simulation Technology. CST Microwave Studio. <https://www.cst.com/Products/CSTMWS>, Retrieved: October 2013.
- [7] Zhijun Zhang. Antenna Design for Mobile Devices. 1st ed. Wiley; 2011.
- [8] K. V. Seshagiri Rao, Pavel V. Nikitin, and Sander F. Lam. Seshagiri Rao, Pavel V. Nikitin, and Sander F. Lam. Antenna design for uhf rfid tags: A review and a practical application. IEEE Transactions on Antennas and Propagation 2005; 53:3870–3876.

[J3] - L.R. Roselli, N. B. Carvalho, F. Alimenti, P. Mezzanotte, G. Orecchini, M. Virili, C. Mariotti, **R. Gonçalves**, P. Pinho, "Smart Surfaces: Large Area Electronics Systems for Internet of Things Enabled by Energy Harvesting", *Proceedings of the IEEE*, Vol. 102, No. 11, pp. 1723 - 1746, November, 2014.

Smart Surfaces: Large Area Electronics Systems for Internet of Things Enabled by Energy Harvesting

This paper focuses on large-area “smart surfaces,” RFID systems, and wearable RF electronics that could substantially benefit from multisource energy harvesting.

By LUCA ROSELLI, *Senior Member IEEE*, NUNO BORGES CARVALHO, *Senior Member IEEE*, FEDERICO ALIMENTI, *Senior Member IEEE*, PAOLO MEZZANOTTE, *Member IEEE*, GIULIA ORECCHINI, MARCO VIRILI, *Student Member IEEE*, CHIARA MARIOTTI, *Student Member IEEE*, RICARDO GONÇALVES, *Student Member IEEE*, AND PEDRO PINHO, *Member IEEE*

ABSTRACT | Energy harvesting is well established as one of the prominent enabling technologies [along with radio-frequency identification (RFID), wireless power transfer, and green electronics] for the pervasive development of Internet of Things (IoT). This paper focuses on a particular, yet broad, class of systems that falls in the IoT category of large area electronics (LAE). This class is represented by “smart surfaces.” The paper, after an introductory overview about how smart surfaces are collocated in the IoT and LAE scenario, first deals with technologies and architectures involved, namely, materials, antennas, RFID systems, and chipless structures; then, some exemplifying solutions are illustrated to show the present development of these concurrent technologies in this area and to stimulate further solutions. Conclusions and future trends are then drawn.

KEYWORDS | Energy harvesting; green electronics; Internet of Things (IoT); large area electronics (LAE); radio-frequency identification (RFID) systems

I. INTRODUCTION

Looking at the telecommunication (TLC) market development worldwide in the last five years, we see an average decrease of about 5% per year, in both gross domestic product (GDP) contribution and employment [1]. Against this trend, the global information and communication technology (ICT) market has remained grossly constant. Some compartments, in fact, are experiencing an opposite trend. Beside some sectors related to new consumer products, such as tablets and smartphones, new Internet of Things (IoT) related products are growing at two digits per year and some estimations from big players report a market value in the order of trillions of dollars in the next decade [2], [3].

The vision behind IoT is in fact to connect objects directly to the Internet so as to allow them to provide information directly to the web without any human intermediation [4]. This vision will have a great impact on several electrical and electronic technologies, ranging from the basic physical layers (technology platforms) to the highest ones: communication protocols, software, human interface, and information management.

Manuscript received May 4, 2014; revised September 1, 2014; accepted September 5, 2014. Date of publication October 13, 2014; date of current version October 16, 2014.

L. Roselli, F. Alimenti, P. Mezzanotte, G. Orecchini, M. Virili, and C. Mariotti are with the Department of Engineering, University of Perugia, Perugia 06123, Italy (e-mail: roselli@ieee.org).

N. Borges Carvalho and R. Gonçalves are with the Instituto de Telecomunicações-Dep. Electrónica Telecomunicações e Informática, Universidade de Aveiro, Aveiro 3810-193, Portugal.

P. Pinho is with the Instituto de Telecomunicações, Instituto Superior de Engenharia de Lisboa, Lisboa 1959-007, Portugal.

Digital Object Identifier: 10.1109/JPROC.2014.2357493

In terms of physical layer, IoT actually inherits the technologies developed for wireless sensor networks (WSNs), bringing the distributed nature of that to the extreme. WSN, in fact, can be synthetically seen as a mesh of sensor nodes purposely conceived to build and communicate a sensed image of a monitored area. Within IoT, the sensing nodes are not purposely deployed to monitor something specific; instead, they are simply hosted by “objects” in order to provide the information they are able to collect and make it available on the web. Conceptually speaking, there is not a big difference, but in terms of related technological challenges, there is. Nodes must be hostable by objects; objects are of many types, and the better the nodes fit themselves transparently to the hosting objects, the denser and more reliable the information they are able to provide.

Several challenges can be envisioned in this evolution: first, electronic systems must be mechanically flexible, thin, and miniaturized in order to conform to the shape of as many objects as possible; second, the adopted materials have to be as recyclable as the hosting objects in order to avoid pollution from guest apparatuses; last but not least, hosted nodes must be autonomous, because they cannot be either connected to the grid or powered by life batteries.

A great technological paradigm shift is going to be pulled by the development of IoT; green materials, autonomous systems, ultralow-power circuits, energy saving protocols, and energy harvesting (EH) are concurrently mandatory.

Conversely, this technological evolution is pushing new solutions and architectures, so far constrained by the limits of conventional technologies. The development of inkjet printing techniques, the introduction of very cheap and eco-friendly materials compatible with roll-to-roll (R2R) circuit realization techniques [5] and so forth, open new horizons also to large area electronics (LAE).

LAE, first applied to printed photovoltaic and organic screens [6], is actually at the onset of its development. The development of R2R techniques and related materials, in fact, is allowing for tremendously increasing the dimensions of LAE circuits and systems, from the present tens of centimeters to meters and beyond. Along this evolutionary scenario, new configurations and architectures, based on massive integration of large circuits over conformable surfaces, can be envisioned, opening the way to what can be called the smart surfaces (SSs) approach.

SS, in turn, can be seen as a branch of IoT evolution. Large 2-D arrays of autonomous sensor nodes, for instance, make possible granular tracking of whatever parameter, ultimately providing augmented imaging of the environment; large 2-D arrays of tags can provide a very low-cost platform for precise localization and location-based services (LBS), thus enabling the realization, for instance, of smart floors [7] and smart wallpapers [8]; inheriting quasi-optical approach [9] contact-less electromagnetic (EM) wave processing (filtering, frequency conversion, selective shielding, etc.) can be conceived even at low frequencies.

On the one hand, SS is thus an approach stimulated by technologies pulled by IoT; on the other hand, it contributes to a class of architectures, within LAE, that can even widen the huge horizons of IoT applications in a sort of virtuous circle.

According to this wide vision, the paper is organized as follows. A review of the technologies suitable for distributed systems implementation to a large extent is given in Section II; then, the explanation about how radio-frequency identification (RFID) can be considered one of the most suitable technologies for the implementation of IoT architecture, and how it can be naturally integrated with SSs, is provided (Section III). In order to deal with the implications of the development of RFID systems compatible with SS and LAE evolution of IoT, two specific sessions have been provided: the first relates to antenna implications (Section IV), and the second relates to electronic architectures for RFID tags (mainly chipless ones; Section V). In order to smoothly bring the reader from relevant technologies to applications, quasi-optics, as an example of general approach concurrently exploiting the mentioned technologies to provide a platform suitable for LAE, is described in Section VI. After this, some application examples of how SS concept can be articulated, according to the IoT paradigm, are described; specifically, smart floor (Section VII), smart shoes as useful subsystems for the implementation of smart floors (Section VIII), and energy skin (Section IX). In order to have a vision of the logical links behind the many topics dealt with in this paper, a synoptic picture can be found in Fig. 1.

II. TECHNOLOGY FOR LAE DISTRIBUTED SYSTEMS

Given the described scenarios of SS, it is clear that the technologies involved have to be compatible with LAE

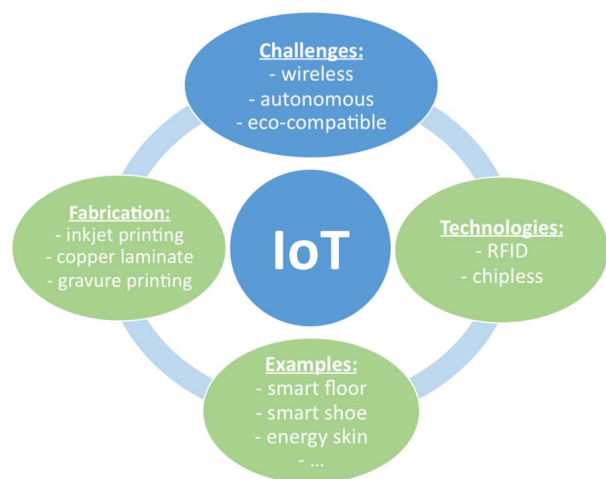


Fig. 1. Synoptic view of the paper structure reflecting the IoT vision described in the Introduction.

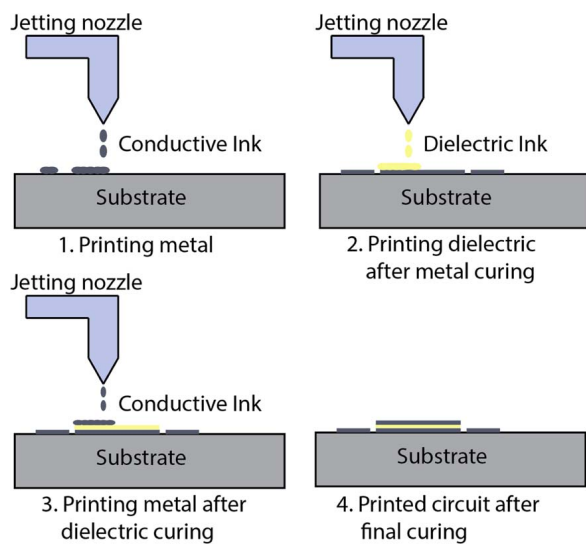


Fig. 2. Inkjet printing technique, synoptic description. The ink is deposited on the substrate with the desired pattern and after a curing procedure the next layer can be printed. The thickness of each film depends on the number of passes.

approach, as described in the Introduction; according to [6], for example, the eco-compatibility of the materials, the mechanical flexibility of the substrates to make the device conformable to the hosting surface, and the life cycle (operability and biodegradability) have to be accounted for.

The new techniques proposed from different research groups [10]–[12] focus mostly on the printing techniques that can be industrialized easily with R2R methods, already investigated for the traditional printing on paper. Within the printing methods, one of the most attractive and investigated in the last decade is the inkjet printing of conductive and dielectric layers (Fig. 2). This technique allows circuits to be printed on almost any kind of substrate: from the photographic paper to liquid crystalline polymers (LCP) or Kapton, that are flexible, thin, and eco-compatible; to glass or poly methyl meta acrylate (PMMA, commonly referred to as Plexiglas) that are usually thicker but not flexible.

A first proof of concept for the inkjet printing technique at radio frequency (RF) and microwaves has been obtained on photographic paper by printing simple structures, such as antennas and other planar circuits and devices [10], [13]–[22], with a technology stack simply composed by the substrate and the conductive layer (usually realized by means of nanoparticle silver ink).

Recently, this method has been improved thanks to the development of new inks, usually composed by a polymer and a solvent (i.e., SU-8, PVP, PMMA, PEDOT, etc.); more complex fabrication procedures of multilayer structures are now possible, as shown in [23] and [24]. Another noticeable feature of this technology is represented by the resolution: conductive tracks of 50 μm of width and space gaps of 50 μm can be printed, allowing the design of

millimeter-wave (mm-wave) frequency devices [25]. The combination of the quite high resolution (considering the simplicity of the technology) with the multilayer featuring also gives the opportunity to manufacture very easily matrix of passive and active devices that can be used in the SS development. It is worth noting that the process can be developed in a few steps based on the design and mostly on the number of layers needed. For example, a metal–insulator–metal (MIM) device can be realized by printing silver on the substrate [26], curing it in the oven in order to create a surface that, with the proper treatment (for instance, UV–Ozone exposure or preheating), is ready for the insulator printing. Then, the dielectric is cured as well and the last metal layer can be printed on top of it. The entire structure can be then cured at temperatures ranging between 130 °C and 200 °C.

In a perspective of industrialization of the inkjet printing technology, the hypothesis of R2R manufacturing of circuits is being investigated and some examples are already reported in literature for solar cells and other devices [27], [28].

Today, many pros have been mentioned for the inkjet printing method, and others can be found in the non-use of wasted chemicals (as is for the traditional lithographic technologies), in the no-need of clean-room environment for the fabrications, in the low-cost and rapidity of manufacture, and in a R2R perspective compatibility. However, the necessity of a curing procedure after the printing of a layer still represents the biggest inkjet limit for two main reasons: first, the time and type of curing are dependent on the inkjetted materials and on the material stack-up; second, especially on a laboratory level, the curing can cause misalignment issues, given the fact that the sample is removed and then replaced in the printer after the last layer curing.

Currently, the platform mostly used worldwide by researchers is the Dimatix 2800 DMP. In terms of inks, it is possible either to buy printable solutions or mix solutions in labs; for example, the combination of polymers and solvents allows layers to be printed with different electrical properties and thicknesses.

Besides the inkjet printing method, in [11], a new technique, suitable for LAE, has been proposed. It uses a metal (copper in that case) adhesive laminate technology based on the application of the standard etching process to an adhesive copper laminate material. This technique was already adopted to produce mm-wave circuits and to characterize the resulting compound substrates, as reported in [29]–[31]. A brief illustration of the metal laminate technique is here reported referring to Fig. 3.

The production process can be divided in five steps. The first step consists of the deposition of a (positive) photoresist film on the copper surface; then, the circuit layout is transferred to the photoresist by means of a photomask and ultraviolet exposure. After that, the unimpressed film of photoresist is removed using a NaOH

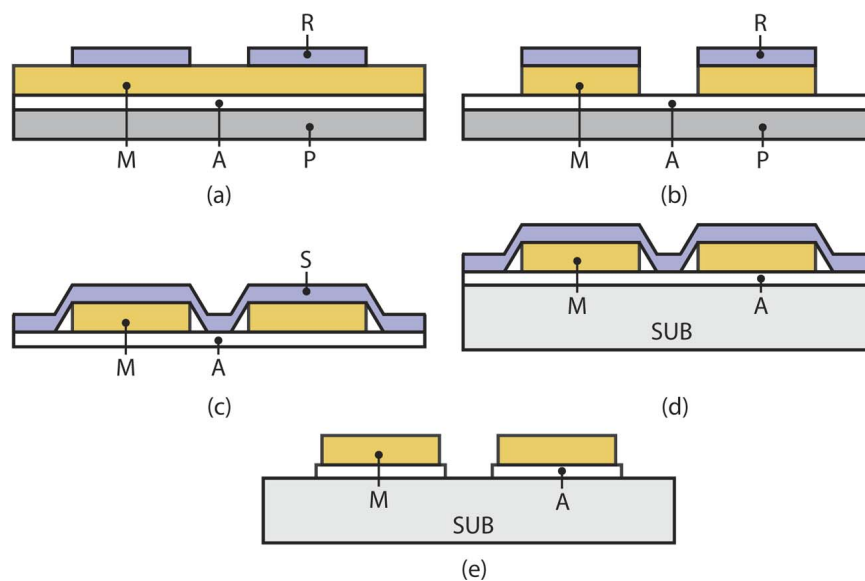


Fig. 3. Process steps for the circuit fabrication using the adhesive metal laminate. *M*: metal, *A*: adhesive, *P*: protection, *R*: photoresist, *S*: sacrificial layer, *SUB*: hosting substrate. After the standard lithographic procedure, the copper pattern can be transferred on top of any substrate by means of a sacrificial layer and exploiting the adhesive face of the copper tape.

developer solution [Fig. 3(a)]. In the second step, the copper tape is wet etched. As can be seen in Fig. 3(b), in this way, the adhesive layer is exposed where the copper was removed, while it remains everywhere else covered by the original copper tape that serves as protection for the adhesive underneath.

The first two steps are, in this example, similar to those adopted in standard photolithographic technology. Moreover, different ways to remove the not needed metal can be used, as, for example, by means of numerical control pattern cutting plotters.

In the third step, depicted in Fig. 3(c), a sacrificial layer is stuck on the top copper side and, finally, the protection layer on the bottom is removed. The sacrificial layer is very important because it keeps the relative distances among the layout features constant even when these are not physically connected.

The fourth step is characterized by the transfer of the etched metal to the hosting paper substrate and, finally, the sacrificial layer can be removed [see Fig. 3(d) and (e)]. The last step is also useful to remove most of the exposed adhesive material.

With this method, quasi-fully-organic circuits and devices can be realized. The performance in terms of tracks width and pitch are, at present, a bit lower than what can be obtained with the inkjet printing, with the advantages of no curing processes, the possibility to fix devices on the circuit using standard soldering techniques, and a better conductivity (the conductivity of copper laminate, in fact, is one order of magnitude higher than that of the cured nanoparticle silver ink: 5.8×10^7 S/m versus about $6 \times 10^6 - 1 \times 10^7$ S/m obtained with at least five layers of silver).

To verify the validity of the metal laminate technology at microwave frequencies, a $50\text{-}\Omega$ microstrip line was manufactured exploiting the Mitsubishi photographic paper as the substrate (thickness $250\text{ }\mu\text{m}$, relative permittivity $\epsilon_r = 3.2$, and loss tangent $\tan \delta = 0.08$). The line is 30 mm long, and the measured scattering parameters are shown in Fig. 4. The same graph also compares the performance of a similar transmission line manufactured with an inkjet printing process. The performance of the

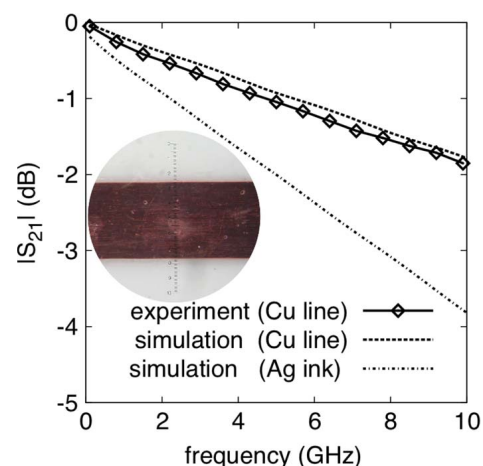


Fig. 4. Measured scattering parameters versus frequency for a $50\text{-}\Omega$ microstrip line on paper substrate. The line, shown in the inset, is 30 mm long; the ruler division corresponds to $17.2\text{ }\mu\text{m}$. The graph also reports a comparison with a microstrip line of equal dimensions made with an inkjet printing process (Ag ink, $3\text{-}\mu\text{m}$ thickness, $\sigma_{\text{ink}} = 1.1 \times 10^7$ S/m after curing). After [11].

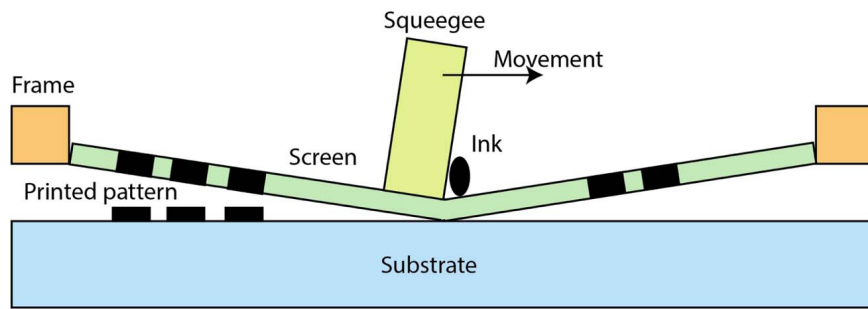


Fig. 5. Screen printing technique. The squeegee is used to press the screen with impressed pattern and transfer it on top of the substrate.

metal laminate structure is superior compared to that of the inkjet printed line. At 10 GHz, the measured specific losses for the metal laminate microstrip are about 0.6 dB/cm [11]. Results at higher frequencies are also reported in [31]; in particular, an insertion loss of about 1.8 dBm/cm at 30 GHz is demonstrated.

The tradeoff is the adoption of a photolithographic step; it is worth mentioning, however, that the process is still compatible with R2R implementation.

Other possibilities for LAE are the screen printing [12] and the gravure printing [12], both of them adaptable to R2R industrialization techniques.

Screen printing consists of dragging a layer of ink across the surface of a screen and squeezing it through the open pores of the patterned mesh onto the substrate (Fig. 5). In general, the thickness of the printed layer and the achievable resolution depend on the density of the mesh and on the ink properties. Usually, the ink viscosity is in a range of $1\text{--}50 \text{ Pa} \cdot \text{s}$, and this allows for printing with a resolution of about $100 \mu\text{m}$ and a thickness up to $100 \mu\text{m}$. Until now screen printing has been adopted to realize low-resistance structures, solar cells, and field effect transistors (FETs), exploiting the possibility of printing very thick layers.

Gravure printing, also known as rotogravure, is considered a very high volume printing (Fig. 6) process, and it is being adopted to produce very conductive structures as, for example, capacitors, antennas, and organic devices such as pentacene-based diodes, organic light-emitting diodes (OLEDs), organic field effect transistors (OFETs), and organic thin film transistors (OTFTs).

The resolution can be of about $20 \mu\text{m}$. The method is implemented by engraving the patterns into a metallic cylinder by a laser, by chemical etching, or electromechanically (as separate cells or intaglio trenches). Typically, the print pressure is high ($1\text{--}5 \text{ MPa}$) in order to achieve a good ink transfer and to reduce the percentage of unprinted dots caused by the surface roughness of the flexible substrate. However, this high pressure of printing makes this technique suitable only for robust substrates with no soft, previously printed, layers that could be damaged.

To summarize, the technologies described in this section are characterized by some common features, such as: flexibility and conformability, compatibility with large area realization of circuits and interconnections, use of additive or mixed (subtractive/additive) deposition techniques, easy use of eco-friendly materials and, in some cases, compatibility with classical bond wiring as well as soldering techniques for electronic device placement.

Table 1 summarizes the main features of the described technologies.

III. RFID: A MIX OF CONCURRENT TECHNOLOGIES FOR SS IMPLEMENTATION

As mentioned in the outline paragraph at the end of the Introduction, after describing the technologies enabling SS development (Section II), here we illustrate RFID as a suitable means to transfer information through EM transmission between tags and readers to the Internet.

An RFID tag has a unique identification code and a memory used to store information, while the reader can

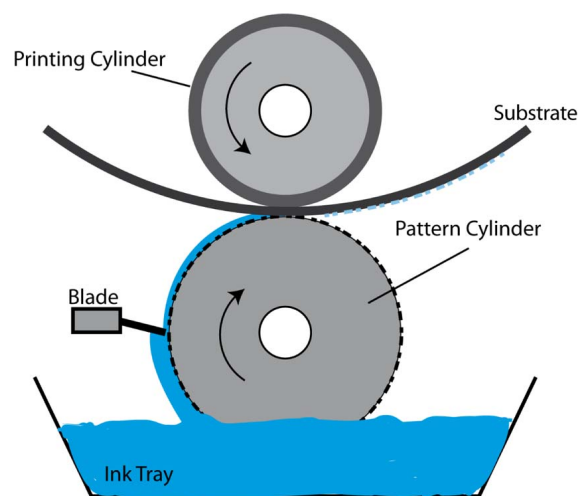


Fig. 6. Gravure printing process. Note that these machines can be from 20 cm to 3 m wide with a diameter ranging from 5 cm to 5 m.

Table 1 Technologies Comparison

Technology	Resolution	Cost	Waste	Speed
Inkjet	50 μm	Low	Low	Fast
Copper	100 μm	Low	High	Medium
Gravure	20 μm	High	Medium	Very fast
Screen	100 μm	Medium	Low	Very fast

write or read data on and from the tag through RF transmissions. The tag is usually attached to an object that needs to be identified and monitored, or contains information to be read. In typical RFID applications [32], the main goal is to provide mapping of physical objects that are equipped with an RFID tag attached or embedded. In this way, RFID technology inherently leads to identifying, tracking, and localizing, but it can also enable the storage and transmission of information regarding object status and surrounding environments by embedding sensing capabilities.

As mentioned previously, IoT is most commonly described as a structured system of technologies concurrently working to capture meaningful data from objects and communicate them through networks to a decision-taking level. Useful keywords, whenever a definition of IoT is given, include: smart objects, autonomous logistics, machine-to-machine communication, RF technologies, centralized information, and so on.

In order to implement these functionalities, an IoT platform, an SS for instance, has to provide at least unique object identification together with wireless communication for data management.

The IoT physical layer can thus be naturally thought of as meshes of RFID and sensor nodes. The RFID tag that embeds a sensor can use the same working principles and protocols of the conventional RFID tags; a differentiation can be made, considering the way sensor tags are powered up, in active, semipassive, and passive tags; actually, the difference consists of the way they are powered.

Active tag sensors may use customarily conceived communication protocols or rely on RFID standards enabling the tag to be easily integrated into the existing wireless infrastructures so that they will not require expensive readers. In [33], a system architecture was developed to integrate WSNs and the RFID systems. Bluetooth and ZigBee technologies are adopted as the communication protocol of WSNs to meet the requirements of a large number of sensor nodes, large areas, and low cost.

Active tags with integrated sensors are used in several applications, including temperature and position monitoring, vibration detection, blood pressure, heart beat monitoring, and more. This type of sensor tags, besides having larger amount of energy provided by batteries, affords both a large range and multiple functionalities; some of them have also external buses that enable the use of connected external sensors [34].

Passive tags with an integrated sensor operate without battery, collecting the needed operational energy from external environment sources. The main requirements of this class are high energy conversion efficiency, large storage capability, and overall low-power consumption. Passive systems have usually low operating range and limited processing capability.

In this field, research activities are directed toward ultralow-power design of integrated sensor tags [35], antenna design for improving reading range [36], sensor overall performance optimization [37], and development of optimum protocols allowing for additional power saving [38], [39].

Typical applications are, for instance, temperature monitoring [40], photodetection [41], motion detections [42], etc.

Semipassive tags use both batteries and energy sources coming from the environment; they can integrate more operational capabilities than the passive ones, since they can exploit a higher amount of energy. For the same reason, semipassive RFID tags are more suitable to integrate a sensor; the operational methodology is similar to the passive one, using the reader signal to interrogate and cause a response from the tag. The primary difference is that the semipassive tag does have a battery used not to generate a response, but only to power electronics, like sensors incorporated in the tag, while exploiting RF circulation to reply to the reader interrogation. Just like passive tags, semipassive ones are limited in terms of slow reading speeds and short reading distances. In [43], the design, realization, and experimental validation of a battery-assisted RFID tag with sensing and computing capabilities, conceived to explore heterogeneous RFID-based sensor network applications, was presented.

Dealing with battery-less devices that are, by far, the most interesting ones for IoT, LAE, and SS applications, we can now focus on the typical energy sources adopted. No battery devices can exploit solar scavenging [44], [45], vibrational [46], [47], or RF radiations [48]–[52].

In many cases, wirelessly powered systems can harvest energy from the incident RF waves, thus generating the required direct current (dc) voltage to power the system. The EM energy present in the environment may be significant in some regions (some urban areas or indoor sites); here the use of proper conversion devices may allow enough energy to be scavenged. RF power harvesters usually consist of an antenna, an impedance transformation network, a rectifier, and a storage element. In [53], a design example of integrated rectifier antennas (rectennas) for wireless powering at low incident power densities, from 25 to 200 $\mu\text{W}/\text{cm}^2$, is given.

Regarding mechanical energy scavengers, they may be categorized upon the kind of energy source exploited; there are scavengers providing energy from a constant motion over extended periods of time (e.g., turbine air flow) or others based on intermittent motion (e.g., human

step). Particular attention is given to vibrational energy sources; in this case, the amount of energy that can be harvested depends mainly on the vibration amplitude and frequency and on the vibrating mass (mass of the harvesting device) [54]–[56].

In order to power the systems by using energy sources available in the working environment, proper energy transducers thus have to be chosen. Focusing on distributed systems (IoT, LAE, and SS), it is worth referring to typical parameters for optimum transducer design since, in these applications, the different kinds of energy available in the various scenarios may lead to the need of integrating more than one energy conversion system into the same device, in order to take advantage of all the accessible energies. The main design parameters are the available power output, the electrical impedance, and the operating voltage. Table 2 summarizes them for the most common energy transductions [57], [58].

To conclude this section, the mentioned reasons why RFID can be considered a useful technology for the implementation and development of LAE and, more specifically for SSs, are summarized. RFID systems, especially in the passive version of tags, are communication systems characterized by the following characteristics: compatibility with very low-power communication protocols, compatibility with the constraints posed by the hosting objects, especially when they are implemented by adopting the technologies described in Section II, inherent capability to gather information from the environment (sensor tags) and from the hosting objects, a low number of electronic devices (inherent circuital simplicity) and, finally, proven compatibility with printing technologies.

For all these reasons, RFID technology has to be considered the leading one to pursue the development of LAE and SSs as a communication platform for the evolution of IoT.

IV. ANTENNA DESIGN FOR NODES

Distributed systems for ubiquitous electronics (UE) and WSNs [59], [60] are, today, increasingly employed for monitoring and sensing applications. These systems can be seen as networks of nodes, massively distributed in the environment and communicating wirelessly with a base station. This massive deployment can be designed and structured to monitor a set of specified parameters by means of purposely conceived sensor nodes, as in the classical WSNs, or it can be obtained by integrating nodes into existing objects, which is the vision of IoT evolution. In general, the nodes can have different functionalities, however they have to provide information collected by embedded sensors (such as, for instance, identification codes, position and monitored environment parameters as well as object status) whenever it is required.

In this scenario, the RFID technology, summarized in Section III, is attractive. When RFID technology meets sensor nodes, information goes from the node to the Internet via a question-and-reply protocol between nodes, hosted by tagged objects, and readers.

Thinking about distributed systems and specifically SS, it is natural to think about radiative coupling in the available industrial–scientific–medical (ISM) frequency bands, including mainly the ultrahigh frequency (UHF) and microwave frequencies (around 0.9, 2.4, 5.8 GHz, and higher), exploiting the communication standard such as the WiFi [61]. Recently, also the ultrawideband (UWB) has been considered in order to minimize the limitations of narrowband systems (mainly localization accuracy and sensitivity to interference) [62].

Multistandard systems are often adopted for large compatibility and higher use flexibility. An example of this recent approach is given in [61] where near-field UHF nodes are combined with far-field transceivers. This allows application fields with compromised radiation capability,

Table 2 Transducer Characteristics for Several Forms of Ambient EH [57], [58]

Energy Source	Typical Electrical Impedance	Typical Voltage	Typical output power
Light	From low to 10s of K Ω	DC: 0.5 V to 5 V	Outdoors: 100s mW/cm ² Indoors: 500 μ W/cm ² <
Vibrational	Constant Impedance 10s of k Ω to 100 k Ω	AC: 10s of Volts	100s μ W/cm ²
Thermal	Constant Impedance 1 Ω to 100s of Ω	DC: 10s of mV to 10 V	10s μ W/cm ² (20° gradient)
Radio Frequency	Constant Impedance Low K Ω s	AC: Varies with distance and power 0.5 V to 5 V	Wide-range

such as in proximity of metal and liquids at short ranges, to be improved.

It is clear that antenna systems are key elements in these apparatuses. The foundation of antenna design rules can be found in [63]. The antenna design specific for distributed systems, in turn, has to take into account several instances. Beyond the typical design criteria, other aspects are: the communication standard, the form and the size in agreement with the application, the communication range as a function of the equivalent isotropic radiated power (EIRP) limits, of the environment and of the orientation, the reliability under several conditions and processes, and the material cost considering massive production [64]–[67]. Among them, the operating environment is the most critical aspect that influences the node behavior [68].

As a consequence, antenna topology and materials for SS and IoT systems, in general, have to be chosen in order to make the antennas capable of operating in variable environmental conditions and to be integrated into objects. As an example, let us think about wearable antennas for body area networks (BANs): they must be washable, flexible, and able to shield the body from radiation [69].

In general, antennas for SS should be flexible, planar, and low profile; moreover, by adopting low-cost materials and technologies (see Section II), cost per unit surface is low, thus large arrays and big elements can be adopted more easily, ultimately allowing for easy developments of LAE distributed systems and SS, even at low frequency.

Materials compliant with SS implementations must be, in turn, mechanically robust, flexible, and very low cost, while exhibiting acceptable EM performance. These materials must also exhibit high tolerance levels in terms of bending repeatability. Flexible materials, often used, are polymers and polymer-ceramics composites such as the poly-di-methyl-siloxane (PDMS) and the titanate-based ceramic [68], which provide flexibility, robustness, and resistance to harsh environments in order to protect antenna and circuit. Moreover, when eco-compatibility has to be guaranteed, recyclable materials and related technologies have to be adopted; among them, cellulose substrates in combination with inkjet printing of conductive inks [18], [70] or with conductive adhesive laminate technology [11] are increasingly frequently adopted. The aforementioned techniques, compatible with the well-known industrial printing and the R2R processes [5], are in agreement with the low-cost fabrication and are expected to facilitate widespread and very low-cost electronics for distributed systems. These fabrication technologies can also be adopted for electronic devices on flexible polymeric substrates. An example of cellulose-based antenna for smart floor applications, such as indoor localization, is documented in [71]: a low-profile planar loop antenna is realized on cellulose substrate exploiting adhesive copper tape.

Although beyond the scope of this paper, which focuses on SS, it is worth mentioning here that this evolution toward the development of more and more sophisticated

“unconventional” materials for electronics has a great impact on other IoT related developments such as, for instance, implantable systems.

When applications require devices with soft visual impact (think about SS, such as smart windows, glass integrated inside and outside buildings and glass for automotive applications, or smart skins [72]), transparent and conductive materials, such as transparent conducting oxides (TCOs), and in particular indium-tin-oxide (ITO) and ITO-based multilayers, have been proposed [73]. These materials afford a good compromise between minimum electrical resistivity and high optical transmittivity in the visible light spectrum when patterned on see-through materials such as glass or transparent polymers. A technique to improve the efficiency of the transparent antennas, without affecting their transparency, is the application of a layer of highly conductive coating or metallization strips on the antenna edges where the current density is high [72].

Among SSs, or in general distributed systems within the IoT vision, a fast growing field of research is represented by wearable electronics for BANs [74]. In this case, the integration of electronic devices in the garments requires the development of wearable and washable antennas and antenna arrays on fabrics. Washable antennas can be realized by covering textile antennas by a breathable thermoplastic polyurethane coating in order to protect the device against water absorption and corrosion [69].

Although dimension constraints are not very critical for distributed systems on cheap materials, they cannot be neglected thoroughly. At RF, for example, high permittivity materials [68] and magnetic composite substrates [75] can be adopted. Artificial magnetic conductors (AMC) can be employed alternatively to the magnetic composites with similar results [76]. These approaches are simply demonstrated from the wavelength equation: wavelength is a function of the relative permittivity and permeability and adopting suitable materials to increase these values, the effective wavelength, and therefore the antenna size, decreases. Anyway, the use of these materials introduces a tradeoff between dimensions and performance: generally the substrate losses decrease the antenna radiation efficiency, thus affecting the communication range of the overall wireless system, as documented in [68], [75], and [76].

In terms of design methodology, the introduction of unconventional materials as well as the environmental constraints posed by distributed systems and systems for IoT influence and drive the design strategies. Some solutions are proposed in the literature to cope simultaneously with these constraints; in [68], shielded configurations have been analyzed to mitigate environmental sensitivity. In [69], an example of robust patch antenna for BAN application that reduces the effect of the body on the performance is illustrated; in [77], the use of broadband antennas, such as the Chebyshev monopoles with a fractional bandwidth of about 40%, is proposed to reduce the frequency

shift introduced by the background materials or by the bending effects.

In SSs, and in general in IoT applications, antennas are used both to transmit and receive information and to harvest the necessary energy from the surrounding environment. Regardless of the fact that the available energy is randomly released in the environment by existing services (GSM, WiFi, and so on, in urban and semi-urban environments [78], [79]) or purposely delivered to empower a distributed population of nodes [80], antennas have to be able to harvest EM energy. This kind of “double effect” antenna is widely referred to in the literature as “rectenna”: it combines rectifying circuitry with EM to electrical energy transduction.

The fundamental codesign techniques of antennas and rectifiers, focusing on the improvement of the conversion efficiency exploiting matching circuits, are described in [53]. Harmonic-balance and load-pull simulations are often used in order to find the optimal impedances that allow best efficiency to be obtained as a function of the EM incident power.

Multiband, broadband, and circularly polarized antennas are often adopted in EH applications to reduce the overall sensitivity to the environment. An example of planar antenna array for EH applications, in agreement with the SS principle, is documented in [81]: spiral antennas are proposed in order to provide a wide operating frequency band, and the rectification circuitry is optimized and characterized for low incident power levels. Similar antenna array for UWB EH is shown in Fig. 7.

A rectenna can be used in addition to the communication antenna or, alternatively, the same antenna can be used for both EH and data transmission. The use of different antennas is generally adopted if harvesting and communication are carried out at different frequencies

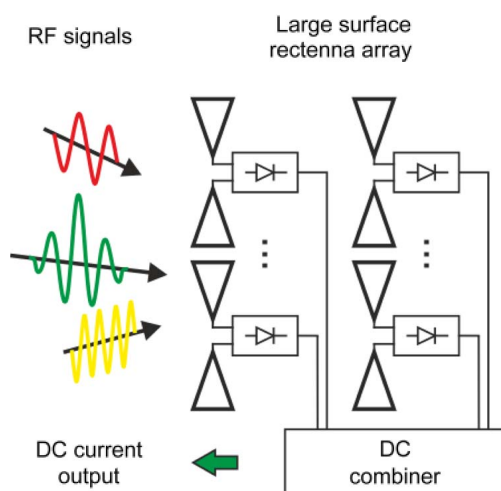


Fig. 7. Scheme of the rectenna array able to collect RF energy even in a broadband (depending of the kind of receiving antenna element), according to the solution adopted in [81].

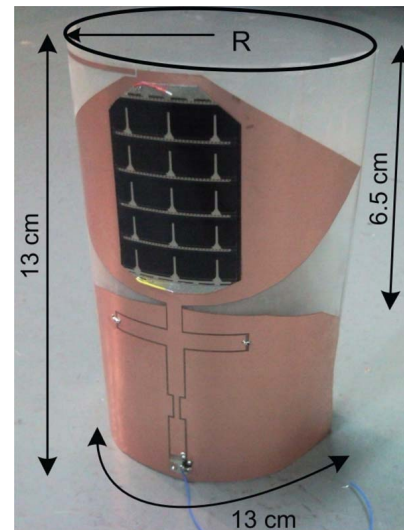


Fig. 8. Hybrid rectenna for solar and EM-EH. The hybrid rectenna consists of a broadband antenna and a solar cell combined in the same structure. After [82].

and, mainly, in order to enhance harvesting efficiency without decreasing communication performance. In any case, this requires a codesign and can affect the node dimension and complexity. Alternatively, a single antenna can be a feasible compromise if communication and harvesting share the same frequency band and if the antenna harvesting efficiency is not the main issue; examples are the passive RFID tags empowered by the reader with a standard RFID antenna able to provide both EH and communication capability, as documented in [64] and [65].

However, the EM-EH is not the only solution to energize nodes and SS elements: hybrid EH, in fact, can be performed by exploiting different energy sources; that is, combining the rectennas with other sources of energy.

Recently, a low-cost and conformal structure for hybrid EH, based on low-cost and flexible poly-ethylene terephthalate (PET) substrate and an amorphous silicon solar cell, has been proposed in [82]; other examples are discussed in [20] and [83]. The use of low-cost, printable photovoltaics deposited on flexible substrates to form part of the antenna radiating structure is documented in [84]. In all these contributions, the main challenge appears to be the codesign of the antenna and solar cell in order to avoid reciprocal detrimental effects. The antenna is designed with a solar cell integrated on top of the radiating surface to obtain good radiation characteristics and to incorporate connections for the extraction of the dc provided by the solar cell. In [82], it was demonstrated that, by adopting thin film solar cells and paying attention to not exceeding the perimeter of the RF antenna, the solar cell can be integrated so as not to significantly affect the performance of the antenna. The hybrid rectenna for solar and EM-EH documented in [82] is shown in Fig. 8.

In terms of industrial assembly, the use of new materials and the need for low-cost and large-scale fabrication techniques would be fostered by architectures more insensitive against geometrical errors and placement misalignments. Following this direction, EM coupling can be exploited instead of ohmic contact to connect antennas on a flexible substrate to Si chips or, more generally, to the active circuitry [85]. This technique exploits a planar heterogeneous transformer, with the primary and secondary windings implemented on the antenna substrate and the Si chip, respectively. In this way, the galvanic contacts and the soldering process are avoided, and the final structures have been proven much more robust to alignment errors than traditional ohmic techniques without any significant performance degradation. By artificially applying a misalignment of $150\text{ }\mu\text{m}$, which is the common dimension of a soldering pad, the technology proposed in [85] causes a loss increment of only 0.1 dB, due to the applied misalignment, while the same misalignment, when adopting ball grid arrays, would have implied missing the contact. This approach is quite attractive especially in combination with nonrigid materials where mechanical stress can result in significant substrate deformations. Recent contributions show the application of the aforementioned approach to inkjet printed antenna on PET substrate coupled to the chip for wireless nodes [86] and a textile patch antenna, magnetically coupled to the active circuitry, suitable for garment integration (see Fig. 9) [87], the reflection coefficient of which is shown in Fig. 10.

In order to testify the robustness of the proposed solution against uncertainties inherent to textile and garment electronics assembly, the radiation efficiency of the antenna, as a function of horizontal and vertical misalignment of the two transformer windings, used to perform the magnetic coupling, is plotted in Fig. 11(a) and (b), respectively. This technique can be extended also to interlayer communications of multilayer devices, and an example is documented in [88], where the circuitry fabricated on different garments communicates by means of overlapped coils.

V. CHIPLESS APPROACH

It has already been discussed that SS represents a possible technology for the development of killer applications within the IoT paradigm. Thanks to the convergence of several technologies, ranging from EH and sensing to RFID and LAE, SS can afford complex functions. For example, SSs can be used in intelligent buildings for structural monitoring and alarms (fire, for instance). To achieve these goals, SS must be equipped with a huge number of tags, each one monitoring a small portion of the surface itself.

The passive RFID systems can be divided into two families, namely, chip-based and chipless tags. The first family usually exploits a low-power complementary metal-oxide-semiconductor (CMOS) chip to implement the

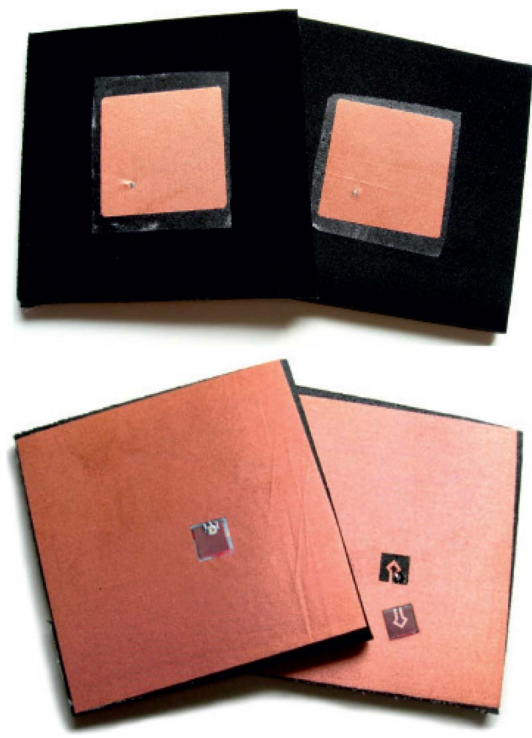


Fig. 9. Example of textile patch antennas operating at 2.4 GHz. The antenna and the ground plane are made of Flectron, a conductive textile, and the substrate is black foam. These materials are flexible and integrable in the garments. Magnetic coupling is exploited to connect the antenna and the active circuitry on flexible substrate. After [87].

main tag functions [RF carrier rectification, dc voltage regulation, amplitude shift-keying (ASK) demodulation, IDentification code (ID) decoding, load modulation, etc.] and thus can be adapted to sensor applications by a few additional circuit blocks [signal conditioning,

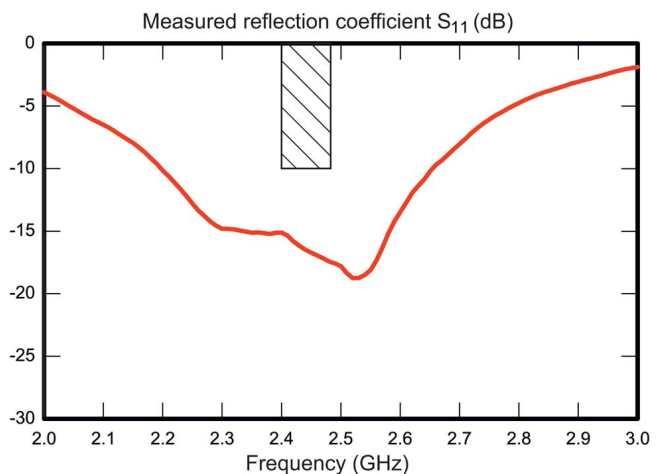


Fig. 10. Measured reflection coefficient of the previous textile antenna in the frequency band 2.4–2.48 GHz. After [87].

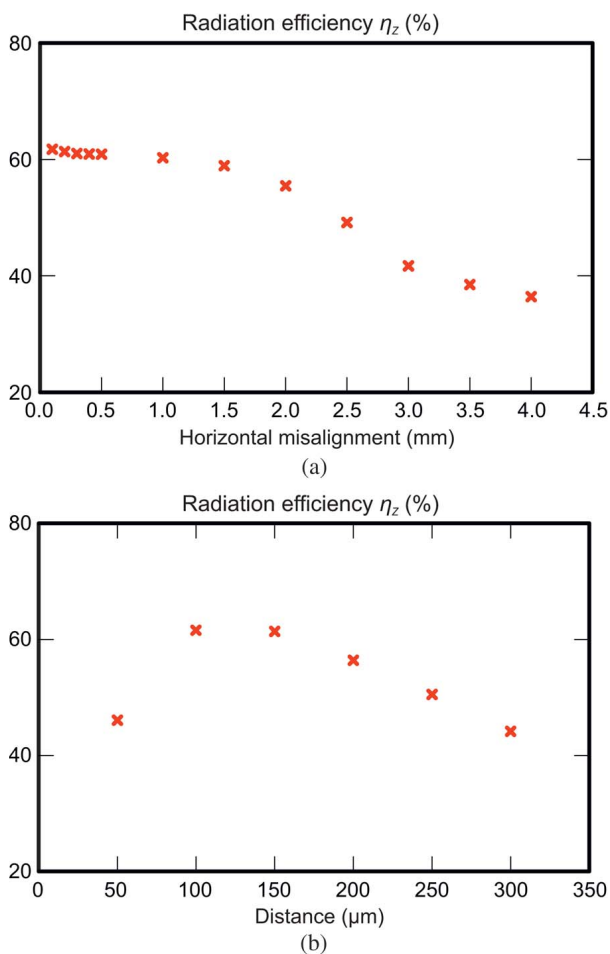


Fig. 11. Variation of the radiation efficiency evaluated versus (a) horizontal and (b) vertical misalignment between the antenna and the circuit windings. This test allows the robustness of the antenna performances against mounting uncertainties inherent to textile electronics to be evaluated at glance. After [87].

analog-to-digital converter (ADC), etc.]. The main advantage of such an approach is the digital modulation of the transmitted signal, and thus the flexibility of the related data treatment, as shown in [89] and [90]. The production costs of chip-based tags are mostly associated with the heterogeneous integration of the silicon chip with the antenna [85], [91], the latter being manufactured typically on a flexible substrate or a textile substrate [92]–[97].

In order to reduce the aforementioned costs and to save as much energy as possible, solutions requiring minimum amount of electronics must be pursued. For this purpose, the chipless tag family was introduced and applied to wireless sensing in the recent years [98]–[103]. It is worth recalling here that the introduced buzzword “chipless” stands for a family of tags that are actually able to implement their functionalities by using only a few lumped components and passive distributed elements, without requiring any electronic integrated circuit (IC), the chip indeed, to be mounted.

The standard chipless tags (i.e., only coding and no sensing) exploit, basically, two mechanisms, namely, time-domain and frequency-domain scattering [64]. In the first case, the elapsed time between multiple reflections is used for coding. These reflections are obtained, at tag level, by connecting the antenna to a transmission line structure with several discontinuities. In the second case, instead, the tag has a specific frequency signature that is decoded at the reader level; to implement such a behavior, a coded series of resonators is realized on the tag antenna in order to reflect or not the corresponding frequency. Both approaches (time and frequency domain) lead to tag circuits that are not necessarily easy to miniaturize; nevertheless, it is worth noting that they are compliant with the LAE paradigm.

When dynamic sensor information has to be added to the static identification, we talk about chipless RFID sensor tags; these exploit an antenna, the electrical properties of which are controlled by the change of the physical parameter to be detected. There are, mostly, two proposed approaches for this. The first one is to induce a permanent change in the antenna property when a certain critical threshold (acceleration, temperature, fluid level, etc.) is exceeded [104]; this is useful for alarm type operations. The second one exploits a sensing load, i.e., a load the impedance of which is controlled by the sensed variable, connected to an antenna [105]. In both cases, the whole wireless sensor system (tag and reader) needs to have absolute accuracy, thus limiting the system performance with respect to both distance and fabrication tolerances.

A different method has been recently introduced in [106]. In this paper, a novel sensing principle is associated to the generation of an intermodulation signal from a tag, the latter being illuminated by two waves at different frequencies. The advantage of this idea is that the tag response is generated at a known frequency, thus the presence or the absence of such a signal can hardly be misinterpreted. Similar techniques have been used in harmonic radar systems [107] and in one-bit frequency doubling tags [108].

In line with the above ideas, a novel and completely original approach was proposed in [20] and [109] to solve the issue of absolute accuracy of the most of the passive chipless RFID sensors. The chipless tag described in [109] is based on the harmonic radar concept [110], [111], i.e., on a tag that, being illuminated by a carrier at frequency f_0 , is capable of generating the second harmonic $2f_0$.

A simplified block diagram of the tag is illustrated in Fig. 12. For this purpose, the sensor information is encoded as the phase difference between two signals, one acting as the reference signal for the other one. First, the tag receives a carrier at frequency f_0 . Then, two equal signals at frequency $2f_0$ are generated by means of a diode-based frequency doubler and a power divider. At this point, one of the two signals is phase-shifted using a passive sensing element. Finally, the $2f_0$ signals are reirradiated by

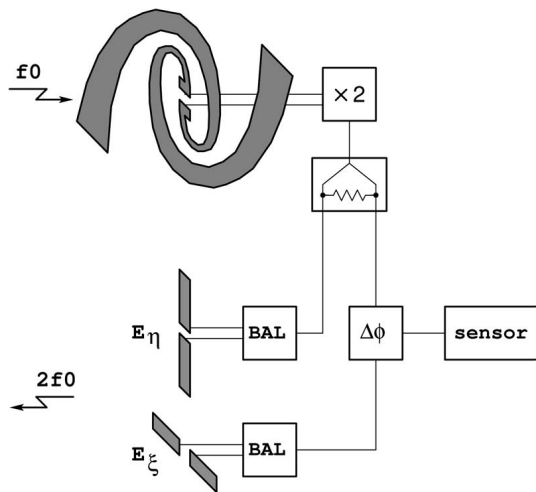


Fig. 12. Simplified block diagram of a harmonic chipless tag with sensing capabilities. After [109].

exploiting two orthogonally polarized antennas. With this approach, the sensor information can be extracted by a suitable reader equipped with two complex (I/Q) receivers.

It must be observed that chipless tags, due to their inherent simplicity and extremely low number of lumped components, are easily realizable on flexible substrates by means of metal laminate [29], [30] and inkjet printing technologies. In particular, antennas [112], diodes [113], and passive sensing elements [114]–[117], i.e., all the main tag components, have already been experimented in cellulose-based materials. This will soon make SSs, equipped with sensing chipless tags, feasible at affordable prices.

VI. QUASI-OPTICS

“Quasi-optics concerns the propagation of EM radiation when the size of the wavelength is comparable to the size of the optical components (e.g., lenses, mirrors, and apertures) and hence diffraction effects become significant” [118].

In optics, operations are usually performed by using lenses. At EM frequencies, by following the quasi-optics analogy, lenses become large arrays, several wavelengths in size, of unconnected elements, each of them being able to get part of the signal incident on the array (usually focused by using a Gaussian beam), to carry out an operation and to irradiate the modified signal. The sum of the radiated signals modified by the array elements ends up in a radiated beacon elaborated with respect to the incident one [118]–[120]. From a historical point of view, quasi-optics was first introduced experimentally by Heinrich Hertz in the late 1880s [120] when he demonstrated the possibility of collimating EM signals on a multiwavelength surface by using cylindrical reflectors and studying effects that, until that time, were observed only at infrared and visible EM spectrum.

After more than 70 years, owing to the increasing demand for bandwidth and to the development of optical wavelength systems, quasi-optics experienced its palinogenesis at the millimeter and submillimeter wavelengths.

We can classify the quasi-optical components into three main categories: frequency independent, frequency selective, and active devices. Frequency-independent surfaces include: delay lines, polarizing grids, hybrid junctions [121], attenuators [122], power dividers [123] and combiners [124], nonreciprocal devices [125], [126], absorbers, and calibration loads. Frequency-selective surfaces [127]–[129] include: inductive grids, capacitive grids, resonant grids, thick structures (perforated plates), and interferometers. Active devices include: oscillators [129], [130], amplifiers [131], [132], mixers [133], [134], phase shifters [135], [136], multipliers [108], [137]–[139], and switches [140]. This approach has been used so far mainly at millimeter and submillimeter frequencies because, being the size of the apparatuses proportional to the wavelength of the radiated wave, lower frequencies would have been prohibitive due to the very large size required. With the present development of technologies for LAE, however, quasi-optics has become a feasible approach even at RF and microwave bands, where large arrays of operational elements can be conceived.

Inheriting the quasi-optical approach, contact-less EM wave processing (filtering, frequency conversion, selective shielding, etc.) can be implemented even at low frequencies (in the order of megahertz). Two pioneer examples are switches [140] and the cross-dipole frequency doubler, proposed in [108], and implemented in [141], where, among various operating principles, the generation of harmonics is chosen to demonstrate the feasibility of such a component at microwave frequencies.

The layout of the proposed quasi-optical frequency doubler is shown in Fig. 13. The structure is inkjet printed on a cellulose-based substrate (a piece of photographic paper from Kodak). It consists of two crossed $\lambda/2$ dipoles. The longest dipole receives the incoming power at the fundamental frequency $f_0 = 3.5$ GHz, while the shortest one transmits the generated power at the doubled frequency $2f_0$ in an orthogonally polarized orientation. The length of the dipole operating at f_0 is 32 mm, while the $2f_0$ dipole is 16 mm long. The width of the tracks used to implement the dipoles is about 2 mm. The multiplication is provided by four diodes in a bridge configuration, thus forming a fully balanced multiplier unit.

Due to the omnidirectional nature of the dipole antenna, the harmonic signal is irradiated with the same intensity in the azimuthal plane (small differences are due to both the dielectric substrate and the planar nature of the dipole conductors). This means that the harmonic signal is reflected toward the reader and the transmitter toward other directions at the same time. A measurement of the received power at $2f_0 = 7$ GHz is reported in Fig. 13(b). Here the interrogation distance is 10 cm and the

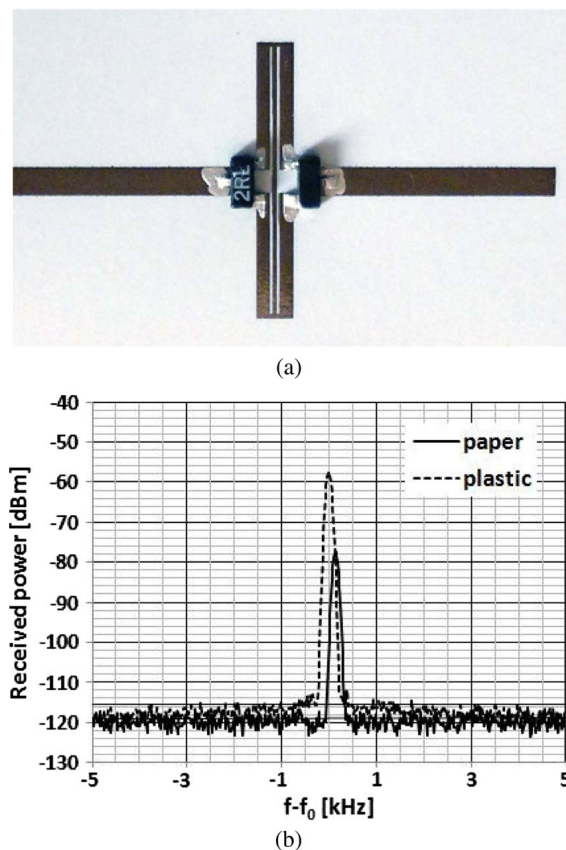


Fig. 13. Cellulose-based prototype of the (a) crossed-dipole frequency doubling tag and (b) measured second-harmonic response. The measurements have been carried out interrogating the tag at $f_0 = 3.5$ GHz and receiving the $2f_0 = 7$ GHz frequency component. The interrogation distance is 10 cm, and the transmitted power is equal to 20 dBm. The transmitter is equipped with a two-element Yagi antenna at f_0 , while the receiver uses a helix antenna at $2f_0$. The fundamental frequency dipole is 32 mm long. After [141].

transmitted power is equal to 20 dBm. The transmitter (reader side) is equipped with a two-element Yagi antenna at f_0 , while the receiver (reader side) uses a helix antenna at $2f_0$. In these conditions, the power received from the cellulose-based (paper) tag prototype at $2f_0$ is about -80 dBm. The same structure implemented on a plastic substrate produces more power, mainly because of a better frequency tuning. An improved efficiency could be achieved by: 1) adopting a frequency multiplier with better harmonic terminations; and 2) using directive antennas in order to address the power only toward the reader.

In the frame of the IoT, the crossed-dipole tag is a very simple one-bit tag that can alarm a system when it is placed within the range of the reader. However, with very simple modifications, this idea can be used to implement a variety of on/off sensors (the paper substrate can be easily torn when a certain mechanical strain is exceeded).

The crossed-dipole structure can also be used as a building block to form arrays, an example being shown in Fig. 14. These arrays are mainly intended for LAE applica-

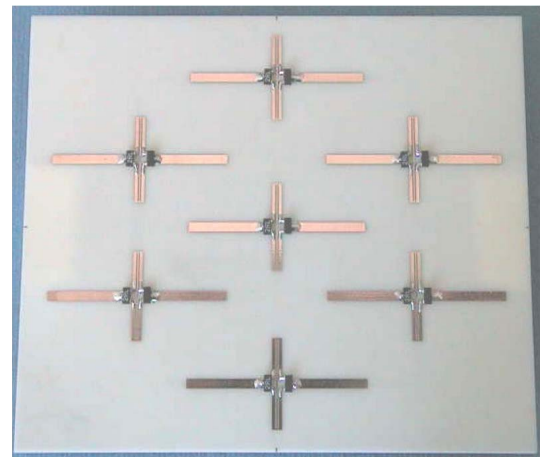


Fig. 14. Example of quasi-optical frequency doubler based on an array of crossed dipoles. This structure is implemented on a Rogers substrate, but this can be substituted with a cellulose-based material to reduce costs and obtain mechanical flexibility.

tions where a complete surface can be interrogated and answered by generating a harmonic signal. The fabricated prototype uses a Rogers substrate, thus it is not flexible. However, adopting a cellulose-based substrate, a flexible structure can be built. The bending capability of cellulose-based circuits is quite good and only limited by the discrete components mounted on them.

The second example consists of a paper-based contactless frequency doubler for harmonic RFID applications [142]. The doubler, realized on paper substrate, generates the harmonic signal by means of a single Schottky diode. The system operates at 7.5 and 15 MHz, and these frequencies are chosen, without lack of generality, to accomplish the realization of a fully organic frequency doubler exploiting paper printed coils and organic diode (pentacene-based), the present frequency limit of which is around 15 MHz [143]. Fig. 15 shows a picture of the organic tag, while Fig. 16 shows the doubling efficiency of the organic tag versus transmitting/receiving (TX/RX) distance, assuming TX power as a parameter (for the sake of completeness, it is worth noting that TX and RX antennas of the reader are equal to the RX and TX antennas of the tag, respectively).

As a final remark, it is worth noting that, to the authors' knowledge, only planar developments of quasi-optical arrays have been proposed so far; reasonably, combining quasi-optics with LAE related technologies can lead, in the near future, to new SS solutions only in a limited planar extent.

VII. SMART FLOOR

The new concept of smart cities is generating a group of new scenarios that will impose a new way people interact with the environment. This immersion brings the IoT to a new level of relationship with people and environment,

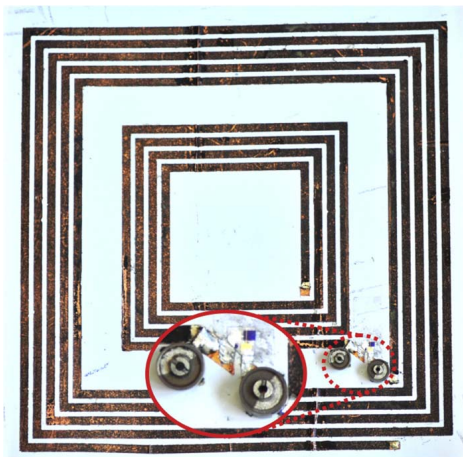


Fig. 15. Fully organic tag prototype of the frequency doubling tag operating at 7.5–15 MHz. After [142].

where the scenario around is aware of people's needs and can interact with their way of living.

This new concept brings IoT to areas that cover broad topics, including transportation, energy distribution, data communications, and all technologies in a sense that they will become transparent to the normal users and citizens.

The growth of smart cities will significantly increase the quality of life, the reduction of energy waste, and the availability of information by using ICT. All these developments have, as a motivation, the overall inclusion of people into the city in a way that ICT should become completely embedded into our surroundings.

These new concepts are viable only if the smart environments are enabled by IoT. IoT is actually taking shape and is growing everyday through the number of devices that get connected to each other.

Nevertheless, most of these devices that team up with each other to build up the IoT world are powered by some

kind of power sources. This is actually the main limitation of present IoT solutions. In order to be able to create real IoT environments, RFID, wireless power transfer (WPT), and EH devices appear as a major enabling technology for the IoT, due to their inherent simplicity and ability to provide sensing to remote objects without the need for constant powering.

In this scenario, the concept of a smart floor becomes real. Smart floors should be capable of interacting with the environment seamlessly and be aware of persons and objects on top of them.

The focus of this section is going to be smart floors as an information system, where RFID capabilities are used to provide an identification and information source embedded into the floor. This massive RFID immersion will allow to create low-power high accuracy location, navigation, and, generally speaking, an information system that can team up with passers in a noninvasive way.

In this approach, the system uses passive RFID tags that are spread beneath a flooring in order to create a map that can be read with a mobile unit that might be self-powered through energy harvested from the movements of the subject to be located [144], [145].

This new location system based on smart floors can actually be extremely competitive when compared with existing solutions; among them, we can take into consideration those based on image processing [146]; they provide a high level of information at the price of high cost, power consumption, and intrusiveness. Another approach is based on pressure sensors [146], [147], providing actually a different type of smart floors; pressure sensors are nonintrusive and can be less expensive in terms of equipment when compared to the imaging systems; however, they can still be quite expensive to install into the floors; moreover, they do not allow for seamless identification of an individual in a given space. Eventually, ultrasounds [148] and RF localization system detection [149] have to be listed; although very flexible, they require dedicated communication infrastructures, additional complexity and costs, and they are mostly sensitive to environmental changes, both in terms of accuracy and functionalities.

The just mentioned smart-floor-based system tackles most of these challenges as it is very low cost, able to have a good, and precisely predictable, accuracy, and able to detect different users in a given space.

A. RFID-Based Smart Floor Including Material Aspects

Smart environments and floors should be completely seamless to the users. This entails the need to embed electronic devices into the environment in a noninvasive way. Nevertheless, this embedding of electronic devices, mainly wireless transceivers into the floor, is not a simple matter. Floors, in fact, have been made by almost the same kind of materials for centuries; tile industries are weakly available to introduce new materials to match

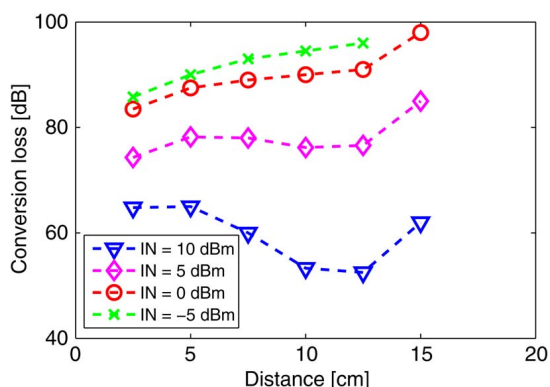


Fig. 16. Conversion (doubling) loss of the reader tag harmonic RFID system as a function of the reader tag distance, assuming the output reader power as a parameter. After [142].

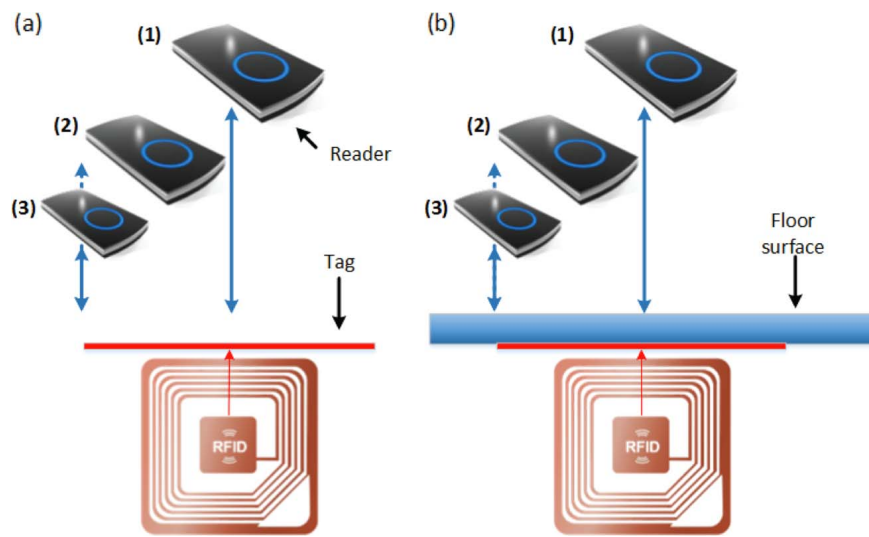


Fig. 17. Readable distance test scheme (a) without and (b) with tile. After [144].

requirements posed by embedded electronics. Similar considerations can be made about the consolidated techniques to build apartments and houses: they are quite mature and whatever adaptation of them to embedded electronic systems is unrealistic. The consequence of this is that constitutive elements of SSs embedded into the floors must be suitable to materials and technologies already present: materials available are those adopted for tiles and SSs must be adapted to building constraints.

In this section, we focus on the most important approaches for the characterization of the EM properties of the materials, commonly adopted in floors, and their interactions with our electronic radio systems. As an example, ceramic tiles are going to be selected as the floor element where electronic tags have to be embedded.

Ceramic tiles have been used for ages to pave floors. These make up a great deal of most floor types in public buildings, from airports to banks, therefore, they are the most interesting flooring elements to investigate.

As the first approach, the study of the influence of some materials for floor surfaces, such as ceramic, cork laminates, and wood, in the communication between the transmitter and receiver devices has to be made; in this

case, low-frequency (13 MHz) inductors are going to be used as the wireless interface.

In order to do the measurements, traditional RFIDs are used, which simplify the measurement approach significantly. A test setup is shown in Fig. 17, and experimental results are summarized in Table 3. What can be seen from the results presented in the table is that none of the tested materials affect the electrical characteristics of the RFID propagation significantly.

Another approach to the measurement is to evaluate the impact of the presence of metal inclusions beneath the ground; these can appear from pipes or from buildings supporting structures. In order to test this scenario, the presence of a metal sheet close to the coil was tested to verify its impact on the RFID reading distance. The test setup is presented in Fig. 18. In this case, when the reader is aligned (1) with the center of the coil beneath the tile, a minimum distance of 10 mm between the metallic sheet and the tag must be guaranteed in order to allow for the proper reading of the tag. In the other approach, the edge aligned scenario (2), the minimum distance between the metallic sheet and the tag increases to 30 mm to allow for communication.

Table 3 Results From Average Readable Distance Test

Tile type	Aligned (1)	Edge aligned (2)	Unaligned (3)
Without tile	4.5 cm	4.3 cm	2.4cm
Ceramic tile 4 mm thick	4.5 cm	4.3 cm	2.4cm
Ceramic tile 6 mm thick	4.5 cm	4.3 cm	2.4cm
Ceramic tile 7 mm thick	4.5 cm	4.3 cm	2.4cm
Cork laminate 5 mm thick	4.5 cm	4.3 cm	2.2cm
Wooden floor 8 mm thick	4.3 cm	4.2 cm	2.2cm

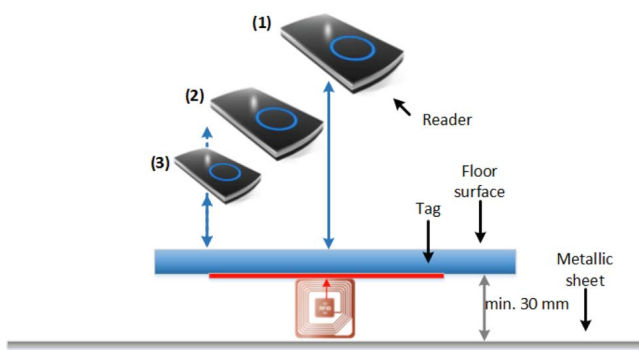


Fig. 18. Readable distance test scheme with metallic sheet presence. After [144].

This test allows us to conclude that, in a real scenario, when considering the typical distance from the antenna to the floor, where the reader is usually embedded into a mobile device, a minimum distance from the tile to any metal inclusions in the ground has to be guaranteed. As seen, this safe distance should be at least 30 mm.

B. Navigation Approach Based on Smart Floors

A meaningful example of the applications of the smart floor concept is the demonstrator developed at the University of Aveiro, Aveiro, Portugal. It allows a nomadic RFID reader on top of it to be identified and localized by means of a smart floor.

The prototype in the present state is composed of four main components: a set of tagged tiles forming the smart floor, the nomadic reader, a wireless communication device to connect the reader to the information system, and a computer on which the location and navigation software is installed. A potential scenario of application for the monitoring of elderly housing is shown in Fig. 19. In the demonstrator presented, the RFID reader is connected to the radio unit and inserted into the user's shoes in order to read the passive tags as the user walks around a given area. The tile IDs are detected by the reader and sent to a

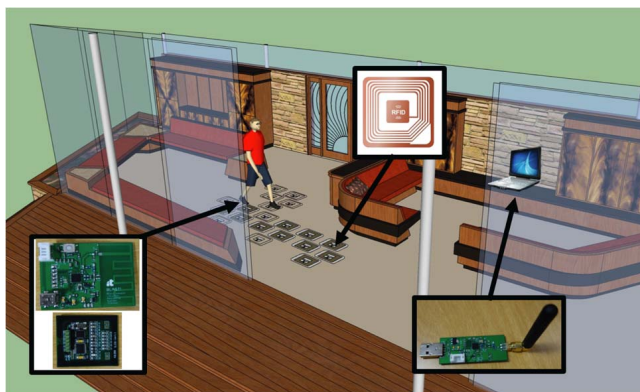


Fig. 19. Example of smart floor application scenario.

centralized information system using, without lack of generality, a nonstandard wireless communication system, purposely developed in the laboratory.

The software in the computer then decodes the ID of the smart tile, and correlates it with a preloaded referenced map, thus being able to provide the precise position of the walker in the environment.

The location can be subsequently translated to a navigation system, and combined with artificial intelligence to allow navigation, situation awareness, etc.

Plenty of applications and related solutions can be envisioned on the basis of this smart floor approach: robot control, automatic pallet managements, prevention in harsh environments, and so forth.

VIII. SMART SHOES AND BAN

The aforementioned smart floor (Section VII), initially proposed to localize moving subjects in a given area, actually allows for the implementation of a very low-cost, accurate, and reliable system able to provide each kind of detectable information from an equipped area to the Internet.

To exploit the potentiality of a smart floor, it is obvious that developing purposely conceived communication units acting, on the one hand, as readers for tag tiles and, on the other hand, as communication systems with the web is needed.

One of the investigated systems for this is the so-called smart shoe [21]. Smart shoes are intended as shoes incorporating a reader able to illuminate the tag embedded into the tile and a wireless interface to communicate data to the web. To this extent, smart shoes can be seen as hubs of BANs able, on the one hand, to get information from the surrounding environment (body included) and, on the other hand, to communicate the collected information to the Internet. According to common buzzwords, they can be seen as the second technological layer, just above the first physical one consisting of tagged objects, in a hierarchical picture of IoT. Alternatively, they provide the cloud of nomadic readers with networking capabilities required for the implementation of the so-called networked RFID (N-RFID) [150] strategies. In the referred structure [21], the necessary antenna system is inkjet printed on paper, thus exploiting the process described in Section II, and it is a trademark-logo-shaped dual-band antenna working at 900 MHz and 2.4 GHz. A block diagram and its equivalent realization are shown in Fig. 20: it is worth noting that the reader itself works at 13.5 MHz exploiting the near-field communication (NFC) concept, according to what is stated in the smart floor section; as a consequence, there are no issues about the interference between the dual-band antenna and the NFC reader. Moreover, an approach similar to [145] is proposed to power the reader: the idea here is as well to harvest the energy produced by the human walking by means of piezoelectric materials embedded into the sole of the shoe.

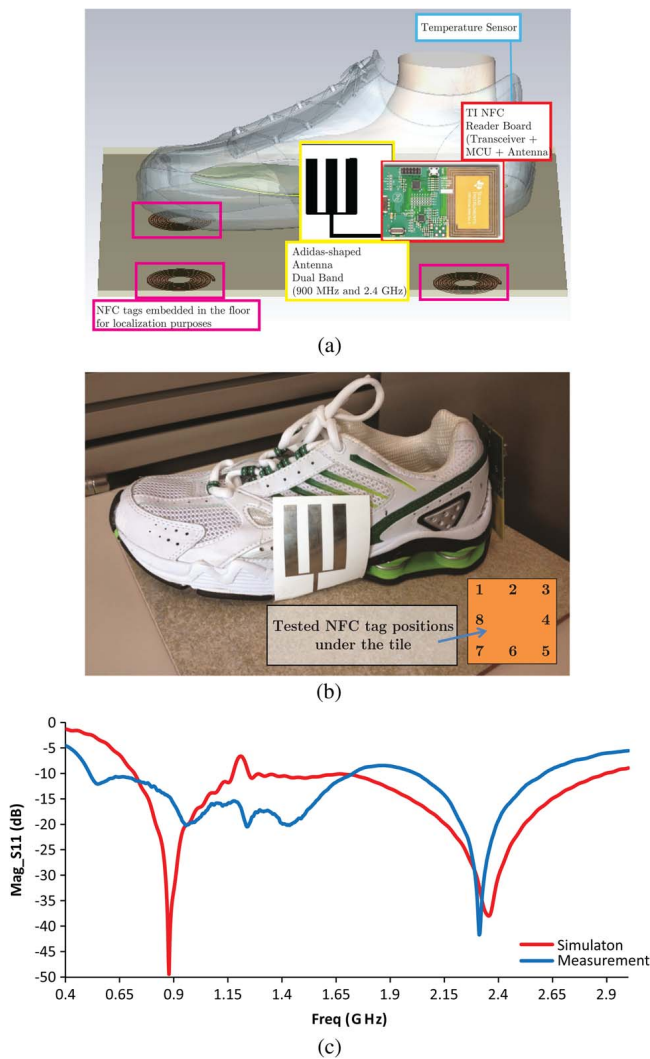


Fig. 20. (a) Block diagram, (b) photo, and (c) dual-band antenna results of the smart shoe that works as an energy autonomous reader for smart floors able to collect the localization data from the smart tiles and send them to a centralized system. After [21].

Fig. 21(a) shows the shoe with the mounted electronics consisting of a trademark-logo antenna inkjet printed on a flexible paper substrate together with the circuits in which the components [Fig. 21(b)] are fixed by conductive epoxy glue. A piezoelectric push button was embedded in the shoe to scavenge energy from human walking strike. This energy is then collected by a simple electronic circuit based on off-the-shelf components and used to supply the RFID transmitter. As reported in [145], the system is composed by the power-generator/energy-conversion device, the energy storage device, the power regulator circuit, and the RF transmitter that can broadcast the tag ID and the stored information.

When the push button is pressed, an inner spring is compressed and when the pressure exceeds a fixed threshold, the spring-loaded hammer will be released to deliver the dynamic mechanical force to the piezoelectric compo-

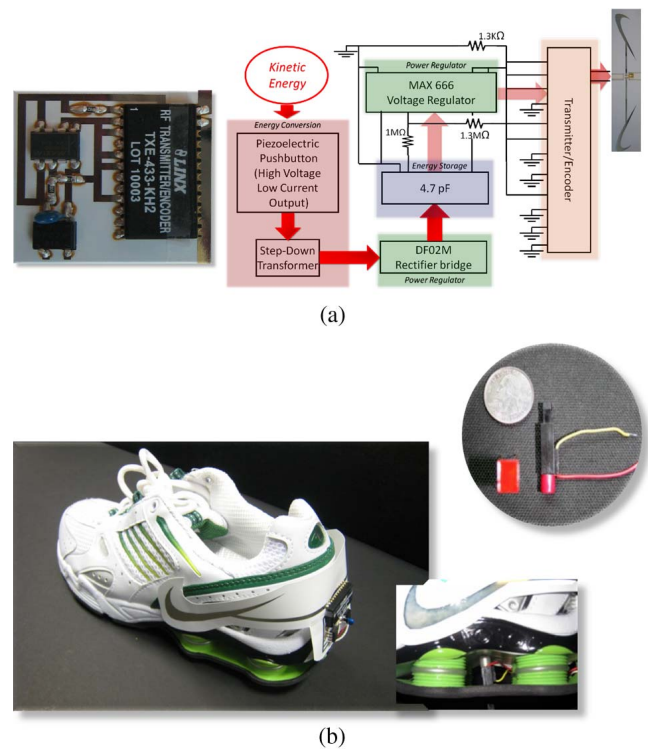


Fig. 21. (a) Mounted electronics on shoe with piezoelectric energy harvester and block diagram of the transmitting tag, driven by the EH unit. (b) Photograph of the assembled prototype showing the key components packaged on an organic flexible substrate. After [145].

nent; once the hammer strikes the piezoelectric element, a pressure wave is generated and reflected a few times between the hammer and the element, creating a mechanical resonance [151]. As a result, the generated output voltage follows closely an alternating current (ac) signal course. The signal out of the piezoelectric element is characterized by high voltage and low current; therefore, since this RF circuitry requires lower voltages at higher currents, a step-down transformer is used for better impedance matching to the following circuitry.

An energy storage device is adopted to collect the electrical energy and to provide it to the transmitter even when the external power source is temporarily unavailable; in fact, the RF transmitter takes tens of milliseconds to transmit one complete word, while the piezoelectric push button harvests energy in a transient time. To store the collected energy, a 4.7- μ F tank capacitor was chosen. An ac-dc full wave diode bridge rectifier is used to convert the ac voltage from a piezoelectric element into a dc source and a dc linear regulator is added to adapt the dc voltage across the capacitor to 3-V transmitter operating voltage. For this purpose, a MAX666 low-dropout linear regulator, providing a stable 3-V supply until the tank capacitor charge is drained below the reference level of the dc linear regulator itself, is chosen. The transmitter used, the LINX

Table 4 Shoe Energy Performance Summary

Energy provided by the pushbutton	stored in the capacitor	848.4 μJ
Utilized energy	below 2.7 V capacitor voltage, the active RFID tag stops transmitting	17.1 μJ
Available energy	$848.4 \mu\text{J} - 17.1 \mu\text{J}$	831.3 μJ
Energy required by the circuit for a one-word transmission	Power Needed for 50 ms operation: 9 mW	450 μJ

TXE-433-KH2 [152], is able to combine a highly optimized RF transmitter with an onboard encoder.

The maximum voltage across the capacitor is 19 V; therefore, the energy stored in the capacitor can be calculated to be close to 850 μJ . After the strike, the regulator becomes active, providing power to the tag circuitry; its 3-V output remains constant before it starts to drop to zero according to the capacitor discharge rate. When the voltage across the capacitor drops below 2.7 V, the active tag stops transmitting. The resulting energy left in the capacitor and not used is about 17 μJ . The required time for successful completion has been measured to be close to 50 ms; the total circuit energy consumption for a 50-ms transmission is then approximately 9 mW (Section IV). Consequently, the energy required for a one word transmission is approximately 450 μJ , much less than the power collected by the energy conversion and regulation unit. The energy performance of the smart shoe is summarized in Table 4.

“Smart” solutions like smart shoes are suitable for smart floor interaction and for collecting information (position included) from them. The smart shoe has actually a double functionality: on the one hand, it is a means to collect information from the environment (smart floor included) and from the on-body sensors and apparatuses; on the other hand, it transfers data to the Internet, via WiFi, for instance, while likely receiving control and feedback signals. To this extent, it contributes to the development of wearable electronics for body-centric communication systems, according to the scheme of Fig. 22. This class of devices is based on the BAN concept (see Fig. 22): a network of wearable computational units, sensors, energy harvesters, and transceivers networked and implemented around the human body. The information is acquired by means of several sensors and, after processing and digital modulation, is transmitted by means of off-body transceivers. The most attractive application of BANs and wearable systems, so far, is probably health monitoring [88], but the number of foreseeable applications is constantly increasing (personal fitness monitoring, personal audio system, personal alarm set, and so on). Today, a big contribution to the BANs is being given by the interaction with portable devices such as smartphones which can be exploited as gateways.

Low-power ICs, sensors, and wireless communications are key elements of the BANs, and the use of EH techniques

and mixed technologies such as RFID, as in the above described smart shoe, can contribute to the development of autonomous BANs. According to the notation adopted in [74] and [153], BANs can exploit wireless communication not only for off-body communications with other systems, but also for on-body and in-body communications to interconnect networked devices [wireless body area networks (WBANs)]. Generally, the proposed WBAN solutions are based on existing communication standards; but, recently, the IEEE 802.15.6 working group has provided a standard for short-range, wireless communications in the vicinity of, or inside, a human body based on ISM bands for BANs [154]. In this rapidly evolving scenario, smart shoes can be seen, in turn, as a promising mean to interface information coming from smart floors to the BANs and ultimately to the Internet, directly or via portable devices.

IX. ENERGY SKIN

Within SSs, another area is emerging, which requires dc energy. The availability of devices that can actually increase the battery life of our electronic gadgets [155] is the holy grail of IoT; the idea is actually to convert energy from

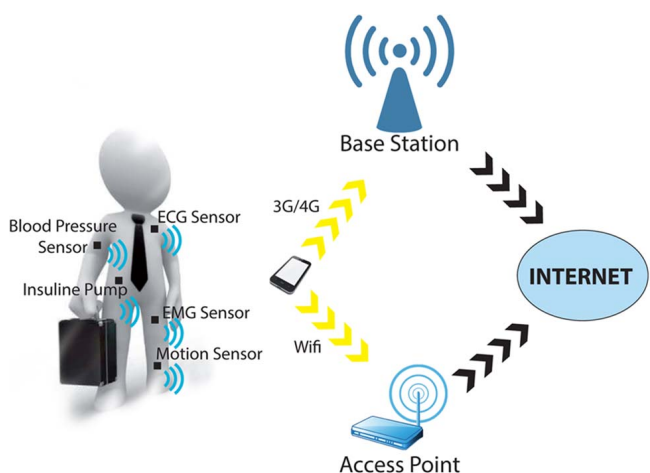


Fig. 22. BAN integrated with IoT: the data sensed on the human body and collected by smart devices are sent to the Internet through the standard protocols like third generation/fourth generation (3G/4G) and WiFi.

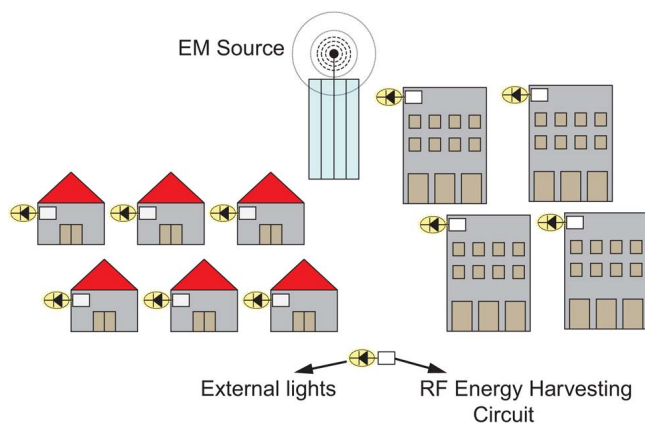


Fig. 23. EM source, likely supplied by solar energy in order to keep eco-friendliness, is used to broadcast energy to the urban neighborhood where houses are equipped with local RF-dc converters able to power supply local devices (external lamps in the example).

different sources, as solar to dc [156], EM radio signals to dc, thermal to dc [156], vibration to dc [157], etc. [158].

Portable converters from solar to dc are today commonly available on the market at very low prize. Similar portable scavengers can be easily envisioned even for other energy converters. On this basis, plenty of sophisticated and more complex solutions are being proposed. Just as an example, we report the solution in Fig. 23, where the solar energy is used to supply an EM source that broadcasts RF energy in the surrounding urban environment; this energy is converted to dc energy at building level and, in turn, exploited to supply external local lamps. This approach was conceived for space applications [159], [160], but could be used in certain conditions in earth stations as well. The concept can actually move forward and be integrated into a smart skin, in the sense that all devices could be powered up by the skin energy conversion that a person can carry

(vibrational, thermal, RF, etc.). This will become possible by integrating paper and textile radio electronic circuits in the smart skin surfaces of our clothes.

X. CONCLUSION

This paper focused on smart surfaces concept. This concept was introduced as a way to provide solutions to societal instances by means of technologies and techniques that today are gaining great momentum thanks to IoT development. The foreseeable IoT evolution, in fact, calls for systems and subsystems that are more and more energy conservative, fully autonomous (battery-less and not connected to the grid), as recyclable as possible (ultimately 100% biodegradable), flexible, and extremely low cost to be embedded in as many objects as possible. In order to meet these expectations, several technologies have to be implemented concurrently. This paper illustrates some of them, namely, recyclable and reliable materials, printing and R2R compatible techniques, conformal antennas on unconventional materials, and chipless RFID.

Subsequently, it has been shown how these technologies enable a fairly new branch of IoT development, represented just by SSs.

SSs are in their infancy; nevertheless, some examples, enabled by the aforementioned technologies, can be cited. Among them, the way to inherit “quasi-optics” and extend them to RF frequencies even below gigahertz is shown, and the smart floor implementation as a means to provide precise localization as well as assisted paths platforms has been reported. Energy skin as a means to convert several energy sources (solar, thermal, vibrational, EM, etc.) in electric one is described as well.

The reported examples must be researched as a new paradigm for potential promising developments aiming at providing new LAE solutions for the future networked society. ■

REFERENCES

- [1] European Union (EU), “The ICT sector and RDI,” Digital Agenda Scoreboard, 2012. [Online]. Available: http://ec.europa.eu/digital-agenda/sites/digital-agenda/files/scoreboard_ict_sector_and_rdi.pdf
- [2] J. Manyika et al., “How the Internet of Things is more like the Industrial Revolution than the Digital Revolution,” MGI Rep., 2013. [Online]. Available: http://www.mckinsey.com/insights/business_technology/disruptive_technologies
- [3] D. Evans, “The Internet of Things: How the next evolution of the internet is changing everything,” CISCO White papers, 2011. [Online]. Available: http://www.cisco.com/web/about/ac79/docs/innov/IoT_IBSG_0411FINAL.pdf
- [4] I. G. Smith, “The Internet of Things 2012 New Horizons,” IERC European Research Cluster on the Internet of Things, 2012.
- [5] J. Morse, “Nanofabrication technologies for roll-to-roll processing,” in *Proc. NIST-NNN Workshop*, Boston, MA, USA, Sep. 2011, pp. 1–31.
- [6] A. Arias, J. MacKenzie, I. McCulloch, J. Rivnay, and A. Salleo, “Materials and applications for large area electronics: Solution-based approaches,” *Chem. Rev.*, vol. 110, no. 1, pp. 3–24, Jan. 2010.
- [7] T. Kampke, B. Kluge, and M. Strobel, *Field and Service Robotics*. New York, NY, USA: Springer-Verlag, 2008, ser. Springer Tracts in Advanced Robotics.
- [8] M. Shur, “Giant area and flexible electronics,” in *Proc. IEEE Nanotechnol. Mater. Devices Conf.*, Oct. 2006, vol. 1, pp. 264–265.
- [9] M. Steer et al., “Global modeling of spatially distributed microwave and millimeter-wave systems,” *IEEE Trans. Microw. Theory Tech.*, vol. 47, no. 6, pp. 830–838, Jun. 1999.
- [10] A. Rida, L. Yang, R. Vyas, and M. Tentzeris, “Conductive inkjet-printed antennas on flexible low-cost paper-based substrates for RFID and WSN applications,” *IEEE Antennas Propag. Mag.*, vol. 51, no. 3, pp. 13–23, Jun. 2009.
- [11] F. Alimenti, P. Mezzanotte, M. Dionigi, M. Virili, and L. Roselli, “Microwave circuits in paper substrates exploiting conductive adhesive tapes,” *IEEE Microw. Wireless Compon. Lett.*, vol. 22, no. 12, pp. 660–662, Dec. 2012.
- [12] D. Tobjörk and R. Österbackaa, “Paper electronics,” *Adv. Mater.*, vol. 23, no. 17, pp. 1935–1961, 2011.
- [13] P. Calvert, “Inkjet printing for materials and devices,” *Chem. Mater.*, vol. 13, no. 10, pp. 3299–3305, 2001.
- [14] G. Orecchini et al., “Inkjet printed organic transistors for sustainable electronics,” in *Proc. 60th Electron. Compon. Technol. Conf.*, Jun. 2010, pp. 985–989.
- [15] L. Yang, G. Orecchini, G. Shaker, H.-S. Lee, and M. Tentzeris, “Battery-free RFID-enabled wireless sensors,” in *IEEE MTT-S Int. Microw. Symp. Dig.*, May 2010, pp. 1528–1531.
- [16] G. Shaker, S. Safavi-Naeini, N. Sangary, and M. Tentzeris, “Inkjet printing of ultrawideband (UWB) antennas on paper-based substrates,” *IEEE Antennas*

- Wireless Propag. Lett., vol. 10, pp. 111–114, 2011.
- [17] R. Vyas et al., “Inkjet printed, self powered, wireless sensors for environmental, gas, and authentication-based sensing,” *IEEE Sensors J.*, vol. 11, no. 12, pp. 3139–3152, Dec. 2011.
- [18] G. Orecchini et al., “Design and fabrication of ultra-low cost radio frequency identification antennas and tags exploiting paper substrates and inkjet printing technology,” *IET Microw. Antennas Propag.*, vol. 5, no. 8, pp. 993–1001, Jun. 2011.
- [19] S. Kim et al., “Monopole antenna with inkjet-printed EBG array on paper substrate for wearable applications,” *IEEE Antennas Wireless Propag. Lett.*, vol. 11, pp. 663–666, 2012.
- [20] S. Kim et al., “No battery required: Perpetual RFID-enabled wireless sensors for cognitive intelligence applications,” *IEEE Microw. Mag.*, vol. 14, no. 5, pp. 66–77, Jul. 2013.
- [21] C. Mariotti, V. Lakafosis, M. Tentzeris, and L. Roselli, “An IPv6-enabled wireless shoe-mounted platform for health-monitoring,” in *Proc. IEEE Top. Conf. Wireless Sensors Sensor Netw.*, Jan. 2013, pp. 46–48.
- [22] K. Sangkil et al., “Inkjet-printed antennas, sensors and circuits on paper substrate,” *IET Microw. Antennas Propag.*, vol. 7, no. 10, pp. 858–868, 2013.
- [23] B. Cook, J. Cooper, and M. Tentzeris, “Multi-layer RF capacitors on flexible substrates utilizing inkjet printed dielectric polymers,” *IEEE Microw. Wireless Compon. Lett.*, vol. 23, no. 7, pp. 353–355, Jul. 2013.
- [24] B. Cook, J. Cooper, S. Kim, and M. Tentzeris, “A novel inkjet-printed passive microfluidic RFID-based sensing platform,” in *IEEE MTT-S Int. Microw. Symp. Dig.*, Jun. 2013, DOI: 10.1109/MWSYM.2013.6697592.
- [25] B. Cook, B. Tehrani, J. Cooper, and M. Tentzeris, “Multilayer inkjet printing of millimeter-wave proximity-fed patch arrays on flexible substrates,” *IEEE Antennas Wireless Propag. Lett.*, vol. 12, pp. 1351–1354, 2013.
- [26] C. Mariotti, B. Cook, L. Roselli, and M. Tentzeris, “High-performance inkjet-printed metal-insulator-metal (MIM) capacitors on lossy silicon substrate *IEEE Microw. Wireless Compon. Lett.*, 2014.
- [27] D. Angmo, T. T. Larsen-Olsen, M. Jorgensen, R. R. Sazndergaard, and F. C. Krebs, “Roll-to-roll inkjet printing and photonic sintering of electrodes for ITO free polymer solar cell modules and facile product integration,” *Adv. Energy Mater.*, vol. 3, no. 2, pp. 172–175, 2013.
- [28] R. Sazndergaard, M. Hessel, D. Angmo, T. T. Larsen-Olsen, and F. C. Krebs, “Roll-to-roll fabrication of polymer solar cells,” *Mater. Today*, vol. 15, no. 1–2, pp. 36–49, 2012.
- [29] F. Alimenti et al., “A 1.2 v, 0.9 mW UHF VCO based on hairpin resonator in paper substrate and Cu adhesive tape,” *IEEE Microw. Wireless Compon. Lett.*, vol. 23, no. 4, pp. 214–216, Apr. 2013.
- [30] F. Alimenti et al., “24 GHz single-balanced diode mixer exploiting cellulose-based materials,” *IEEE Microw. Wireless Compon. Lett.*, vol. 23, no. 11, pp. 596–598, Nov. 2013.
- [31] C. Mariotti et al., “Modeling and characterization of copper tape microstrips on paper substrate and application to 24 GHz branch-line couplers,” in *Proc. Eur. Microw. Conf.*, Oct. 2013, pp. 794–797.
- [32] L. Guoyu and W. Zhenkai, “Summarize of rfid technology and typical application,” in *Proc. Cross Strait Quad-Regional Radio Sci. Wireless Technol. Conf.*, Jul. 2011, vol. 2, pp. 1032–1036.
- [33] L. Wang, L. D. Xu, Z. Bi, and Y. Xu, “Data cleaning for RFID and WSN integration,” *IEEE Trans. Ind. Inf.*, vol. 10, no. 1, pp. 408–418, Feb. 2014.
- [34] H. Deng et al., “Design of sensor-embedded radio frequency identification (SE-RFID) systems,” in *Proc. IEEE Int. Conf. Mechatron. Autom.*, Jun. 2006, pp. 792–796.
- [35] S. Mohamad, F. Tang, A. Amira, A. Bermak, and M. Benammar, “A low power oscillator based temperature sensor for RFID applications,” in *Proc. 5th Asia Symp. Quality Electron. Design*, Aug. 2013, pp. 50–54.
- [36] D. Hotte, R. Siragusa, Y. Duroc, and S. Tedjini, “Performance optimization for the choice of impedances in the design of passive RFID tags,” in *Proc. IEEE-APS Top. Conf. Antennas Propag. Wireless Commun.*, Sep. 2013, pp. 1349–1352.
- [37] M. Donelli, “Guidelines for the design and optimization of wireless sensors based on the modulated scattering technique,” *IEEE Trans. Instrum. Meas.*, vol. 63, no. 7, pp. 1824–1833, Jul. 2014.
- [38] A. Ricci, M. Grisanti, I. De Munari, and P. Ciampolini, “Improved pervasive sensing with RFID: An ultra-low power baseband processor for UHF tags,” *IEEE Trans. Very Large Scale Integr. (VLSI) Syst.*, vol. 17, no. 12, pp. 1719–1729, Dec. 2009.
- [39] L. Chen et al., “Range extension of passive wake-up radio systems through energy harvesting,” in *Proc. IEEE Int. Conf. Commun.*, Jun. 2013, pp. 1549–1554.
- [40] S. Sauer, A. Turke, A. Weder, and W.-J. Fischer, “Inkjet printed humidity threshold monitoring sensor solution with irreversible resistance change for passive RFID applications,” in *Proc. IEEE Sensors*, Nov. 2013, DOI: 10.1109/ICSENS.2013.6688307.
- [41] N. Cho, S.-J. Song, S. Kim, S. Kim, and H.-J. Yoo, “A 5.1-uW UHF RFID tag chip integrated with sensors for wireless environmental monitoring,” in *Proc. 31st Eur. Solid-State Circuits Conf.*, Sep. 2005, pp. 279–282.
- [42] M. Philipose et al., “Battery-free wireless identification and sensing,” *IEEE Perv. Comput.*, vol. 4, no. 1, pp. 37–45, Jan. 2005.
- [43] D. De Donno, L. Catarinucci, and L. Tarricone, “A battery-assisted sensor-enhanced RFID tag enabling heterogeneous wireless sensor networks,” *IEEE Sensors J.*, vol. 14, no. 4, pp. 1048–1055, Apr. 2014.
- [44] N. Guilar, T. Kleeburg, A. Chen, D. Yankelevich, and R. Amirtharajah, “Integrated solar energy harvesting and storage,” *IEEE Trans. Very Large Scale Integr. (VLSI) Syst.*, vol. 17, no. 5, pp. 627–637, May 2009.
- [45] D. Brunelli, C. Moser, L. Thiele, and L. Benini, “Design of a solar-harvesting circuit for batteryless embedded systems,” *IEEE Trans. Circuits Syst. I, Reg. Papers*, vol. 56, no. 11, pp. 2519–2528, Nov. 2009.
- [46] D. Kwon, G. Rincon-Mora, and E. Torres, “Harvesting ambient kinetic energy with switched-inductor converters,” *IEEE Trans. Circuits Syst. I, Reg. Papers*, vol. 58, no. 7, pp. 1551–1560, Jul. 2011.
- [47] S. Mehraeen, S. Jagannathan, and K. Corzine, “Energy harvesting from vibration with alternate scavenging circuitry and tapered cantilever beam,” *IEEE Trans. Ind. Electron.*, vol. 57, no. 3, pp. 820–830, Mar. 2010.
- [48] T. Le, K. Mayaram, and T. Fiez, “Efficient far-field radio frequency energy harvesting for passively powered sensor networks,” *IEEE J. Solid-State Circuits*, vol. 43, no. 5, pp. 1287–1302, May 2008.
- [49] G. Papotto, F. Carrara, and G. Palmisano, “A 90-nm CMOS threshold-compensated RF energy harvester,” *IEEE J. Solid-State Circuits*, vol. 46, no. 9, pp. 1985–1997, Sep. 2011.
- [50] S. Rahimzadeh, S. Korhummel, B. Kaslon, and Z. Popovic, “Scalable adaptive wireless powering of multiple electronic devices in an over-moded cavity,” in *Proc. IEEE Wireless Power Transfer*, May 2013, pp. 84–87.
- [51] S. Scorcioni, L. Larcher, A. Bertacchini, L. Vincetti, and M. Maini, “An integrated RF energy harvester for UHF wireless powering applications,” in *Proc. IEEE Wireless Power Transfer*, May 2013, pp. 92–95.
- [52] Z. Popovic, “Far-field wireless power delivery and power management for low-power sensors,” in *Proc. IEEE Wireless Power Transfer*, May 2013, DOI: 10.1109/WPT.2013.6556867.
- [53] E. Falkenstein, M. Roberg, and Z. Popovic, “Low-power wireless power delivery,” *IEEE Trans. Microw. Theory Tech.*, vol. 60, no. 7, pp. 2277–2286, Jul. 2012.
- [54] S. Roundy, P. K. Wright, and J. Rabaey, “A study of low level vibrations as a power source for wireless sensor nodes,” *Comput. Commun.*, vol. 26, no. 11, pp. 1131–1144, 2003.
- [55] C. D. Richards, M. J. Anderson, D. F. Bahr, and R. F. Richards, “Efficiency of energy conversion for devices containing a piezoelectric component,” *J. Micromech. Microeng.*, vol. 14, no. 5, 2004, DOI: 10.1088/0960-1317/14/5/009.
- [56] S. R. Anton and H. A. Sodano, “A review of power harvesting using piezoelectric materials (2003–2006),” *Smart Mater. Struct.*, vol. 16, no. 3, 2007, DOI: 10.1088/0964-1726/16/3/R01.
- [57] Cymbet Corporation, “Energy harvesting and storage.” [Online]. Available: <http://www.cymbet.com/design-center/energy-harvesting.php#>
- [58] T. Armstrong, “Energy harvesting applications are everywhere,” *RTC*, May 2011. [Online]. Available: <http://www.rtcmagazine.com/articles/view/102133>
- [59] D. Puccinelli and M. Haenggi, “Wireless sensor networks: Applications and challenges of ubiquitous sensing,” *IEEE Circuits Syst. Mag.*, vol. 5, no. 3, pp. 19–31, 2005.
- [60] L. Roselli et al., “WPT, RFID and energy harvesting: Concurrent technologies for the future networked society,” in *Proc. Asia-Pacific Microw. Conf.*, Nov. 2013, pp. 462–464.
- [61] H. Liu, M. Bolic, A. Nayak, and I. Stojmenovic, “Taxonomy and challenges of the integration of RFID and wireless sensor networks,” *IEEE Network*, vol. 22, no. 6, pp. 26–35, Nov. 2008.
- [62] D. Dardari, R. D’Errico, C. Roblin, A. Sibille, and M. Win, “Ultrawide bandwidth RFID: The next generation?” *Proc. IEEE*, vol. 98, no. 9, pp. 1570–1582, Sep. 2010.
- [63] C. Balanis, *Antenna Theory: Analysis and Design*. New York, NY, USA: Wiley, 2005, ser. Knovel Library.
- [64] K. Finkenzeller and D. Müller, *RFID Handbook: Fundamentals and Applications*

- in *Contactless Smart Cards, Radio Frequency Identification and Near-Field Communication*. New York, NY, USA: Wiley, 2010.
- [65] E. Perret, S. Tedjini, and R. Nair, "Design of antennas for UHF RFID tags," *Proc. IEEE*, vol. 100, no. 7, pp. 2330–2340, Jul. 2012.
- [66] K. V. S. Rao, P. Nikitin, and S. Lam, "Antenna design for UHF RFID tags: A review and a practical application," *IEEE Trans. Antennas Propag.*, vol. 53, no. 12, pp. 3870–3876, Dec. 2005.
- [67] H. Chaabane, E. Perret, and S. Tedjini, "A methodology for the design of frequency and environment robust UHF RFID tags," *IEEE Trans. Antennas Propag.*, vol. 59, no. 9, pp. 3436–3441, Sep. 2011.
- [68] A. Babar, A. Elsherbeni, L. Sydanheimo, and L. Ukkonen, "RFID tags for challenging environments: Flexible high-dielectric materials and ink-jet printing technology for compact platform tolerant RFID tags," *IEEE Microw. Mag.*, vol. 14, no. 5, pp. 26–35, Jul. 2013.
- [69] M. Scarpello, I. Kazani, C. Hertleer, H. Rogier, and D. Vande Ginste, "Stability and efficiency of screen-printed wearable and washable antennas," *IEEE Antennas Wireless Propag. Lett.*, vol. 11, pp. 838–841, 2012.
- [70] V. Lakafosis et al., "Progress towards the first wireless sensor networks consisting of inkjet-printed, paper-based RFID-enabled sensor tags," *Proc. IEEE*, vol. 98, no. 9, pp. 1601–1609, Sep. 2010.
- [71] C. Mariotti, G. Orecchini, M. Virili, F. Alimenti, and L. Roselli, "Wireless localization in buildings by smart tiles," in *Proc. IEEE Workshop Environ. Energy Struct. Monitoring Syst.*, Sep. 2012, pp. 7–11.
- [72] H. J. Song et al., "A method for improving the efficiency of transparent film antennas," *IEEE Antennas Wireless Propag. Lett.*, vol. 7, pp. 753–756, 2008.
- [73] F. Colombel et al., "Ultra-thin metal layer, ITO film and ITO/Cu/ITO multilayer towards transparent antenna," *IET Sci. Meas. Technol.*, vol. 3, no. 3, pp. 229–234, May 2009.
- [74] D. Zito and D. Pepe, "System-on-a-chip radio transceivers for 60-GHz wireless body-centric communications," in *Ultra-Wideband and 60 GHz Communications*. New York, NY, USA: Springer-Verlag, 2014, pp. 177–187.
- [75] L. Martin et al., "Effect of permittivity and permeability of a flexible magnetic composite material on the performance and miniaturization capability of planar antennas for RFID and wearable wireless applications," *IEEE Trans. Compon. Packag. Technol.*, vol. 32, no. 4, pp. 849–858, Dec. 2009.
- [76] D. Kim and J. Yeo, "Low-profile RFID tag antenna using compact AMC substrate for metallic objects," *IEEE Antennas Wireless Propag. Lett.*, vol. 7, pp. 718–720, 2008.
- [77] C. Kakoyiannis and P. Constantinou, "Compact WSN antennas of analytic geometry based on Chebyshev polynomials," in *Proc. Antennas Propag. Conf.*, Nov. 2012, DOI: 10.1109/LAPC.2012.6402976.
- [78] H. Visser and R. Vullers, "RF energy harvesting and transport for wireless sensor network applications: Principles and requirements," *Proc. IEEE*, vol. 101, no. 6, pp. 1410–1423, Jun. 2013.
- [79] M. Pinuela, P. Mitcheson, and S. Lucyszyn, "Ambient RF energy harvesting in urban and semi-urban environments," *IEEE Trans. Microw. Theory Tech.*, vol. 61, no. 7, pp. 2715–2726, Jul. 2013.
- [80] K. M. Farinholt, G. Park, and C. Farrar, "RF energy transmission for a low-power wireless impedance sensor node," *IEEE Sensors J.*, vol. 9, no. 7, pp. 793–800, Jul. 2009.
- [81] J. Hagerty, F. Helmbrecht, W. McCalpin, R. Zane, and Z. Popovic, "Recycling ambient microwave energy with broad-band rectenna arrays," *IEEE Trans. Microw. Theory Tech.*, vol. 52, no. 3, pp. 1014–1024, Mar. 2004.
- [82] A. Collado and A. Georgiadis, "Conformal hybrid solar and electromagnetic (EM) energy harvesting rectenna," *IEEE Trans. Circuits Syst. I, Reg. Papers*, vol. 60, no. 8, pp. 2225–2234, Aug. 2013.
- [83] T. Wu, R. Li, and M. Tentzeris, "A scalable solar antenna for autonomous integrated wireless sensor nodes," *IEEE Antennas Wireless Propag. Lett.*, vol. 10, pp. 510–513, 2011.
- [84] A. Sample, J. Braun, A. Parks, and J. Smith, "Photovoltaic enhanced UHF RFID tag antennas for dual purpose energy harvesting," in *Proc. IEEE Int. Conf. RFID*, Apr. 2011, pp. 146–153.
- [85] F. Alimenti et al., "A new contactless assembly method for paper substrate antennas and UHF RFID chips," *IEEE Trans. Microw. Theory Tech.*, vol. 59, no. 3, pp. 627–637, Mar. 2011.
- [86] W. Pachler et al., "A silver ink-jet printed UHF booster antenna on flexible substratum with magnetically coupled RFID die on-chip antenna," in *Proc. 7th Eur. Conf. Antennas Propag.*, Apr. 2013, pp. 1730–1733.
- [87] M. Virili, H. Rogier, F. Alimenti, P. Mezzanotte, and L. Roselli, "Wearable textile antenna magnetically coupled to flexible active electronic circuits," *IEEE Antennas Wireless Propag. Lett.*, vol. 13, pp. 209–212, 2014.
- [88] H.-J. Yoo, "Your heart on your sleeve: Advances in textile-based electronics are weaving computers right into the clothes we wear," *IEEE Solid-State Circuits Mag.*, vol. 5, no. 1, pp. 59–70, Mar. 2013.
- [89] X. Jingtian et al., "Low-cost low-power UHF RFID tag with on-chip antenna," *J. Semicond.*, vol. 30, no. 7, pp. 075012/1–075012/6, Jul. 2009.
- [90] M. Law, A. Bermak, and H. Luong, "A sub- μ W embedded CMOS temperature sensor for RFID food monitoring application," *IEEE J. Solid-State Circuits*, vol. 45, no. 6, pp. 1246–1255, Jun. 2010.
- [91] Alien Technology Corporation, "Fluidic self assembly," White Paper, 1999. [Online]. Available: <http://www.alientechnology.com>
- [92] C. Hertleer, H. Rogier, L. Vallozzi, and L. V. Langenhove, "A textile antenna for off-body communication integrated into protective clothing for firefighters," *IEEE Trans. Antennas Propag.*, vol. 57, no. 4, pp. 919–925, Apr. 2009.
- [93] X. Li, J. Liao, Y. Yuan, and D. Yu, "Eye-shaped segmented reader antenna for near-field UHF RFID applications," *Progr. Electromagn. Res.*, vol. 114, pp. 481–493, 2011.
- [94] J.-J. Tiang, M. Islam, N. Misran, and J. S. Mandeep, "Circular microstrip slot antenna for dual-frequency RFID application," *Progr. Electromagn. Res.*, vol. 120, pp. 499–512, 2011.
- [95] Y. Amin, Q. Chen, H. Tenhunen, and L.-R. Zheng, "Performance-optimized quadrate bowtie RFID antennas for cost-effective and eco-friendly industrial applications," *Progr. Electromagn. Res.*, vol. 126, pp. 49–64, 2012.
- [96] Y. Amin, Q. Chen, L.-R. Zheng, and H. Tenhunen, "Development and analysis of flexible UHF RFID antennas for "green" electronics," *Progr. Electromagn. Res.*, vol. 130, pp. 1–15, 2012.
- [97] F. Viani, M. Salucci, G. Olivieri, F. Robol, and A. Massa, "Design of UHF RFID/GPS fractal antenna for logistic management," *J. Electromagn. Waves Appl.*, vol. 26, no. 4, pp. 480–492, 2012.
- [98] A. Springer, R. Weigel, A. Pohl, and F. Seifert, "Wireless identification and sensing using surface acoustic wave devices," *Mechatronics*, vol. 9, no. 7, pp. 745–756, Oct. 1999.
- [99] K. Chang, Y. Kim, Y. Kim, and Y. Yoon, "Functional antenna integrated with relative humidity sensor using synthesised polyimide for passive RFID sensing," *Electron. Lett.*, vol. 43, no. 5, pp. 1918–1923, May 2007.
- [100] S. Shrestha, M. Balachandran, M. Agarwal, V. Phoha, and K. Varahramyan, "A chipless RFID sensor system for cyber centric monitoring applications," *IEEE Trans. Microw. Theory Tech.*, vol. 57, no. 5, pp. 1303–1309, May 2009.
- [101] C. Occhiuzzi, S. Cippitelli, and G. Marrocco, "Modeling, design and experimentation of wearable RFID sensor tag," *IEEE Trans. Antennas Propag.*, vol. 58, no. 8, pp. 2490–2498, Aug. 2010.
- [102] A. Ramos, A. Lazaro, D. Giraub, and R. Villarino, "Time-domain measurement of time-coded UWB chipless RFID tags," *Progr. Electromagn. Res.*, vol. 116, pp. 313–331, 2011.
- [103] R. Nair, E. Perret, and S. Tedjini, "Temporal multi-frequency encoding technique for chipless RFID applications," in *IEEE MTT-S Int. Microw. Symp. Dig.*, Montreal, QC, Canada, Jun. 2012, DOI: 10.1109/MWSYM.2012.6259483.
- [104] R. Bhattacharyya, C. Floerkemeier, and S. Sarma, "Low-cost, ubiquitous RFID-tag-antenna-based sensing," *Proc. IEEE*, vol. 98, no. 9, pp. 1593–1600, Sep. 2010.
- [105] R. Potyrailo et al., "Development of radio-frequency identification sensors based on organic electronic sensing materials for selective detection of toxic vapors," *J. Appl. Phys.*, vol. 106, no. 12, pp. 124 902–124 902-6, Dec. 2009.
- [106] V. Viikari and H. Seppa, "RFID MEMS sensor concept based on intermodulation distortion," *IEEE Sensor J.*, vol. 9, no. 12, pp. 1918–1923, Dec. 2009.
- [107] J. Riley et al., "Tracking bees with harmonic radar," *Nature*, vol. 379, pp. 29–30, Jan. 1996.
- [108] S. Helbing et al., "Design and verification of a novel crossed dipole structure for quasi-optical frequency doublers," *IEEE Microw. Guided Wave Lett.*, vol. 10, no. 3, pp. 105–107, Mar. 2000.
- [109] F. Alimenti and L. Roselli, "Theory of zero-power RFID sensors based on harmonic generation and orthogonally polarized antennas," *Progr. Electromagn. Res.*, vol. 134, pp. 337–357, 2013.
- [110] G. Lovei, I. Stringer, C. Devine, and M. Cartellieri, "Harmonic radar—A method using inexpensive tags to study invertebrate movement on land," *New Zealand J. Ecology*, vol. 21, no. 2, pp. 187–193, 1997.

- [111] B. Colpitts and G. Boiteau, "Harmonic radar transceiver design: Miniature tags for insect tracking," *IEEE Trans. Antennas Propag.*, vol. 52, no. 11, pp. 2825–2832, Nov. 2004.
- [112] G. Orecchini et al., "Green technologies and RFID: Present and future," *Appl. Comput. Electromagn. Soc. J.*, vol. 25, no. 3, pp. 230–238, Mar. 2010.
- [113] S. Steudel et al., "Comparison of organic diode structures regarding high-frequency rectification behavior in radio-frequency identification tags," *J. Appl. Phys.*, vol. 99, no. 11, Jun. 2006, 114519.
- [114] L. Valentini and J. Kenny, "Novel approaches to developing carbon nanotube based polymer composites: Fundamental studies and nanotech applications," *Polymer*, vol. 46, no. 17, pp. 6715–6718, Aug. 2005.
- [115] V. Marinov et al., "Direct-write vapor sensors on FR4 plastic substrates," *IEEE Sensor J.*, vol. 7, no. 6, pp. 937–944, Jun. 2007.
- [116] T. Unander and H.-E. Nilsson, "Characterization of printed moisture sensors in packaging surveillance applications," *IEEE Sensor J.*, vol. 9, no. 8, pp. 922–928, Aug. 2009.
- [117] S. Couderc, B. Kim, and T. Someya, "Cellulose-based composite as a raw material for flexible ANS ultra-lightweight mechanical switch devices," in *Proc. IEEE 22nd Int. Conf. Micro Electro Mech. Syst.*, Sorrento, Italy, Jan. 2009, pp. 646–649.
- [118] P. F. Goldsmith, "Quasioptics in millimeterwave systems," in *Proc. 12th Eur. Microw. Conf.*, Sep. 1982, pp. 16–24.
- [119] P. Goldsmith, "Quasi-optical techniques," *Proc. IEEE*, vol. 80, no. 11, pp. 1729–1747, Nov. 1992.
- [120] P. F. Goldsmith, *Quasioptical Systems*. New York, NY, USA: IEEE Press, 1998.
- [121] T. Djerafi, K. Wu, and S. Tatu, "3 dB 90° hybrid quasi-optical coupler with air field slab in SIW technology," *IEEE Microw. Wireless Compon. Lett.*, vol. 24, no. 4, pp. 221–223, Apr. 2014.
- [122] A. Gonzalez, Y. Fujii, K. Kaneko, and Y. Uzawa, "Quasi-optical attenuators for alma band 10 receiver," in *Proc. Asia-Pacific Microw. Conf. Proc.*, Dec. 2011, pp. 1977–1980.
- [123] K. Song, F. Zhang, S. Hu, and Y. Fan, "Millimeter-wave-wave quasi-optical low-loss power combiner based on dipole antenna," *Electron. Lett.*, vol. 49, no. 18, pp. 1160–1162, Aug. 2013.
- [124] S. Kawasaki and T. Itoh, "Quasi-optical planar arrays with fets and slots," *IEEE Trans. Microw. Theory Tech.*, vol. 41, no. 10, pp. 1838–1844, Oct. 1993.
- [125] S. Hollung, W. Shiroma, M. Markovic, and Z. Popovic, "A quasi-optical isolator," *IEEE Microw. Guided Wave Lett.*, vol. 6, no. 5, pp. 205–206, May 1996.
- [126] N. Gagnon and J. Shaker, "Accurate phase measurement of passive non-reciprocal quasi-optical components," *IEE Proc.—Microw. Antennas Propag.*, vol. 152, no. 2, pp. 111–116, Apr. 2005.
- [127] R. Dickie, R. Cahill, V. Fusco, H. Gamble, and N. Mitchell, "THz frequency selective surface filters for earth observation remote sensing instruments," *IEEE Trans. Terahertz Sci. Technol.*, vol. 1, no. 2, pp. 450–461, Nov. 2011.
- [128] M. Euler and V. Fusco, "Quasi optical circulator X-band scale model utilizing a circular polarization frequency selective surface," in *Proc. 4th Eur. Conf. Antennas Propag.*, Apr. 2010, pp. 1–4.
- [129] W. Shiroma, S. Bundy, S. Hollung, B. Bauernfeind, and Z. Popovic, "Cascaded active and passive quasi-optical grids," *IEEE Trans. Microw. Theory Tech.*, vol. 43, no. 12, pp. 2904–2909, Dec. 1995.
- [130] J. Birkeland and T. Itoh, "A 16 element quasi-optical fet oscillator power combining array with external injection locking," *IEEE Trans. Microw. Theory Tech.*, vol. 40, no. 3, pp. 475–481, Mar. 1992.
- [131] M. Forman, T. Marshall, and Z. Popovic, "Two Ka-band quasi-optical amplifier arrays," in *IEEE MTT-S Int. Microw. Symp. Dig.*, Jun. 1999, vol. 4, pp. 1829–1832.
- [132] S. Hollung, A. Cox, and Z. Popovic, "A bi-directional quasi-optical lens amplifier," *IEEE Trans. Microw. Theory Tech.*, vol. 45, no. 12, pp. 2352–2357, Dec. 1997.
- [133] J. Hacker, R. Weikle, M. Kim, P. De Lisio, and D. Rutledge, "A 100-element planar Schottky diode grid mixer," *IEEE Trans. Microw. Theory Tech.*, vol. 40, no. 3, pp. 557–562, Mar. 1992.
- [134] G. Chattopadhyay, D. Miller, H. LeDuc, and J. Zmuidzinas, "A dual-polarized quasi-optical SIS mixer at 550 GHz," *IEEE Trans. Microw. Theory Tech.*, vol. 48, no. 10, pp. 1680–1686, Oct. 2000.
- [135] V. Bezborodov, V. Kiseliyov, Y. Kuleshov, and M. Yanovsky, "A terahertz quasi-optical polarization phase shifter with the crystal quartz phase sections," in *Proc. 5th Int. Kharkov Symp. Phys. Eng. Microw. Millimeter Submillimeter Waves*, Jun. 2004, vol. 2, pp. 603–605.
- [136] G. Denisov et al., "Fast quasi-optical phase shifter based on induced photoconductivity in silicon," in *Proc. Joint 32nd Int. Conf. Infrared Millimeter Waves/15th Int. Conf. Terahertz Electron.*, Sep. 2007, pp. 795–796.
- [137] N. Camilleri, "A quasi-optical multiplying slot array," *IEEE Trans. Microw. Theory Tech.*, vol. 33, no. 11, pp. 1189–1195, Nov. 1985.
- [138] A. Moussessian et al., "A terahertz grid frequency doubler," *IEEE Trans. Microw. Theory Tech.*, vol. 46, no. 11, pp. 1976–1981, Nov. 1998.
- [139] M. Cryan et al., "Simulation and measurement of quasi-optical multipliers," *IEEE Trans. Microw. Theory Tech.*, vol. 49, no. 3, pp. 451–464, Mar. 2001.
- [140] F. Jiang et al., "High-speed monolithic millimeter-wave switch array," *IEEE Microw. Guided Wave Lett.*, vol. 8, no. 3, pp. 112–114, Mar. 1998.
- [141] F. Alimenti et al., "Crossed dipole frequency doubling RFID TAG based on paper substrate and ink-jet printing technology," in *Proc. IEEE MTT-S Int. Microw. Symp. Dig.*, May 2010, pp. 840–842.
- [142] M. Virili et al., "7.5–15 MHz organic frequency doubler made with pentacene-based diode and paper substrate," in *IEEE MTT-S Int. Microw. Symp. Dig.*, Tampa, FL, USA, Jun. 2014, DOI: 10.1109/MWSYM.2014.6848395.
- [143] L. Roselli et al., "Feasibility study of a fully organic frequency doubler for harmonic RFID applications," in *Proc. IEEE 12th Top. Meeting Silicon Monolithic Integr. Circuits RF Syst.*, Jan. 2012, pp. 203–206.
- [144] R. Goncalves et al., "Smart floor: Indoor navigation based on RFID," in *Proc. IEEE Wireless Power Transfer*, May 2013, pp. 103–106.
- [145] G. Orecchini, L. Yang, M. Tentzeris, and L. Roselli, "Wearable battery-free active paper printed RFID tag with human-energy scavenger," in *IEEE MTT-S Int. Microw. Symp. Dig.*, Jun. 2011, DOI: 10.1109/MWSYM.2011.5973290.
- [146] C.-R. Yu, C.-L. Wu, C.-H. Lu, and L.-C. Fu, "Human localization via multi-cameras and floor sensors in smart home," in *Proc. IEEE Int. Conf. Syst. Man Cybern.*, Oct. 2006, vol. 5, pp. 3822–3827.
- [147] S. Chang, S. Ham, S. Kim, D. Suh, and H. Kim, "Ubi-floor: Design and pilot implementation of an interactive floor system," in *Proc. 2nd Int. Conf. Intell. Human-Mach. Syst. Cybern.*, Aug. 2010, vol. 2, pp. 290–293.
- [148] J. Morgado and A. Konig, "Low-power concept and prototype of distributed resistive pressure sensor array for smart floor and surfaces in intelligent environments," in *Proc. 9th Int. Multi-Conf. Syst. Signals Devices*, Mar. 2012, DOI: 10.1109/SSD.2012.6198020.
- [149] J. Zhao and Y. Wang, "Autonomous ultrasonic indoor tracking system," in *Proc. Int. Symp. Parallel Distrib. Process. Appl.*, Dec. 2008, pp. 532–539.
- [150] R. Imura, "The role of networked RFID for driving the ubiquitous," in *Proc. IEEE Conf. Emerging Technol. Factory Autom.*, Sep. 2006, pp. 1115–1118.
- [151] Y. Tan, K. Y. Hoe, and S. Panda, "Energy harvesting using piezoelectric igniter for self-powered radio frequency (RF) wireless sensors," in *Proc. IEEE Int. Conf. Ind. Technol.*, Dec. 2006, pp. 1711–1716.
- [152] Linx Technologies, "KH2 series transmitter/encoder data guide." [Online]. Available: <https://www.linxtechnologies.com/resources/data-guides/txe-xxx-kh2.pdf>
- [153] D. Smith, D. Miniutti, T. Lamahe, and L. Hanlen, "Propagation models for body-area networks: A survey and new outlook," *IEEE Antennas Propag. Mag.*, vol. 55, no. 5, pp. 97–117, Oct. 2013.
- [154] *IEEE Standard for Local and Metropolitan Area Networks—Part 15.6: Wireless Body Area Networks*, IEEE Std. 802.15.6-2012, Feb. 2012.
- [155] J. Thomas and M. Qidwai, "The design and application of multifunctional structure-battery materials systems," *JOM*, vol. 57, no. 3, pp. 18–24, Mar. 2005.
- [156] A. Bonfiglio and D. De Rossi, *Wearable Monitoring Systems*. New York, NY, USA: Springer-Verlag, 2011.
- [157] S. Lee and B. Youn, "A design and experimental verification methodology for an energy harvester skin structure," *Smart Mater. Struct.*, vol. 20, no. 5, May 2011, DOI: 10.1088/0964-1726/20/5/057001.
- [158] R. Vullers, R. van Schaijk, I. Doms, C. van Hoof, and R. Mertens, "Microwave energy harvesting," *Solid-State Electron.*, vol. 53, no. 4, pp. 684–693, Apr. 2009.
- [159] P. Jaffe and J. McSpadden, "Energy conversion and transmission modules for space solar power," *Proc. IEEE*, vol. 101, no. 6, pp. 1424–1437, Jun. 2013.
- [160] J. McSpadden and J. Mankins, "Space solar power programs and microwave wireless power transmission technology," *IEEE Microw. Mag.*, vol. 3, no. 4, pp. 46–57, Dec. 2002.

ABOUT THE AUTHORS

Luca Roselli (Senior Member, IEEE) was born in Florence, Italy, in 1962. He received the “Laurea” degree in electronic engineering from the University of Florence, Florence, Italy, in 1988.

From 1988 to 1991, he worked at the University of Florence on SAW devices. In November 1991, he joined the University of Perugia, Perugia, Italy, where he is currently working as an Associate Professor and where he has been teaching several classes on electronic devices, microwave electronics, high-frequency (HF) electronic components, and applied electronics. Since 2000, he has been coordinating research activity at the High Frequency Electronics (HFE) Laboratory. In that year, he also founded the spin-off company WiS (Wireless Solutions) Srl, operating in the field of microwave electronic systems with which he cooperated as a consultant until it joined the new company ART Srl. In 2008. From 2008 to 2012, he was the Director of the Technical and Scientific Committee of ART Srl and a member of the Board of Directors. In 2005, he founded a second spin-off company: DiES (Digital Electronic Solutions) Srl. His research interests mainly focus on the design of high-frequency electronic circuits and systems, including the development of numerical methods for electronic circuit analysis with special attention to RFID-NFC systems, new materials (including organic and recyclable ones), and far-field wireless power transfer. In these fields, he published more than 220 contributions in international reviews and peer-reviewed conferences, the interest in which is testified by an HF index of 20 (source Google Scholar) and more than 1350 citations.

Mr. Roselli was the Chairman of the VII Computational Electromagnetic in Time Domain Workshop in 2007. In 2013, he was the Chairman of the First IEEE Wireless Power Transfer Conference (WPTC). Currently, he is member of the list of experts of Italian Ministry of Research and University (MIUR); member of several IEEE Technical Committees [MTT-24 RFID Technologies (past chair), MTT-25 RF nanotechnologies, MTT-26 Wireless Power Transfer]; member of the Sub Committee 32 RFID Technologies of International Microwave Symposium (IMS) (past chair); member of the European Research Council (ERC) Panel PE7; member of the Advisory Committee of IEEE WPTC. He is involved in the boards of several international conference (RWCOM, RFID-TA, EuCAP, MAREW). He is a reviewer for many international conferences and journals (the PROCEEDINGS OF THE IEEE, the IEEE TRANSACTIONS ON MICROWAVE THEORY AND TECHNIQUES, IEEE MICROWAVE AND WIRELESS COMPONENTS LETTERS, *ACES Journal*, *Radioengineering Journal*, Hindawi publishing corporation, *Elsevier Organic Electronics*, *ASP Nanoscience and Nanotechnology Letters*).

Nuno Borges Carvalho (Senior Member, IEEE) was born in Luanda, Angola, in 1972. He received the Diploma and Doctoral degrees in electronics and telecommunications engineering from the University of Aveiro, Aveiro, Portugal, in 1995 and 2000, respectively.

He is a Full Professor at the Universidade de Aveiro, Aveiro, Portugal and a Senior Research Scientist with the Instituto de Telecomunicações (IT), Universidade de Aveiro, where he coordinates the wireless communication thematic area and the Radio Systems Group. He coauthored *Intermodulation in Microwave and Wireless Circuits* (Reading, MA, USA: Artech House, 2003) and *Microwave and Wireless Measurement Techniques* (Cambridge, U.K.: Cambridge Univ. Press, 2013). He has been a reviewer and author of over 200 papers in magazines and conferences. He holds four patents. His main research interests include software-defined radio front-ends, wireless power transmission, nonlinear distortion analysis in microwave/wireless circuits and systems, and measurement of nonlinear phenomena. He has recently been involved in the design of dedicated radios and systems for newly emerging wireless technologies.



Dr. Borges Carvalho is the Chair of the IEEE MTT-11 Technical Committee. He is a member of IEEE MTT-20, MTT-24, and MTT-26 and the IEEE Portugal Section Chair. He is an Associate Editor for the IEEE TRANSACTIONS ON MICROWAVE THEORY AND TECHNIQUES, IEEE MICROWAVE MAGAZINE, *Cambridge Journal on Wireless Power Transmission* and the Chair of the URSI-Portugal Metrology Group.

Federico Alimenti (Senior Member, IEEE) was born in Foligno, Italy, in 1968. He received the Laurea degree (*magna cum laude*) and the Ph.D. degree from the University of Perugia, Perugia, Italy, in 1993 and 1997 respectively, both in electronic engineering.

In 1993, he held an internship at Daimler-Benz Aerospace, Ulm, Germany. In 1996, he was recipient of the URSI young scientist award and visiting scientist at the Technical University of Munich, Munich, Germany. Since 2001, he has been with the Department of Engineering, University of Perugia, as an Aggregate Professor, teaching the class of microwave electronics. Between 2006 and 2010, he was a member of the Academic Senate in the same university. He authored more than 150 papers in refereed journals and conference proceedings. He coauthored several book chapters and a European patent (EP13161946.2) on zero-power wireless sensors. His scientific interests concern the design and the experimental characterization of radio-frequency (RF)-integrated circuits in complementary metal-oxide-semiconductor (CMOS) and BiCMOS technologies.

Prof. Alimenti was a recipient of the IET Premium (Best Paper) Award in 2013 and was the Technical Program Committee (TPC) Chair of the IEEE Wireless Power Transfer (WPT) Conference. He has been a local coordinator of the ARTEMOS project, ENIAC, call 3, 2010. His H-index is equal to 14 (source: Google Scholar).



Paolo Mezzanotte (Member, IEEE) was born in Perugia, Italy, in 1965. He received the Ph.D. degree in electrical engineering from the University of Perugia, Perugia, Italy, in 1997.

Since 1992, he has been involved with FDTD analysis of microwave structures in cooperation with the Department of Electronic and Information Engineering (DIEI), University of Perugia. In 1999, he was appointed Research Associate. Since January 2007, he has been an Associate Professor with the same university, teaching the classes on radio-frequency engineering. His research activities concern numerical methods and computer-aided design (CAD) techniques for passive microwave structures and the analysis and design of microwave and millimeter-wave circuits. More recently his research interests have mainly focused on the study of advanced technologies such as LTCC, RF-MEMS, and microwave circuits printed on green substrates. These research activities are testified by more than 100 publications in the most important specialized journals and at the main conferences of the microwave scientific community.

Prof. Mezzanotte serves as a Reviewer of a number of IEEE journals and belongs to the Top Amplifier Research Group in a European Team (TARGET) and to the Advanced MEMS for RF and Millimeterwave Communications (AMICOM) Networks of Excellence. He is a member of the IMS Technical Program Review Committee and of the Technical Committee MTT-24 RFID Technologies. He serves as an Associate Editor of the *ACES Journal*. He was the Co-Chairman of the Seventh International Workshop on Computational Electromagnetics in Time Domain (CEM-TD 2007). His present H-index (ISI journals) is equal to 13.



Giulia Orecchini received the Laurea degree in electronic engineering and the Ph.D. degree in electronic and information engineering from the University of Perugia, Perugia, Italy, in 2008 and 2012, respectively.

During her Ph.D. studies she joined the ATHENA Research Group, Georgia Institute of Technology, Atlanta, GA, USA. Her research interests concern the development of radio-frequency identification (RFID) electronic systems and technologies. She is currently working as a Research Assistant at the University of Perugia.



Marco Virili (Student Member, IEEE) was born in Terni, Italy, in 1983. He received the Laurea degree in electronic engineering from the University of Perugia, Perugia, Italy, in 2009, where he is currently working toward the Ph.D. degree at the Department of Engineering.

His scientific interests concern the design and the experimental validation of radio-frequency (RF) and microwave circuits. He has a strong experience in using the main electromagnetic computer-aided design (CAD) tools for characterization and design of microwave devices. He is focused on chipless radio-frequency identification (RFID) tags and green electronics.



Chiara Mariotti (Student Member, IEEE) was born in Assisi, Italy, in 1987. She received the Laurea degree (*magna cum laude*) in electronic and telecommunication engineering from the University of Perugia, Perugia, Italy, in 2011, where she is currently working toward the Ph.D. degree at the High Frequency Electronics (HFE) Laboratory, working on green technologies for passive and energetically autonomous radio-frequency identification (RFID) tags.

In Spring 2012, she joined the ATHENA Research Group, Georgia Institute of Technology, Atlanta, GA, USA, for six months, working on eco-compatible indoor localization systems and other types of sensors fabricated by means of inkjet printing technology. At the end of 2013, she again joined the ATHENA Research Group for six months to work on multilayer inkjet printed systems and devices such as passives and microfluidics sensors.



Ricardo Gonçalves (Student Member, IEEE) was born in Lisbon, Portugal, in 1988. He received the B.Sc. and M.Sc. (*magna cum laude*) degrees in electronics and telecommunications engineering from the Instituto Superior de Engenharia de Lisboa, Lisbon, Portugal, in 2010 and 2012, respectively. He is currently working toward the Ph.D. degree in electrical engineering at the University of Aveiro, Aveiro, Portugal.

He is a Researcher at the Instituto de Telecomunicações, Aveiro, Portugal. In 2011, he was awarded with merit scholarship for exceptional academic performances. From 2010 to 2012, he worked at Dailywork I&D as a Developer Engineer in Embedded Electronic Systems for Vehicular Location Systems and Healthcare Platforms. His main research interests include wireless power transfer systems, radio-frequency identification (RFID), and wireless passive sensor networks. His current focus is on the development of printed antennas and microwave circuits in nonconventional materials such as textiles, ceramics, plastic, paper, and cork, for the former applications.



Pedro Pinho (Member, IEEE) was born in Vale de Cambra, Portugal, in 1974. He received the Licenciado and M.S. degrees in electrical and telecommunications engineering and the Ph.D. degree in electrical engineering from the University of Aveiro, Aveiro, Portugal, in 1995 and 2000, respectively. from the University of Aveiro, Aveiro, Portugal, in 1997, 2000, and 2004, respectively.

He is currently a Professor Adjunto at the Department of Electrical Telecommunications and Computers Engineering, Instituto Superior de Engenharia de Lisboa, Instituto Politécnico de Lisboa, Lisbon, Portugal, and a Member of the Research Staff at the Institute for Telecommunications, Aveiro, Portugal (since 1997). He authored or coauthored more than 90 papers in conferences and international journals and four book chapters. His current research interest is in antennas for location systems, reconfigurable antennas, and antenna design for passive sensors in nonconventional materials.



[J4] - **R. Gonçalves**, S. Rima, R. Magueta, P. Pinho, A. Collado, A. Georgiadis, J. Hester, N. B. Carvalho, M. M. Tentzeris, "RFID-based wireless passive sensors utilizing cork materials", *IEEE Sensors Journal*, Vol. 15, No. 12, pp. 7242-7251, 2015

RFID-Based Wireless Passive Sensors Utilizing Cork Materials

Ricardo Gonçalves, *Student Member, IEEE*, Sergi Rima, Roberto Magueta, Pedro Pinho, *Member, IEEE*, Ana Collado, *Senior Member, IEEE*, Apostolos Georgiadis, *Senior Member, IEEE*, Jimmy Hester, *Student Member, IEEE*, Nuno Borges Carvalho, *Fellow, IEEE*, and Manos M. Tentzeris, *Fellow, IEEE*

Abstract—This paper presents the design of low-cost, conformal UHF antennas and RFID tags on two types of cork substrates: 1) natural cork and 2) agglomerate cork. Such RFID tags find an application in wine bottle and barrel identification, and in addition, they are suitable for numerous antenna-based sensing applications. This paper includes the high-frequency characterization of the selected cork substrates considering the anisotropic behavior of such materials. In addition, the variation of their permittivity values as a function of the humidity is also verified. As a proof-of-concept demonstration, three conformal RFID tags have been implemented on cork, and their performance has been evaluated using both a commercial Alien ALR8800 reader and an in-house measurement setup. The reading of all tags has been checked, and a satisfactory performance has been verified, with reading ranges spanning from 0.3 to 6 m. In addition, this paper discusses how inkjet printing can be applied to cork surfaces, and an RFID tag printed on cork is used as a humidity sensor. Its performance is tested under different humidity conditions, and a good range in excess of 3 m has been achieved, allied to a good sensitivity obtained with a shift of >5 dB in threshold power of the tag for different humid conditions.

Index Terms—UHF RFID, cork characterization, passive sensor, humidity sensor, wireless sensor, inkjet printing.

I. INTRODUCTION

RFID technology has been applied in an increasing number of applications ranging from identification and localization to various types of monitoring and sensing [1]. The large and diverse number of application scenarios has resulted in various challenges for the tag design, which include the use of a diverse range of substrate materials such as paper, plastic (PET) [1], plywood [2], to name a few, as well as the use of different fabrication techniques targeting large volume production such as inkjet printing [3], and consideration of low cost conductive materials such as paperclips [3].

A characteristic example of the requirement for low-profile, conformal RFID tags is related to liquid bottle tagging, including water, wine as well as a variety of other liquids. The challenge for conformal and low-profile antennas, has led to different designs, such as a meander monopole placed inside a hollow plastic bottle closure [4], and several designs consisting of dipole antennas placed around the bottle plastic or glass neck [5], [6] or body [7].

This paper is a more in-depth analysis and an extension of the work presented at [8] and [9]. In this work we discuss in detail the design and analysis of the UHF tag antennas proposed in the symposium papers and how the presented solutions are viable for efficient bottle tagging. We also propose a possible implementation of a humidity sensor using the supporting cork as the sensing element.

RFID has been used as the foundation technology for the implementation of several passive remote sensors for different application scenarios, from temperature to chemical sensors [10]. The basic techniques to perform sensing in a wireless way are usually based on resonant frequency shifts [11] and/or wake-up power changes of the passive tags [12].

Temperature sensing using passive RFID tags has been explored in [11]–[13], in the first and second cases by using substrates with permittivity sensitive to the temperature changes, while in the third case thermistors are used in the tag matching network to shift the resonant frequency of the tag according to the temperature.

Instead of just temperature measurements, in [14] a combined temperature and humidity sensor is explored. In this

Manuscript received June 25, 2015; revised August 18, 2015; accepted August 18, 2015. Date of publication August 25, 2015; date of current version October 15, 2015. This work was supported in part by the Portuguese Fundação para a Ciência e a Tecnologia/Ministério da Ciência, Tecnologia e Ensino Superior under Grant SFRH/BD/91249/2012 through the CREATION Project under Grant EXCL/EEI-TEL/0067/2012 and in part by the framework of the European Union Cooperation in Science and Technology Action IC1301 Wireless Power Transmission for Sustainable Electronics. The work of S. Rima, A. Collado, and A. Georgiadis was supported in part by the Spanish Ministry of Economy and Competitiveness and Fondo Europeo de Desarrollo Regional Funds under Project TEC2012-39143 and in part by the Generalitat de Catalunya under Grant 2014 SGR 1551. This is an expanded paper from the IEEE SENSORS 2014 Conference. The associate editor coordinating the review of this paper and approving it for publication was Prof. Danilo Demarchi.

R. Gonçalves, R. Magueta, and N. B. Carvalho are with the Department of Electronics, Telecommunications and Informatics, Instituto de Telecomunicações, University of Aveiro, Aveiro 3819-193, Portugal (e-mail: rgoncalves@av.it.pt; rlm@ua.pt; nbcarvalho@ua.pt).

S. Rima, A. Collado, and A. Georgiadis are with the Department of Microwave Systems and Nanotechnology, Centre Tecnològic de Telecomunicacions de Catalunya, Castelldefels 08860, Spain (e-mail: srima@cttc.es; acollado@cttc.es; ageorgiadis@cttc.es).

P. Pinho is with the Instituto de Telecomunicações, University of Aveiro, Aveiro 3819-193, Portugal, and also with the Instituto Superior de Engenharia de Lisboa, Lisbon 1959-007, Portugal (e-mail: ppinho@deetc.isel.pt).

J. Hester and M. M. Tentzeris are with the Georgia Electronic Design Center, School of Electrical and Computer Engineering, Georgia Institute of Technology, Atlanta, GA 30332 USA (e-mail: jimmy.hester@gatech.edu; etentze@ece.gatech.edu).

Color versions of one or more of the figures in this paper are available online at <http://ieeexplore.ieee.org>.

Digital Object Identifier 10.1109/JSEN.2015.2472980

case a proposal for HF and UHF sensor tags is presented. A micro-controller is used to interface a RFID chip and the sensor elements or ICs responsible for the temperature and humidity measurements. The micro-controller reads the data from the sensors and writes it in the RFID chip memory, which is then accessed with a regular RFID reader. This solution seems to be the most mature and most reliable although it is also the more expensive. It has been also considered for harsh environments but it is severely dependent on the packaging which may affect the accurate temperature and humidity sensing in many scenarios.

Other sensing capabilities are explored in [15] and [16]. In the first case a passive sensor for pH of solutions is presented. This one is based on HF RFID approach, by connecting pH sensing electrodes in parallel to an inductive coil which will result in a resonant frequency shift of the coil. Every measured resonant frequency value is matched to a specific pH level of the target solution. A temperature-dependent resistor is used in parallel with a varactor and the electrodes and coil in order to monitor the temperature. Temperature shifts will impose a change in the quality factor of the coil which can be detected therefore allowing a temperature compensated pH measurement. In [16] a microfluidic channel are used to create a varactor sensor for chemicals which are introduced into an UHF RFID tag antenna. These microfluidic structures impose a resonant frequency shift of the antenna for different chemicals, therefore allowing the detection of certain substances using passive remote sensing.

In addition to its application in wine and bottle industry, cork material has found increasing applicability as an insulator in various fields, including space technology, due to characteristic properties such as lightweight and low thermal conductivity [17]. Therefore the characterization of this material and the successful design of antennas and circuits in it might open the door for many diverse and interesting applications.

There are several ways to etch the cork with conductive materials in order to fabricate the antennas or circuits on cork. Standard milling fabrication is used to transfer the antenna design on a low cost adhesive copper tape, which is then attached to the cork substrate, allowing for a fast and cost effective fabrication. Another possible implementation is the use of inkjet printing, if care is taken to create a coating on the cork that has enough surface energy to sustain the ink in place.

This paper describes the dielectric properties of cork and introduces the cork as a possible substrate for the implementation of antennas at high frequencies and explores its use for sensing of humidity. This document is organized as follows. In the following section the electrical properties of two types of cork samples are characterized. The permittivity and loss factor of a natural cork sample and a fabricated pressed agglomerated cork sample are extracted with two characterization methods for comparison purposes. Section III shows the design of three different antennas for passive RFID tags to be embedded into barrels or bottles for inventory. Section IV presents the measurement setup and the measured results for all the proposed tags. Section V investigates the permittivity shift with humidity variation and shows a possible

implementation of a passive humidity sensor based on RFID using cork as the sensitive mechanism. Finally, section VI draws the main conclusions about this work.

II. CORK PERMITTIVITY AND LOSS ESTIMATION

Antenna design requires knowledge of the electrical properties of the materials which comprise the antenna topology; in the case of cork, its electrical properties have been relative unknown in the RF frequency range. Moreover, through visual inspection of the cork material and given the structure of the material of the cork laminates, we expect to see an anisotropic behavior of the dielectric material. Therefore, different orientations should be considered when analyzing cork's electrical properties.

A. Permittivity and Loss Estimation: Theory

In order to estimate the permittivity and loss tangent of the cork we used transmission/reflection methods based on microstrip transmission lines.

The method utilized to characterize the cork is based on the measurement of S parameters of two different length lines, as described in [18] and [19]. For the implementation of the given method two microstrip lines with the same characteristic impedance (not necessarily 50 Ω), that is, same width and slightly different lengths are fabricated with the Material Under Test (MUT) as substrate. The permittivity is estimated based on the measurement of the propagation constant, γ , of both lines and relating the unwrapped propagation phase constant, β , with the propagation phase constant in vacuum, k_0 .

$$\epsilon_{r,eff} = \left(\frac{\beta}{k_0} \right)^2 \quad (1)$$

The loss tangent in this case is calculated according to (2) as described in [20] and assuming the entire transmission line losses are due to the dielectric, which is not entirely true but provides a reasonable estimation of the loss tangent value.

$$\tan \delta = 0.0366 \frac{\alpha \lambda_0 \sqrt{\epsilon_{r,eff}(\epsilon_r - 1)}}{\epsilon_r(\epsilon_{r,eff} - 1)} \quad (2)$$

where α is the losses obtained from the propagation constant measured, λ_0 is the wavelength, $\epsilon_{r,eff}$ is the effective dielectric constant of the substrate and ϵ_r is the relative permittivity of the material.

B. Permittivity and Loss Estimation: Measurements

There are numerous types of cork materials that are used for the elaboration of wine cork bottle stoppers (Fig. 1). Among them we can disguise the wine corks punched directly from a panel of natural cork and the ones fabricated with pressed or agglomerate cork. Apart from the fabrication method, these types of corks can be distinguished easily by visual inspection, as can be seen in Fig. 1 and 2. In this section we demonstrate the permittivity and loss factor calculation for the above cork type materials.

The microstrip lines utilized for material characterization are shown in Fig. 2, where the difference in their respective lengths is quite clear, in a similar way as proposed

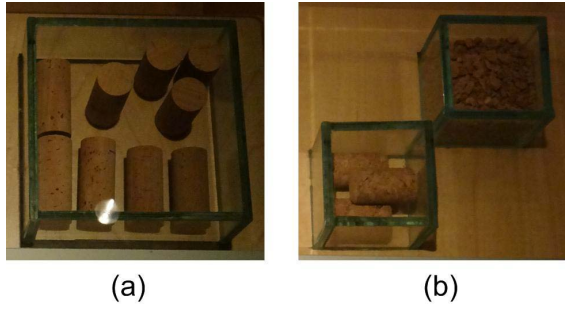


Fig. 1. Two different types of wine bottle corks (a) natural cork and (b) agglomerated cork.

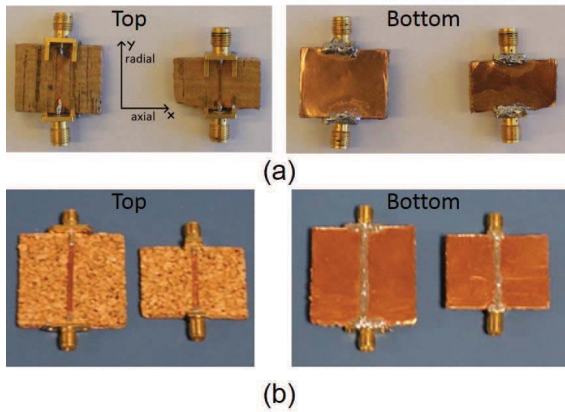


Fig. 2. Photograph of two microstrip lines placed on (a) natural and (b) agglomerate cork substrate.

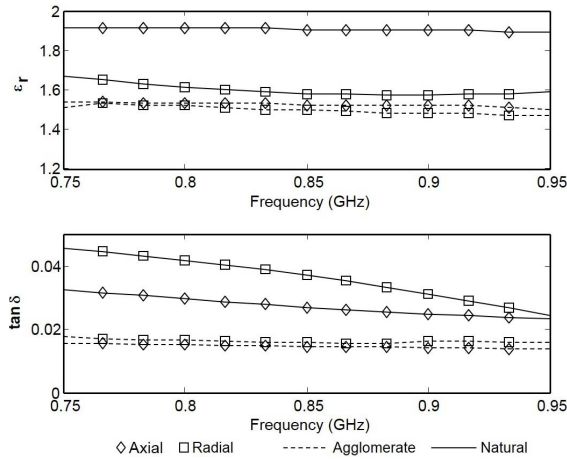


Fig. 3. Measured dielectric constant and loss tangent of axial and radial samples of natural and agglomerate cork in the range from 750 to 950 MHz.

in [18], [19], and [21]. Due to the expected anisotropic behavior of the cork, which is confirmed by the results shown in Fig. 3, slices of the material were cut in two different directions: axial and radial.

S-parameter measurements were performed on both pairs of microstrip lines of lengths l_1 and l_2 , being l_1 of 15 mm and l_2 of 25 mm. One pair of microstrip lines were placed on

the cork substrate corresponding on the axial axis cut and the other to the radial one. The conducting strips were fabricated by milling of adhesive copper tape, with $35 \mu\text{m}$ thickness and $4.7 \times 10^8 \text{ S/m}$ conductivity, and placing them on the cork samples. SMA connectors were soldered to the edges of the microstrip lines for interfacing.

A vector network analyzer from Agilent Technologies with reference E8361A was used to perform the two-port S-parameters measurements in the frequency range from 750 to 950 MHz. The estimated permittivity for the cork is depicted in Fig. 3.

The measured permittivity for the cork is rather low, with values ranging between 1.49 and 1.91, which was expected due to the existing air gaps in the cork [17]. Another characteristic that can be easily observed in the depicted results is the anisotropic (permittivity is different for different directions) behavior of the natural cork in contrast with the nearly isotropic (permittivity is the same in both axis) behavior of the agglomerate cork. This is mainly due to the random distribution of the cork pieces on the agglomerate cork, in comparison to the clearly stratified structure of the natural cork. The lower permittivity of the agglomerate cork is also explained by the larger number of air gaps in its slabs, which is clear from the photographs in Fig. 2.

The isotropy/anisotropy of the the different cork materials is also clear in the loss tangent values. The measured losses for the natural cork are different over different directions while they are roughly the same for the agglomerate cork. Besides, the dissipation factor of the agglomerate cork is slightly lower than the natural cork, as shown in Fig. 3. This indicates that agglomerate cork might be a better candidate for use in antennas and microwave circuits applications.

After the characterization of the cork materials up to 950 MHz, we were able to incorporate them on CST and use them to simulate various UHF RFID tag antennas as described in the following sections.

III. UHF RFID TAG ANTENNAS

In this section, three different types of UHF RFID tag antennas are presented. The first one is a meandered dipole antenna wrapped around a cork cube to be placed inside a barrel cork stopper. The second design is a compact design based on a meandered monopole antenna to be placed inside a bottle cork stopper. The third prototype is a miniaturized configuration of a dipole antenna, achieved by reducing the antenna to the matching ring and a lumped component. This is wrapped around the surface of a regular bottle cork stopper. In the last two approaches the glass bottle filled with water were included in the simulation model in order to better match the real operation environment where the antenna will be placed.

A. RFID Tag for Barrel Cork Stopper

As a proof of concept and without loss of generality, a compact meandered dipole antenna was designed and modeled to fit in a barrel cork. The designed prototype, that is shown in Fig. 4, uses a cubic shape in order to facilitate the

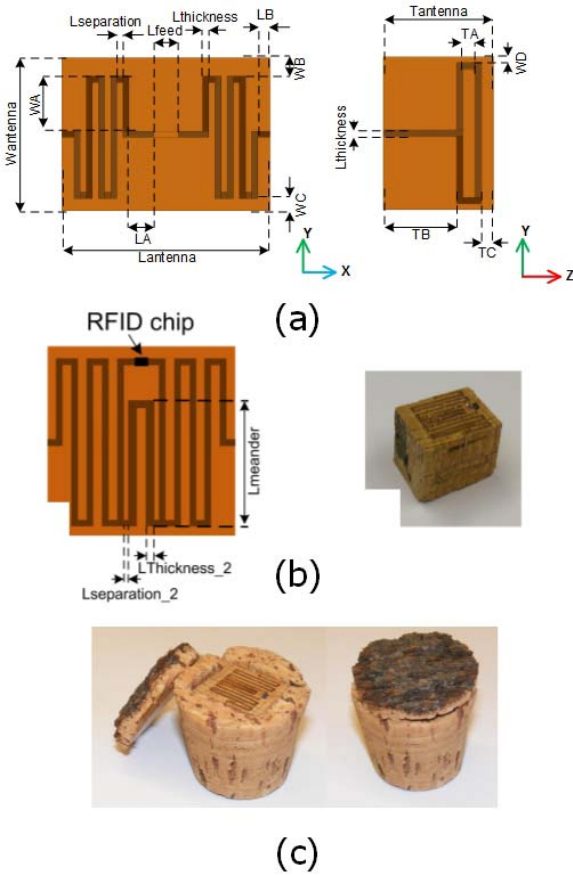


Fig. 4. Compact meandered dipole antenna (a) Dimensions of the compact meandered dipole antenna matched to 50 Ω , (b) with matching inductive ring matched to the RFIC, and (c) photograph of the implemented prototype.

cutting of the material. It was made with natural cork, the most commonly used for barrel cork stoppers.

When meandering the dipole arms, the direction of the current flow in the radial direction of the dipole is inverted, so to some extent these currents cancel when viewed from far field and effectively do not contribute to radiation [22]. Additionally, a meandered structure features a significantly smaller inductance per unit length than a straight dipole and since the resonant frequency of the antenna is inversely proportional to the product of inductance and capacitance when these are reduced, the resonant frequency is increased, which means that for the same total length, a meandered dipole has a higher resonant frequency than a straight dipole. This change in the resonant frequency was considered and the design of the compact meandered antenna, the dimensions of which are reported in Table I, were modified to re-tune the resonant frequency.

The compact cubic antenna shown in Fig. 4 (a) was initially designed to be matched to 50 Ω . An RFIC chip was then connected to the compact meandered dipole antenna, and a loop ring is inserted around the chip making the connection to the dipole arms, as shown in Fig. 4 (b). The selected chip is the Higgs 3 from Alien Technology. This IC is EPCglobal Gen2 and ISO/IEC 1800-6c compliant, requires low power to

TABLE I
MEANDERED DIPOLE ANTENNA DIMENSIONS

Parameters	sizes (mm)
$L_{thickness}, L_{feed}$	0.75, 4.0
$L_{separation}, W_{antenna}$	1.0, 25.0
$L_{antenna}, T_{antenna}$	32.0, 18.0
L_A, L_B, W_A	4.0, 2.0, 9.0
W_B, W_C, W_D	3.0, 2.0, 1.0
T_A, T_B, T_C	2.0, 12.0, 2.0
$L_{separation_2}, L_{thickness_2}$	0.65, 1.15
$L_{meander}$	14.0

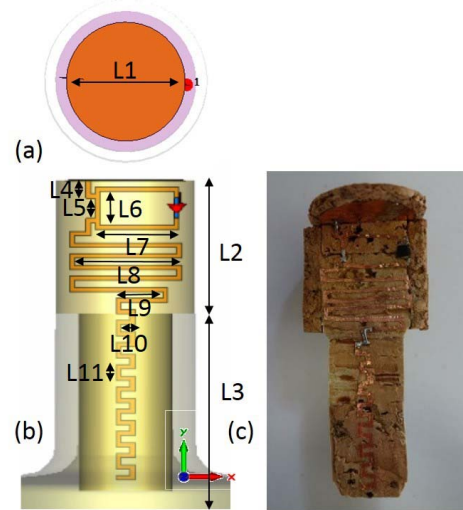


Fig. 5. Agglomerate Cork RFID antenna (a) top view (b) front view and (c) photograph.

perform the reading operation and operates in the RFID UHF bands (860-960 MHz). The input impedance of the RFID chip can be modeled as a series equivalent circuit with a resistance R of 1500 Ω in parallel with a 0.9 pF capacitor C , which results in a complex input impedance at 866 MHz of 27.35 - j200.5 Ω .

B. RFID Tag for Bottle Cork Stopper

In this subsection we used agglomerate pressed cork and designed an antenna for an RFID tag that could be inserted into a cork stopper for a wine bottle.

It was necessary to reduce the size of the antenna when compared to the previous topology in order to make it fit into a typical wine bottle. Therefore, we opted to make a monopole instead of a dipole. The proposed RFID tag antenna design for the wine bottle cork stopper is depicted in Fig. 5.

As we can see from the picture the antenna is connected to a conductive circular disk on the top of the cork stopper that functions as a ground plane. Similar to the previous case, there is an inductive loop at the feed point, in order to match the antenna to the complex input impedance of the chip. In this case, a UCODE SL3ICS1002 from NXP was used, which has an input impedance of 16-j158 Ω at 866 MHz.

The dimensions of this antenna are presented in Table II.

The radiation pattern is essentially omnidirectional which was expected considering the antenna geometry. This can

TABLE II
MEANDERED MONOPOLE ANTENNA DIMENSIONS

Parameters	sizes (mm)
L ₁ , L ₂ , L ₃	26.0, 30.0, 40.0
L ₄ , L ₅ , L ₆	3.0, 4.5, 7.4
L ₇ , L ₈ , L ₉	17.0, 23.0, 10.0
L ₁₀ , L ₁₁	3.0, 3.5

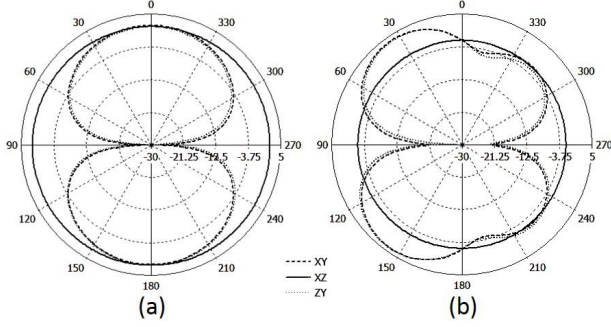


Fig. 6. Simulated radiation patterns of the meandered monopole RFID antenna (a) with empty bottle and (b) with filled bottle.

be observed in the simulation results depicted in Fig. 6 (a). However, this is true when the bottle is empty. The simulation model was designed with a glass ($\epsilon_r=4.8$) bottle with a thickness of 6 mm, which is the thickness of the glass measured from a typical wine bottle. The presence of liquid inside the bottle has a considerable effect on the radiation pattern, which is shown in Fig. 6 (b). For simulation purposes, water was considered inside the bottle. Most beverages are mainly composed of water, which means that for electromagnetic simulation purposes it will render similar results as wine. Water has an estimated permittivity of 78.3 at 25 °C [23]. The water is set at a distance of around 15 mm of the stopper edge.

Nevertheless the gain of the antenna remains essentially the same in both cases. The monopole antenna was optimized to work in the filled bottle, therefore, when the bottle is empty there is a slight mismatch in the antenna impedance. This allied to the smaller directivity of the radiation on the empty bottle, result in a total efficiency that is very close to the one achieved in the filled bottle case, even with the lower radiation efficiency occurring from the liquids absorption.

This prototype has rather large dimensions that extrude the top of the bottle. Due to the visual impact we decided to reduce the size of the antenna further in order to make it fit into regular bottle stoppers. The proposed prototype was designed in order to fit on the surface of a regular T-cork stopper, which is a stopper commonly found on liquors, that provides a secure grip while applying little deformation to the antenna.

The proposed prototype is presented in Fig. 7.

In order to miniaturize the antenna an SMD resistor of 6.2 Ω is used in the impedance matching ring in order to reduce the size while maintaining a good matching of the antenna impedance. This of course dissipates a great deal of the input power, therefore reducing the overall efficiency of the antenna in 90%. However, the impedance mismatch

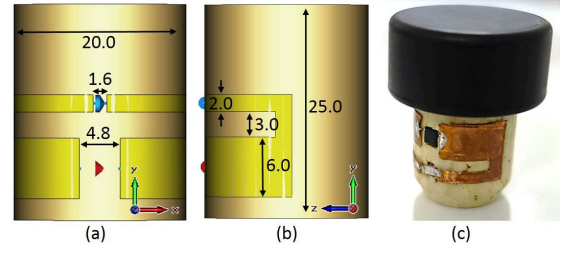


Fig. 7. Agglomerate Cork RFID antenna (a) front view (b) left-side view, and (c) prototype photograph. All dimensions in mm.

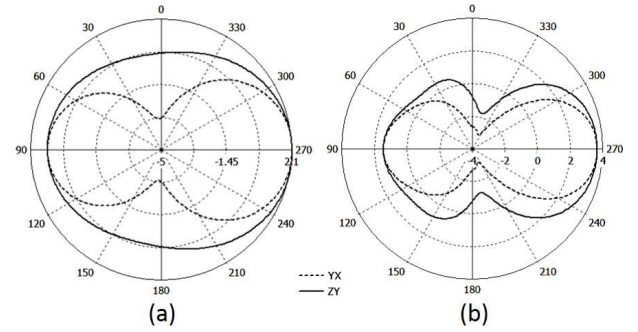


Fig. 8. Simulated radiation pattern of the conformal RFID tag considering (a) only the bottle neck and (b) full filled bottle.

before the insertion of the resistor corresponds to a reflection of $\Gamma = 0.98$, which results in a total efficiency below 1%, that is effectively lower when compared to the efficiency with the resistive element, which is around 5%.

The antenna is simulated in two different scenarios, an empty and a water filled bottle, for comparison. The bottle is designed considering a thickness of 8 mm of glass, which is a typical value for wine bottles, where the glass is modeled with the default values from the simulator library, with a permittivity of 4.82. The presence of the liquid has a large influence in the radiation pattern and also in the total efficiency, due to the fact that water absorbs electromagnetic energy [24]. The changes of the radiation pattern of the antenna when considering the empty bottle versus the liquid filled bottle is depicted in Fig. 8.

Due to the radiation efficiency reduction in this prototype the reading range of the tag is considerably reduced.

IV. RFID TAGS MEASUREMENTS

The read range of the designed RFID tags was tested using a signal generator, an oscilloscope or a vector signal analyzer (VSA) and an antenna that is used for transmit and receive using a directional coupler, as depicted in Fig. 9. In order to evaluate the distance of communication with the tag, a query is sent to the tag and the back-scattered response is analyzed to see if a modulation is discernible.

The back-scattered signal from the RFID tag is received by the digital oscilloscope which can be configured to perform the FFT over the received time window and show the frequency spectrum. A VSA can also be used to check

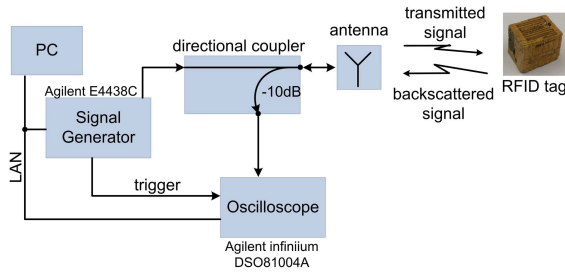


Fig. 9. RFID read range measurement setup.

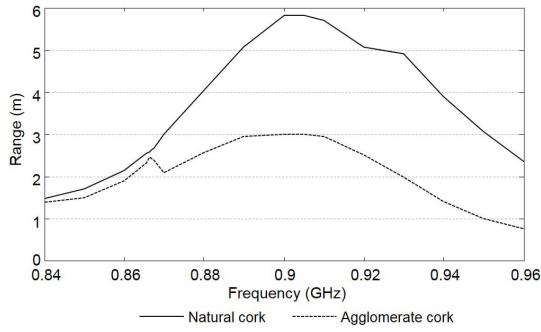


Fig. 10. Read range for the natural cork and agglomerate cork RFID antenna.

the frequency spectrum. Since the tag uses amplitude shift keying (ASK) to modulate the back-scatter signal, the presence of the tag response is discerned by the presence of sub-carriers around the interrogation carrier.

In order to determine the read range, a fixed distance between the antenna and the RFID tag is set ($d=38$ cm) and then the transmitted power from the generator is varied to find the minimum threshold power (P_{th}) necessary to turn on the tag. The read range for a given transmitted power ($EIRP$) can be determined using the following expression [25]

$$r = d \sqrt{\frac{EIRP}{P_{th} L G_t}} \quad (3)$$

where L are the losses in the cables and G_t is the gain of the transmitting antenna (since only one antenna is being used).

The maximum read range for different operation frequencies and for a EIRP maximum of 1 W was determined using this method. Fig. 10 shows the maximum reading ranges obtained for the barrel cork stopper tag and the bottle cork stopper tag. For both cases, the peak reading range occurs around 900 MHz, corresponding to nearly 6 m for the barrel stopper and 3 m for the bottle cork stopper.

The range of the bottle stopper tag is smaller than that of the barrel stopper tag. However, we need to consider that the bottle cork stopper was tested in a real application scenario, inserted into a water (which is similar to wine in terms of electromagnetic properties and effects on radiation) filled bottle, while the barrel stopper was tested by itself, outside any barrels and without any liquids in its vicinity.

The third prototype, the miniaturized bottle stopper tag, showcased the smallest reading range. This is mainly due to the smaller efficiency of the antenna. The reading range of

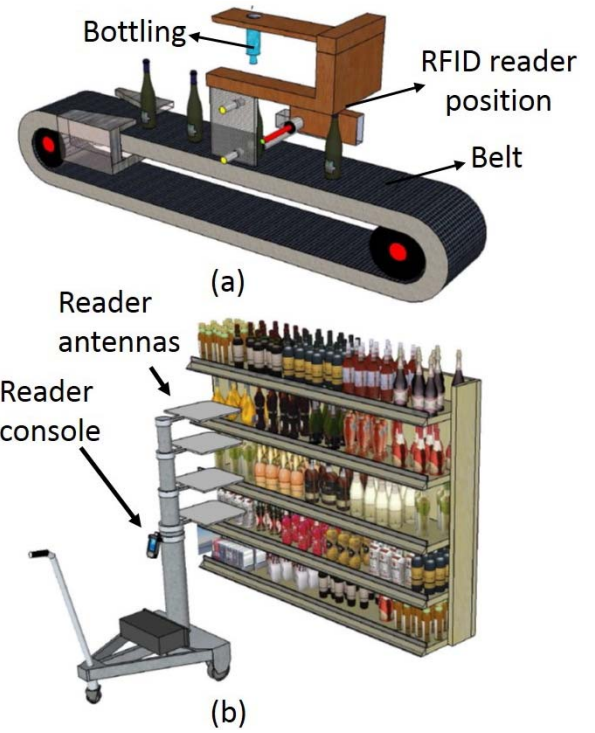


Fig. 11. Scenarios of application of the bottle stopper tag and reading solutions (a) at bottling stage and (b) at distribution stage in supermarket.

the considered prototype in an application scenario condition, that is, inserted into a water filled glass bottle, was of 0.3 m at 866.6 MHz, achieved for the maximum output power (30 dBm) of a commercial RFID reader. However, this reading range is obtained regardless of the orientation of the bottle. That is, either if the bottle is placed horizontally or vertically, the reading range obtained in the maximum direction of radiation is the same.

Although small, the reading range obtained is rather acceptable if we consider the following application scenarios. In the first case during bottling process, the RFID reader antennas can be mounted in a platform hanging over the belt that circulates the bottles around the bottling facilities, as illustrated in Fig. 11 (a). On a distribution scenario, for instance, on supermarket shelves, the readings can be obtained by an employee with a portable reader, which points the reader to the shelves, as illustrated in Fig. 11 (b). In both cases the readings are obtained in close vicinity to the bottles, therefore we can say that the reading ranges obtained with the considered tags, although small, are acceptable.

It is important to note that the work presented in this paper is meant as a proof of concept. That is, this investigation goes into the development of possible RFID tag antennas that can work within the vicinity of liquids while inserted into glass bottles. When we consider the possibility of industrialization of these designs, some issues arise, which can only be tackled with a careful design having into consideration the cork manufacturing and the bottling processes. For instance, the bottle tag of Fig. 5 is not a common shape cork stopper, therefore, a new cork stopper model would need to be used and

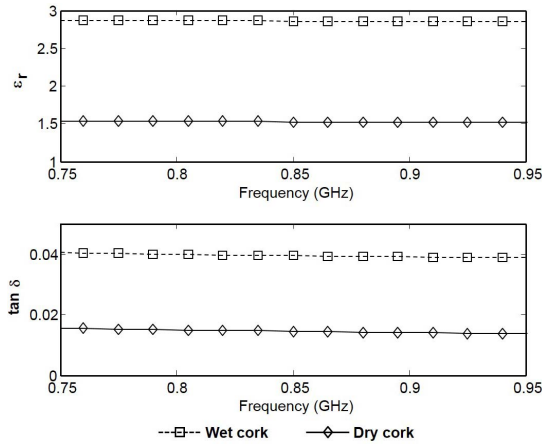


Fig. 12. Measured permittivity of the dry and wet cork applying the two-line method with two different length microstrip lines.

the bottling processes would need to adapt to this new shape, besides, the manufacturing process of the cork stopper would also need to be changed. In the case of the tag in Fig. 7, due to its application on the surface of the cork and its compact size, it can be used with common shaped stoppers. However, since it is located on the surface, it requires some cover material around the cork, which is not advisable. Besides, it requires the bottling to be done slowly and with little pressure, contrary to what is the current bottling process.

V. HUMIDITY SENSORS BASED ON CORK

In order to develop a passive humidity sensor, we're using cork as the sensing surface. Cork is a porous dielectric material, and as such, it absorbs water. This results in a material that is sensitive to humidity changes. In order to determine to which extent the cork permittivity changes with the difference in water content, permittivity measurements were performed on the dry and soaked cork slabs, using the two-line method, according to [19], with microstrip lines. The effective permittivity values are presented in Fig. 12.

We can see that the permittivity changes considerably, between 1.5 when dry to 3 when in wet condition, which proves the water absorption properties of the cork. Besides, we can also observe an increase in the losses, from around 0.015 when dry to 0.04 when wet.

In order to develop the passive sensor we designed an UHF RFID antenna inserted in between two cork slabs. The antenna was fabricated by inkjet printing a silver nanoparticle (SNP) ink from ANP.

In order to be able to print the ink on top of the cork, a coating surface has to be created so that it doesn't absorb the ink. Epoxy and SU-8 were used for this purpose. By placing a slim layer of epoxy on the surface of the cork we were able to create a smooth surface for printing. The SU-8 was then inkjet-printed on top of the epoxy layer, to furthermore increase the smoothness of the surface while providing an optimal wet-ability for the SNP ink printing.

The simulated prototype comprised three different dielectric layers. An epoxy layer on top of which the antenna was printed

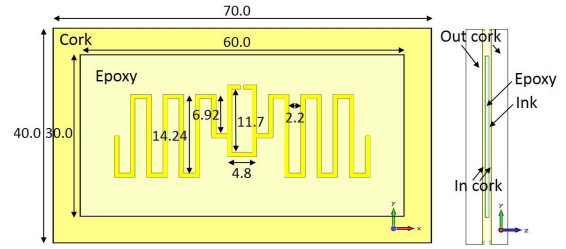


Fig. 13. Proposed RFID tag using cork slabs prototype. All dimensions in mm.

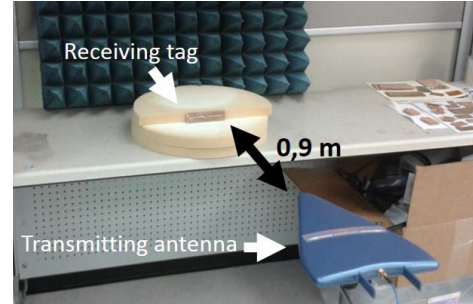


Fig. 14. Measurement setup.

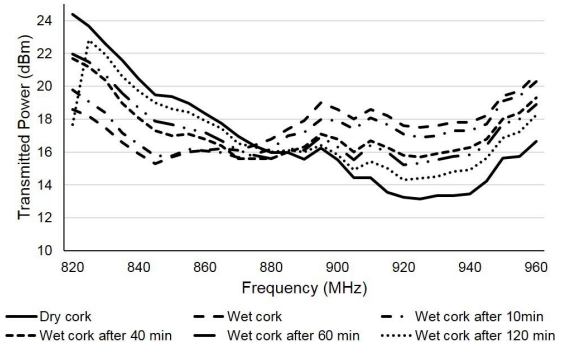


Fig. 15. Minimum transmitted power to activate the prototype tag with different wetting conditions.

and then two different layers which emulate the cork. A slim fixed permittivity cork slice which accounts for the fact that not all the dielectric cork slab will absorb water and an outside slab with varying permittivity which is going to change based on the humidity. The proposed prototype is shown in Fig. 13. The antenna was designed to match the input impedance of a Higgs 4 RFID chip from Alien at 915 Mhz, which corresponds to $18.4 + j181.2 \Omega$. The size and placement of the inductive ring is determined according to the guidelines from [26].

In order to access the behavior of the tag, the minimum threshold power to turn on the tag is measured at each frequency. For that purpose a more easy setup was used, with the Voyantic Tagformance 7, RFID test equipment. A picture of the measurement scenario is shown in Fig. 14. The frequency at which the tag presents the lowest turn on power corresponds to the frequency at which the antenna has the better match to the chip input impedance. The measured threshold power of the tag is shown in Fig. 15.

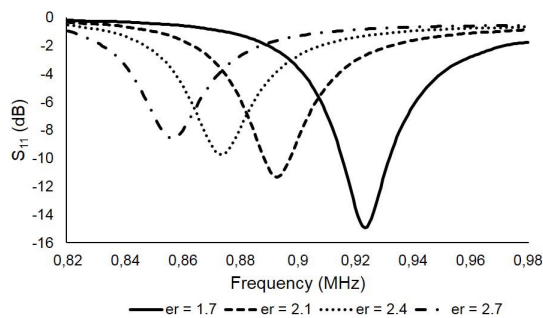


Fig. 16. Simulated reflection coefficient of the sensor tag antenna for different permittivity values of the outside cork slabs.

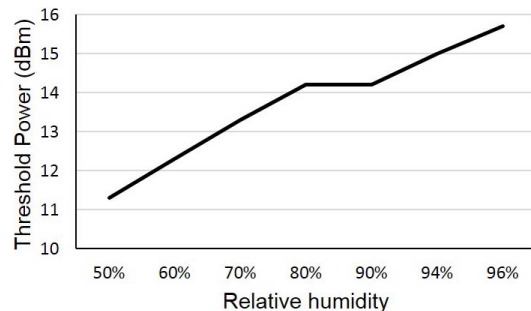


Fig. 17. Threshold power variation with humidity measured within the thermal chamber with humidity control.

By looking to the transmitted power measurements it is easy to identify a shift in the matched resonance of the antenna to the chip for different humidity values. It is also possible to just look into the turn on power at a single frequency and match the minimum power level required to a given humidity level. Considering the relative humidity levels inside the lab were of 60%, we can see that there is a large and easily traceable power shift up to $\approx 100\%$ at 920 MHz, which is the frequency at which the antenna is matched for the dry cork condition.

Still on the plot from Fig 15 we can see that when the cork becomes wet, the best matched frequency is around 845 MHz, which matches with the simulation prediction for the wet condition. The simulated reflection coefficient, of the sensor tag antenna for different permittivity values of the outside slabs, is depicted in Fig. 16.

Comparing the simulation and the measurements we can see a relationship between the threshold power to turn on the tag and the reflection coefficient of the sensor tag antenna. For a permittivity of 1.7, which corresponds to the near dry cork, the resonant frequency is around 920 MHz where a good match (reflection coefficient at -15 dB) is obtained, which correlates to the lowest threshold power measured, happening for the dry cork at 920 Mhz. While for a permittivity of 2.8, which is almost the value obtained for $\approx 100\%$, the resonance is around 850 MHz with a poor match (reflection coefficient at -8 dB), which correlates to the wet condition with the lowest threshold happening at 845 MHz with 3 dB difference to the dry condition.

Another measurement was performed inside a thermal chamber with humidity control. The threshold power was measured at 915 MHz for different humidity conditions. There's a threshold power difference of roughly 4.4 dB,

between 50 to 96% relative humidity. The threshold power variation with humidity is shown in Fig. 17.

This behavior confirms the response obtained for the previous measurements by spraying and drying the cork. The threshold power difference, between this measurement and the one shown in Fig. 15, is due to the propagation environment in which the measurements were made. The thermal chamber has metallic walls, therefore the propagation inside is unknown and random with multiple reflections happening. For that reason the frequency sweep was not performed and an accurate threshold power can't be obtained, since the propagation environment is very different from open space.

VI. CONCLUSION

In this paper, three types of RFID tags implemented in cork based substrates have been presented. These RFID tags aim to be used in wine bottles or barrels integrated in their cork stoppers for inventory and monitoring of bottled beverages. One of the contributions of this paper is the dielectric characterization of natural and agglomerate pressed cork. It is shown that this material has a very low dielectric constant and also a reasonable dissipation factor that makes it suitable to the design and implementation of printed antennas for different applications. The RFID tags proposed in this paper have shown a very good result in terms of reading ranges while maintaining conformity with the targeted application dimensions constraints. The proposed RFID tag for bottle labeling is small enough to fit regular cork bottle stoppers and shows a reading distance of 30 cm, which for the application envisioned is an acceptable value.

Cork is also explored as a possible way to implement an humidity sensor. Its properties are explored and it is shown that cork has a considerable sensitivity to the water contents due to its absorption characteristic. A passive humidity sensor can be developed taking advantage of these properties and using RFID technology.

REFERENCES

- [1] A. Rida, L. Yang, and M. Tentzeris, *RFID-Enabled Sensor Design and Applications*. Norwood, MA, USA: Artech House, 2010.
- [2] J. Virkki, J. Virtanen, L. Sydanheimo, L. Ukkonen, and M. Tentzeris, "Embedding inkjet-printed antennas into plywood structures for identification and sensing," in *Proc. IEEE Int. Conf. RFID Technol. Appl.*, Nov. 2012, pp. 34–39.
- [3] P. V. Nikitin, S. Lam, and K. V. S. Rao, "RFID paperclip tags," in *Proc. IEEE Int. Conf. RFID*, Apr. 2011, pp. 162–169.
- [4] Z. Hu and P. H. Cole, "Bottle packaged wine product detection by UHF RFID systems," in *Proc. Int. Conf. Electromagn. Adv. Appl.*, Sep. 2010, pp. 301–304.
- [5] Y. Kim, "Design of near omnidirectional UHF RFID tag with one-off seal function for liquid bottles," *Microw. Opt. Technol. Lett.*, vol. 55, no. 2, pp. 375–379, 2013.
- [6] J. Xi and T. T. Ye, "Conformal UHF RFID tag antenna mountable on winebottle neck," in *Proc. IEEE Antennas Propag. Soc. Int. Symp.*, Jul. 2012, pp. 1–2.
- [7] T. Bjorninen, A. Z. Elsherbeni, and L. Ukkonen, "Low-profile conformal UHF RFID tag antenna for integration with water bottles," *IEEE Antennas Wireless Propag. Lett.*, vol. 10, pp. 1147–1150, Oct. 2011.
- [8] R. Goncalves *et al.*, "RFID tags on cork stoppers for bottle identification," in *Proc. IEEE MTT-S Int. Microw. Symp.*, Tampa, FL, USA, Jun. 2014, pp. 1–6.
- [9] R. Goncalves, R. Magueta, P. Pinho, and N. B. Carvalho, "RFID passive tag antenna for cork bottle stopper," in *Proc. IEEE Antennas Propag. Soc. Int. Symp. (APSURSI)*, Jul. 2014, pp. 1518–1519.

- [10] S. Kim *et al.*, "No battery required: Perpetual RFID-enabled wireless sensors for cognitive intelligence applications," *IEEE Microw. Mag.*, vol. 14, no. 5, pp. 66–77, Jul./Aug. 2013.
- [11] H. Cheng, S. Ebadi, and X. Gong, "A low-profile wireless passive temperature sensor using resonator/antenna integration up to 1000 °C," *IEEE Antennas Wireless Propag. Lett.*, vol. 11, pp. 369–372, Apr. 2012.
- [12] J. Virtanen, L. Ukkonen, T. Bjorninen, L. Sydanheimo, and A. Z. Elsherbeni, "Temperature sensor tag for passive UHF RFID systems," in *Proc. IEEE Sensors Appl. Symp. (SAS)*, Feb. 2011, pp. 312–317.
- [13] D. Girbau, A. Ramos, A. Lazaro, S. Rima, and R. Villarino, "Passive wireless temperature sensor based on time-coded uwb chipless RFID tags," *IEEE Trans. Microw. Theory Techn.*, vol. 60, no. 11, pp. 3623–3632, Nov. 2012.
- [14] P. Pursula, I. Marttila, K. Nummila, and H. Seppa, "High frequency and ultrahigh frequency radio frequency identification passive sensor transponders for humidity and temperature measurement within building structures," *IEEE Trans. Instrum. Meas.*, vol. 62, no. 9, pp. 2559–2566, Sep. 2013.
- [15] S. Bhadra, D. S. Y. Tan, D. J. Thomson, M. S. Freund, and G. E. Bridges, "A wireless passive sensor for temperature compensated remote pH monitoring," *IEEE Sensors J.*, vol. 13, no. 6, pp. 2428–2436, Jun. 2013.
- [16] B. S. Cook, J. R. Cooper, and M. M. Tentzeris, "An inkjet-printed microfluidic RFID-enabled platform for wireless lab-on-chip applications," *IEEE Trans. Microw. Theory Techn.*, vol. 61, no. 12, pp. 4714–4723, Dec. 2013.
- [17] S. P. Silva, M. A. Sabino, E. M. Fernandes, V. M. Correlo, L. F. Boesel, and R. L. Reis, "Cork: Properties, capabilities and applications," *Int. Mater. Rev.*, vol. 50, no. 6, pp. 345–365, 2005.
- [18] M.-Q. Lee and S. Nam, "An accurate broadband measurement of substrate dielectric constant," *IEEE Microw. Guid. Wave Lett.*, vol. 6, no. 4, pp. 168–170, Apr. 1996.
- [19] M. D. Janezic and J. A. Jargon, "Complex permittivity determination from propagation constant measurements," *IEEE Microw. Guided Wave Lett.*, vol. 9, no. 2, pp. 76–78, Feb. 1999.
- [20] D. M. Pozar, *Microwave Engineering*. New York, NY, USA: Wiley, 2012.
- [21] F. Declercq, H. Rogier, and C. Hertleer, "Permittivity and loss tangent characterization for garment antennas based on a new matrix-pencil two-line method," *IEEE Trans. Antennas Propag.*, vol. 56, no. 8, pp. 2548–2554, Aug. 2008.
- [22] D. M. Dobkin, *The RF in RFID*, 2nd ed. Oxford, U.K.: Newnes, 2013.
- [23] C. G. Malmberg and A. A. Maryott, "Dielectric constant of water from 0 ° to 100 °C," *J. Res. Nat. Bureau Standards*, vol. 56, no. 1, pp. 1–8, 1956.
- [24] B. Wozniak and J. Dera, "Light absorption by water molecules and inorganic substances dissolved in sea water," in *Light Absorption in Sea Water*, vol. 33. New York, NY, USA: Springer, 2007, pp. 11–81.
- [25] K. V. S. Rao, P. V. Nikitin, and S. F. Lam, "Antenna design for UHF RFID tags: A review and a practical application," *IEEE Trans. Antennas Propag.*, vol. 53, no. 12, pp. 3870–3876, Dec. 2005.
- [26] G. Zamora, S. Zuffanelli, F. Paredes, F. Martín, and J. Bonache, "Design and synthesis methodology for UHF-RFID tags based on the T-match network," *IEEE Trans. Microw. Theory Techn.*, vol. 61, no. 12, pp. 4090–4098, Dec. 2013.



Ricardo Gonçalves (S'13) was born in Lisbon, Portugal, in 1988. He received the B.Sc. and M.Sc. degrees in electronics and telecommunications engineering from the Instituto Superior de Engenharia de Lisboa, Lisbon, in 2010 and 2012, respectively. He is currently pursuing the Ph.D. degree in electrical engineering with the University of Aveiro.

He was with Dailywork I&D, from 2010 to 2012, as a Developer Engineer of Embedded Electronic Systems for Vehicular Location Systems and

Healthcare Platforms. His main research interests include wireless power transfer systems, radio-frequency identification, and wireless passive sensor networks. His main research interests are in the development of antenna solutions in nonconventional materials for wireless applications and wireless power transfer systems. He is currently a Researcher with the Instituto de Telecomunicações, Aveiro, Portugal. He is a member of the IEEE MTT-S and AP-S. In 2011, he received the merit scholarship for exceptional academic performances.



Sergi Rima was born in Tortosa, Spain, in 1988. He received the B.Sc. degree in telecommunication engineering from Universitat Rovira i Virgili, Tarragona, Spain, in 2011, and the M.Sc. degree from the Universitat Politècnica de Catalunya, Barcelona, Spain, in 2014.

He joined the CTTC Laboratory, in 2013, to work on his M.Sc. thesis entitled UHF Radio-Frequency Identification (RFID) Tag Design on Cork Substrate for Wine Bottle Monitoring. His research interests lie in the field of antennas and RFID technology.



Roberto Magueta received the M.Sc. degree in electronics and telecommunications engineering from the University of Aveiro, Portugal, in 2013. He joined the Instituto de Telecomunicações, Aveiro, as a Researcher, in the Project RadioVoip-Smart Antenna for Maritime Communications.

He is currently pursuing the Ph.D. degree. His thesis' work is focused on transmitter and receiver designs for future mm-wave and massive MIMO-based wireless systems.



Pedro Pinho (M'14) was born in Vale de Cambra, Portugal, in 1974. He received the Licenciado and M.Sc. degrees in electrical and telecommunications engineering and the Ph.D. degree in electrical engineering from the University of Aveiro, Aveiro, Portugal, in 1997, 2000, and 2004, respectively.

He has been a member of the Research Staff with the Instituto de Telecomunicações, Aveiro, Portugal, since 1997. He is currently a Professor Adjunto with the Department of Electrical Telecommunications and Computers Engineering, Instituto Superior de Engenharia de Lisboa, Lisbon, Portugal. He has authored or co-authored over 90 papers in conferences and international journals, four book chapters, and a book. His current research interests are in antennas for location systems, reconfigurable antennas, and antenna design for passive sensors in nonconventional materials.



Ana Collado (SM'12) received the M.Sc. and Ph.D. degrees in telecommunications engineering from the University of Cantabria, Spain, in 2002 and 2007, respectively. She is currently a Senior Research Associate and the Project Management Coordinator with the Technological Telecommunications Center of Catalonia, Barcelona, Spain, where she performs her professional activities. Her professional interests include active antennas, substrate integrated waveguide structures, nonlinear circuit design, and energy harvesting and wireless power

transmission solutions for self-sustainable and energy efficient systems.

She has participated in several national and international research projects and has co-authored over 70 papers in journals and conferences. Among her activities, she has collaborated in the organization of several international workshops in different countries of the European Union and also a Training School for Ph.D. students. She was a Marie Curie Fellow of the FP7 project Symbiotic Wireless Autonomous Powered System. She serves on the Editorial Board of *Radioengineering Journal* and she is currently an Associate Editor of the *IEEE Microwave Magazine* and a member of the IEEE MTT-26 Wireless Energy Transfer and Conversion and MTT-24 Radio-Frequency Identification Technologies.



Apostolos Georgiadis (SM'08) was born in Thessaloniki, Greece. He received the B.S. degree in physics and the M.S. degree in telecommunications from the Aristotle University of Thessaloniki, Greece, in 1993 and 1996, respectively, and the Ph.D. degree in electrical engineering from the University of Massachusetts at Amherst, in 2002. He is currently a Senior Researcher and Group Leader of the Microwave Systems and Nanotechnology Department with the Centre Tecnològic de Telecomunicacions de Catalunya, Barcelona, Spain,

in the area of communications subsystems, where he is involved in active antennas and antenna arrays and more recently with Radio-Frequency Identification (RFID) technology and energy harvesting.

Dr. Georgiadis was a Marie Curie Fellow. He was the Chairman of COST Action IC0803, RF/Microwave Communication Subsystems for Emerging Wireless Technologies, and the Co-ordinator of Marie Curie Industry-Academia Pathways and Partnerships Project was entitled Symbiotic Wireless Autonomous Powered System. He is a member of the IEEE MTT-S TC-24 RFID Technologies (Chair 2012-2014) and the IEEE MTT-S TC-26 Wireless Energy Transfer and Conversion. He serves as an Associate Editor of the IEEE MICROWAVE AND WIRELESS COMPONENTS LETTERS and the *IET Microwaves Antennas and Propagation Journal*. He is the Editor-in-Chief of the *Wireless Power Transfer* (Cambridge University Press). He is also a Distinguished Lecturer of the IEEE Council on RFID and the Vice Chair of URSI Commission D.



Jimmy Hester (S'14) received the degree and M.S. degree in electrical and signal processing engineering from INP Toulouse, ENSEEIHT, in 2012 and 2014, respectively, and the M.S. degree in electrical and computer engineering from the Georgia Institute of Technology, Atlanta, in 2014, where he is currently pursuing the Ph.D. degree in electrical and computer engineering. He is a Research Assistant with the ATHENA Group, Georgia Institute of Technology.

He has been working toward the use of carbon nanomaterials applied to inkjet-printed RF sensing components for flexible low-cost ubiquitous gas sensing applications. His work covers the entire development process, from the development of inkjet inks, improvement of fabrication methods, sensor component design, high-frequency characterization and environmental testing to the design, and simulation and fabrication of the RF system embedding the sensor. His research interests lie at the interface between radio frequency engineering and material science, in the form of flexible electronics technologies and nanotechnologies.



Nuno Borges Carvalho (S'97-M'00-SM'05-F'15) was born in Luanda, Angola, in 1972. He received the Diploma and Ph.D. degrees in electronics and telecommunications engineering from the University of Aveiro, Aveiro, Portugal, in 1995 and 2000, respectively.

He is currently a Full Professor with the Universidade de Aveiro, Aveiro, and a Senior Research Scientist with the Instituto de Telecomunicações, Universidade de Aveiro, where he coordinates the wireless communication thematic area and the Radio

Systems Group.

He co-authored *Intermodulation in Microwave and Wireless Circuits* (Reading, MA, USA: Artech House, 2003) and *Microwave and Wireless Measurement Techniques* (Cambridge, U.K.: Cambridge Univ. Press, 2013). He has been a Reviewer and has authored over 200 papers in magazines and conferences. He co-holds four patents. His main research interests include software-defined radio front-ends, wireless power transmission, nonlinear distortion analysis in microwave/wireless circuits and systems, and measurement of nonlinear phenomena. He has recently been involved in the design of dedicated radios and systems for newly emerging wireless technologies.

Dr. Carvalho is the Chair of the IEEE MTT-11 Technical Committee. He is a member of IEEE MTT-20, MTT-24, and MTT-26, and the IEEE Portugal Section Chair. He is also an Associate Editor of the IEEE TRANSACTIONS ON MICROWAVE THEORY AND TECHNIQUES, the *IEEE Microwave Magazine*, and the *Cambridge Journal on Wireless Power Transmission*, and the Chair of the URSI-Portugal Metrology Group.



Manos M. Tentzeris (S'89-M'92-SM'03-F'10) received the Diploma (*magna cum laude*) degree in electrical and computer engineering from the National Technical University of Athens, Greece, and the M.S. and Ph.D. degrees in electrical engineering and computer science from the University of Michigan, Ann Arbor, MI. He has authored over 500 papers in refereed journals and conference proceedings, five books, and 19 book chapters. He has helped to develop academic programs in highly integrated/multilayer packaging

for RF and wireless applications using ceramic and organic flexible materials, paper-based radio-frequency identifications' (RFIDs) and sensors, biosensors, wearable electronics, inkjet-printed electronics, Green electronics and power scavenging, nanotechnology applications in RF, Microwave MEMs, SOP-integrated (UWB, multiband, mmW, conformal) antennas, and been the Head of the ATHENA Research Group (20 researchers). He is currently a Professor with the School of Electrical and Computer Engineering, Georgia Institute of Technology (GT), Atlanta, GA. He is the Head of the GT-ECE Electromagnetics Technical Interest Group, and he has served as the Associate Director of the Georgia Electronic Design Center for RFID/Sensors research from 2006 to 2010, and the Associate Director of RF Research with the GT NSF-Packaging Research Center and the RF Alliance Leader from 2003 to 2006.

He was a recipient/co-recipient of the 2014 GT-ECE Distinguished Faculty Achievement Award, the 2013 IET Microwaves, Antennas and Propagation Premium Award, the 2012 FiDiPro Award in Finland, the iCMG Architecture Award of Excellence, the 2010 IEEE Antennas and Propagation Society Piergiorgio L. E. Uslenghi Letters Prize Paper Award, the 2011 International Workshop on Structural Health Monitoring Best Student Paper Award, the 2010 Georgia Tech Senior Faculty Outstanding Undergraduate Research Mentor Award, the 2009 IEEE Transactions on Components and Packaging Technologies Best Paper Award, the 2009 E.T.S. Walton Award from the Irish Science Foundation, the 2007 IEEE APS Symposium Best Student Paper Award, the 2007 IEEE IMS Third Best Student Paper Award, the 2007 ISAP 2007 Poster Presentation Award, the 2006 IEEE MTT Outstanding Young Engineer Award, the 2006 Asian-Pacific Microwave Conference Award, the 2004 IEEE TRANSACTIONS ON ADVANCED PACKAGING Commendable Paper Award, the 2003 NASA Godfrey Art Anzic Collaborative Distinguished Publication Award, the 2003 IBC International Educator of the Year Award, the 2003 IEEE CPMT Outstanding Young Engineer Award, the 2002 International Conference on Microwave and Millimeter-Wave Technology Best Paper Award (Beijing, China), the 2002 GT-ECE Outstanding Junior Faculty Award, the 2001 ACES Conference Best Paper Award and the 2000 NSF CAREER Award, and the 1997 Best Paper Award of the International Hybrid Microelectronics and Packaging Society. He was the TPC Chair of the IEEE IMS 2008 Symposium and the Chair of the 2005 IEEE CEM-TD Workshop and he is the Vice Chair of the RF Technical Committee of the IEEE CPMT Society. He is the Founder and Chair of the RFID Technical Committee of the IEEE MTT Society and the Secretary/Treasurer of the IEEE C-RFID. He is the Associate Editor of the IEEE TRANSACTIONS ON MICROWAVE THEORY AND TECHNIQUES, the IEEE TRANSACTIONS ON ADVANCED PACKAGING, and the *International Journal on Antennas and Propagation*. He was a Visiting Professor with the Technical University of Munich, Germany, in the summer of 2002, GTRI-Ireland in Athlone, Ireland, in the summer of 2009, and LAAS-CNRS, Toulouse, France, in the summer of 2010.

He has given more than 100 invited talks to various universities and companies all over the world. He is also a member of URSI-Commission D, a member of MTT-15 Committee, an Associate Member of EuMA, a Fellow of the Electromagnetic Academy, and a member of the Technical Chamber of Greece. He served as one of the IEEE MTT-S Distinguished Microwave Lecturers from 2010 to 2012.

[J5] - C. Loss, **R. Gonçalves**, C. Lopes, P. Pinho, R. Salvado, "Smart Coat with a Fully-Embedded Textile Antenna for IoT Applications", *Sensors*, Vol. 16, No. 6, pp. 938, 2016

Article

Smart Coat with a Fully-Embedded Textile Antenna for IoT Applications

Caroline Loss ^{1,2,3,*}, Ricardo Gonçalves ^{2,4}, Catarina Lopes ^{1,2}, Pedro Pinho ^{2,5} and Rita Salvado ¹

¹ FibEnTech Research Unit, Universidade da Beira Interior, Rua Marquês D'Ávila e Bolama, Covilhã 6201-001, Portugal; catarina.lopes@ubi.pt (C.L.); lrbss@ubi.pt (R.S.)

² Instituto de Telecomunicações, Campus Universitário de Santiago, Aveiro 3810-135, Portugal; rgoncalves@av.it.pt (R.G.); ppinho@deetc.isel.pt (P.P.)

³ Capes Foundation, Ministry of Education of Brazil, Brasília 70040-020, Brazil

⁴ Departamento de Eletrônica, Telecomunicações e Informática, Universidade de Aveiro, Campus Universitário de Santiago, Aveiro 3810-135, Portugal

⁵ Instituto Superior de Engenharia de Lisboa, Rua Conselheiro Emílio Navarro, Lisboa 1959-009, Portugal

* Correspondence: carol@ubi.pt; Tel.: +351-275-319-852

Academic Editors: Stefano Mariani, Dirk Lehmhus, Francesco Ciucci, Alberto Vallan and Thomas B. Messervey
Received: 22 April 2016; Accepted: 17 June 2016; Published: 22 June 2016

Abstract: The Internet of Things (IoT) scenario is strongly related with the advance of the development of wireless sensor networks (WSN) and radio frequency identification (RFID) systems. Additionally, in the WSN context, for a continuous feed, the integration of textile antennas for energy harvesting into smart clothing is a particularly interesting solution when the replacement of batteries is not easy to practice, such as in wearable devices. This paper presents the *E-Caption: Smart and Sustainable Coat*. It has an embedded dual-band textile antenna for electromagnetic energy harvesting, operating at global system for mobile communication (GSM) 900 and digital cellular system (DCS) 1800 bands. This printed antenna is fully integrated, as its dielectric is the textile material composing the coat itself. The *E-Caption* illustrates the innovative concept of textile antennas that can be manipulated as simple emblems. Seven prototypes of these “emblem” antennas, manufactured by lamination and embroidering techniques are also presented. It is shown that the orientation of the conductive fabric does not influence the performance of the antenna. It is also shown that the direction and number of the stitches in the embroidery may influence the performance of the antenna. Moreover, the comparison of results obtained before and after the integration of the antenna into cloth shows the integration does not affect the behavior of the antenna.

Keywords: textile antenna; energy harvesting; smart clothing; wearable devices

1. Introduction

Nowadays, the socio-economic development and lifestyle trends indicate an increasing consumption of technological products and processes, powered by emergent concepts such as the Internet of Things (IoT), where everything is connected in a single network [1]. The development of smart objects for IoT applications, include the capacity of this objects to be identifiable, to communicate and to interact [2]. In this context, wearable technology has been addressed to make the person, mainly through his clothes, able to communicate with, and be part of, this technological network [3].

Wireless communication systems are made up of several electronic components, which, over the years, have been miniaturized and made more flexible, such as batteries, sensors, actuators, data processing units, interconnectors, and antennas [4]. In the systems for on-body applications, the antennas have been challenging, because they are conventionally built on rigid substrates, hindering their efficient and comfortable integration into the garment.

However, embedding antennas into clothing allows expanding the interaction of the user with some electronic devices, making them less invasive and more discrete. Thus, textile antennas that are designed combining the traditional textile materials with new technologies emerge as a potential interface of the human-technology-environment relationship. Textile antennas, thus, become an active part in the wireless communication systems [5–9], aiming applications, such as tracking and navigation [10–12], mobile computing, and others [13].

1.1. Textile Antennas

For IoT applications, embedding antennas into clothing makes the garments become a smart interface for the interaction between the user and the network. The wearable antennas should be thin, lightweight, of easy or no maintenance, robust, and resistant to washing cycles and usage and, moreover, must be low cost for manufacturing and commercializing [14]. In this way, textile planar antennas, the microstrip patch type, have been proposed for garment applications, because they present all of these characteristics, and also are adaptable to any surface [15]. This type of antenna is usually formed by overlapping conductive (patch and ground plane) and dielectric (substrate) layers [16]. Therefore, the knowledge of the properties of textile materials that are used is crucial, as well as the manufacturing techniques for connecting the layers, such as gluing, seaming, and laminating with adhesive sheets. Furthermore, the microstrip patch antenna radiates perpendicularly to a ground plane, which serves as a shield to the antenna radiation, assuring that the human body absorbs only a very small fraction of the radiation.

1.2. Electromagnetic Energy Harvesting

The integration of electronic devices on clothing puts the question about how to feed them. The batteries are an obvious choice, but they are bulky, require frequent replacement or recharging, and their short longevity is an ecological concern of current times. Additionally, the research of self-sustainable wireless devices is a growing challenge in IoT applications [17]. In this context, energy harvesting is a promising solution to consider in the next generation of wireless sensor networks (WSN). Nowadays, radio frequency (RF) energy is currently broadcasted from billions of radio transmitters and, thus, can be collected from the ambient environment or from dedicated sources [18]. Moreover, the advance of technology stimulates the growing number of wireless transmitters, especially in highly populated urban areas, increasing the power density of available RF in the environment [19].

Coherently, in the past years, different proposals of textile antennas for RF energy harvesting have been proposed [19–21]. However, only two works [19,20] have outlined the integration of these antennas in smart clothing. In [20] a scheme of jacket with harvester circuit is presented. A triple-band ring textile antenna for RF energy harvesting, operating at GSM900, GSM1800, and WiFi frequencies is also proposed. This antenna was developed with a multilayer configuration and for its conductive parts, the Global EMC shielding fabric with surface resistivity of $0.02 \Omega/\text{sq.}$ was used. An unspecified fabric with $\epsilon_r = 1.23$ was used as a substrate support of the antenna. The Kapton[®] fabric with $\epsilon_r = 3.4$, $\tan\delta = 0.002$ and 1 mm of thickness, was used as the dielectric substrate. The predicted antenna efficiencies are 61% at 900 MHz, 54% at 1750 MHz, and 85% at 2450 MHz. In [21] the draft of a coat is presented, where multiple body-worn embroidered textile antennas are proposed to be integrated into a harvester system operating in the 2.45 GHz WLAN band.

2. Materials and Methods

This paper is based on the dual-band textile antenna for GSM900 and DCS1800 frequency bands proposed in [22] that is shown in Figure 1 and which dimensions are given in Table 1 below. The next subsections will analyze the manufacturing process of making this antenna, presenting seven prototypes, made using two different manufacturing techniques: thermal adhesive lamination and embroidering. Further, the integration of the antenna into a smart coat, by fully embedding it into the material constituting the coat, is described.

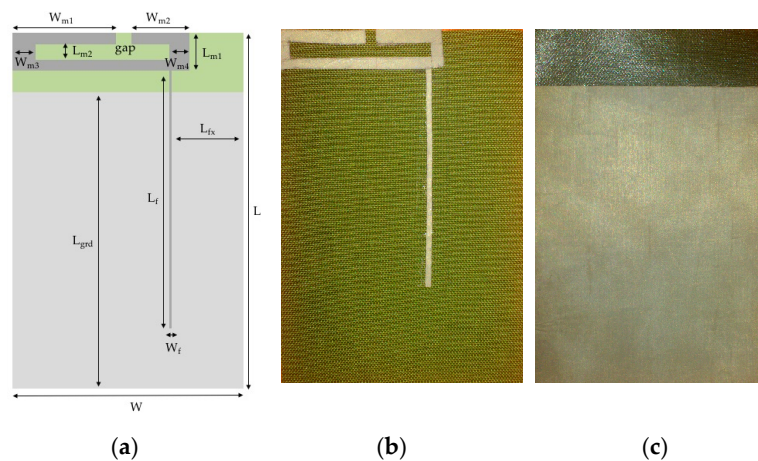


Figure 1. Textile antenna. (a) Design of the dual-band antenna; (b) Front; and (c) Back.

Table 1. Dimensions of the textile antenna.

Parameter	Dimension (mm)
L, L_{gnd}, L_f, L_{fx}	120, 100, 78, 30
$L_{m1}, L_{m2}, \text{gap}, W$	12, 5, 3.1, 80
$W_f, W_{m1}, W_{m2}, W_{m3}, W_{m4}$	1.5, 31, 21, 8, 4

2.1. Materials

The selection of textile materials for the development of antennas is critical, as discussed in [14]. In this work, all materials used to manufacture the wearable antennas are commercially available and described in the Table 2. For the dielectric substrate, a synthetic fabric with low regain was chosen, in order to minimize the effect of the moisture absorption on lowering the resonance frequency of the antenna.

Table 2. Characteristics of the textile materials used to develop wearable antennas.

Dielectric Materials	Fabric	Mass per Unit Surface (g/m ²)	Composition	Finish	Thickness (mm)	ϵ_r	$\tan \delta$
	Cordura® Light	280	100% PA 6.6	Polyurethane coated	0.5	1.9	0.0098
Conductive Materials	Fabric	Mass per Unit Surface (g/m ²)	Composition	Finish	Thickness (mm)	Conductivity (S/m)	
	Zelt	55.87	100% Polyamide	Copper and tin plated	0.06	1.75105	
	Yarn	Linear Mass (dtex) ¹	Composition	Finish	-	Conductivity (S/m)	
	Silverpam	250	100% Polyamide	Silver plated	-	0.005	
Other Materials	Fabric	Mass per Unit Surface (g/m ²)	Composition	Finish	Thickness (mm)		
	Atlantic	120	100% Polyester	Oil + water repellent	0.3		
	Adhesive Sheet Type	Mass per Unit Surface (g/m ²)	Composition	-	Thickness (mm)		
	Fixorete Losango	0.28	100% Polyamide	-	0.01		

¹ Tex is the unit of the International System of Units used to characterize the linear mass of fibers and yarns. Tex is defined as the mass in grams per 1000 m. The subunit *decitex* (dtex) is the mass in grams per 10,000 m [23].

2.2. Manufacturing Techniques

Beyond choosing the textile materials, the construction technique of the antenna is also crucial because the textile materials are highly deformable. The geometrical dimensions of the conductive patch and of the dielectric substrate should remain stable when connecting them, as the mechanical stabilization of both materials is essential to preserve the desired characteristics of the antenna. The geometrical precision of the conductive patch is also critical as the proposed antenna has thin details, as shown in Table 1.

Moreover, the technique to connect the various layers should not affect the electrical properties of the patch, particularly its electrical resistivity. All antennas presented in the following sections were produced assembling the components with the thermal adhesive sheet (JAU Têxteis, Serzedo, Portugal), previously described in the Table 2. The antennas were glued by ironing without steam in a vacuum table. Steam was not used deliberately, especially on materials with copper, to avoid oxidation of the conductive material and the consequent increase of its electrical resistivity.

However, an extra antenna was produced by an ironing process with steam in order to analyse the influence of the steam in the performance of the antenna. Both antennas, with and without steam, were assembled using the same ironing conditions, presented in the Table 3. Additionally, in order to ensure the geometrical accuracy, the patches were cut by an LC6090C CCD (Jinan G. Weike Science & Tecnology Co. Ltd., Jinan, China) laser cutting machine. The obtained results are shown in the Figure 2.

Table 3. Ironing conditions.

Temperature (°C)	Pressure (bar)	Time (s)
200	10	12 (6 for patch + 6 for ground plane)

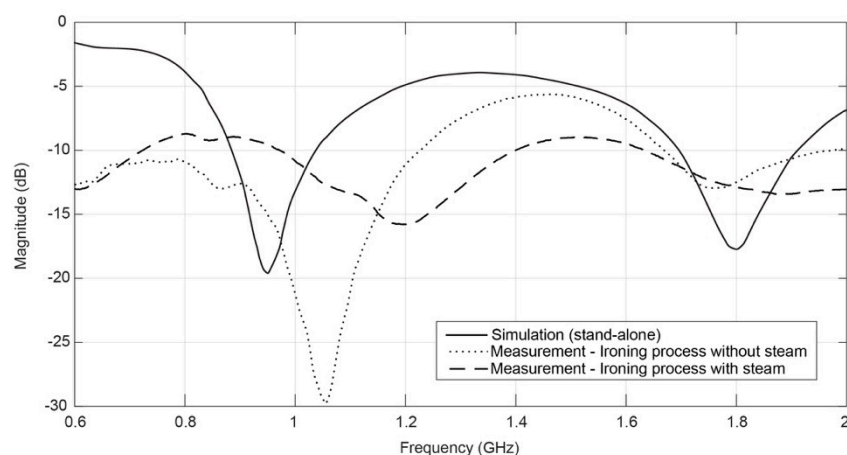


Figure 2. Comparison between ironing processes with, and without, steam.

According to the measured results presented on Figure 2, one can see a higher frequency shift in the antenna made using steam in the ironing process. In order to investigate the cause of this shift, the thickness of the antenna was measured, using Kawabata's Evaluation System (KES) for fabrics (KES-F-3 Compressional Tester). For the antenna without steam, the thickness is 0.62 mm, and for the antenna with steam it is 0.60 mm. This difference can be due to the higher compaction of the materials when steam is applied. As one can see in the scanning electron microscope (SEM) images in Figure 3, in the antenna without steam the adhesive sheet (see yellow arrows) remains at the interface between the conductive and dielectric layers. However, when the steam is applied, the adhesive sheet merges with the textile structure (see green arrows).

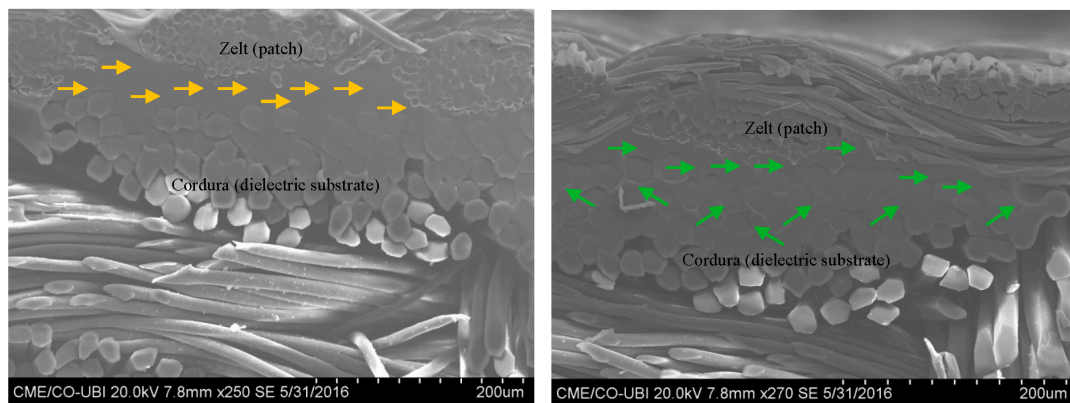


Figure 3. SEM images: cross-section of the antenna assembled (a) without steam and (b) with steam.

This effect may be responsible for a decrease in conductivity due to the presence of the glue among the conductive yarns. Moreover, the presence of the adhesive sheet into the Cordura fabric (B. W. Wernerfelt Group, Søborg, Denmark) will presumably change, even if slightly, its permittivity. Finally, the shift in frequency may be due to other factors, such as the precision of cutting during the manufacturing process.

Nevertheless, it is worth noting that it is important to further study the effect of steam in the performance of the antenna, in order to consider and compensate for it in the design of the antenna.

2.2.1. Laminated Antennas

These antennas are made by superposing fabrics and attaching them with a thermal adhesive sheet. The cutting process of the conductive material is critical, as the antenna has very thin lines; for instance, the W_f dimension (see Table 1). In order to increase the geometrical accuracy, the patches were cut by an LC6090C CCD laser cutting machine. This procedure also reduces the common fraying effect that appears when cutting thin fabrics with scissors.

Two antennas were fabricated with this lamination technique. In order to test the influence of the direction of the structure of the conductive fabric (Zelt) on the performance of the antenna, the patch of antenna A was cut parallel to the warp, and the patch of antenna B was cut at 45° (bias). Figure 4 presents the simulated and measured values of S_{11} parameter of both antennas, measured with a vector network analyser (VNA).

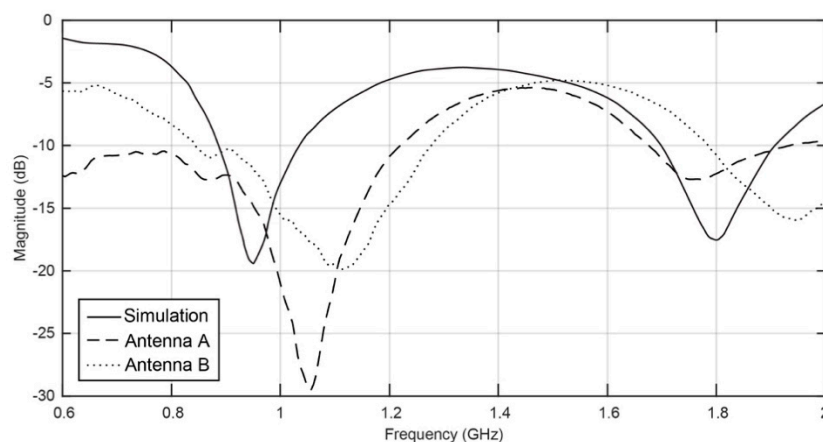


Figure 4. Simulated and measured return loss of laminated antennas.

The antennas produced by the lamination technique have shown good results, as the S_{11} parameter shows. As one can see in Figure 4, the measurements match the simulation fairly well, although there is a small shift of the frequency. This shift of frequency might be due to the narrow manufacturing tolerances that exist even when cutting the fabric by laser. Still, the reflection coefficient (S_{11}) is low at the operating frequencies, meaning that the antenna presents a good impedance mismatch in both GSM and DCS bands.

Thus, with the laminated manufacturing technique, by controlling the ironing conditions, the adhesive may remain at the interface of the conductive and dielectric materials, as one can see in the SEM image in Figure 5, showing the cross-section of a laminated antenna assembled without steam. Therefore, in this antenna, made by ironing without steam, the electrical surface resistance of the patch and the relative permittivity of the substrate are not significantly changed. This observation is corroborated by the S_{11} measurements previously showed in the Figure 4.

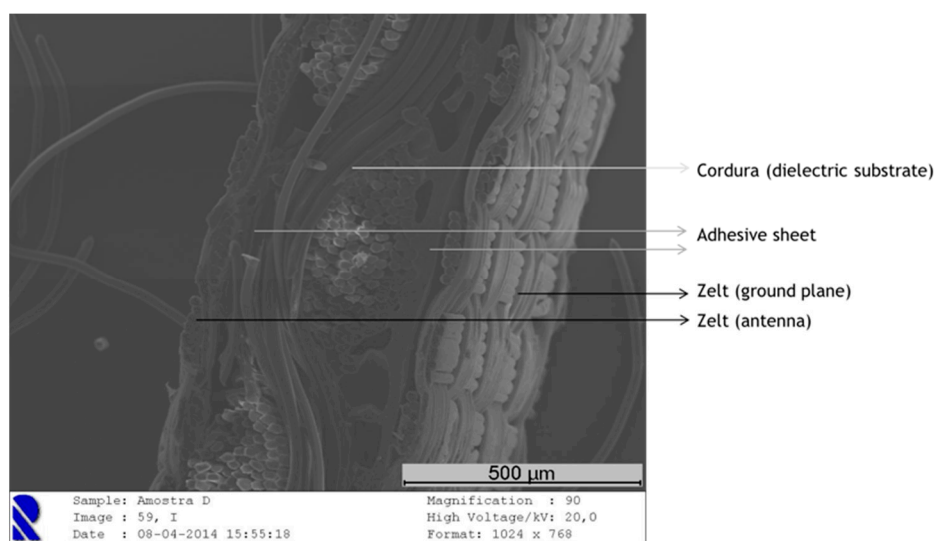


Figure 5. SEM image: cross-section of the textile antenna after assembly with adhesive sheet, without steam.

2.2.2. Embroidered Antennas

Embroidering is a promising method in terms of repeatability and mass-manufacturing [24], as the embroidered antennas do not need a cutting or lamination process, thus reducing the production costs. For this reason, several embroidered antennas have been proposed; for instance, spiral antennas [25,26], RFID tags [27,28], and antennas without a ground plane [29–31]. This paper explores the embroidering technique to produce antennas that can be easily applied in clothing as an emblem. This way the embroidering technique might enlarge the dissemination of the textile antennas into clothing.

As the antenna considered in this paper is a printed monopole antenna which requires a ground plane, the manufacturing process has to be adapted in order to eliminate the short cuts caused by the embroidering technique in both sides of the dielectric material. Therefore, the construction technique of the embroidered antenna was: firstly, embroidering the patch in a thin textile; secondly, cut the embroidery; and, finally, attach the embroidery to the dielectric substrate using the thermal adhesive sheet. This process is the same one used to produce the traditional emblems for cloth customization.

Five antennas were developed with this technique, using a SWF MA-6 automatic embroidering machine. The patches were embroidered in the Atlantic fabric (B. W. Wernerfelt Group, Søborg, Denmark) using Silverpam yarn (Tibtech Innovations, Pierre Mauroy, France) (see Table 2). The parameters of the embroidery are described in Table 4. The orientation of the stitch was considered by performing stitches along four different directions for antennas 1, 3, 4, and 5. The number of stitches

was considered by varying the float of the stitch for antennas 2 and 3. To avoid differences in the fringe effect on the feed line ($W_f \times L_f$) due the different directions of the stitches, all antennas have feed lines embroidered with a horizontal step stitch.

Table 4. Parameters of the embroidered antennas.

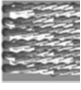
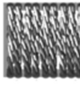

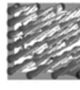
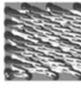
Antenna	1	2	3	4	5
Description of Stitch	Horizontal step stitch	Satin with vertical step	Vertical step stitch, with horizontal step	Diagonal step stitch (direction: 152°/quadrant 2), with horizontal step	Diagonal step stitch (direction: 30°/quadrant 1), with horizontal step
Draft of Stitch					
Number of Stitches	1255	2084	1378	1360	1361
Yarn Consumption (g)	0.27	0.39	0.22	0.23	0.27
Yarn Consumption per Embroidered Area (g/m ²)	489	706	398	416	489

Figure 6 shows the simulated and measured values of the S_{11} parameter of these antennas, measured with a VNA. It is clean that the measurements match closely to the simulations. Where antenna 3 is the one with the best match of the reflection coefficient.

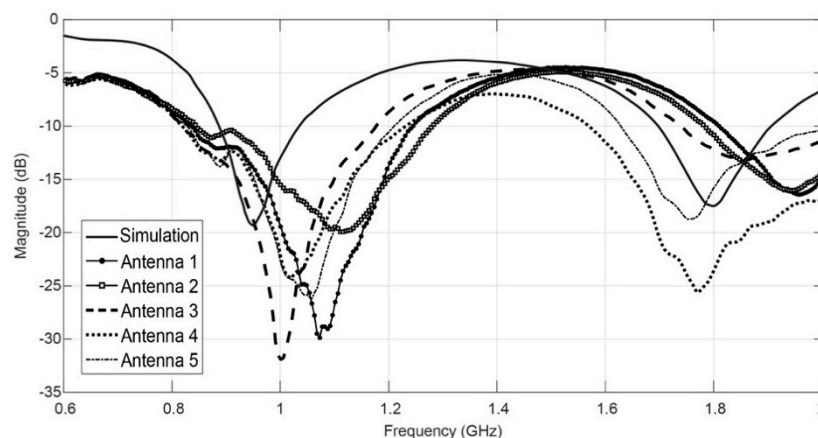


Figure 6. Simulated and measured return loss of embroidered antennas.

The antenna 3 presents the closest result to the simulation line. This can be due to the fact the embroidery stitch direction is parallel of the feed line, homogenizing the current flow [24]. Antennas 4 and 5 present very similar behavior that might indicate the angle of the diagonal direction is not influencing it. Coherently, antenna 1 shows the higher shift of the frequency that can be due to the fact the direction of the embroidery stitch is perpendicular to the feed line. Additionally, antenna 2 was made using a vertical stitch, as was antenna 3, having however, a higher number of stitches. This makes the current flow less continuous, due the constant breaks and higher number of air gaps in the embroidery [15], reducing the conductivity of the patch, which may explain the difference between the magnitudes of the return loss of antennas 3 and 2.

2.3. Integration into Clothing

When developing smart textile products, bringing technologies to the consumer in an acceptable and desirable format is a challenge. Some authors have been integrating textile antennas in products in a pleasing way, for instance, as wearable antennas for commercial advertisement proposes, dissimulated in brand names and logotypes [32,33]. However, until now, the microstrip patch textile

antennas have been built ex situ and then posteriorly integrated in the lining of the garment or into pockets or simply glued to the cloth.

This paper proposes an innovative solution that presents the first antenna prototype manufactured directly in the clothing as it is made with the same textile materials composing the cloth. This cloth is a smart coat for electromagnetic harvesting—the *E-Caption: Smart and Sustainable Coat*, in which the antenna has a substrate that is continuous and was cut according to the pattern-making of the coat, thus being part of it.

This innovative solution to integrate antennas into cloths is illustrated in Figure 7. The antenna is integrated into the clothing by manipulating it as a simple emblem. In the future, the antennas can be incorporated into patterns and drawings, mixing conductive and non-conductive embroideries, creating fashionable emblems that function as antennas. These “emblem” antennas may be accessible to the end user for customization of smart cloth, for several applications.

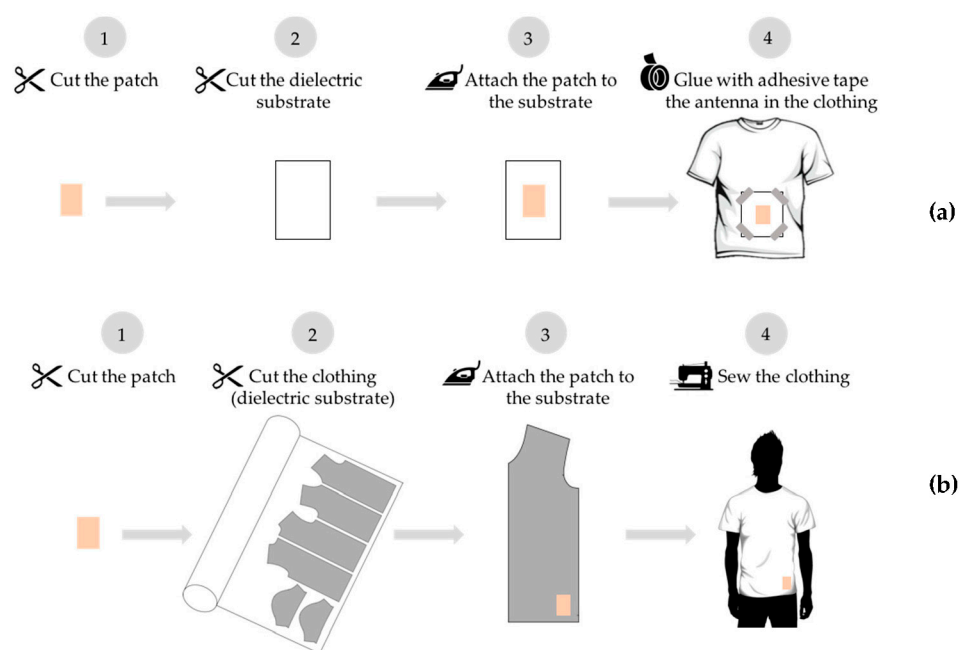


Figure 7. Comparison of techniques of integration of antennas into cloth (a) typical integration and (b) “emblem” approach.

E-Caption: Smart and Sustainable Coat

The integration of textile antennas for energy harvesting into smart clothing emerges as a particularly interesting solution when the replacement of batteries is not easy to practice, such as in wearable devices. A fully-embedded antenna in clothing contributes for the integration of electronic devices in less obtrusive ways, improving the good aesthetic and the technical design, making the garment more comfortable and desirable to the final consumer. This might enhance niche markets where form and function work together in order to create new attractive textile products that can assist the user in many aspects of their daily routine.

The *E-Caption: Smart and Sustainable Coat* was developed combining these concepts, integrating antenna A produced by the lamination manufacturing technique presented in previous sections. It is the first prototype of a smart coat with a printed monopole antenna fully integrated, as its dielectric is the textile material composing the coat itself. The coat is made of Cordura and of a 3D fabric (Reference 3003—3D fabric, from LMA—Leandro Manuel Araújo, Ltda.). Figure 8 shows the *E-Caption* coat with the textile antenna for RF energy harvesting.

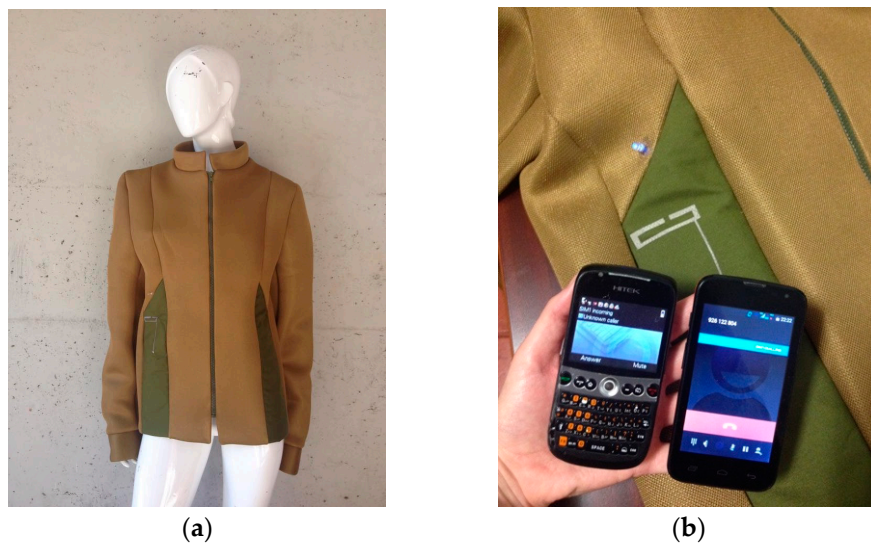


Figure 8. *E-Caption: Smart and Sustainable Coat.* (a) Design of the coat and (b) integrated antenna, in detail.

In the past years, some authors have been analyzing the influence of the human body on the performance of textile antennas [34,35]. However, no one has analyzed the influence of its integration on clothing on its performance. Therefore, the analysis of the integration of antennas and the evaluation of their behavior after integration into clothing are discussed in Section 3.

3. Results

The performance of the antenna of the *E-Caption: Smart and Sustainable Coat* was tested in the anechoic chamber, as shown in Figure 9.

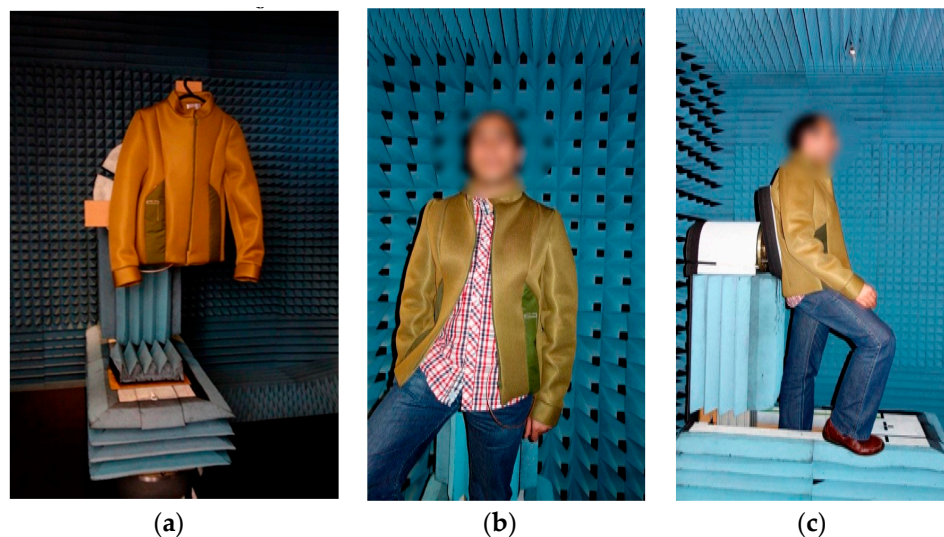


Figure 9. Performance of the antenna in the anechoic chamber (a) in free space and (b,c) on-body measurements.

Figure 10 presents the variation in the S_{11} parameter obtained through numerical simulation and measured in free space, before and after the integration into the smart coat. It is possible to see the agreement between the simulated and measured values even in the on-body measurements. The

textile antenna presents an operating frequency range capable of completely covering the GSM900 (880–960 MHz) and the DCS1800 (1710–1880 MHz).

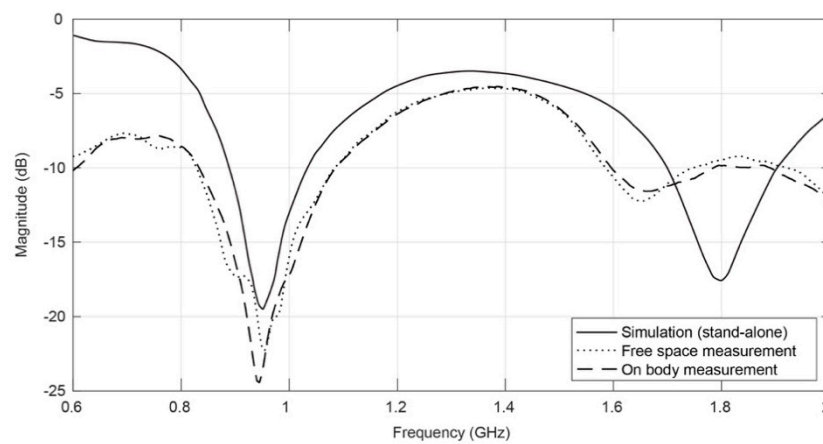


Figure 10. Simulated and measured return loss, before/after the integration on clothing.

Even after integrated into clothing, the radiation pattern of the antenna is clearly omnidirectional. The Figure 11 shows the radiation pattern of the antenna fully integrated into the smart coat structure and also measured on-body. The results depicted in Figure 11 correspond to the XZ plane. This is the only measurable plane (see Figure 9), due to the configuration and placement of the antenna on the coat. Nevertheless, it is the most relevant plane in order to evaluate the omnidirectional characteristic of the antenna.

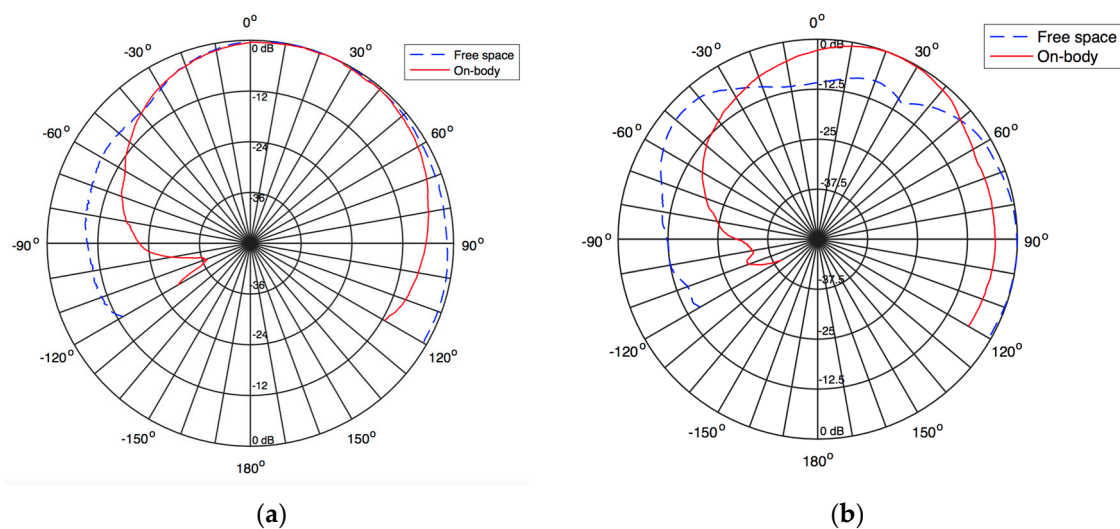


Figure 11. Measured radiation pattern of the textile antenna into the coat at (a) 900 MHz and (b) 1800 MHz.

Moreover, given the position of the antenna on the coat, previously shown in Figure 8, it is clear that the direction at which the antenna will present less influence from the coat or from the person occurs at nearly 30° in the broadside direction. This is confirmed by the results depicted in Figure 11.

According to the results presented in Figure 11, one may conclude that, as expected, the mass of the coat and mainly of the person influence the radiation characteristic of the antenna. In the measurement of the empty jacket, when the coat places between the probe antenna and the test antenna, around

160°, there is a reduction in the gain of the antenna, which is due to the presence of a large dielectric body, that is, the coat. Nevertheless, the antenna shows a nearly omnidirectional pattern.

The on-body antenna performs differently. Since the human body is conductive, it absorbs and reflects radiofrequency waves. The results on Figure 11 show that when the body is behind the test antenna, at 30° broadside, a slight increase in gain is measured. However, when the body is between the probe and the test antenna, at 160°, it will absorb a high amount of radiation and will reflect the rest in the opposite direction, shielding the test antenna and, thus, create a null of radiation at this point. This happens for both frequencies, being clearer at 1800 MHz.

4. Discussion

In the future, garments will not only communicate social conditions or protect the human body against the extremes of nature, but will also provide information and communication tools. Clothes are becoming able to communicate wirelessly without the need of large and expensive equipment. This is possible because textile technologies can produce new types of sensors and antennas that are so small, flexible, and inexpensive that they can be applied in different types of clothing, shoes, and accessories.

The effective integration of wearable systems contributes to the advance of the IoT. The innovative concept of producing textile antennas to integrate into clothing by simply manipulating it as an “emblem” may improve the usage of the wearable technologies. In the future, the wearable antennas can be incorporated into textile patterns and drawings, creating fashionable antennas. These “emblem” antennas may be easily acceded by the end user, for customization of smart cloth for several applications.

The *E-Caption: Smart and Sustainable Coat* is the first prototype of this concept, integrating an “emblem” antenna capable of completely covering GSM900 (880–960 MHz) and the DCS1800 (1710–1880 MHz) bands, for IoT applications. In this context, the integration of textile antennas for energy harvesting into smart clothing can be a solution for recharging wearable devices, such as low-power electronics and WBSN.

5. Conclusions

Embedding antennas in clothing contributes for the advance of the integration of electronic devices in less obtrusive way making the smart clothes more comfortable. In the *E-caption*, the antenna is manufactured directly on the clothing, having a continuous dielectric substrate made with the textile materials composing the coat. Therefore, a continuous substrate of the antenna does not influence its performance. Moreover, the presented results show that, despite the masses of the coat and of the body influencing the radiation characteristic of the integrated antenna, it still shows a nearly omnidirectional pattern.

This work shows that “emblem” antennas, including the ones having ground planes, may be manufactured by lamination and embroidering techniques. When laminating, the ironing process without steam seems to be preferable as it better preserves the electromagnetic performance of the materials. Additionally, this work shows the orientation of the conductive fabric used for the patch is not influencing the performance of the laminated antenna. In addition, it shows the direction and number of the stitches in the embroidery may contribute to increasing the conductivity of some elements, thus improving the performance.

Other techniques to produce “emblem” antennas may be considered in the future, for instance, transfer, screen printing, and inkjet methods. Finally, this innovative concept of textile antennas for energy harvesting might open new horizons in the clothing development and in sustainable communication.

Acknowledgments: The authors would like to thank CAPES Foundation for the Ph.D. grant, process No. 9371-13/3; the FCT/MEC for the Ph.D. grant SFRH/BD/91249/2012. This work is funded by FCT/MEC through national funds and when applicable co-funder by FEDER-PT2020 in partnership agreement under the project UID/EEA/50008/2013 and UID/Multi/00195/2013.

Author Contributions: Caroline Loss and Rita Salvado designed the experimental plan. Caroline Loss manufactured the antennas. Catarina Lopes made the embroidering. Caroline Loss and Catarina Lopes made the “E-Caption: Smart and Sustainable Coat” prototype. Ricardo Gonçalves and Pedro Pinho designed the textile antenna. Ricardo Gonçalves and Caroline Loss made the measurements. Caroline Loss and Rita Salvado wrote the manuscript. All authors revised the manuscript.

Conflicts of Interest: The authors declare no conflict of interest.

References

1. Kopetz, H. Internet of Things. In *Real-Time Systems: Design Principles for Distributed Embedded Applications*; Springer: New York, NY, USA, 2011; pp. 307–323.
2. Miorandi, D.; Sicari, S.; de Pellegrini, F.; Chlamtac, I. Internet of Things: Vision, applications and research challenges. *Ad Hoc Netw.* **2012**, *10*, 1497–1516. [[CrossRef](#)]
3. Stoppa, M.; Chiolerio, A. Wearable electronics and smart textiles: A critical review. *Sensors* **2014**, *14*, 11957–11992. [[CrossRef](#)] [[PubMed](#)]
4. Khaleel, H. *Innovation in Wearable and Flexible Antennas*; WIT Press: Southampton, UK, 2015.
5. Gupta, B.; Sankaralingam, S.; Dhar, S. Development of wearable and implantable antennas in the last decade: A review. *IEEE Conf. Publ.* **2010**, 251–267. [[CrossRef](#)]
6. Hertleer, C.; Rogier, H.; Vallozzi, L.; van Langenhove, L. A textile antenna for off-body communication integrated into protective clothing for firefighters. *IEEE Trans. Antennas Propag.* **2009**, *57*, 919–925. [[CrossRef](#)]
7. Zhang, L.; Wang, Z.; Psychoudakis, D.; Volakis, J.L. Flexible textile antennas for body-worn communication. In Proceedings of the IEEE International Workshop on Antenna Technology, Tucson, AZ, USA, 5–7 March 2012.
8. Salonen, P.; Keskilampi, M.; Rantanen, J.; Sydanheimo, L. A novel bluetooth antenna on flexible substrate for smart clothing. *IEEE Conf. Publ.* **2001**, 2, 789–794.
9. Salonen, P.; Hurme, H. A novel fabric WLAN Antenna for wearable applications. *IEEE Conf. Publ.* **2003**, 2, 100–103.
10. Salonen, P.; Rahmat-samii, Y.; Schafth, M.; Kivikoski, M. Effect of textile materials on wearable antenna performance: A case study of GPS antenna. *IEEE Conf. Publ.* **2004**, 1, 459–462.
11. Vallozzi, L.; Vandendriessche, W.; Rogier, H.; Hertleer, C.; Scarpello, M.L. Wearable textile GPS antenna for integration in protective garments. In Proceedings of the 4th European Conference on Antennas and Propagation, Barcelona, Spain, 12–16 April 2010; pp. 1–4.
12. Dierck, A.; Declercq, F.; Rogier, H. A wearable active antenna for global positioning system and satellite phone. *IEEE Trans. Antennas Propag.* **2013**, *61*, 532–538. [[CrossRef](#)]
13. Paul, D.L.; Giddens, H.; Paterson, M.G.; Hilton, G.S.; Mcgeehan, J.P. Impact of body and clothing on a wearable textile dual band antenna at digital television and wireless communications bands. *IEEE Trans. Antennas Propag.* **2013**, *61*, 2188–2194. [[CrossRef](#)]
14. Salvado, R.; Loss, C.; Pinho, P.; Gonçalves, R. Textile materials for the design of wearable antennas: A survey. *Sensors* **2012**, *12*, 15841–15857. [[CrossRef](#)] [[PubMed](#)]
15. Locher, I.; Klemm, M.; Kirstein, T.; Tröster, G. Design and characterization of purely textile patch antennas. **2006**, *29*, 777–788. [[CrossRef](#)]
16. Balanis, C.A. *Antenna Theory: Analysis and Design*, 3rd ed.; Wiley Interscience: Hoboken, NJ, USA, 2005.
17. Gubbi, J.; Buyya, R.; Marusic, S.; Palaniswami, M. Internet of Things (IoT): A vision, architectural elements, and future directions. *Future Gener. Comput. Syst.* **2013**, *29*, 1645–1660. [[CrossRef](#)]
18. Jabbar, H.; Song, Y.S.; Jeong, T.T. RF energy harvesting system and circuits for charging of mobile devices. *IEEE Trans. Consum. Electron.* **2010**, *56*, 247–253. [[CrossRef](#)]
19. Tavares, J.; Barroca, N.; Saraiva, H.; Borges, L.; Velez, F.; Loss, C.; Salvado, R.; Pinho, P.; Gonçalves, R.; Carvalho, N. Spectrum opportunities for electromagnetic energy harvesting from 350 MHz to 3 GHz. In Proceedings of the 7th International Symposium on Medical Information in Communication Technology, Tokyo, Japan, 6–8 March 2013; pp. 126–130.
20. Masotti, D.; Costanzo, A.; Adami, S. Design and realization of a wearable multi-frequency RF energy harvesting system. In Proceedings of the 5th European Conference on Antennas and Propagation, Rome, Italy, 11–15 April 2011; pp. 517–520.

21. Tallos, R.K.; Wang, Z.; Volakis, J.L. Wi-Fi energy harvesting system using body-worn antennas. In Proceedings of the Antennas and Propagation Society International Symposium (APSURSI), Memphis, TN, USA, 6–11 July 2014; pp. 1405–1406.
22. Gonçalves, R.; Carvalho, N.; Pinho, P.; Loss, C.; Salvado, R. Textile antenna for electromagnetic energy harvesting for GSM900 and DCS1800 bands. In Proceedings of the Antennas and Propagation Society International Symposium (APSURSI) 2013, Orlando, FL, USA, 7–13 July 2013; pp. 1206–1207.
23. Collier, A.M. *A Handbook of Textiles*, 3rd ed.; Wheaton: Exeter, UK, 1980.
24. Tsois, A.; Whittow, W.G.; Alexandridis, A.A.; Vardaxoglou Yiannis, J.C. Embroidery and related manufacturing techniques for wearable antennas: Challenges and opportunities. *Electronics* **2014**, *3*, 314–338. [[CrossRef](#)]
25. Brebels, S.; Ryckaert, J.; Boris, C.; Donnay, S.; de Raedt, W.; Beyne, E.; Mertens, R.P. SOP integration and codesign of antennas. *IEEE Trans. Adv. Packag.* **2004**, *27*, 341–351. [[CrossRef](#)]
26. Zhang, S.; Speight, D.; Paraskevopoulos, A.; Fonseca, D.; Luxey, C.; Whittow, W.; Pinto, J. On-body measurements of embroidered spiral antenna. In Proceedings of the Loughborough Antennas and Propagation Conference, Loughborough, UK, 2–3 November 2015; pp. 1–5.
27. Ukkonen, L.; Sydänheimo, L.; Rahmat-Samii, Y. Sewed textile RFID tag and sensor antennas for on-body use. In Proceedings of the 6th European Conference on Antennas and Propagation, Prague, Czech Republic, 25–30 March 2012; pp. 3450–3454.
28. Elmahgoub, K.; Elsherbeni, T.; Yang, F.; Elsherbeni, A.Z.; Sydänheimo, L.; Ukkonen, L. Logo-antenna based RFID tags for advertising application. *Appl. Comput. Electromagn. Soc. J.* **2010**, *25*, 174–181.
29. Huang, Y.P. Effect of sewing types on flexible embroidery antennas in UHF band. In Proceedings of the 43rd European Microwave Conference, Nuremberg, UK, 7–10 October 2013; pp. 88–91.
30. Acti, T.; Chauraya, A.; Zhang, S.; Whittow, W.G.; Seager, R.; Vardaxoglou, J.C.; Dias, T. Embroidered wire dipole antennas using novel copper yarns. *IEEE Antennas Propag. Lett.* **2015**, *14*, 638–641. [[CrossRef](#)]
31. Kiourti, A.; Volakis, J.L. Stretchable and flexible e-fiber antennas with high geometrical accuracy. In Proceedings of the 9th European Conference on Antennas and Propagation, Lisbon, Portugal, 12–17 April 2015; pp. 4–5.
32. Tak, J.; Choi, J. An all-Textile Louis Vuitton Logo Antenna. *IEEE Antennas Propag. Lett.* **2015**, *1225*, 3–6. [[CrossRef](#)]
33. Mahmud, M.S.; Dey, S. Design, performance and implementation of UWB wearable logo textile antenna. In Proceedings of the 15th International Symposium on Antenna Technology and Applied Electromagnetics ANTEM 2012, Toulouse, France, 25–28 June 2012; pp. 1–4.
34. Blecha, T.; Linhart, R.; Reboun, J. Screen-printed antennas on textile substrate. In Proceedings of the 2014 Electronics System-Integration Conference, Helsinki, Finland, 16–18 September 2014; pp. 1–4.
35. Boyes, S.J.; Soh, P.J.; Huang, Y.; Vandenbosch, G.E.; Khiabani, N. Measurement and performance of textile antenna efficiency on a human body in a reverberation chamber. *IEEE Trans. Antennas Propag.* **2013**, *61*, 871–881. [[CrossRef](#)]



[J6] - **R. Gonçalves**, R. Magueta, P. Pinho, N. B. Carvalho, "Dissipation Factor and Permittivity Estimation of Dielectric Substrates Using a Single Microstrip Line Measurement", *Applied Computational Electromagnetic Society Journal*, Vol. 31, No. 2, pp. 118-125, 2016

Dissipation Factor and Permittivity Estimation of Dielectric Substrates Using a Single Microstrip Line Measurement

Ricardo Gonçalves¹, Roberto Magueta¹, Pedro Pinho², and Nuno B. Carvalho¹

¹ DETI, Instituto de Telecomunicações
Universidade de Aveiro, 3810-193 Aveiro, Portugal
rmrgoncalves@ua.pt, rlm@ua.pt, nbcarvalho@ua.pt

² Instituto de Telecomunicações
Instituto Superior de Engenharia de Lisboa, 1959-007 Lisboa, Portugal
ppinho@deetc.isel.pt

Abstract — The knowledge of the dielectric properties of materials, for the design of several components and circuits at high frequencies, is mandatory. In this paper, we present a simple method for the estimation of the dissipation factor (loss tangent) of dielectric materials based on the reflection measurement of a single microstrip line, which is applied to some common known materials, such as FR-4 and Rogers RO3010 laminates. The obtained results match well with the data on the literature for the considered materials.

Index Terms — Dielectric characterization, loss factor estimation, microwaves, permittivity estimation.

I. INTRODUCTION

Adaptability and integration of electronic systems is a major concern for current design engineers. In order to promote these, even at high frequencies, new solutions are constantly being proposed. One of those, is the use of alternative substrate materials [1,2].

Common substrates, used for the design of antennas and circuits for RF applications, can be replaced by other materials, that are, most of the times, easily available and preferably less expensive and ecofriendly; like plastic, fabrics, paper, or ceramics.

A very clear example is RFID (radio frequency identification) which is responsible for an increased diversity of the electronics printing techniques. It's being extensively used in many different kinds of applications and is one of the most promising bets for the development of the Internet of Things concept [3]. RFID systems operating in the HF (high frequency) band have been designed upon paper and plastic surfaces for mass production and implementation at the lowest costs possible. However, this has been done due to the low frequency of operation and simplicity of the system design. When the application envisioned is operating at UHF (ultra high frequency) or microwave frequencies

there are more limitations and constraints to consider when designing the system.

According to [4], printed antennas and transmission lines have dimensions directly related to the wavelength, and hence the frequency of the desired system. The wavelength is dependent on the permittivity and permeability of the propagation medium. Therefore, in order to efficiently design a printed antenna or RF circuit, the electrical properties: relative permittivity (ϵ_r); relative permeability (μ_r); and the dissipation factor, also known as loss tangent ($\tan \delta$), of the substrate must be known.

The information regarding these parameters is commonly found on the laminate's datasheets, but this does not happen for common materials not intended for electronic applications (e.g., fabrics, ceramics, paper, or plastic). So when designing RF circuitry using such materials, characterization in terms of permittivity and losses must be performed. In many cases, the substrates are dielectric non-magnetic materials; therefore, the relative permeability is unitary.

Permittivity and loss estimation is an old research subject and there's extensive literature regarding several methods to characterize different kinds of materials that can be found in reviews [5], application notes [6] and books [7]. In many of these methods, specific equipment is required, and might not be available in every lab.

The simplest methods available that allow the estimation of the permittivity, require the measurement of the scattering parameters of microstrip lines, such as presented in [8,9]. In these proposals, the dielectric under test is used as the substrate for the microstrip lines. Two different lines, with different lengths are required, for which the exact lengths and widths must be known with high precision. Other possibility is presented in [10], using a similar approach based on two lines with different lengths, but in which the material under test is placed above the lines, as a superstrate.

Submitted On: August 7, 2015

Accepted On: December 6, 2015

In this paper, we propose a method that only requires a single measurement of the reflection coefficient of an open-ended microstrip line, for the estimation of the permittivity and dissipation factor of the line substrate. The dissipation factor estimation proposed is the actual novelty. It is shown, that the proposed method can achieve better estimations when compared to other common methods, and does not require any prior knowledge of the conductivity, or other sources of losses, in the line. Since the permittivity is required for the calculation of the dissipation factor, we show the steps based on transmission line theory and microstrip line theory that allow the estimation of its value.

This paper is organized as follows. In the following section we present the steps for the permittivity and loss estimation based on reflection of microstrip lines method. In Section III we explain the experimental setup and present the results for permittivity and loss tangent obtained through measurements of different dielectric samples; namely, FR-4, Plastic and a Rogers RT5880. Finally, Section IV contains the uncertainty analysis of the proposed method, and Section V presents the conclusions.

II. PERMITTIVITY AND DISSIPATION FACTOR ESTIMATION: THEORY

Microstrip lines are simpler to design and fabricate when compared to coplanar or striplines. Especially if we consider creating such lines in a material that doesn't have electrodeposited conductors and where such processes are very hard and costly to apply.

As mentioned in the previous section, there are other approaches to characterize dielectric materials that can be made with microstrip lines. However, it requires the development of two lines, with different lengths, in which, the lengths, width and the height of the substrate must be known with high precision. Any error present in this dimensions can lead to large errors in the permittivity estimation. Especially an error in the width of the lines or in the length difference between them. By using a single microstrip line we avoid this sources of errors.

In order to determine the dissipation factor of a given material, its permittivity value is needed. Therefore, if not accessible in references, one must first assess its value. In the following subsection we describe a way to calculate it based on the measurement of a single microstrip line. It is derived from the known transmission line and microstrip line theory. In Subsection B, we present the techniques to determine the dissipation factor along with our novel approach.

A. Permittivity estimation with a microstrip line

If we terminate a transmission line with an open-circuit ($Z_L = \infty$) then, according to [4], the impedance

seen at the entrance of the line along l is:

$$Z_{in} = \frac{Z_0}{\tanh(\alpha l + j\beta l)}, \quad (1)$$

being Z_0 the characteristic impedance of the line and α and β the propagation attenuation and phase constant. Considering $\beta = 2\pi/\lambda$ and $l = \lambda_r/2$, where λ_r is the wavelength at the line resonance, then we have $\beta l = \pi/2$. If we replace this into (1), separate the real from the imaginary part, and consider the input impedance at one fourth of the resonant frequency ($\beta l = \pi/4$), then (1) becomes:

$$Z_{in} = Z_0 \left\{ \frac{2 \tanh(\alpha l)}{1 + \tanh^2(\alpha l)} - j \frac{1 - \tanh^2(\alpha l)}{1 + \tanh^2(\alpha l)} \right\}. \quad (2)$$

If we assume the losses are positive (which is correct for the majority of materials), and considering $Z_{in} = R - jX$, we can say:

$$\tanh(\alpha l) = -\frac{X}{R} + \sqrt{\left(\frac{X}{R}\right)^2 + 1}, \quad (3a)$$

$$Z_0 = X \frac{1 + \tanh^2(\alpha l)}{1 - \tanh^2(\alpha l)} = R \frac{1 + \tanh^2(\alpha l)}{2 \tanh(\alpha l)}. \quad (3b)$$

This process to determine the characteristic impedance of the line is rather simple, since we just have to measure the input impedance of the line at one fourth of the first resonant frequency, which can be done simply with a network analyzer. With that impedance value we can calculate (3a) and then determine the characteristic impedance with (3b).

With the knowledge of the characteristic impedance of the line we can relate it to the effective permittivity of the substrate. For a microstrip line, according to [11], we have:

$$\epsilon_{eff} = \left(\frac{60}{Z_0} \ln \left(\frac{8h}{W} + \frac{W}{4h} \right) \right)^2, \quad (4a)$$

$$\epsilon_{eff} = \left(\frac{120\pi}{Z_0} \frac{1}{\frac{W}{h} + 1.393 + 0.667 \ln \left(\frac{W}{h} + 1.444 \right)} \right)^2, \quad (4b)$$

where (4a) should be used when $W/h \leq 1$, and (4b) when otherwise. Being W the width of the microstrip line and h the height of the substrate. These can be solved for the relative permittivity of the substrate as:

$$\epsilon_r = \frac{2\epsilon_{eff} + \frac{1}{\sqrt{1+12h/W}} - 1}{1 + \frac{1}{\sqrt{1+12h/W}}}. \quad (5)$$

B. Dissipation factor estimation with a microstrip line

The dissipation factor, also known as loss tangent ($\tan \delta$), of a dielectric material in a microstrip line

substrate, can be related, according to [4], to the attenuation of the dielectric material (α_d) as:

$$\tan \delta = \frac{\alpha_d \sqrt{\epsilon_{eff}} (\epsilon_r - 1) c}{\pi \epsilon_r (\epsilon_{eff} - 1) f}. \quad (6)$$

The total attenuation applied to the propagation is characterized by the sum of the dielectric, conductor, radiation and leakage losses. In order to determine the losses from the dielectric the total loss and the contribution from each of the other sources must be known. The total attenuation can be determined from the input impedance measurement as shown in (3a) or by:

$$\alpha = -\frac{\ln(|T|)}{l}, \quad (7)$$

where T is the transmission parameter which is determined according to the NRW (Nicolson-Ross-Wier) method [12,13]. The conductor losses can be calculated using empiric closed form expressions as shown in [14]. However, these expressions are empirical, meaning they're dissociated from what actually is being measured and are frequency independent. Since the losses from the dielectric change with frequency, a small error in the calculation of the conductor losses can lead to a large error in the overall result. Besides, it is very hard to account the contribution from radiation and leakage losses. Even though leakage can be negligible and radiation is more significant for high microwave and/or millimeter wave frequencies. Therefore, we developed an iterative method to calculate the dissipation factors that does not require knowledge of the radiation, conductor or leakage losses and still provides reasonable estimations.

Considering a lossless line, with perfect conductors and a lossless substrate, terminated in an open circuit, then the input impedance measured at the resonant frequency of the line is infinite. However, when considering the losses, either from the conductor or dielectric, the input impedance decreases as the losses rise.

Using ADS Momentum EM simulator, we designed several lines with different lengths and widths and changed the characteristics of the substrate material. Some of the simulated lines and the corresponding impedance values obtained are presented in Table 1. Where z_{in} is the normalized input impedance, at the resonant frequency, when considering perfect conductors (the only source of considerable loss is from the dielectric). While z_c is the normalized input impedance, considering also the conductor losses.

It is noticeable from the presented values, that there is a decrease in the input impedance as the losses increase. Besides, there is a direct proportionality between the characteristic impedance of the lines and the input impedance at resonance. We can see this tendency in Fig. 1, where the variation of the characteristic

impedance of several lines with their input impedance at resonance, considering $\tan \delta = 0.01$, is depicted. Moreover, it is also shown a possible linearization of this relation, as:

$$z_{in} = 1.95Z_0 - 27.4, \quad (8)$$

and since the loss tangent is inversely proportional to this input impedance, we reach:

$$\tan \delta = \frac{0.0195Z_0 - 0.274}{z_{in}}. \quad (9)$$

This expressions can give a first estimation of the loss tangent. However, it only takes into account the dielectric loss. In order to consider the remaining sources of losses in the microstrip line, for the correct calculation of the dissipation factor, we consider a normalized impedance z_m that tends towards z_{in} as the conductivity increases, which can be also devised by the results on Table 1. We approximate this relationship according to expression (10):

$$z_m = z_{in} \left(1 - K e^{-\frac{Z_0 W}{\tau}} \right)^{-1}. \quad (10)$$

So by knowing the characteristic impedance of the line, the width of the line and the factors K and τ , one can determine an equivalent input impedance z_m and then determine a more accurate estimation of the loss tangent with (9) by replacing z_{in} with z_m . To reach the correct factors K and τ , we can rearrange (10) in order to get a relation between K , τ and $Z_0 W$, being W expressed in millimeters, as:

$$Z_0 W = -\tau \ln \left(1 - \frac{z_m}{z_{in}} \right) + \tau \ln K, \quad (11)$$

since z_m is the input impedance considering all the losses, which will tend towards z_{in} as the conductivity increases, one can calculate the K and τ factors for different loss tangents and different conductivity values. By doing so, we reached the values presented in Table 2.

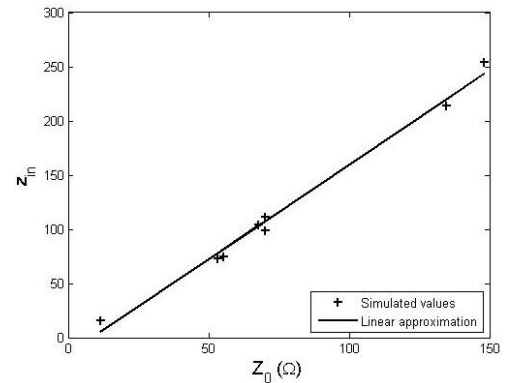


Fig. 1. Relation between the characteristic impedance of microstrip lines and the input impedance at resonance for perfect conductor lines.

Table 1: Input impedance of microstrip line simulations using ADS Momentum for different substrate materials

Line Properties	$\tan \delta$	$z_{in} (\Omega)$	σ (S/m)	$z_c (\Omega)$
Line 1 Z0 = 11.53 W = 2 mm h = 0.1 mm $\epsilon_r = 2$	0.01	15.55	1.0E6	3.03
			10.0E6	5.87
			60.0E6	9.01
	0.03	5.15	1.0E6	2.20
			10.0E6	3.35
			60.0E6	4.17
	0.05	3.07	1.0E6	1.73
			10.0E6	2.34
			60.0E6	2.70
Line 2 Z0 = 53.23 W = 1 mm h = 1 mm $\epsilon_r = 8$	0.01	72.77	1.0E6	30.43
			10.0E6	46.99
			60.0E6	58.28
	0.03	24.20	1.0E6	16.62
			10.0E6	20.51
			60.0E6	22.42
	0.05	14.49	1.0E6	11.42
			10.0E6	13.10
			60.0E6	13.84
Line 3 Z0 = 70.18 W = 2 mm h = 1 mm $\epsilon_r = 1.8$	0.01	110.94	1.0E6	60.39
			10.0E6	47.28
			60.0E6	48.91
	0.03	36.77	1.0E6	28.50
			10.0E6	33.09
			60.0E6	35.08
	0.05	21.93	1.0E6	18.94
			10.0E6	20.67
			60.0E6	21.38
Line 4 Z0 = 148.13 W = 1 mm h = 3 mm $\epsilon_r = 2$	0.01	254.03	1.0E6	137.74
			10.0E6	190.75
			60.0E6	221.63
	0.03	84.09	1.0E6	65.18
			10.0E6	75.63
			60.0E6	80.19
	0.05	50.29	1.0E6	43.29
			10.0E6	47.28
			60.0E6	48.91

Table 2: Calculated K and τ factors for different simulated microstrip lines

$\tan \delta$	σ (MS/m)	τ	K
0.01	1.0	210.63	0.858
	10.0	141.62	0.673
	60.0	118.54	0.426
0.03	1.0	139.59	0.600
	10.0	114.82	0.349
	60.0	105.18	0.185
0.05	1.0	125.45	0.436
	10.0	109.28	0.228
	60.0	103.62	0.114

According to these values, we can see that there is an inverse linear relation of K and τ with the square root of the conductivity as depicted in Figs. 2 and 3.

Based on these results, we can write K and τ in the form:

$$K = \frac{a_K}{\sqrt{\sigma_a}} + b_K, \quad (11a)$$

$$\tau = \frac{a_\tau}{\sqrt{\sigma_a}} + b_\tau, \quad (11b)$$

where σ_a is an educated guess of the conductivity value and the factors a_τ , a_K , b_τ and b_K , are obtained from a linearization that relates to the loss tangent as follows:

$$a_K = -2.105 \tan \delta + 0.475, \quad (12a)$$

$$b_K = \frac{0.0644}{\sqrt{\tan \delta}} - 0.203, \quad (12b)$$

$$a_\tau = -1991.0 \tan \delta + 115.6, \quad (12c)$$

$$b_\tau = \frac{1.097}{\sqrt{\tan \delta}} + 95.53, \quad (12d)$$

Since these factors depend on the loss tangent itself, we need an iterative method in order to solve this problem.

The algorithm is described as follows: We start by calculating a first approximation to the loss tangent with (9), after that we can calculate the K and τ factors that allow the calculation of (10). Using that new estimated impedance we can recalculate the loss tangent with (9), by replacing z_{in} with z_m .

A good approximation for the loss factor is achieved usually after four iterations. The convergence graphic is shown in Fig. 4.

A comparison about the estimation of the loss tangent with three different methods is shown in Fig. 5. These results are obtained from simulation for dielectrics with different losses (0.01, 0.02 and 0.005).

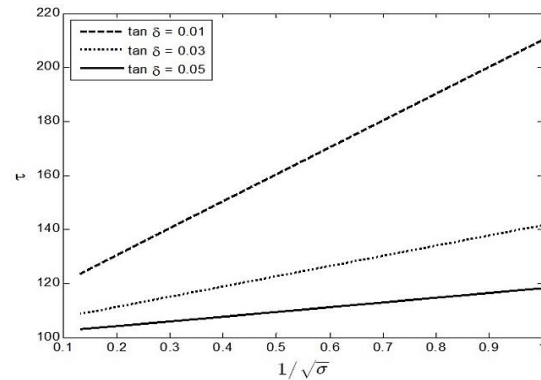


Fig. 2. Relation between the τ coefficient and the conductivity of the line conductors for different loss tangent values.

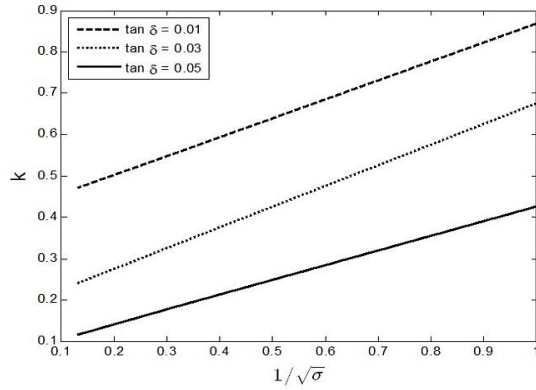


Fig. 3. Relation between the K coefficient and the conductivity of the line conductors for different loss tangent values.

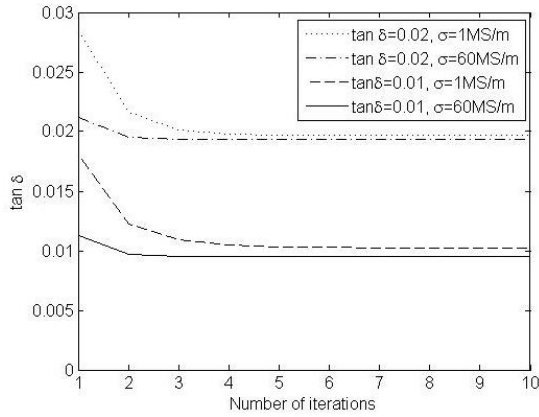


Fig. 4. Convergence of the dissipation factor determination method with the number of iterations, for different conductivities and dielectrics losses.

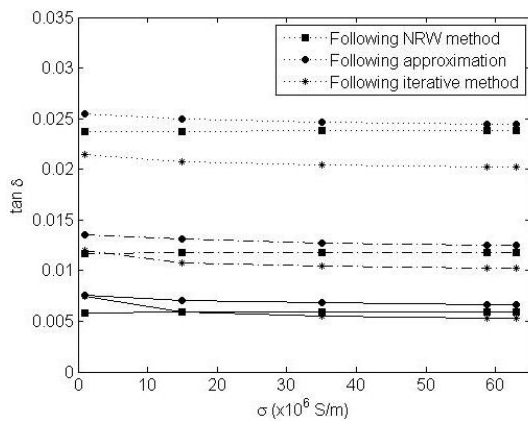


Fig. 5. Loss tangent determination for different loss dielectrics with NRW method, approximation (3a) and the iterative method.

From the results in Fig. 4 we can see that, independently of the loss tangent or the conductivity losses, the method converges for a very reasonable value after the fourth iteration. Moreover, even for very different conductor loss values, the method converges for a very approximate dielectric loss; therefore, showcasing low dependence on this parameter. This means that even if the conductivity value is not precise, one can reach accurate dielectric loss values.

It is clear, from the results depicted in Fig. 5, that the iterative method proposed leads to better estimations of the loss tangent, independently of the dielectric or conductor losses, when compared to other estimation methods.

III. PERMITTIVITY AND DISSIPATION FACTOR ESTIMATION: MEASUREMENTS

To ensure the accuracy of the results obtained by applying the previously described expressions, we tried to characterize three different dielectric substrates, from low to higher permittivity and different losses. The three dielectrics used are presented in Fig. 6.

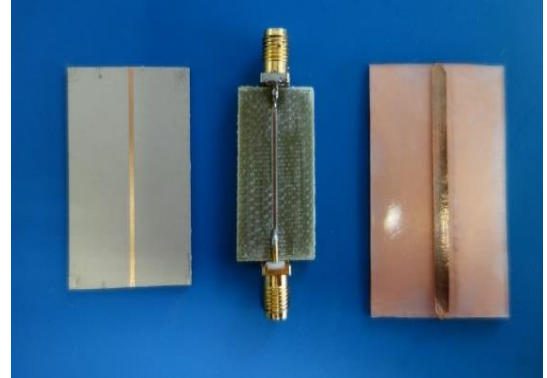


Fig. 6. Picture of the transmission lines tested. From left to right: Rogers RT6010 substrate, FR-4 substrate and LDPE (low density polyethylene) substrate.

There is no special considerations to take for the microstrip line dimensions. However, one thing to keep in mind which might help to achieve better results, is to have a ratio of the width of the line (W) to the height of the substrate (h) such that avoids being in the border intervals as referenced for the calculations of (4).

As we can see from Table 3, we used different ratios for the line, so that the calculations would fall into the different intervals for each.

The microstrip lines on the Rogers and the FR-4 substrates were etched traditionally, using a milling process. For the plastic, since these had no conductor electrodeposited in it, we used copper tape for the conductive parts of the lines.

Table 3: Dielectric substrate samples physical dimensions

Material	L (cm)	H (mm)	W (mm)	Ws (mm)
FR-4	3.96	1.59	0.8	18
Rogers RT6010	4.42	0.635	1.0	26
LDPE	4.60	1.00	1.16	31

The first step to extract the permittivity is therefore to measure the input impedance of the line with an open circuit in the end. Ensuring that the line is ended in an open circuit is important, connecting an open circuit load from the VNA calibration kit is a way to ensure it. Leaving an open terminated line or an SMA connector does not guarantee an open circuit for the frequency band in consideration, which leads to errors in the loss determination.

To calculate the permittivity of the considered lines first we need to measure the characteristic impedance of the line, which is the real part of the measured the input impedance at one fourth of the resonant frequency. With the input impedance value we can use expression (3) in order to calculate the characteristic impedance of the line. With the characteristic impedance of the lines we use expression (4) to extract ϵ_{eff} . In order to obtain better results we can consider the effective width of the lines (W_e), as described in [11]. With the effective permittivity we can then calculate the relative permittivity of the substrate with (5).

As for the loss tangent determination the iterative method as described in the previous section should be used. The method stops when the variation of the value between iterations is very small or when you reach a negative value, in which case, the current and previous values should be discarded and second to last value obtained is the one considered the closest to the loss tangent of the dielectric under test.

The results obtained for the considered lines based on the measurements and calculations described, yield the results presented in Table 4.

Table 4: Estimated values of the three sample dielectric slabs based on the proposed method and reference values from literature

Sample	Z_0 (Ω)	ϵ_r	Ref. ϵ_r	$\tan \delta$	Ref. $\tan \delta$
FR-4	93.3	4.29	4.30 – 4.70	0.018	0.025
Rogers RT6010	36.9	10.15	10.20	0.003	0.0023
LDPE	84.8	2.30	2.20 – 2.35	0.07	0.001

Comparing the obtained values for the permittivity

and the dissipation factor with the reported values in the materials datasheets we can see a good agreement. However, these values are only relative references since the frequencies and methods used to characterize such materials differ. Besides, it is known, as stated earlier, that these parameters are dependent on frequency and temperature. Therefore, it is expected to observe some differences regarding the estimated values.

IV. UNCERTAINTY ANALYSIS

Although the results reported in the previous section match closely with reported values in the materials datasheets, the reliability of the characterization method must be assessed. In order to do so, we did a set of measurements to the same microstrip lines and verified the error and variation obtained for the permittivity and the loss tangent.

Every measurement is susceptible to errors and therefore it is important to assess the sources of possible mismatches than can occur during measurement that lead to errors in the results. The method proposed here has a few sources which can introduce errors. Those are the measurement of the physical dimensions of the microstrip line, the error occurring from the uncertainty of the VNA, the use of SMA connectors or a test fixture for transmission lines and the added losses from corrosion of the material.

The contribution of some of these sources of error are nearly impossible to separate from the others; therefore, in this section we show the results obtained from several measurements performed to the microstrip lines and analyze the variations of each main parameter that occur in order to certify the robustness of the method.

It is depicted in Figs. 7 and 8 the probability functions, obtained from the measurements of the three dielectric samples, for the permittivity and loss tangents.

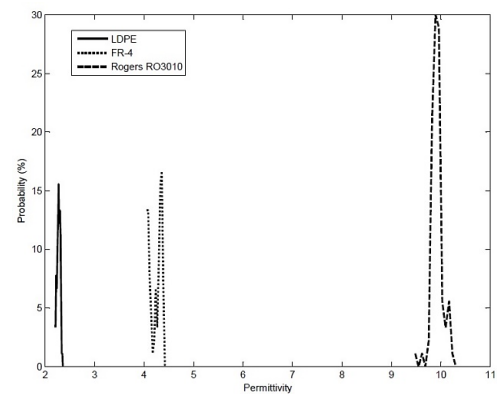


Fig. 7. Probability function of the microstrip lines substrate permittivity (ϵ_r).

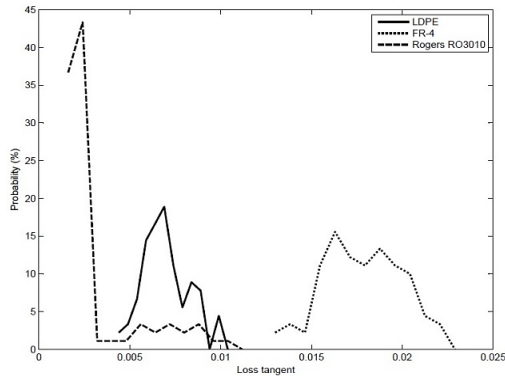


Fig. 8. Probability function of the microstrip lines substrate loss tangent ($\tan \delta$).

The uncertainty is characterized by the standard deviation observed in a probability function obtained from a large set of measurements performed under the same conditions. Table 5 resumes the mean values and uncertainty values obtained for the different parameters for each of the dielectric slabs.

Table 5: Mean values and uncertainty obtained in the measurement of the different dielectric sample materials

Sample		f_0 (MHz)	Z_0 (Ω)	ϵ_r	$\tan \delta$
FR-4	\bar{X}	1453	93.32	4.32	0.019
	\bar{U}	6.91	1.13	0.12	0.002
Rogers RT3010	\bar{X}	1152	36.89	10.16	0.003
	\bar{U}	65.4	0.48	0.28	0.002
LDPE	\bar{X}	1344	84.80	2.30	0.007
	\bar{U}	1.82	0.40	0.027	0.0012

From the results obtained we can see that the estimation of the permittivity of the LDPE and FR4 are rather accurate, with obtained values in close relation to the reported in the manufacturer datasheet. The estimation of the RT6010 has shown the highest deviation from the documented values, since we obtained estimations for permittivity ranging from 9.8 to 10.8, with the highest incidence around 10 while the manufacturer reports a permittivity of 10.2 to 10.8. It is therefore clear, that although the method shows reliable results for low and medium permittivity materials, it may provide worst estimations for high permittivity low loss materials.

V. CONCLUSION

The method for permittivity estimation proposed here is quite simple to apply and is obtained directly from the equations that characterize printed transmission lines. It is less expensive when compared to other methods which require specific equipment. However, it is only suitable for the measurement of thin dielectrics, since it requires a microstrip line with the test dielectric

as substrate.

Although the input impedance should be calculated at a fourth of the resonant frequency, this method allows the calculation of the permittivity at multiple frequencies. Multiples of half of the resonant frequency should be avoided since these will not provide any reasonable value. Still, one must take into account that the losses and therefore the error increases with frequency.

The proposed iterative method for the estimation of the dissipation factor presents better estimations than other commonly used methods at the cost of requiring more calculations. Still, it is shown that the method usually converges after few iterations.

The main drawback of this method is the error, especially in the estimation of higher permittivity low loss dielectrics. Still, the obtained results agree fairly with values reported in datasheets of the considered dielectrics and also with simulation results for printed transmission lines. This means that it can be used to obtain a rough first estimation of an uncharacterized dielectric material that might be used as a substrate for RF circuitry.

As a final remark we can say that the robustness of the method increases if the mean value of multiple measurements on lines with the same substrate is used.

ACKNOWLEDGMENT

The authors acknowledge the Portuguese FCT/MCTES for financing the Ph.D. grant SFRH/BD/91249/2012, the project CREATION EXCL/EEI-TEL/0067/2012 and the project UID/EEA/50008/2013.

REFERENCES

- [1] R. Salvado, C. Loss, R. Gonçalves, and P. Pinho, "Textile materials for the design of wearable antennas: a survey," *Sensors* 2012, 12, 15841-15857, 2012.
- [2] R. Goncalves, S. Rima, R. Magueta, A. Collado, P. Pinho, N. B. Carvalho, and A. Georgiadis, "RFID tags on cork stoppers for bottle identification," *IEEE MTT-S Int. Microwave Symp. Dig.*, Tampa Bay, FL, 2014.
- [3] L. Roselli, N. B. Carvalho, F. Alimenti, P. Mezzanotte, G. Orecchini, M. Virili, C. Mariotti, R. Goncalves, and P. Pinho, "Smart surfaces: large area electronics systems for internet of things enabled by energy harvesting," *Proc. of the IEEE*, vol. 102, no. 11, pp. 1723,1746, Nov. 2014.
- [4] D. M. Pozar, *Microwave Engineering*, 4th ed., John Wiley & Sons, Inc., 2012.
- [5] J. Baker-Jarvis, R. G. Geyer, J. H. Grosvenor, Jr., M. D. Janezic, C. A. Jones, B. Riddle, C. M. Weil, and J. Krupka, "Dielectric characterization of low-loss materials a comparison of techniques," *IEEE Trans. Dielectrics Electrical Insulation*, vol. 5, no. 4, pp. 571-577, Aug. 1998.

- [6] K. C. Yaw, "Measurement of dielectric material properties: application note," *Rhode & Schwarz*, 04.2012-RAC-0607-0019_1_5E, 2012.
- [7] L. Chen, C. K. Ong, V. V. Varadan, and V. K. Varadan, *Microwave Electronics: Measurement and Materials Characterization*, John Wiley & Sons, Inc., 2004.
- [8] M. Q. Lee and S. Nam, "An accurate broadband measurement of substrate dielectric constant," *IEEE Microw. Guided Wave Lett.*, vol. 6, pp. 168-170, 1996.
- [9] S. F. Declercq, H. Rogier, and C. Hertleer, "Permittivity and loss tangent characterization for garment antennas based on a new matrix pencil two line method," *IEEE Trans. Antennas Propagat.*, vol. 56, pp. 2548-2554, 2008.
- [10] J. Roelvink, S. Trabelsi, and S. O. Nelson, "A planar transmission-line sensor for measuring the microwave permittivity of liquid and semisolid biological materials," *IEEE Trans. Instrum. Meas.*, vol. 62, no. 11, pp. 2974-2982, Nov. 2013.
- [11] B. C. Wadell, *Transmission Line Design Handbook*, Artech House, Inc., 1991.
- [12] A. Nicolson and G. Ross, "Measurement of the intrinsic properties of materials by time domain techniques," *IEEE Trans. Instrum. Meas.*, vol. 19, no. 4, pp. 377-382, Nov. 1970.
- [13] W. B. Weir, "Automatic measurement of complex dielectric constant and permeability at microwave frequencies," *Proc. of the IEEE*, vol. 62, no. 1, pp. 33-36, Jan. 1974.
- [14] R. A. Pucel, D. J. Massé, and C. P. Hartwig, "Losses in microstrip," *IEEE Trans. Microw. Theory Tech.*, vol. 16, pp. 342-350, 1968.



Ricardo Gonçalves was born in Lisbon, Portugal, in 1988. He received the B.Sc. and M.Sc. degrees in Electronics and Telecommunications Engineering from the Instituto Superior de Engenharia de Lisboa, Lisbon, in 2010 and 2012, respectively. He is currently working toward the Ph.D. in Electrical Engineering at the University of Aveiro. He is a Researcher at the Instituto de Telecomunicações, Aveiro, Portugal.

His main research interests include wireless power transfer systems, radio-frequency identification (RFID), and wireless passive sensor networks. He is a Student Member of the IEEE MTT-S and AP-S societies and a Member and Founder of the MTT-S Student Branch at the University of Aveiro. He is also a Student Member of the ACES society.



Roberto Magueta received his M.Sc. degree in Electronics and Telecommunications Engineering from University of Aveiro, Portugal, in 2013. After which he joined Instituto de Telecomunicações, Aveiro, as a Researcher in the project RadioVoip - Smart Antenna for Maritime Communications. He is currently working towards his Ph.D., his thesis is focused on transmitter and receiver designs for future mm-wave and massive MIMO based Wireless Systems.



Pedro Pinho was born in Vale de Cambra, Portugal, in 1974. He received the Licenciado and M.Sc. degrees in Electrical and Telecommunications Engineering and the Ph.D. degree in Electrical Engineering from the University of Aveiro, Aveiro, Portugal, in 1997, 2000 and 2004, respectively. He is currently a Professor Adjunto at the Department of Electrical Telecommunications and Computers Engineering, Instituto Superior de Engenharia de Lisboa, Lisbon, Portugal, and a Researcher at the Instituto de Telecomunicações, in Aveiro, since 1997. His current research interests are in antennas for location systems, reconfigurable antennas, and antenna design for passive sensors in nonconventional materials.



Nuno Borges Carvalho was born in Luanda, Angola, in 1972. He received the Diploma and Doctoral degrees in Electronics and Telecommunications Engineering from the University of Aveiro, Aveiro, Portugal, in 1995 and 2000, respectively. He is a Full Professor at the Universidade de Aveiro, Aveiro, Portugal and a Senior Research Scientist with the Instituto de Telecomunicações (IT), in Aveiro, where he coordinates the Radio Systems Group.

He has co-authored over 200 papers in journals and conferences and two books. He co-holds four patents. His main research interests include wireless power transmission, nonlinear distortion analysis in microwave/wireless circuits and systems, and measurement of nonlinear phenomena. He has recently been involved in the design of dedicated radios and systems for newly emerging wireless technologies.

Borges Carvalho is an IEEE Fellow and the Chair of the IEEE MTT-11 Technical Committee. He is a Member of IEEE MTT-20, MTT-24, and MTT-26. He is an Associate Editor for the IEEE Transactions on Microwave Theory and Techniques, IEEE Microwave Magazine, Cambridge Journal on Wireless Power Transmission and the Chair of the URSI-Portugal Metrology Group.

[J7] - **R. Gonçalves**, N. B. Carvalho and P. Pinho, "Wireless energy transfer: Dielectric lens antennas for beam shaping in wireless power transfer applications", Accepted for publication in future issue of *Comptes Rendus Physique*



Contents lists available at ScienceDirect

Comptes Rendus Physique

www.sciencedirect.com



Energy and radiosciences / Énergie et radiosciences

Wireless energy transfer: Dielectric lens antennas for beam shaping in wireless power-transfer applications

*Transfert d'énergie sans fil : antennes diélectriques pour la mise en forme des faisceaux dans les applications de transfert d'énergie sans fil*Ricardo Gonçalves^{a,b,*}, Nuno B. Carvalho^{a,b}, Pedro Pinho^{b,c}^a DETI, University of Aveiro, Aveiro, Portugal^b Instituto de Telecomunicações, Aveiro, Portugal^c Instituto Superior de Engenharia de Lisboa, Lisboa, Portugal

ARTICLE INFO

Article history:

Available online xxxx

Keywords:

Lens antennas

Wireless power transfer

3D Printing

Mots-clés :

Antennes lentilles

Transfert d'énergie sans fil

Impression 3D

ABSTRACT

In the current contest of wireless systems, the last frontier remains the cut of the power cord. In that sense, the interest over wireless energy transfer technologies in the past years has grown exponentially. However, there are still many challenges to be overcome in order to enable wireless energy transfer full potential. One of the focus in the development of such systems is the design of very-high-gain, highly efficient, antennas that can compensate for the propagation loss of radio signals over the air.

In this paper, we explore the design and manufacturing process of dielectric lenses, fabricated using a professional-grade desktop 3D printer. Lens antennas are used in order to increase beam efficiency and therefore maximize the efficiency of a wireless power-transfer system operating at microwave frequencies in the K_u band. Measurements of two fabricated prototypes showcase a large directivity, as predicted with simulations.

© 2016 Académie des sciences. Published by Elsevier Masson SAS. All rights reserved.

R É S U M É

Dans la compétition actuelle entre les systèmes sans fil, la dernière frontière reste la coupure du cordon électrique. Dans ce sens, l'intérêt des technologies de transfert d'énergie sans fil a crû exponentiellement au cours des dernières années. Cependant, de nombreux défis à surmonter demeurent pour qu'on puisse déployer à son plein potentiel le transfert d'énergie sans fil. L'un des objectifs poursuivis dans le cadre du développement de tels systèmes est la conception d'antennes à très haut gain, très efficaces, qui permettraient de compenser les pertes liées à la propagation des signaux radio dans l'air. Dans cet article, nous explorons la conception et la fabrication de lentilles diélectriques, réalisées à l'aide d'une imprimante 3D de bureau de qualité professionnelle. Les antennes à lentilles sont utilisées en vue d'accroître l'efficacité du réseau et donc de maximiser celle d'un système de transfert d'énergie actif aux fréquences des micro-ondes dans la bande K_u . Les mesures

* Corresponding author at: Instituto de Telecomunicações, Campus Universitario de Santiago, 3810-148 Aveiro, Portugal.

E-mail address: rgoncalves@av.it.pt (R. Gonçalves).<http://dx.doi.org/10.1016/j.crhy.2016.11.004>

1631-0705/© 2016 Académie des sciences. Published by Elsevier Masson SAS. All rights reserved.

réalisées sur deux prototypes mettent en évidence une grande directivité, ainsi que les simulations le prédisaient.

© 2016 Académie des sciences. Published by Elsevier Masson SAS. All rights reserved.

1. Introduction

Wireless power transfer (WPT) is a technology that has been idealized by Nikola Tesla more than a century ago. However, only recently the advances in technology have allowed it to become a reality. After the boom in the wireless communications in the past decades, only the power cord is left to cut in order to create truly wireless systems.

The first approach to wireless power transfer was based in inductive coupling, also referred as near-field power transfer, appearing in the toothbrushes charging systems and more recently in the form of charging pads for cell phones. This is a well-established technology; however, near-field power transfer only allows the transmission of energy in very close distances of communication. The transfer of energy over larger distances is yet a field of high interest and one that has motivated a lot of research in the past few years.

Far-field WPT is a current research topic of high interest. It is being thought of for applications to Wireless Sensor Networks (WSNs), in Radio Frequency Identification (RFID), and is a key feature for enabling the implementation of the concept of the Internet of Things [1]. More than that, WPT solutions are being considered for a wide variety of applications such as electric vehicle charging [2,3], to power up exploration probes in space [4], and for space-to-earth power transmission [5,6].

The major drawback in these systems is their efficiency in energy transfer. The wavefronts of electromagnetic waves spread in space, dissipating the energy in all directions. From this realization comes the well-known Friis transmission equation that allows the calculation of the ratio of power transmitted to power received by two antennas separated by a distance $R > 2D^2/\lambda$, being D the biggest dimensions of the antennas, which imposes that those antennas be in the far-field region of each other. The Friis transmission equation states that

$$P_r = P_t(1 - |\Gamma_t|^2)(1 - |\Gamma_r|^2) \left(\frac{\lambda}{4\pi R} \right)^2 G_t(\theta_t, \phi_t) G_r(\theta_r, \phi_r) |\hat{\rho}_t \cdot \hat{\rho}_r|^2 \quad (1)$$

being P_r the received power, P_t the transmitted power, Γ the reflection coefficient of the antenna, G the gain of the antenna, and $|\hat{\rho}_t \cdot \hat{\rho}_r|^2$ the polarization ratio.

From this relation, it is easy to realize that in order to maximize the power received, one should provide antennas that have the best matching possible, and are perfectly aligned in the direction of maximum gain to each other, as well as polarization. The hardest part is overcoming the losses due to wave-front spreading $(\frac{\lambda}{4\pi R})^2$. To compensate this loss, very high gain antennas are needed, such as antenna arrays of several elements, parabolic antennas, or lens antennas.

Parabolic antennas have dimensions and weights that make them very difficult to integrate in many systems, even in space applications, where the size of satellites is being constantly decreased. Antenna arrays are very interesting, however, when the number of elements in the array increases, the feeding networks increase as well and the insertion losses can become quite considerable, hindering the overall gain of the antenna.

In this paper, we present the development of a dielectric lens antenna for transmission and harvesting of energy in the K_u band for space applications; more specifically, to be used as a transmitting source to power up passive sensors in space.

The dielectric lens is developed using 3D printing techniques, which allows the reduction of the cost, but specially to perform quick prototyping and optimization of the structures. The interest and availability of household 3D printers have increased in the past few years. Due to that, the prices of these equipments have decreased considerably. Most low-cost household 3D printers work based on the superposition of layers of a polymer material, known as thermoplastics, such as ABS (acrylonitrile butadiene styrene) or PLA (polylactic acid). These polymeric-type materials are non-magnetic dielectric and therefore can be useful for microwave applications. That has launched a new interest on this kind of technology and has incited the development of quick prototyping in many fields of science, namely electronics and including microwave circuits and antennas [7–9].

In this paper, we show the development of a 3D-printed convex paraboloid dielectric lens with a microstrip patch feed for the K_u band. This antenna is especially useful for WPT applications when compared to the use of antenna arrays. Arrays usually comprise a feeding network that will inevitably introduce power losses. With a lens antenna, we can, with a single-feed radiating element, achieve very high directivities, comparable to those obtained with a 16- to 20-element antenna array, without the inherent feeding network losses. The paper is organized as follows. In the following section, the dielectric lens as well as the feeding patch characteristics are described. In section 3, the simulation and measurement results are discussed. Section 4 draws the main conclusions about this work.

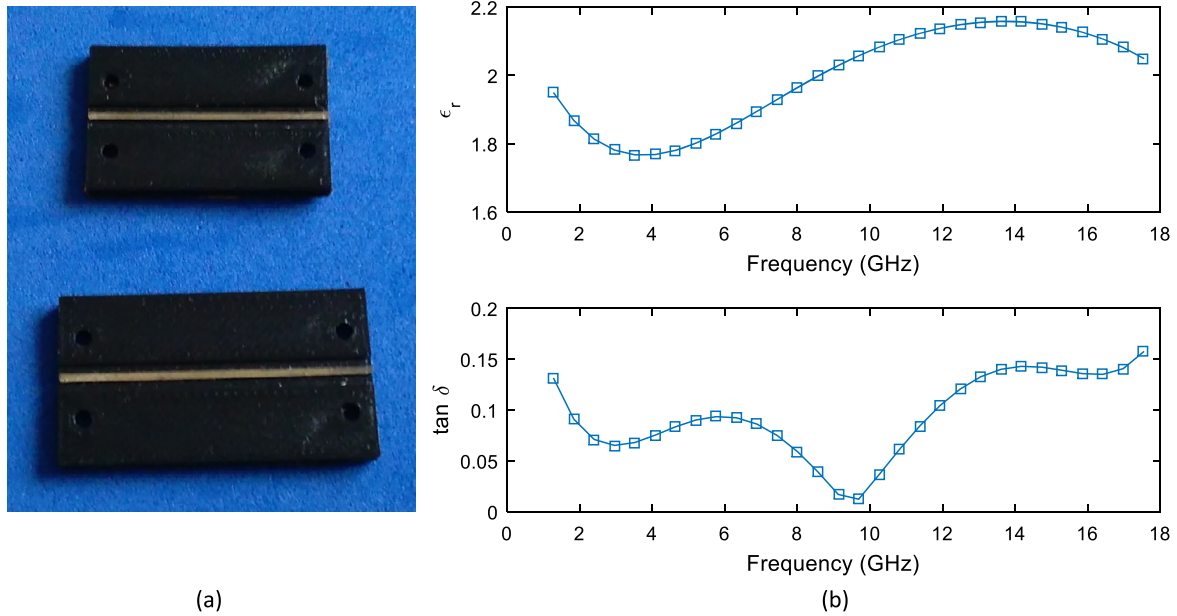


Fig. 1. Photograph of the microstrip lines on PLA substrate prototypes (a) and the estimated permittivity and dissipation factor of PLA between 1 and 18 GHz (b) using the method in [13,14].

2. Lens antenna design

Lens are used to shape wavefronts and are usually classified as dielectric lenses or constrained lenses [10]. Dielectric lenses can be hard to fabricate, requiring molds that can be expensive. This cost can be significantly lowered and the fabrication process eased and speeded if we consider 3D printing technology.

The lens shape is bound to the radiation properties one pretends to achieve. That is, the profile of the lens can be shaped in order to provide the highest gain possible (narrower beam), provide broader beams, or even be shaped to provide an isoflux-type pattern [11]. For low frequencies, the large size and weight of the lens can make its use prohibitive; it is the case when one wants to achieve very high directivities, beyond 30 dBi, for which the losses inside the dielectric of the lenses can hinder radiation efficiency. Still, lens antennas are a very attractive solution to easily manipulate the radiation shape of a given source and to create planar front waves, specially when working on high frequencies above the X-band.

The lens can have flat surfaces, in either the focal plane or the wavefront, spherical surfaces on both planes, but can also take arbitrary shapes, in order to achieve a very particular radiation shape [12]. In this particular case, we chose an ellipsoidal profile lens.

2.1. Material properties

In order to properly dimension the lens antenna and predict the antenna radiation properties, the permittivity of the dielectric used for the lens must be known in order to determine its refractive index.

The dielectric lenses proposed in this paper were fabricated with a BEEtheFirst 3D printer from BEEVeryCreative using PLA with an infill density of 80%. Since there is no information regarding the permittivity and dissipation factors of the considered material at the frequencies of interest; these had to be determined. For that purpose, we employed a differential phase method with microstrip lines [13,14]. In order to implement this method, two microstrip lines with different lengths were fabricated using a conductive silver-based ink, which was deposited onto two slabs of PLA, as shown in Fig. 1(a).

In this method, the effective permittivity of the substrate can be related to the difference between the phase constant (β) obtained from the propagation constant (γ) of the lines and the propagation phase in the vacuum (β_0) as

$$\epsilon_{r,\text{eff}} = \left(\frac{\beta}{\beta_0} \right)^2 \quad (2)$$

where the propagation constant of the lines is obtained by solving the following eigenvalue equation

$$\lambda_{1,2} = \frac{1}{2} \left[\text{Tr}(M) \pm \sqrt{\text{Tr}(M)^2 - 4\Delta M} \right] \quad (3)$$

where $\text{Tr}(M)$ is the trace and ΔM is the determinant of M , being M the transmission matrix corresponding to the section of line difference between the two transmission lines. Since it is a transmission matrix it is the direct ratio between the transmission matrix of each line

$$\bar{M} = \bar{M}_1 \cdot \bar{M}_2^{-1} \quad (4)$$

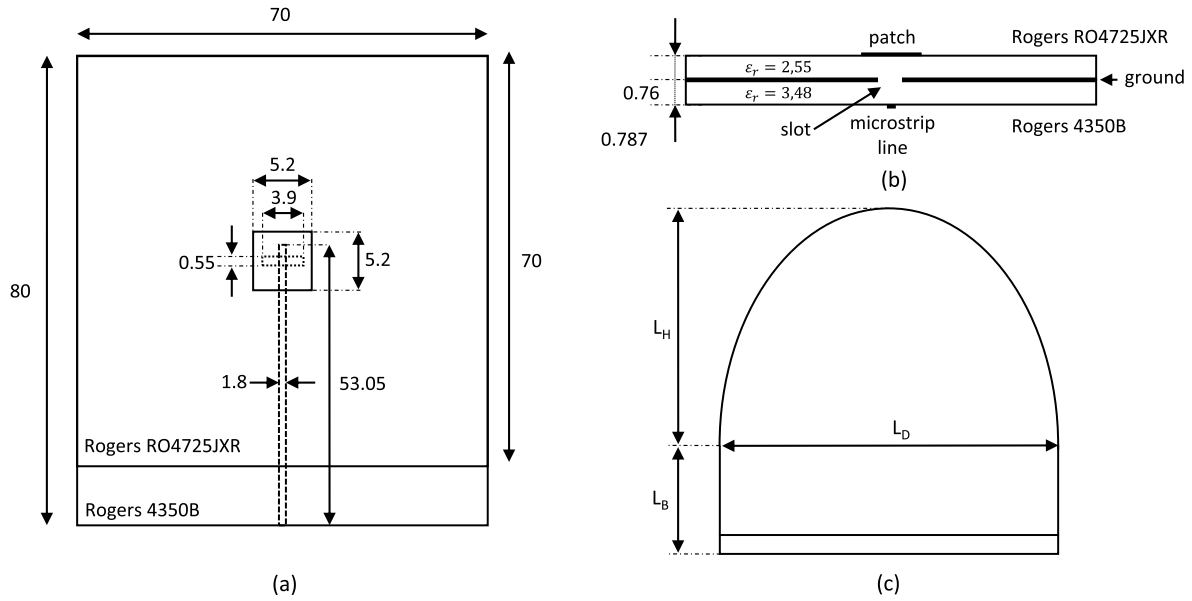


Fig. 2. Schematic of the proposed antenna (a) top view of the slot coupled microstrip patch antenna, (b) profile view, and (c) lens profile characteristics.

and this can be obtained from the measured S-parameters as

$$M_i = \frac{1}{S_{21i}} \begin{bmatrix} (S_{12i}S_{21i} - S_{11i}S_{22i}) & S_{11i} \\ -S_{22i} & 1 \end{bmatrix} \quad (5)$$

Since the system is passive, the relation $|e^{-\gamma \Delta l}| < 1$ imposes a particular signal for the solution of (3). The propagation constant can then be defined as

$$\gamma = \frac{1}{\Delta l} \ln \lambda_{av} + j \frac{2\pi n}{\Delta l} \quad (6)$$

being $\lambda_{av} = \frac{1}{2} \left(\lambda_1 + \frac{1}{\lambda_2} \right)$ the average of the solution of (6); if $\Delta l < \lambda_0/2$, then $n = 0$.

The results obtained from the application of the referenced method are depicted in Fig. 1, and the permittivity estimated at 13.5 GHz is 2.16.

As can be seen from the results in Fig. 1, permittivity exhibits a strange behavior with frequency. An increase in permittivity is expected; however, it decreases for the lowest frequencies and again for the higher frequencies, this is rather unexpected. Therefore, we used the characterization technique as proposed in [15] in order to confirm the permittivity of the PLA material at frequencies close to 13.5 GHz. The obtained value was $\epsilon_r = 2.04$, which is lower than the value calculated with the previous method.

Considering these results, we used a relative permittivity of $\epsilon_r = 2.0$ to model the lens material during simulations. This value has proven to be accurate considering the measured results shown in the following sections.

The dissipation factor determined with the first method presents an awkward behavior; therefore, the values obtained were not considered. Instead, we considered a dissipation factor of $\tan \delta = 0.01$. This value has little effect on the input impedance of the antenna, and mainly influences radiation efficiency. Therefore, by comparing the simulated and measured gain, we could conclude about the real loss factor, which is discussed further.

2.2. Antenna design

The lens antenna is fed by a microstrip patch antenna. In order to feed the lens with a symmetrical electric field and to avoid interference that could disrupt the radiation pattern, we used a slot-coupled fed microstrip patch, as shown in Fig. 3(a). The use of the slot coupled microstrip patch, as opposed to a microstrip line fed patch, isolates the feed line and the patch electric fields, preventing leakage radiation from the line to feed the lens and therefore disturbing the radiation pattern.

The dimensions of the slot-coupled microstrip patch antenna are presented in Fig. 2, along with the lens schematic profile. A photograph of the prototypes is shown in Fig. 3, and the dimensions of the two lenses are described in Table 1.

The shape of the radiation beam depends on the curve profile of the lens and the ellipsoidal profile is a natural evolution of the hemispherical lens in order to maximize the directivity while keeping the same lens base diameter. The profile of the lens is obtained from the following expression

$$y = h \sqrt{1 - \frac{x^2}{r^2}} \quad (7)$$

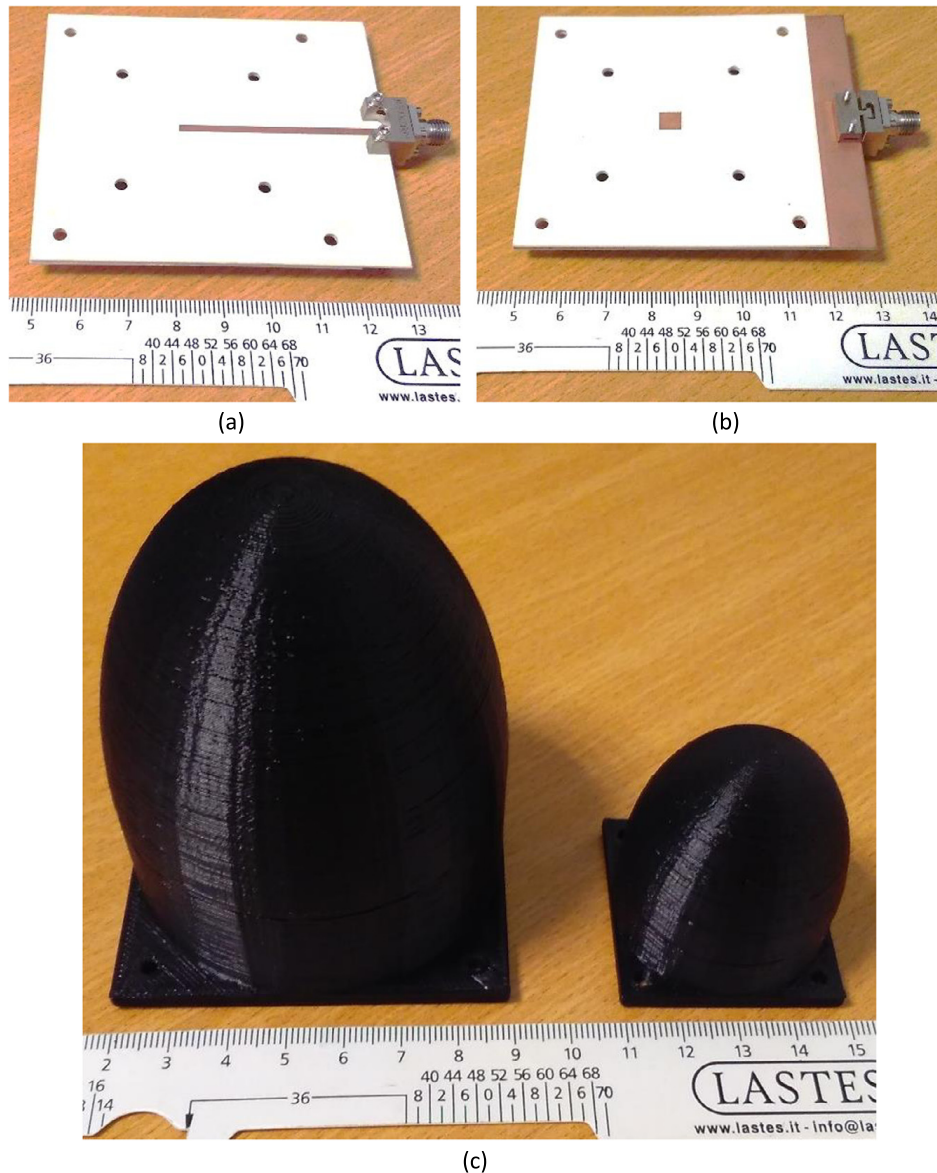


Fig. 3. Photograph of the built prototypes: (a) bottom side of the slot-coupled microstrip patch antenna, (b) top side of the microstrip patch antenna, and (c) lens antenna prototypes.

Table 1

Lens antenna dimensions and weight.

	Lens 1	Lens 2
L_H (mm)	58.9	33.0
L_B (mm)	29.0	15.0
L_D (mm)	35.0	20.0
Weight (g)	245	43

being h the height of the lens (L_H) and r is the radius of the lens base ($L_D/2$). The length of the cylindrical extension is obtained according to geometrical optics rules [16], and it should be $L_B = L_H \times n$, where n is the refractive index of the lens.

After defining the profile that could maximize directivity considering a given diameter for the lens, we increased the diameter of the lens in order to study the improvement in terms of directivity versus the overall size of the lens. It is important to note that the increase in size of the lens increases directivity; however, the dielectric used for the lens has losses, therefore these can hinder the radiation gain of the antenna.

In order to evaluate the behavior of the lens antennas and the compromise between size, weight and overall radiation gain, two prototypes for the lens antenna were built, while using the same microstrip patch antenna for feeding.

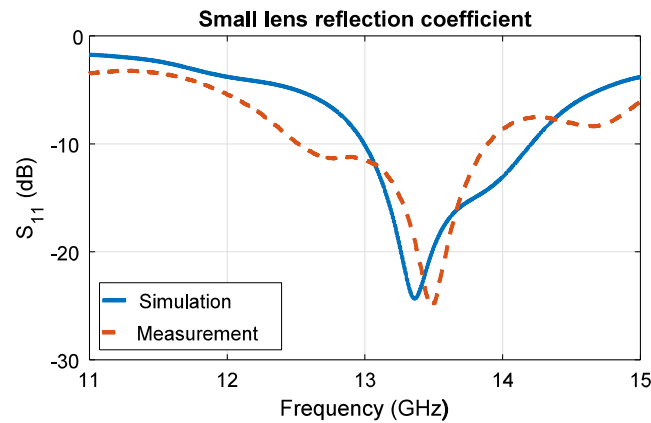


Fig. 4. Simulated and measured reflection coefficient of the small-lens antenna.

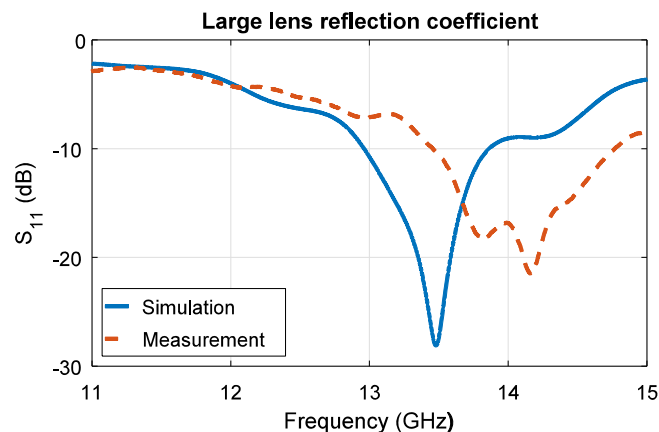


Fig. 5. Simulated and measured reflection coefficient of the large-lens antenna.

3. Antenna characteristics

The microstrip patch antenna used to feed the lens is considerably influenced by the superposition of the dielectric material; therefore, its dimensions as well as the coupling slot and the stub are designed in order to match its input impedance, at the desired frequency, considering the dielectric lens attached to it. For that reason, the reflection coefficient of the microstrip patch is non-relevant without the presence of the lens.

According to simulations, the reflection coefficients of the microstrip patch with the two lenses is not very different, as can be seen in the simulation curves presented in Fig. 4. However, as can be seen from the results in Figs. 4 and 5, the measured reflection coefficient of the antenna with the larger lens presents a shift in frequency when compared to the smaller lens measurements and when compared to the simulation curves. This can be explained by some warping effects that occurred during printing. Since the larger lens is a rather big and heavy object, it is very difficult to keep the whole surface on the printing table during the whole process, therefore creating some warping in the edges. Even after sanding the bottom surface, there is always a little warping around the corners of the structure; this causes the microstrip patch board to bend on the edges when screwed together with the lens. We believe that this is the cause for the shift in frequency occurring in the measurements, which is not observable in the simulations. Two lens were printed, the second one at a lower speed, but the warping problem has proved difficult to overcome. Nevertheless, the results are satisfactory, since we can always re-tune the feeding antenna if the larger lens is selected.

The simulated versus measured normalized radiation pattern obtained with the lens is depicted in Fig. 6.

The agreement between simulation and measurement for both lens antenna prototypes in both measured planes is clear. In most cases, the HPBW difference between simulation and measurement was less than 1° , with an exception for the small lens in the XZ plane with a difference of 4.5° .

As stated before, the change in the lens curvature as well as the increase in the lens size will increase its directivity, but also hinder the efficiency due to dielectric losses. The maximum simulated directivity for the small lens was 14.7 dBi, with a radiation efficiency of 75.9%, which translates in a gain of 13.6 dBi, which is close to the 14.1 dBi measured. The maximum simulated directivity for the large lens was 18.7 dBi, with a radiation efficiency of 66.1%, which translates in a gain of 16.0 dBi, which is close to the 16.4 dBi measured.

The fact that we measured higher gains than the simulated ones proves that the dissipation factor of the dielectric material is actually lower than the one considered during initial simulations. We performed a parametric sweep in order

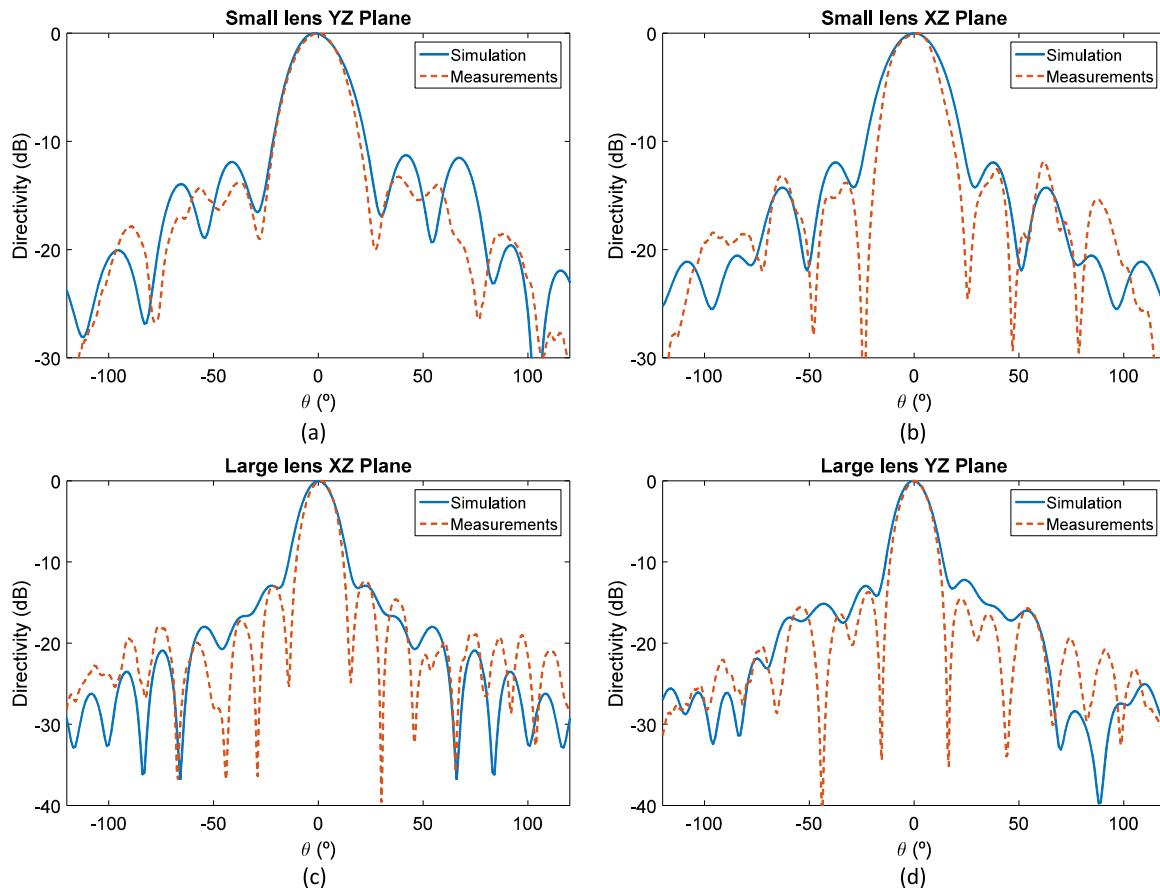


Fig. 6. Simulated and measured normalized radiation pattern of (a) the XZ plane of small lens, (b) the YZ plane of the small lens, (c) the XZ plane of the large lens antenna, and (d) the YZ plane of the large lens.

to find which dissipation factor would approximate the measured gain at best, reaching an actual dissipation factor of $\tan \delta = 0.005$.

4. Conclusion

Lens antennas are particularly useful for frequencies above the X band to create narrow-beam and high-gain wireless transmission systems. The prototypes described in this paper prove that 3D printing technology can be a very useful tool to create dielectric structures, in this case dielectric lenses, but can be extended to dielectric resonators. The utility that one can get from a 3D printer is immense, the infill manipulation can be useful to shape dielectric structures for radiation shaping such as Luneberg or Fresnel lenses.

The antennas proposed in this paper exhibit a high radiation gain, which is rather useful for, but is not limited to, applications to wireless power transfer. When compared to antenna arrays, this approach has the advantage of discarding the use of complex feeding network that have inherent transmission losses, therefore increasing the transmitted power. There is, however, a compromise between the gain and the size and weight of the lens; therefore, depending on the gain levels one pretends to reach, the viability of a lens antenna has to be carefully assessed. Therefore, dielectric lens antennas can prove to be a solution for very high-gain antenna design for wireless energy transfer systems.

References

- [1] L. Roselli, N.B. Carvalho, F. Alimenti, P. Mezzanotte, G. Orecchini, M. Virili, C. Mariotti, R. Gonçalves, P. Pinho, Smart surfaces: large area electronics systems for internet of things enabled by energy harvesting, *Proc. IEEE* 102 (11) (2014) 1723–1746, <http://dx.doi.org/10.1109/JPROC.2014.2357493>.
- [2] N. Shinohara, Y. Kubo, H. Tonomura, Wireless charging for electric vehicle with microwaves, in: *Proc. 3rd International Electric Drives Production Conference, EDPC, 2013*, pp. 1–4.
- [3] N. Shinohara, Y. Kubo, H. Tonomura, Mid-distance wireless power transmission for electric truck via microwaves, in: *Proc. URSI International Symposium on Electromagnetic Theory, EMTS, 2013*, pp. 841–843.
- [4] S. Kawasaki, Microwave WPT to a rover using active integrated phased array antennas, in: *Proc. 5th European Conference on Antennas and Propagation, EUCAP, 2011*, pp. 3909–3912.
- [5] H. Matsumoto, Research on solar power satellites and microwave power transmission in Japan, *IEEE Microw. Mag.* 3 (4) (2002) 36–45, <http://dx.doi.org/10.1109/MMW.2002.1145674>.
- [6] N. Shinohara, Beam control technologies with a high-efficiency phased array for microwave power transmission in Japan, *Proc. IEEE* 101 (6) (2013) 1448–1463, <http://dx.doi.org/10.1109/JPROC.2013.2253062>.

- [7] A. Bisognin, D. Titz, F. Ferrero, R. Pilard, C.A. Fernandes, J.R. Costa, C. Corre, P. Calascibetta, J.M. Rivière, A. Poulain, C. Badard, F. Giancesello, C. Luxey, P. Busson, D. Gloria, D. Belot, 3D printed plastic 60 GHz lens: enabling innovative millimeter wave antenna solution and system, in: IEEE MTT-S International Microwave Symposium, IMS2014, 2014, pp. 1–4.
- [8] K. Gbele, M. Liang, W.R. Ng, M.E. Gehm, H. Xin, Millimeter wave Luneburg lens antenna fabricated by polymer jetting rapid prototyping, in: 39th International Conference on Infrared, Millimeter, and Terahertz Waves, IRMMW-THz, 2014, pp. 1.
- [9] S. Zhang, Design and fabrication of 3D-printed planar Fresnel zone plate lens, *Electron. Lett.* 52 (10) (2016) 833–835, <http://dx.doi.org/10.1049/el.2016.0736>.
- [10] J.J. Lee, *Antenna Handbook*, vol. II, Chapter 16, Van Nostrand Reinhold, 1993.
- [11] J.R. Costa, C.A. Fernandes, G. Godi, R. Sauleau, L.L. Coq, H. Legay, Compact ka-band lens antennas for LEO satellites, *IEEE Trans. Antennas Propag.* 56 (5) (2008) 1251–1258, <http://dx.doi.org/10.1109/TAP.2008.922690>.
- [12] R. Sauleau, B. Bares, A complete procedure for the design and optimization of arbitrarily shaped integrated lens antennas, *IEEE Trans. Antennas Propag.* 54 (4) (2006) 1122–1133, <http://dx.doi.org/10.1109/TAP.2006.872563>.
- [13] M.D. Janezic, J.A. Jargon, Complex permittivity determination from propagation constant measurements, *IEEE Microw. Guided Wave Lett.* 9 (2) (1999) 76–78, <http://dx.doi.org/10.1109/75.755052>.
- [14] F. Declercq, I. Couckuyt, H. Rogier, T. Dhaene, Environmental high-frequency characterization of fabrics based on a novel surrogate modelling antenna technique, *IEEE Trans. Antennas Propag.* 61 (10) (2013) 5200–5213, <http://dx.doi.org/10.1109/TAP.2013.2274031>.
- [15] R. Gonçalves, R. Magueta, P. Pinho, N.B. Carvalho, Dissipation factor and permittivity estimation of dielectric substrates using a single microstrip line measurement, *Appl. Comput. Electromagn. Soc. J.* 31 (2) (2016) 118–125.
- [16] X. Wu, G.V. Eleftheriades, T.E. van Deventer-Perkins, Design and characterization of single- and multiple-beam mm-wave circularly polarized substrate lens antennas for wireless communications, *IEEE Trans. Microw. Theory Tech.* 49 (3) (2001) 431–441, <http://dx.doi.org/10.1109/22.910546>.

Bibliography

- [1] T. C. M. U. C. S. D. C. Machine, "The "only" coke machine on the internet," October, 2016. [Online]. Available: http://www.cs.cmu.edu/~coke/history_long.txt
- [2] R. S. Raji, "Smart networks for control," *IEEE Spectrum*, vol. 31, no. 6, pp. 49–55, June 1994.
- [3] S. Sarma, D. L. Brock, and K. Ashton, "The networked physical world," *TR MIT-AUTOIDWH-001*, MIT Auto-ID Center, 2000.
- [4] L. Roselli, N. Borges Carvalho, F. Alimenti, P. Mezzanotte, G. Orecchini, M. Virili, C. Mariotti, R. Goncalves, and P. Pinho, "Smart surfaces: Large area electronics systems for internet of things enabled by energy harvesting," *Proceedings of the IEEE*, vol. 102, no. 11, pp. 1723–1746, Nov 2014.
- [5] A. Rida, L. Yang, and M. Tentzeris, *RFID-Enabled Sensor Design and Applications*. Artech House, Inc., 2010.
- [6] K. Finkenzeller, *RFID Handbook: Fundamentals and Applications in Contactless Smart Cards and Identification*. John Wiley & Sons, Ltd, 2003.
- [7] J. Virkki, J. Virtanen, L. Sydanheimo., L. Ukkonen, and M. M. Tentzeris, "Embedding inkjet-printed antennas into plywood structures for identification and sensing," *Proc. 2012 IEEE International Conference on RFID Technologies and Applications*, pp. 34–39, November 2012, 2012.
- [8] R. Goncalves, J. Reis, E. Santana, N. Carvalho, P. Pinho, and L. Roselli, "Smart floor: Indoor navigation based on rfid," in *Wireless Power Transfer (WPT), 2013 IEEE*, May 2013, pp. 103–106.
- [9] R. Goncalves, S. Rima, R. Magueta, A. Collado, P. Pinho, N. Carvalho, and A. Georgiadis, "Rfid tags on cork stoppers for bottle identification," in *Microwave Symposium (IMS), 2014 IEEE MTT-S International*, June 2014, pp. 1–4.
- [10] R. Goncalves, A. Duarte, R. Magueta, N. B. Carvalho, and P. Pinho, "Rfid tags on paper substrate for bottle labelling," *Procedia Technology*, vol. 17, pp. 65 – 72, 2014.

-
- [11] R. Goncalves, R. Magueta, P. Pinho, and N. Carvalho, "Rfid passive tag antenna for cork bottle stopper," in *Antennas and Propagation Society International Symposium (APSURSI), 2014 IEEE*, July 2014, pp. 1518–1519.
- [12] A. Babar, T. Bjorninen, V. Bhagavati, L. Sydanheimo, P. Kallio, and L. Ukkonen, "Small and flexible metal mountable passive uhf rfid tag on high-dielectric polymer-ceramic composite substrate," *Antennas and Wireless Propagation Letters, IEEE*, vol. 11, pp. 1319–1322, 2012.
- [13] Q. Luo, "Design synthesis and miniaturization of multiband and reconfigurable microstrip antenna for future wireless applications," Ph.D. dissertation, Faculdade de Engenharia da Universidade do Porto, 2012.
- [14] M. U. Khan, M. S. Sharawi, and R. Mittra, "Microstrip patch antenna miniaturisation techniques: a review," *IET Microwaves, Antennas Propagation*, vol. 9, no. 9, pp. 913–922, 2015.
- [15] S. R. Best, *Modern Antenna Handbook, Chapter 10*, C. A. Balanis, Ed. John Wiley & Sons, Inc., 2008.
- [16] R. Goncalves, P. Pinho, and N. B. Carvalho, "Compact, frequency reconfigurable, printed monopole antenna," *International Journal of Antennas and Propagation*, vol. 2012, 2012.
- [17] A. Bonfiglio and D. D. Rossi, Eds., *Wearable Monitoring Systems*. Springer Science & Business Media, 2011. [Online]. Available: <http://dx.doi.org/10.1007/978-1-4419-7384-9>
- [18] A. Pantelopoulos and N. Bourbakis, "A survey on wearable sensor-based systems for health monitoring and prognosis," *IEEE Transactions on Systems, Man, and Cybernetics, Part C (Applications and Reviews)*, vol. 40, no. 1, pp. 1–12, jan 2010. [Online]. Available: <http://dx.doi.org/10.1109/TSMCC.2009.2032660>
- [19] C. Loss, R. Goncalves, C. Lopes, P. Pinho, and R. Salvado, "Smart coat with a fully-embedded textile antenna for iot applications," *Sensors*, vol. 16, no. 6, p. 938, 2016. [Online]. Available: <http://www.mdpi.com/1424-8220/16/6/938>
- [20] P. J. Massey, "Gsm fabric antenna for mobile phones integrated within clothing," *Proc. of Int. Conf. on Antennas and Propagation*, vol. 1, pp. 344 – 347, Manchester, 2001.
- [21] B. Gupta, S. Sankaralingam, and S. Dhar, "Development of wearable and implantable antennas in the last decade: A review," in *2010 10th Mediterranean Microwave Symposium*, Aug 2010, pp. 251–267.

- [22] R. Salvado, C. Loss, R. Goncalves, and P. Pinho, "Textile materials for the design of wearable antennas: A survey," *Sensors ISSN 1424-8220*, vol. 12, doi:10.3390/s121115841, pp. 15 841 – 15 857, 2012.
- [23] M. Bozzi and R. Moro, "Low-cost fabrication, eco-friendly materials, and easy integration: The new technological paradigm for the future wireless sensor networks," in *Microwave Conference (EuMC), 2013 European*, Oct 2013, pp. 858–861.
- [24] E. Moradi, K. Koski, T. Bjorninen, L. Sydanheimo, J. Rabaey, J. Carmena, Y. Rahmat-Samii, and L. Ukkonen, "Miniature implantable and wearable on-body antennas: towards the new era of wireless body-centric systems [antenna applications corner]," *Antennas and Propagation Magazine, IEEE*, vol. 56, no. 1, pp. 271–291, Feb 2014.
- [25] P. Soh, G. Vandenbosch, S. L. Ooi, and N. Rais, "Design of a broadband all-textile slotted pifa," *IEEE Transactions on Antennas and Propagation*, vol. 60, no. 1, pp. 379–384, 2012.
- [26] S. Agneessens, S. Lemey, T. Vervust, and H. Rogier, "Wearable, small, and robust: the circular quarter-mode textile antenna," *Antennas and Wireless Propagation Letters, IEEE*, vol. PP, no. 99, pp. 1–1, 2015.
- [27] J. Tak and J. Choi, "An all-textile louis vuitton logo antenna," *Antennas and Wireless Propagation Letters, IEEE*, vol. PP, no. 99, pp. 1–1, 2015.
- [28] K. ElMahgoub, T. Elsherbeni, F. Yang, A. Z. Elsherbeni, L. Sydanheimo, and L. Ukkonen, "Logo-antenna based rfid tags for advertising application," *Applied Computational Electromagnetics Society Journal*, vol. 25, no. 3, pp. 174–181, 2010.
- [29] M. S. Mahmud and S. Dey, "Design, performance and implementation of uwb wearable logo textile antenna," in *Antenna Technology and Applied Electromagnetics (ANTEM), 2012 15th International Symposium on*, June 2012, pp. 1–4.
- [30] R. Goncalves, N. B. Carvalho, P. Pinho, C. Loss, and R. Salvado, "Textile antenna for electromagnetic energy harvesting for gsm900 and dcs1800 bands," in *2013 IEEE Antennas and Propagation Society International Symposium (APSURSI)*, July 2013, pp. 1206–1207.
- [31] R. K. Tallos, Z. Wang, and J. L. Volakis, "Wi-fi energy harvesting system using body-worn antennas," jul 2014. [Online]. Available: <http://dx.doi.org/10.1109/APS.2014.6905028>
- [32] F. Declercq, A. Georgiadis, and H. Rogier, "Wearable aperture-coupled shorted solar patch antenna for remote tracking and monitoring applications," in *Proceedings of the*

- 5th European Conference on Antennas and Propagation (EUCAP)*, April 2011, pp. 2992–2996.
- [33] D. Masotti, A. Costanzo, and S. Adami, “Design and realization of a wearable multi-frequency rf energy harvesting system,” in *Proceedings of the 5th European Conference on Antennas and Propagation (EUCAP)*, April 2011, pp. 517–520.
- [34] T. Nguyen, J.-Y. Chung, and B. Lee, “Radiation characteristics of woven patch antennas composed of conductive threads,” *Antennas and Propagation, IEEE Transactions on*, vol. PP, no. 99, pp. 1–1, 2015.
- [35] Q. Bai and R. Langley, “Crumpling of pifa textile antenna,” *IEEE Transactions on Antennas and Propagation*, vol. 60, no. 1, pp. 63–70, Jan 2012.
- [36] M. L. Scarpello, I. Kazani, C. Hertleer, H. Rogier, and D. V. Ginste, “Stability and efficiency of screen-printed wearable and washable antennas,” *IEEE Antennas and Wireless Propagation Letters*, vol. 11, pp. 838–841, 2012. [Online]. Available: <http://dx.doi.org/10.1109/LAWP.2012.2207941>
- [37] Y. Y. Fu, Y. L. Chan, M. H. Yang, Y.-C. Chan, J. Virkki, T. Bjorninen, L. Sydanheimo, and L. Ukkonen, “Experimental study on the washing durability of electro-textile uhf rfid tags,” *Antennas and Wireless Propagation Letters, IEEE*, vol. 14, pp. 466–469, 2015.
- [38] I. Locher, M. Klemm, T. Kirstein, and G. Trster, “Design and characterization of purely textile patch antennas,” *IEEE Transactions on Advanced Packaging*, vol. 29, no. 4, pp. 777–788, nov 2006. [Online]. Available: <http://dx.doi.org/10.1109/TADVP.2006.884780>
- [39] N. Amaro, C. Mendes, and P. Pinho, “Bending effects on a textile microstrip antenna,” jul 2011. [Online]. Available: <http://dx.doi.org/10.1109/APS.2011.5996697>
- [40] S. Agneessens and H. Rogier, “Compact half diamond dual-band textile HMSIW on-body antenna,” *IEEE Trans. Antennas Propagat.*, vol. 62, no. 5, pp. 2374–2381, may 2014. [Online]. Available: <http://dx.doi.org/10.1109/TAP.2014.2308526>
- [41] T. Kaija, J. Lilja, and P. Salonen, “Exposing textile antennas for harsh environment,” oct 2010. [Online]. Available: <http://dx.doi.org/10.1109/MILCOM.2010.5680300>
- [42] D. C. Thompson, O. Tantot, H. Jallageas, G. E. Ponchak, M. M. Tentzeris, and J. Papapolymerou, “Characterization of liquid crystal polymer (LCP) material and transmission line on LCP substrates from 30 to 110 ghz,” *IEEE Transactions on Microwave Theory and Techniques*, vol. 52, pp. 1343 – 1352, 2004.

- [43] G. DeJean, R. Bairavasubramanian, D. Thompson, G. E. Ponchak, M. M. Tentzeris, and J. Papapolymerou, "Liquid crystal polymer (lcp): a new organic material for the development of multilayer dual-frequency/dual-polarization flexible antenna arrays," *IEEE Antennas and Wireless Propagation Letters*, vol. 4, pp. 22 – 26, 2005.
- [44] S. S. Basat, S. Bhattacharya, L. Yang, A. Rida, M. M. Tentzeris, and J. Laskar, "Design of a novel high-efficiency UHF RFID antenna on flexible LCP substrate with high read-range capability," *Proc. IEEE Ant. Propag. Soc. Int. Symp.*, vol. 1, pp. 1031 – 1034, Albuquerque, 2006.
- [45] R. Vyas, A. Rida, S. Bhattacharya, and M. M. Tentzeris, "Liquid crystal polymer (LCP): The ultimate solution for low-cost RF flexible electronics and antennas," *Proc. IEEE Ant. Propag. Soc. Int. Symp.*, vol. 1, pp. 1729 – 1732, Honolulu, Hawaii, 2007.
- [46] A. C. Durgun, M. S. Reese, C. A. Balanis, C. R. Birtcher, and D. R. Allee, "Flexible bow-tie antennas," *Proc. IEEE Ant. Propag. Soc. Int. Symp.*, vol. 1, pp. 1 – 4, Toronto, 2010.
- [47] A. C. Durgun, M. S. Reese, C. A. Balanis, C. R. Birtcher, D. R. Allee, and S. Vanugopal, "Flexible bow-tie antennas with reduced metallization," *Proc. IEEE Radio Wireless Symp.*, vol. 1, pp. 50 – 53, Phoenix, Arizona, USA, 2011.
- [48] A. C. Durgun, C. A. Balanis, C. R. Birtcher, and D. R. Allee, "Design, simulation, fabrication and testing of flexible bow-tie antennas," *IEEE Transactions on Antennas and Propagation*, vol. 59, pp. 4425 – 4435, 2011.
- [49] H.-E. Nilsson, J. Siden, T. Olsson, P. Jonsson, and A. Koptioug, "Evaluation of a printed patch antenna for robust microwave RFID tags," *IET Microw. Antennas Propag.*, vol. 1, pp. 776 – 781, 2007.
- [50] S. Shao, A. Kiourti, R. Burkholder, and J. Volakis, "Broadband textile-based passive uhf rfid tag antenna for elastic material," *Antennas and Wireless Propagation Letters, IEEE*, vol. PP, no. 99, pp. 1–1, 2015.
- [51] S.-H. Wi, Y.-B. Sun, I.-S. Song, S.-H. Choa, I.-S. Koh, Y.-S. Lee, and J.-G. Yook, "Package-level integrated antennas based on ltcc technology," *IEEE Transactions on Antennas and Propagation*, vol. 54, pp. 2190 – 2197, 2006.
- [52] M.-R. Hsu and K.-L. Wong, "Ceramic chip antenna for WWAN operation," *Asia-Pacific Microwave Conference*, vol. 1, pp. 1 – 4, Macau, 2008.
- [53] A. E. I. Lamminen, J. Säily, and A. R. Vimpari, "60-ghz patch antennas and arrays on LTCC with embedded-cavity substrates," *IEEE Transactions on Antennas and Propagation*, vol. 56, pp. 2865 – 2874, 2008.

- [54] Y. P. Zhang and D. Liu, "Antenna-on-chip and antenna-in-package solutions to highly integrated millimeter-wave devices for wireless communications," *IEEE Transactions on Antennas and Propagation*, vol. 57, pp. 2830 – 2841, 2009.
- [55] C.-F. Yang, C.-Y. Hsieh, and C.-M. Cheng, "Design small-size and wide-band t-shaped patch antenna on ceramic substrate," *IEEE Wireless Communications and Networking Conference*, vol. 1, pp. 2919 – 2922, Kowloon, 2007.
- [56] C. F. Yang, C. Y. Huang, C. M. Cheng, W. K. Chia, and M. Cheung, "Print a small size u-shape modified broadband slot antenna on ceramic substrate," *Asia-Pacific Microwave Conference*, vol. 1, pp. 1 – 4, Macau, 2008.
- [57] H.-H. Kim, K.-Y. Kim, J.-H. Lee, and J.-M. Woo, "Surface-mounted chip dielectric ceramic antenna for pcs phone," in *Antennas, Propagation and EM Theory, 2000. Proceedings. ISAPE 2000. 5th International Symposium on*, Aug 2000, pp. 582–585.
- [58] T. Zhihong, Y. Zhang, C. Luxey, A. Bisognin, D. Titz, and F. Ferrero, "A ceramic antenna for tri-band radio devices," *Antennas and Propagation, IEEE Transactions on*, vol. 61, no. 11, pp. 5776–5780, Nov 2013.
- [59] T. Chien, C. Cheng, H. Yang, and C. Luo, "Develop implantable ceramic antennas with no superstrate," in *Antennas and Propagation Society International Symposium (APSURSI), 2010 IEEE*, July 2010, pp. 1–4.
- [60] Locosys, <http://www.locosystech.com/product.php?zln=en&zcat=GNSS2015>.
- [61] Trimble, "Antenna companion modules," <http://www.trimble.com/embeddedsystems/antenna-companion-modules.aspx?dtID=overview&>, 2015.
- [62] A. Technology, "Tags," <http://www.alientechnology.com/tags/>, 2014. [Online]. Available: <http://www.alientechnology.com/tags/>
- [63] L. Yang and M. M. Tentzeris, "Design and characterization of novel paper-based inkjet-printed RFID and microwave structures for telecommunication and sensing applications," *IEEE Int. Microwave Symp.*, vol. 1, pp. 1633 – 1636, Honolulu, Haiti, 2007.
- [64] A. Rida, R. Vyas, S. Basat, A. Ferrer-Vidal, L. Yang, S. Bhattacharya, and M. M. Tentzeris, "Paper-based ultra-low-cost integrated RFID tags for sensing and tracking applications," *Proc. 57th Electronic Compon. and Tech. Conf.*, vol. 1, pp. 1977 – 1980, Reno, Nevada, 2007.
- [65] L. Yang, A. Rida, R. Vyas, and M. M. Tentzeris, "Rfid tag and rf structures on a paper substrate using inkjet-printing technology," *IEEE Transactions on Microwave Theory and Techniques*, vol. 55, no. 12, pp. 2894–2901, Dec 2007.

- [66] A. Rida, L. Yang, R. Vyas, and M. M. Tentzeris, "Conductive inkjet-printed antennas on flexible low-cost paper-based substrates for RFID and WSN applications," *IEEE Antennas and Propagation Magazine*, vol. 51, pp. 13 – 23, 2009.
- [67] L. Yang, R. Zhang, D. Staiculescu, C. P. Wong, and M. M. Tentzeris, "Anovel conformal rfid-enabled module utilizing inkjet-printed antennas and carbon nanotubes for gas detection applications," *IEEE Antennas and Wireless Propagation Letters*, vol. 8, pp. 653 – 565, 2009.
- [68] B. S. Cook and A. Shamim, "Inkjet printing of novel wideband and high gain antennas on low cost paper substrate," *IEEE Transactions on Antennas and Propagation*, vol. 60, pp. 4148 – 4156, 2012.
- [69] G. Shaker, S. Safavi-Naeini, N. Sangary, and M. M. Tentzeris, "Inkjet printing of ultra-wideband (UWB) antennas on paper-based substrates," *IEEE Antennas and Wireless Propagation Letters*, vol. 10, pp. 111 – 114, 2011.
- [70] S. Kim, M. M. Tentzeris, and S. Nikolaou, "Wearable biomonitoring monopole antennas using inkjet printed electromagnetic band gap structures," *Proc. 6th Euro. Conf. on Ant. and Propag.*, vol. 1, pp. 181 – 184, Prague, 2011.
- [71] G. Shaker, H. Lee, K. Duncan, and M. M. Tentzeris, "Integrated antenna with inkjet-printed compact artificial magnetic surface for UHF applications," *IEEE Int. Conf. on Wirel. Info. Tech. and Syst.*, vol. 1, pp. 1 – 4, Honolulu, Haiti, 2010.
- [72] B. S. Cook and A. Shamim, "Utilizing wideband AMC structures for high gain inkjet-printed antennas on lossy paper substrate," *IEEE Antennas and Wireless Propagation Letters*, vol. PP, pp. 1 – 4, 2013.
- [73] S. Brzeziński, T. Rybicki, I. Karbownik, G. Malinowska, and K. Śledzińska, "Textile multi-layer systems for protection against electromagnetic radiation," vol. 10, no. 5. Walter de Gruyter GmbH, jan 2012. [Online]. Available: <http://dx.doi.org/10.2478/s11534-012-0094-z>
- [74] A. Chauraya, S. Zhang, W. Whittow, T. Acti, R. Seager, T. Dias, and Y. C. Vardaxoglou, "Addressing the challenges of fabricating microwave antennas using conductive threads," mar 2012. [Online]. Available: <http://dx.doi.org/10.1109/EuCAP.2012.6205910>
- [75] J. L. Volakis, L. Zhang, Z. Wang, and Y. Bayram, "Embroidered flexible RF electronics," mar 2012. [Online]. Available: <http://dx.doi.org/10.1109/IWAT.2012.6178385>
- [76] Z. Wang, L. Zhang, Y. Bayram, and J. L. Volakis, "Embroidered conductive fibers on polymer composite for conformal antennas," *IEEE Transactions on Antennas*

- and Propagation*, vol. 60, no. 9, pp. 4141–4147, sep 2012. [Online]. Available: <http://dx.doi.org/10.1109/TAP.2012.2207055>
- [77] L. Yao and Y. Qiu, “Design and fabrication of microstrip antennas integrated in three dimensional orthogonal woven composites,” *Composites Science and Technology*, vol. 69, no. 7-8, pp. 1004–1008, jun 2009. [Online]. Available: <http://dx.doi.org/10.1016/j.compscitech.2009.01.013>
- [78] R. Goncalves, S. Rima, R. Magueta, A. Collado, P. Pinho, N. Carvalho, and A. Georgiadis, “Rfid tags on cork stoppers for bottle identification,” in *Microwave Symposium (IMS), 2014 IEEE MTT-S International*, June 2014, pp. 1–4.
- [79] F. Alimenti, C. Mariotti, P. Mezzanotte, M. Dionigi, M. Virili, and L. Roselli, “A 1.2 v, 0.9 mw uhf vco based on hairpin resonator in paper substrate and cu adhesive tape,” *Microwave and Wireless Components Letters, IEEE*, vol. 23, no. 4, pp. 214–216, April 2013.
- [80] I. Kazani, F. Declercq, M. L. Scarpello, C. Hertleer, H. Rogier, D. V. Ginste, G. D. Mey, G. Guxho, and L. V. Langenhove, “Performance study of screen-printed textile antennas after repeated washing,” *Autex Research Journal*, vol. 14, no. 2, jan 2014. [Online]. Available: <http://dx.doi.org/10.2478/v10304-012-0049-x>
- [81] S.-E. Adami, D. Zhu, Y. Li, E. Mellios, B. H. Stark, and S. Beeby, “A 2.45 GHz rectenna screen-printed on polycotton for on-body RF power transfer and harvesting,” may 2015. [Online]. Available: <http://dx.doi.org/10.1109/WPT.2015.7140161>
- [82] C. A. Balanis, *Antenna Theory: Analysis and Design*. John Wiley & Sons, Inc., 2005.
- [83] D. M. Pozar, *Microwave Engineering*. John Wiley & Sons, Inc., 3rd Edition, 1998.
- [84] M. N. O. Sadiku, *Elements of Electromagnetics*. Oxford University Press, 4th Edition, 2006.
- [85] V. der Pauw, “A method of measuring specific resistivity and hall effect of discs of arbitrary shape,” *Philips Res. Rep.*, vol. 13, no. 1, pp. 1 – 9, 1958.
- [86] G. Rietveld, C. V. Kojmans, L. C. A. Henderson, M. J. Hall, S. Harmon, P. Warnecke, and B. Schumacher, “Dc conductivity measurements in the van der pauw geometry,” *IEEE Transactions on Instrumentation and Measurement*, vol. 52, no. 2, pp. 449–453, April 2003.
- [87] L. B. Valdes, “Resistivity measurements on germanium for transistors,” *Proceedings of the IRE*, vol. 42, no. 2, pp. 420–427, Feb 1954.

- [88] E. P. D. W. Robert Thurber, NIST, "The hall effect," October, 2016. [Online]. Available: <https://www.nist.gov/pml/engineering-physics-division/hall-effect#evolution>
- [89] *ASTM F390-11, Standard Test Method for Sheet Resistance of Thin Metallic Films With a Collinear Four-Probe Array*, ASTM International, West Conshohocken, PA, 2011. [Online]. Available: www.astm.org
- [90] U. Kaatze, *Electromagnetic Aquametry*, 1st ed., K. Kupfer, Ed. Springer, 2005, vol. Chapter 2: Electromagnetic Wave Interactions with Water and Aqueous Solutions.
- [91] R. Feynman, R. Leighton, and M. Sands, *The Feynman Lectures on Physics, Volume 2: Mainly Electromagnetism and Matter*, M. A. Gottlieb and R. Pfeiffer, Eds. Basic Books, A Member of the Perseus Books Group, 1964.
- [92] "Matweb material property data." [Online]. Available: <http://www.matweb.com>
- [93] F. Kremer and A. Schnhals, Eds., *Broadband Dielectric Spectroscopy*. Springer Science & Business Media, 2003. [Online]. Available: <http://dx.doi.org/10.1007/978-3-642-56120-7>
- [94] C. A. Balanis, *Advanced Engineering Electromagnetics*, 2nd ed. John Wiley & Sons, Inc., 2012.
- [95] J. Baker-Jarvis, R. Geyer, J. Grosvenor, J.H., M. Janezic, C. Jones, B. Riddle, C. Weil, and J. Krupka, "Dielectric characterization of low-loss materials a comparison of techniques," *IEEE Transactions on Dielectrics and Electrical Insulation*, vol. 5, no. 4, pp. 571–577, Aug 1998.
- [96] J. Krupka, R. G. Geyer, J. Baker-Jarvis, and J. Ceremuga, "Measurements of the complex permittivity of microwave circuit board substrates using split dielectric resonator and reentrant cavity techniques," in *Dielectric Materials, Measurements and Applications, Seventh International Conference on (Conf. Publ. No. 430)*, Sep 1996, pp. 21–24.
- [97] G. Kent, "Nondestructive permittivity measurement of substrates," *Instrumentation and Measurement, IEEE Transactions on*, vol. 45, no. 1, pp. 102–106, Feb 1996.
- [98] G. Kent and S. Bell, "The gap correction for the resonant-mode dielectrometer," *Instrumentation and Measurement, IEEE Transactions on*, vol. 45, no. 1, pp. 98–101, Feb 1996.
- [99] G. Kent, "An evanescent-mode tester for ceramic dielectric substrates," *Microwave Theory and Techniques, IEEE Transactions on*, vol. 36, no. 10, pp. 1451–1454, Oct 1988.

-
- [100] B. W. Hakki and P. D. Coleman, "A dielectric resonator method of measuring inductive capacities in the millimeter range," *IRE Transactions on Microwave Theory and Techniques*, vol. 8, no. 4, pp. 402–410, July 1960.
- [101] W. E. Courtney, "Analysis and evaluation of a method of measuring the complex permittivity and permeability microwave insulators," *IEEE Transactions on Microwave Theory and Techniques*, vol. 18, no. 8, pp. 476–485, Aug 1970.
- [102] Y. Kobayashi and S. Tanaka, "Resonant modes of a dielectric rod resonator short-circuited at both ends by parallel conducting plates," *IEEE Transactions on Microwave Theory and Techniques*, vol. 28, no. 10, pp. 1077–1085, Oct 1980.
- [103] Y. Kobayashi and M. Katoh, "Microwave measurement of dielectric properties of low-loss materials by the dielectric rod resonator method," *IEEE Transactions on Microwave Theory and Techniques*, vol. 33, no. 7, pp. 586–592, Jul 1985.
- [104] M. Janezic and J. Baker-Jarvis, "Full-wave analysis of a split-cylinder resonator for nondestructive permittivity measurements," *Microwave Theory and Techniques, IEEE Transactions on*, vol. 47, no. 10, pp. 2014–2020, Oct 1999.
- [105] M. Janezic, U. Arz, S. Begley, and P. Bartley, "Improved permittivity measurement of dielectric substrates by use of the te₁₁₁ mode of a split-cylinder cavity," in *Microwave Measurement Conference, 2009 73rd ARFTG*, June 2009, pp. 1–3.
- [106] E. Semouchkina, W. Cao, and M. Lanagan, "High frequency permittivity determination by spectra simulation and measurement of microstrip ring resonators," *Electronics Letters*, vol. 36, no. 11, pp. 956–958, May 2000.
- [107] G. Zou, H. Gronqvist, P. Starski, and J. Liu, "High frequency characteristics of liquid crystal polymer for system in a package application," in *Advanced Packaging Materials, 2002. Proceedings. 2002 8th International Symposium on*, 2002, pp. 337–341.
- [108] J. M. Heinola and K. Tolsa, "Dielectric characterization of printed wiring board materials using ring resonator techniques: a comparison of calculation models," *IEEE Transactions on Dielectrics and Electrical Insulation*, vol. 13, no. 4, pp. 717–726, Aug 2006.
- [109] *IPC-TM-650 Test Methods Manual, Number 2.5.5.5, Revision C, Stripline Test for Permittivity and Loss Tangent (Dielectric Constant and Dissipation Factor) at X-Band*, Institute for Printed Circuits, March 1998.
- [110] D. Misra, M. Chhabra, B. R. Epstein, and M. Microtznik, "Noninvasive electrical characterization of materials at microwave frequencies using an open-ended coaxial line:

- test of an improved calibration technique," *IEEE Transactions on Microwave Theory and Techniques*, vol. 38, pp. 8 – 14, 1990.
- [111] P. D. Langhe, K. Blomme, L. Martens, and D. D. Zutter, "Measurement of low-permittivity materials based on a spectral-domain analysis for the open-ended coaxial probe," *IEEE Transactions on Instrumentation and Measurement*, vol. 42, pp. 879 – 886, 1993.
- [112] J. Baker-Jarvis, M. D. Janezic, P. D. Domich, and R. G. Geyer, "Analysis of an open-ended coaxial probe with lift-off for nondestructive testing," *IEEE Transactions on Instrumentation and Measurement*, vol. 43, pp. 711 – 718, 1994.
- [113] D. V. Blackham and R. D. Pollard, "An improved technique for permittivity measurements using a coaxial probe," *IEEE Transactions on Instrumentation and Measurement*, vol. 46, pp. 1093 – 1099, 1997.
- [114] E. C. Burdette, F. L. Clain, and J. Seals, "In-vivo probe measurement technique for determining dielectric properties at vhf through microwave frequencies," *IEEE Transactions on Microwave Theory and Techniques*, vol. 28, pp. 414–427, 1980.
- [115] C. L. Pournaropoulos and D. K. Misra, "The coaxial aperture electromagnetic sensor and its application in material characterization," *Meas. Sci. Technol.*, vol. 8, pp. 1191–1202, 1997.
- [116] D. Berube, F. M. Ganouchi, and P. Savard, "A comparative study of four open-ended coaxial probe models for permittivity measurements of lossy dielectric biological materials at microwave frequencies," *IEEE Transactions on Microwave Theory and Techniques*, vol. 44, pp. 1928 – 1934, 1996.
- [117] T. W. Athey, M. A. Stuchly, and S. S. Stuchly, "Measurement of radio frequency permittivity of biological tissues with an open-ended coaxial line: Part i," *IEEE Transactions on Microwave Theory and Techniques*, vol. 30, pp. 82–86, 1982.
- [118] M. A. Stuchly, T. H. Athey, C. M. Samaras, and G. E. Taylor, "Measurement of radio frequency permittivity of biological tissues with an open-ended coaxial line: Part ii," *IEEE Transactions on Microwave Theory and Techniques*, vol. 30, pp. 87–91, 1982.
- [119] S. S. Stuchly, C. L. Sibbald, and J. M. Anderson, "A new admittance model for open-ended waveguides," *IEEE Transactions on Microwave Theory and Techniques*, vol. 42, pp. 192–198, 1994.
- [120] R. Zajicek, L. Oppla, and J. Vrba, "Broadband measurement of complex permittivity using reflection method and coaxial probe," *Radioengineering*, vol. 17, p. 1, 2008.

-
- [121] D. K. Ghodgaonkar, V. V. Varadan, and V. K. Varadan, "A free-space method for measurement of dielectric constants and loss tangents at microwave frequencies," *IEEE Transactions on Instrumentation and Measurement*, vol. 37, pp. 787–793, 1989.
- [122] M. H. Umari, D. K. Ghodgaonkar, V. V. Varadan, and V. K. Varadan, "A free-space bi-static calibration technique for the measurement of parallel and perpendicular reflection coefficients of planar samples," *IEEE Transactions on Instrumentation and Measurement*, vol. 40, pp. 19–24, 1991.
- [123] A. Nicolson and G. Ross, "Measurement of the intrinsic properties of materials by time-domain techniques," *Instrumentation and Measurement, IEEE Transactions on*, vol. 19, no. 4, pp. 377–382, Nov 1970.
- [124] W. B. Weir, "Automatic measurement of complex dielectric constant and permeability at microwave frequencies," *Proceedings of the IEEE*, vol. 62, no. 1, pp. 33–36, Jan 1974.
- [125] O. Luukkonen, S. I. Maslovski, and S. Tretyakov, "A stepwise nicolson-ross-weir-based material parameter extraction method," *Antennas and Wireless Propagation Letters, IEEE*, vol. 10, pp. 1295–1298, 2011.
- [126] J. Baker-Jarvis, "Transmission/reflection and short-circuit line permittivity measurements," *NIST Technical Note, National Institute of Standards and Technology*, 1990.
- [127] J. Baker-Jarvis, M. D. Janezic, J. H. G. Jr., and R. G. Geyer, "Transmission/reflection and short-circuit line method for measuring permittivity and permeability," *NIST Technical Note, National Institute of Standards and Technology*, 1993.
- [128] J. Baker-Jarvis, E. Vanzura, and W. Kissick, "Improved technique for determining complex permittivity with the transmission/reflection method," *IEEE Transactions on Microwave Theory and Techniques*, vol. 38, no. 8, pp. 1096–1103, Aug 1990.
- [129] M. Pauli, T. Kayser, and W. Wiesbeck, "A versatile measurement system for the determination of dielectric parameters of various materials," *Measurement Science and Technology*, vol. 18, no. 4, p. 1046, 2007. [Online]. Available: <http://stacks.iop.org/0957-0233/18/i=4/a=012>
- [130] M. D. Deshpande, C. Jagadeswara reddy, P. Tiemsin, and R. Cravey, "A new approach to estimate complex permittivity of dielectric materials at microwave frequencies using waveguide measurements," *Microwave Theory and Techniques, IEEE Transactions on*, vol. 45, no. 3, pp. 359–366, Mar 1997.
- [131] J. Catala-Civera, A. Canos, F. Penaranda-Foix, and E. de los Reyes Davo, "Accurate determination of the complex permittivity of materials with transmission reflection

- measurements in partially filled rectangular waveguides,” *Microwave Theory and Techniques, IEEE Transactions on*, vol. 51, no. 1, pp. 16–24, Jan 2003.
- [132] M.-Q. Lee and S. Nam, “An accurate broadband measurement of substrate dielectric constant,” *Microwave and Guided Wave Letters, IEEE*, vol. 6, no. 4, pp. 168–170, Apr 1996.
- [133] M. Janezic and J. Jargon, “Complex permittivity determination from propagation constant measurements,” *Microwave and Guided Wave Letters, IEEE*, vol. 9, no. 2, pp. 76–78, Feb 1999.
- [134] F. Declercq, H. Rogier, and C. Hertleer, “Permittivity and loss tangent characterization for garment antennas based on a new matrix-pencil two-line method,” *Antennas and Propagation, IEEE Transactions on*, vol. 56, no. 8, pp. 2548–2554, Aug 2008.
- [135] J. Roelvink, S. Trabelsi, and S. Nelson, “A planar transmission-line sensor for measuring the microwave permittivity of liquid and semisolid biological materials,” *Instrumentation and Measurement, IEEE Transactions on*, vol. 62, no. 11, pp. 2974–2982, Nov 2013.
- [136] J. Roelvink, S. Trabelsi, and S. O. Nelson, “Determining complex permittivity from propagation constant measurements with planar transmission lines,” *Measurement Science and Technology*, vol. 24, no. 10, p. 105001, 2013. [Online]. Available: <http://stacks.iop.org/0957-0233/24/i=10/a=105001>
- [137] D. Ghodgaonkar, V. Varadan, and V. Varadan, “Free-space measurement of complex permittivity and complex permeability of magnetic materials at microwave frequencies,” *Instrumentation and Measurement, IEEE Transactions on*, vol. 39, no. 2, pp. 387–394, Apr 1990.
- [138] V. Varadan, R. Hollinger, D. Ghodgaonkar, and V. K. Varadan, “Free-space, broadband measurements of high-temperature, complex dielectric properties at microwave frequencies,” *Instrumentation and Measurement, IEEE Transactions on*, vol. 40, no. 5, pp. 842–846, Oct 1991.
- [139] B. C. Wadell, *Transmission Line Design Handbook*. Artech House, Inc., 1991.
- [140] R. Goncalves, R. Magueta, P. Pinho, and N. B. Carvalho, “Dissipation factor and permittivity estimation of dielectric substrates using a single microstrip line measurement,” *Applied Computational Electromagnetics Society Journal*, vol. 31, no. 2, pp. 118–125, February 2016.
- [141] R. A. Pucel, D. J. Masse, and C. P. Hartwig, “Losses in microstrip,” *IEEE Transactions on Microwave Theory and Techniques*, vol. 16, no. 6, pp. 342–350, Jun 1968.

- [142] K. C. Yaw, *Measurement of Dielectric Material Properties*, Rhode & Schwarz, 2010.
- [143] A. Kumar and D. G. Smith, "Microwave properties of yarns and textiles using a resonant microwave cavity," *IEEE Transactions on Instrumentation and Measurement*, vol. 26, no. 2, pp. 95–98, June 1977.
- [144] P. Salonen, Y. Rahmat-Samii, M. Schaffrath, and M. Kivikoski, "Effect of textile materials on wearable antenna performance: a case study of gps antennas," in *Antennas and Propagation Society International Symposium, 2004. IEEE*, vol. 1, June 2004, pp. 459–462 Vol.1.
- [145] P. Salonen and L. Hurme, "A novel fabric wlan antenna for wearable applications," in *Antennas and Propagation Society International Symposium, 2003. IEEE*, vol. 2, June 2003, pp. 700–703 vol.2.
- [146] S. Sankaralingam and B. Gupta, "Determination of dielectric constant of fabric materials and their use as substrates for design and development of antennas for wearable applications," *IEEE Transactions on Instrumentation and Measurement*, vol. 59, no. 12, pp. 3122–3130, Dec 2010.
- [147] M. Klemm and G. Troester, "Textile uwb antennas for wireless body area networks," *IEEE Transactions on Antennas and Propagation*, vol. 54, no. 11, pp. 3192–3197, Nov 2006.
- [148] A. S. A. Bakar, M. I. Misnon, D. K. Ghodgaonkar, N. Khadri, J. H. Salleh, W. Y. W. Ahmad, M. D. M. Ramli, Y. M. Taib, and Z. Salleh, "Comparison of electrical physical and mechanical properties of textile composites using microwave nondestructive evaluation," in *RF and Microwave Conference, 2004. RFM 2004. Proceedings*, Oct 2004, pp. 164–168.
- [149] M. M. A. C. Tarot, S. Collardey, and K. Mahdjoubi, "Investigation of flexible textile antennas and AMC reflectors," *International Journal of Antennas and Propagation*, vol. 2012, no. Article ID 236505, p. 10 pages, 2012. [Online]. Available: <http://dx.doi.org/10.1155/2012/236505>
- [150] Goodfellow, October 2016. [Online]. Available: <http://www.goodfellow.com/catalogue/GFCat2C.php?ewd.token=PxOSK32vd9uFD1Y0Zdgb8LnxlZYrmQ&n=By40VqexOO4rtK91wQgYAnUKa3lyc3&ewd.urlNo=GFCat26&type=30&prop=5>
- [151] K. Shinyama, T. Oi, and S. Fujita, "Dielectric relaxation phenomena of polylactic acid with β -crystalline chitin," *International Journal of Polymer Science*, vol. 2012, pp. 1–5, 2012. [Online]. Available: <http://dx.doi.org/10.1155/2012/389491>

- [152] A. Bisognin, D. Titz, F. Ferrero, R. Pilard, C. A. Fernandes, J. R. Costa, C. Corre, P. Calascibetta, J.-M. Riviere, A. Poulain, C. Badard, F. Giancesello, C. Luxey, P. Busson, D. Gloria, and D. Belot, "3D printed plastic 60 GHz lens: Enabling innovative millimeter wave antenna solution and system," in *2014 IEEE MTT-S International Microwave Symposium (IMS2014)*. Institute of Electrical and Electronics Engineers (IEEE), June 2014. [Online]. Available: <http://dx.doi.org/10.1109/MWSYM.2014.6848450>
- [153] C. G. Malmberg and A. A. Maryott, "Dielectric constant of water from 0° to 100°C," *Journal of Research of the National Bureau of Standards*, vol. 56, pp. —, 1956.
- [154] M.-T. Zhang, Y.-C. Jiao, F.-S. Zhang, and W.-T. Wang, "Design of antennas for RFID application," in *Development and Implementation of RFID Technology*, C. Turcu, Ed. InTech, jan 2009. [Online]. Available: <http://dx.doi.org/10.5772/6516>
- [155] B. Wozniak and J. Dera, "Light absorption by water molecules and inorganic substances dissolved in sea water," in *Light Absorption in Sea Water*. Springer New York, 2007, vol. 33, pp. 11–81.
- [156] ANP, "Nano-silver ink for inkjet printing," October, 2016. [Online]. Available: http://anapro.com/eng/product/silver_inkjet_ink.html
- [157] G. Zamora, S. Zuffanelli, F. Paredes, F. Martín, and J. Bonache, "Design and synthesis methodology for uhf-rfid tags based on the t-match network," *IEEE Transactions on Microwave Theory and Techniques*, vol. 61, pp. 4090 – 4098, 2013.
- [158] A. Tsolis, W. G. Whittow, A. A. Alexandridis, and J. C. Vardaxoglou, "Embroidery and related manufacturing techniques for wearable antennas: Challenges and opportunities," *Electronics*, vol. 3, no. 2, p. 314, 2014. [Online]. Available: <http://www.mdpi.com/2079-9292/3/2/314>
- [159] V. authors, *The ARRL Antenna Book for Radio Communications*, 23rd ed. The American Radio Relay League, Inc., September 2015.
- [160] R. Goncalves, P. Pinho, and N. B. Carvalho, "Design and implementation of a 3d printed discone antenna for tv broadcasting system," in *2015 IEEE International Symposium on Antennas and Propagation USNC/URSI National Radio Science Meeting*, July 2015, pp. 314–315.
- [161] J. J. Lee, *Antenna Handbook - Vol II, Chapter 16*, Y. T. Lo and S. W. Lee, Eds. Van Nostrand Reinhold, 1993.

- [162] J. R. Costa, C. A. Fernandes, G. Godi, R. Sauleau, L. L. Coq, and H. Legay, "Compact ka-band lens antennas for leo satellites," *IEEE Transactions on Antennas and Propagation*, vol. 56, no. 5, pp. 1251–1258, May 2008.
- [163] C. A. Fernandes, J. R. Costa, E. B. Lima, and M. G. Silveirinha, "Review of 20 years of research on microwave and millimeter-wave lenses at "instituto de telecomunicações"," *IEEE Antennas and Propagation Magazine*, vol. 57, no. 1, pp. 249–268, feb 2015. [Online]. Available: <http://dx.doi.org/10.1109/MAP.2015.2397156>
- [164] R. Sauleau and B. Bares, "A complete procedure for the design and optimization of arbitrarily shaped integrated lens antennas," *Antennas and Propagation, IEEE Transactions on*, vol. 54, no. 4, pp. 1122–1133, April 2006.
- [165] W. Rotman, "Analysis of an ehf aplanatic zoned dielectric lens antenna," *IEEE Transactions on Antennas and Propagation*, vol. 32, no. 6, pp. 611–617, Jun 1984.
- [166] X. Wu, G. V. Eleftheriades, and T. E. van Deventer-Perkins, "Design and characterization of single- and multiple-beam mm-wave circularly polarized substrate lens antennas for wireless communications," *IEEE Transactions on Microwave Theory and Techniques*, vol. 49, no. 3, pp. 431–441, Mar 2001.